Probing the Magnetized Medium of Galaxies and AGNs using Wideband Radio Polarimetry

Dissertation

zur

Erlangung des Doktorgrades (*Dr. rer. nat.*)
der

Mathematisch–Naturwissenschaftlichen Fakultät

der

Rheinischen Friedrich–Wilhelms–Universität, Bonn

vorgelegt von
Maja Kierdorf
aus
Büren, Deutschland

Bonn 2019

Angefertigt mit Genehmigung der Mathematisch-Naturwissenschaftlichen Fakultät
der Rheinischen Friedrich–Wilhelms–Universität Bonn

1. Referent: Prof. Dr. Michael Kramer
2. Referent: Prof. Dr. Pavel Kroupa
Tag der Promotion: 11.07.2019
Erscheinungsjahr: 2019

RHEINISCHE FRIEDRICH–WILHELMS–UNIVERSITÄT BONN

Abstract

by Maja Kierdorf

for the degree of

Doctor rerum naturalium

I performed an observational study of diffuse linearly polarized synchrotron emission of a nearby galaxy and of extragalactic background sources in order to study cosmic magnetism. The speciality of my work is given by the polarimetric observations using *broadband* and multi-channel capabilities of the observing instrument. With these new broadband observations, depolarization mechanisms were used as a powerful new tool to probe the 3D structure of magnetic fields in a spiral galaxy. Additionally, modern techniques such as Rotation Measure (RM) Synthesis combines broadband multi-channel observations into Faraday depth spectra which encode the polarized emission from different origins along the line-of-sight and within a resolution element. For both studying wavelength dependent depolarization and applying RM-Synthesis, the key instrumental parameter for a successful scientific polarization analysis is the total wavelength coverage and the spectral resolution.

In Chapter 1, I summarize the current understanding of cosmic magnetic fields, specifically on their origin, structure, and strength in spiral galaxies and Active Galactic Nuclei (AGNs). This is followed by an overview on radio continuum processes and Faraday rotation and how I use polarization observations to study magnetic fields in Chapter 2. Chapter 3 treats the main technical methods used for the thesis specifically radio interferometry and RM-Synthesis.

In Chapter 4, I describe the new high angular resolution and broadband polarization observations of the nearby face-on oriented spiral galaxy M51 at S-band (2 – 4 GHz) using the Very Large Array (VLA). I discuss in detail the different imaging parameters used for wideband polarimetric data.

In Chapter 5, I present new images of the total intensity, the polarized intensity, the magnetic field structure, and the RM of M51. The observed frequency range probes the magnetic field in a so far unknown layer of the transition region between the disk and the halo[1] in M51. The high angular resolution data provide insights on the magnetic field structure on scales down to about 360 pc. The good sensitivity of about 20 μJy beam^{-1} (per spectral window) and the broad bandwidth provided by the VLA allow me to apply RM-Synthesis to obtain the first and high quality polarized intensity and RM maps of M51 at this frequency range. I computed the radial profile of the field regularity and depolarization in M51 and show that the total magnetic field must be more ordered at larger radii, i.e. the ordered field decreases more slowly as a function of radius than the turbulent field. Surprisingly, I found the observed RM in the disk-halo transition region to be dominated by fluctuations. This was also shown by the RM structure function at S-band. A fluctuating RM pattern indicates that the magnetic field in the disk-halo transition region is dominated by vertical (with respect to the galaxy plane) magnetic fields.

In Chapter 6, I present the study of wavelength-dependent depolarization in M51 across a frequency range of 1 – 8 GHz. I combined the new S-band polarization data with radio polarization VLA+Effelsberg data at C- and X-band at 4.85 GHz and 8.35 GHz and with broadband L-band (1 – 2 GHz) VLA data. This provides me with the widest wavelength coverage in a polarization data set ever existed for a nearby face-on spiral galaxy. The observed degree of polarization as a function of wavelength was compared to an analytical depolarization model developed by Shneider et al. (2014a). The model contains a multi-layer approach to decompose different magnetic field components in different layers of M51. The model makes distinct predictions of a two-layer (disk – halo) and three-layer (far-side halo – disk – near-side halo) system. Since the model predictions strongly differ within the wavelength range of S-band, the new S-band data are essential to distinguish between the different systems. I developed a python tool to visually inspect the influence of varying different model parameters to the behavior of the predicted fractional polarization as a function of wavelength and thus to find the best-fit

[1] I adopt the notification 'halo' for a physical layer between the synchrotron emitting disk and the observer (containing baryonic matter – not to be confused with a dark matter halo).

parameter values. With this tool, I attempted but failed to fit the three-layer model to the radio polarization data at S-band and thus a far-side halo is inconsistent with the new radio polarization observations and therefore, a two-layer system is more likely for M51. For a representative sector at a location with a high signal-to-noise radio in polarized intensity, I found a total regular field strength of $B_{\mathrm{tot,d}} \approx 10\,\mu\mathrm{G}$ in the disk and $B_{\mathrm{tot,h}} \approx 3\,\mu\mathrm{G}$ in the (near-side) halo and a total turbulent field strength of $b_{\mathrm{tot,d}} \approx 14\,\mu\mathrm{G}$ in the disk.

In Chapter 7, I present the second observational data set I have studied in this thesis where I investigate magnetic fields of unresolved extragalactic radio sources (EGSs). I observed 77 sources with the VLA at L-band (1 – 2 GHz) which were selected to have degrees of polarization $> 30\,\%$ at 1.4 GHz. Polarized emission of EGSs is believed to be produced in the jets and radio lobes of AGNs. The degrees of polarization of my sample are exceptionally high and thus could originate from extremely well-ordered magnetic fields. Given the typical redshifts of our target sample provided by the Sloan Digital Sky Survey (SDSS), with the high angular resolution observations I probe magnetic fields of AGNs on kpc scales. Due to imaging issues such as artifacts from poor uv-coverages and particularly weak signals in total intensity, only 12 targets were usable for scientific analysis. The final sample consists of sources with the highest signal-to-noise ratio ($>$ 10 in total intensity and $\geq$ 6 in polarized intensity). For those sources the newly observed degrees of polarization range from 20 – 50 %. I found a linearly increasing degree of polarization with increasing synchrotron spectral index with a correlation coefficient of 0.7 ($I \propto \nu^{\alpha}$, with spectral index α). I propose this to be related to the jet location traced by the observation: The radio emission of EGSs with flat spectral indices may originate from the region near the central core of the AGN where the jet is collimated and hence the magnetic field is well-ordered. Furthermore, I found all Faraday spectra to be simple with only one prominent peak (given the resolution in Faraday depth of $126\,\mathrm{rad\,m^{-2}}$). This shows that the sources probably experience only little Faraday depolarization intrinsic to the source and along the line-of-sight which is in agreement with the observed high degrees of polarization. It is remarkable to be able to draw such conclusions considering that I was not able to spatially resolve the sources in my observations. Hence, broadband polarization observations of

unresolved EGSs provide a new opportunity to study the characteristics of radio jets and lobes in AGNs.

In my thesis, I successfully probed the 3D structure of magnetic fields in the nearby spiral galaxy M51 and in a sample of extragalactic polarized background sources. I used modern tools such as wavelength-dependent depolarization mechanisms and RM-Synthesis technique and devised new ways of analyzing and interpreting broadband multi-channel polarimetric data. This thesis is one of the first projects analyzing broadband polarization data and provides important insights towards studying magnetic fields during the new era of radio astronomy provided by the Square Kilometre Array (SKA) which will be the leading instrument with the best resolution, sensitivity, and broadband capabilities for future research.

“If you only do what you can do, you will never be more than what you are now.”

– Master Shifu

Acknowledgment

I would like to thank those people who have accompanied me on many different ways.

My deep thank goes to **Dr. Sui Ann Mao**. As my advisor, she not only gave me the opportunity to work on this great and interesting project, she also inspired me and pushed me to get the best out of myself. She has an excellent expertise and I am glad to have learned a lot from her.

I would also like to thank **Prof. Dr. Michael Kramer**. I highly respect him for leading such a great research group. Thank you for giving me the opportunity to be part of this group. Michael was able to always find the right words to calm me down from my (sometimes very high) stress level and to motivate me at the same time.

Thank you also to **Prof. Dr. Pavel Kroupa** for step in as the second referee. It was always a pleasure to discuss with him about the project during the regular thesis committee meetings since he asked important and interesting questions and hence reminds me to not lose sight of the big picture.

I would also like to thank **Prof. Dr. Jochen Dingfelder** and **Prof. Dr. Barbara Kirchner** for being part of my PhD commission as the external examiners.

Many thanks also goes to **Dr. Rainer Beck** who supported me since my masters degree. Thank you for many interesting discussions about life, the universe and everything (especially during lunch time).

I also want to thank **Dr. Aritra Basu** who supported me and helped me understanding many difficult astrophysical and technical issues especially during the first year of my PhD.

Thank you **Yik Ki (Jackie) Ma** for being a great colleague and friend. We went through many awesome adventures together, be it understanding the complicated techniques used for our projects or traveling together through many different countries.

Many thanks also to **Dr. Wolfgang Reich**, **Dr. Olaf Wucknitz**, and **Nataliya Porayko** for carefully reading parts of my thesis and providing helpful comments. Special thanks goes to **Dr. Patricia Reich**, for not only reading parts of my thesis for correction, but also for her kind words and personal support whenever it was needed.

Also I want to thank my office mates **Madhuri Gaikwad** and **Weiwei Chen** and all other students in our group. We spend a great time together and especially I would like to thank you for giving me insights in all the different cultures from around the world! I think the multi-cultural shape makes our research group a very special and valuable place.

Thank you **Marilyn Cruces** for supporting me especially during the last very stressful phase of my PhD. Thanks a lot for sharing your tea and for all the wonderful conversations.

Thank you **Fabian Schwartzkopff** for the uncountable messages almost daily at 13:37 pm which always remind me being a real nerd.

One person who was with me for my whole life is my wonderful sister **Daniela Kierdorf**. She is by far the most sympathetic person I know and I love her not only for supporting me in the best possible way since many many years.

I also want to thank my very good friend **Stephanie Krämer**. Thank you for always making me laugh, for believing in me, and for being my friend!

Contents

Motivation

Magnetic fields are present everywhere in the Universe. They are observed on nearly all scales, from stars and galaxies up to galaxy clusters and even beyond. Magnetic fields on their own are invisible. Studying cosmic magnetic fields requires indirect methods to probe their strength, structure and impact on the Universe. Radio observations suggest that magnetic fields are essential for many astrophysical processes, such as cosmic ray electron (CRE) propagation in the interstellar medium (ISM), star formation and the evolution of galaxies (e.g. Beck, 2016) and collimation of jets in Active Galactic Nuclei (AGNs) (see e.g. Marscher, 2006 as a review). Yet despite their importance, our knowledge on the structure, origin and evolution of galactic-scale magnetic fields remains very limited. In turn, the lack of knowledge makes cosmic magnetism a subject of intense and exciting study.

For the understanding of the evolution of spiral galaxies, the process of the exchange of material between the disk and the halo is crucial. The interaction is believed to be driven by gas flows from so-called galactic fountains (e.g. Shapiro and Field, 1976; Bregman, 1980). Thermal pressure from the hot gas alone is not sufficient to produce the observed gas flows. Instead, magnetic pressure together with CREs can sufficiently drive fast flows of hot gas at least in massive star-forming galaxies (e.g Hanasz et al., 2013). However, the detailed influence of magnetic fields on galaxy evolution is still not fully understood.

While traditional mean-field dynamo predicts coherent magnetic fields predominately within the disks of galaxies, there is growing observational evidence that coherent fields also exist in galactic halos in the Milky Way and external galaxies (e.g. Krause, 2014; Beck and Wielebinski, 2013; Mao et al., 2012c). Some galaxies, including the Milky Way, show evidence for an X-shape halo field component (Jansson and Farrar, 2012; Heald et al., 2009; Krause, 2012; Irwin et al., 2012). These large-scale halo fields could result from advection of disk fields into the halo via large-scale winds, or from a dynamo operating in the halo (Sokoloff and Shukurov, 1990; Moss et al., 2010; Braun et al., 2010). Due to the lack of simultaneous measurements of both disk and halo field structures in galaxies, the origin of large-scale halo fields and how they are connected to the underlying galactic disk remains poorly understood.

As a major part of this thesis we investigate the magnetic field properties in the *transition region between the disk and halo* of the grand design spiral galaxy M51 using new data observed with the Very Large Array (VLA), providing high angular and high spectral reso-

lution. The new polarimetric data cover a frequency range from 2 – 4 GHz which allows us to study wavelength-dependent Faraday depolarization effects and to perform rotation measure (RM)-Synthesis to obtain an unambiguous RM distribution across the galaxy. Together with our new observational data set, we complete the set of polarization measurements at multiple frequencies and investigate the magnetic field properties over the widest frequency coverage in polarization of a nearby face-on galaxy to date. Shneider et al. (2014a) developed a model of the depolarization of synchrotron radiation in a multi-layer magneto-ionic medium. They developed model predictions for the degree of polarization as a function of wavelength for a two-layer system with a disk and a halo and a three-layer system with a far-side halo, a disk and a near-side halo. Since the model predictions strongly differ within the wavelength range of S-band, our new S-band data are essential to distinguish between the different systems.

The second project investigates the properties of unresolved extragalactic polarized background sources with exceptionally high degree of polarization. Strong polarized radio emission (a few tens of percent in fractional polarization) is most likely produced by powerful AGNs and radio jets and lobes. Sources with ultrahigh fractional polarization could represent a class of EGSs with intrinsically extremely well ordered magnetic fields. Thus, characterizing the polarization properties of highly polarized EGSs opens a new window towards understanding the process that generates extremely well ordered magnetic fields. Not only do polarization properties of individual sources reveal to us their intrinsic magnetic field structures, the Faraday RM of polarized EGSs are also used as background probes of magnetism in extended Galactic HII regions (Harvey-Smith et al., 2011), in nearby external galaxies such as the Small Magellanic Cloud (e.g. Mao et al., 2012a) as well as in galaxy systems at high redshifts (e.g. Kronberg and Perry, 1982). For such foreground magnetism studies and for the so called RM grid experiment (Gaensler et al., 2015), understanding the polarization and magnetic properties of EGSs is essential to distinguish the intrinsic and intervening signal.

The structure of the thesis is as follows. Chapter 1 gives a review on the current knowledge on the origin and structure of magnetic fields in galaxies and AGNs. In Chapter 2, methods to study cosmic magnetic fields are addressed and discussed. Chapter 3 provides an overview on observational and analytical techniques mainly used for this thesis. Chapter 4 treats the observation, data reduction, and imaging procedures of the new wideband polarimetric data. Chapter 5 summarizes the scientific analysis and results of the magnetic field in the nearby face-on spiral galaxy M51. In particular, we study the transition region between the disk and the halo in order to understand the origin of large-scale magnetic fields (on scales down to a few hundreds of pc) in halos of galaxies. In Chapter 6, we discuss a model of depolarization applied to polarization data of M51 between 1 – 8 GHz. Chapter 7 treats the study of magnetic fields on larger scales of up to several hundred kpc in EGSs with the goal to understand the process that generates extremely well ordered magnetic fields. In the last Chapter 8, we summarize the results and draw a broad conclusion of the work of this thesis.

CHAPTER 1

Introduction

In this thesis, the magnetic properties in a nearby spiral galaxy and in unresolved extragalactic background sources are investigated. To address open questions on cosmic magnetic fields in both kind of sources, this first chapter gives an introduction to our current knowledge on the structure and origin of magnetic fields in galaxies and in AGNs.

1.1 Origin and Structure of Cosmic Magnetic Fields

The origin of cosmic magnetic fields still is under debate. One possible scenario is the induction of magnetic fields by initial currents in the early universe. The ISM of galaxies, for example, consists of plasma mostly containing free electrons and protons. Due to the asymmetry of the proton-to-electron mass and the associated difference of their kinetic energy, a separation of charges occurs in rotating media such as galaxies, which forms electrical currents. These electrical currents can induce magnetic fields with field strength of $10^{-18} - 10^{-21}$ G into the ISM of galaxies (this number is based on numerical simulations on cosmological time-scales, Zweibel, 2011). The formation of initial magnetic fields due to charge separation is called *Biermann battery* effect (Biermann, 1950). However, this effect is by far not strong enough to explain the required currents to induce the observed μG magnetic field strengths.

Another scenario for the origin of cosmic magnetic fields is the formation of primordial fields, generated in the early Universe. These weak "seed" fields could even be involved in supporting the gravitationally collapse responsible for structure formation (Durrer and Neronov, 2013). Primordial seed fields can be amplified and aligned due to turbulence and compression in e.g the ISM of galaxies or the intra-cluster medium of galaxy clusters. For details on the origin of cosmic magnetic fields see also Wielebinski and Beck (2005).

The process of forming the present day observed magnetic fields with their strength and structure is separated into three stages. First, a seed field must be *generated*, which can

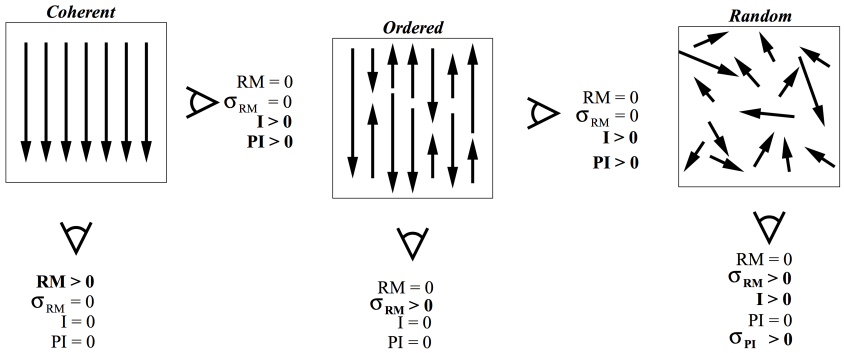

Figure 1.1.1: Simplified illustration of different field configurations and the corresponding observables total synchrotron intensity I, linearly polarized intensity PI, rotation measure RM, and the variance of the rotation measure σ_{RM}, for an ideal case with a well defined beam size. Note that in reality, the magnetic field lines are always connected, which is not illustrated in these Figures. Also note that the observed quantities are strongly dependent on the viewing angle of the observer. The different observables will be explained in Section 2 and 2.2. Image from Jaffe et al. (2010).

result from charge separation in different cosmological scenarios, such as plasma fluctuations in protogalaxies, injection by the first stars, or generation of seed fields by jets (see Section 1.3) produced by the first black holes (see Beck (2016) as a review). Secondly, to reach the present day μG magnetic field strengths, seed fields must be *amplified* on different scales and through different mechanisms. The effect of amplifying seed fields by turbulence in the gas is called small-scale dynamo. In the ISM of galaxies, the small-scale dynamo is predominantly driven by supernova explosions and stellar winds (e.g. Kim et al., 2006; Ferriere, 1996). The resulting field is an *isotropic turbulent magnetic field* (statistically random distribution of direction and orientation), also referred as *random magnetic field*. Figure 1.1.1 shows a simplified illustration of different magnetic field configurations. The right panel shows an illustration of a random magnetic field configuration. As a third step, turbulent fields can be *ordered* on larger scales (from kpc- up to Mpc-scales) for example by differential rotation in spiral galaxies, galaxy interactions (Elmegreen and Scalo, 2004) or by shock waves from supernova explosions in the ISM of galaxies (e.g. Balsara et al., 2004) or shock waves generated by mergers of galaxy clusters (e.g. Iapichino and Brüggen, 2012). The resulting *anisotropic turbulent magnetic field* where the field lines are aligned in a certain orientation with frequently occurring field reversals (middle panel of Figure 1.1.1), also referred to as *ordered magnetic field*, follows the spiral structure of the galaxy or is aligned parallel to the shock front. In spiral galaxies it is even possible to generate *coherent magnetic fields* (field lines with the same direction - left panel in Figure 1.1.1) on kpc-scales. Coherent fields are also referred to as *regular magnetic fields* with coherence scales much larger than the turbulence scales and no field reversals within the telescope beam (Kulsrud and Zweibel, 2008). Those regular fields are generated by the so-called large-scale or mean-field dynamo. Details on the formation process of regular magnetic fields in galaxies are described in the next section.

1.2 Magnetic Fields in Galaxies

The ISM of galaxies consists of different components, where the largest volume is present in form of ionized gas (up to 70 %) followed by neutral atoms (10 – 20 %) and molecules, dust, and cosmic rays (CRs) (e.g Longair, 2011). For the induction of magnetic fields from currents, positive and negative charges need to be separated. Thus, magnetic fields can be observed in the diffuse ionized medium (i.e. magneto-ionic medium), since there, the ions and electrons are apart from each other. Magnetic fields are present everywhere but only observable if certain circumstances are fulfilled: magnetic fields can be illuminated by CR electrons(CREs), for which the dominant key-acceleration process are supernova remnants. If the magnetic fields have μG strengths, they can be observed in the radio regime via synchrotron radiation (Section 2.1.2). In optical, magnetic fields can be traced by the emission from dust grains whose magnetic moments align along the magnetic field lines, producing a linearly polarized optical signal. In absorption and emission lines, the strength and direction of the parallel (with respect to the line-of-sight) component of the magnetic field can be directly measured via the Zeeman effect. Since Zeeman splitting needs high magnetic field strengths to be observable ($\sim$ 10 μG in the Milky Way and mG strengths in external galaxies), this effect can only be used to measure the strength of magnetic fields in dense regions of molecular gas. For the aim of this thesis, observations of radio emission generated by synchrotron radiation are used because this is a tracer of the structure of the large-scale magnetic field in the plane of the sky and can be observed across the entire extend of the diffuse ISM. Furthermore, synchrotron radiation provides information on the 3D structure of the magnetic field, since Faraday rotation of linearly polarized emission yields information on the line-of-sight component of the magnetic field and its direction (see Section 2.2.1).

Magnetic fields in spiral galaxies are well studied in both edge-on (inclination close to 90°) and face-on (inclination close to 0°) oriented galaxies. It has been observationally shown that the magnetic field in the disk of spiral galaxies is oriented mostly parallel to the spiral structure. More precisely, fields including random orientations are concentrated in spiral arms, especially in star-forming regions, while ordered fields are strongest in inter-arm regions, following the orientation of the adjacent gas spiral arms (Beck, 2009). One prominent example for a spiral structured magnetic field is seen in the face-on grand design "whirlpool" galaxy M51 and is shown in the left panel of Figure 1.2.1. Observations of edge-on spiral galaxies show plane-parallel magnetic fields along the disk, as expected from face-on observations. However, in the halo of edge-on galaxies the large-scale magnetic fields shows X-shape structures, as seen in the right panel of Figure 1.2.1. The origin of the magnetic field in the halo is still under debate. A possible origin could be a transport of the disk magnetic field via galactic winds from the disk into the halo (Krause, 2014; Heald, 2012). This is one of the key-questions addressed by an observational study of the nearby face-on spiral galaxy M51 in this thesis.

The strength of the total magnetic field in our own Galaxy is about 6 μG in the solar neighborhood, obtained from synchrotron radiation (assuming equipartition - see Section

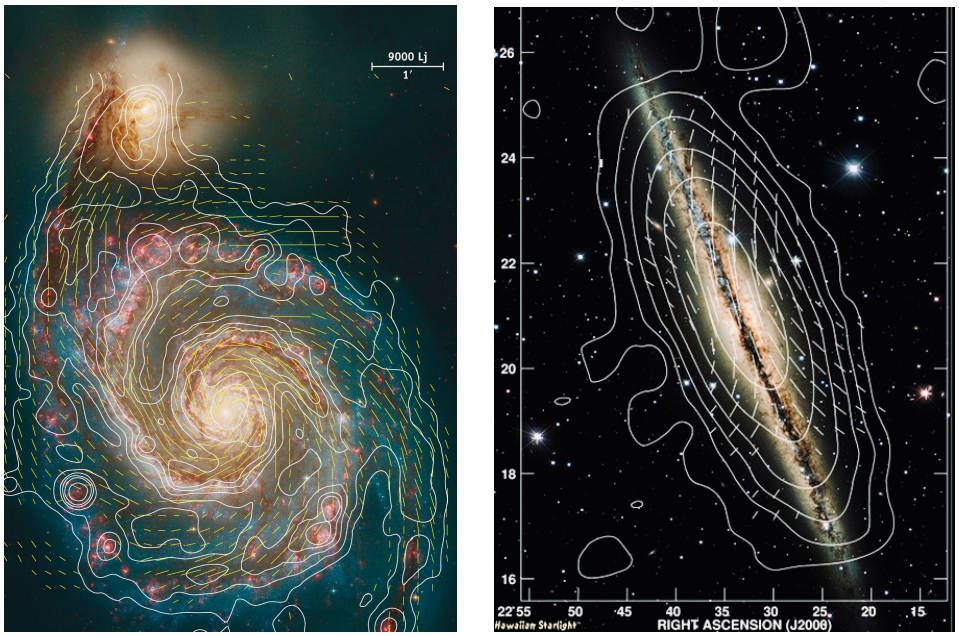

Figure 1.2.1: *Left:* Magnetic field lines in M51 and contours of total emission at $\lambda\,6\,\mathrm{cm}$ (VLA+Effelsberg), overlaid on an optical image (Fletcher et al., 2011). *Right:* Magnetic field lines and contours of the total radio emission at $\lambda\,3.6\,\mathrm{cm}$ of the edge-on spiral galaxy NGC 891, observed with the 100-m telescope in Effelsberg. The radio map is overlaid on an optical image of NG891 taken with the Canada-France-Hawaii Telescope (from M. Krause, MPIfR).

2.1.2 in Chapter 2), see review by Beck (2016) and references therein. The typical magnetic field strengths of external galaxies are found to be $10\,\mu\mathrm{G}$ on average. Stronger magnetic fields are found in galaxies with high star formation rates where the magnetic fields can reach strengths of typically up to $30\,\mu\mathrm{G}$ (Beck, 2009). Stronger star formation leads to stronger dynamo action which causes higher field strengths. The above described mechanisms of amplification and alignment of magnetic fields take place in the ISM of galaxies but can also be applied to the intra-cluster medium of galaxy clusters. So far, no magnetic fields were detected in elliptical galaxies (without central AGNs), possibly invisible due to the lack of CREs (produced by star formation processes such as supernova explosions and stellar winds) illuminating the magnetic fields. Some detections of large-scale magnetic fields were made in irregular galaxies such as, for example, the Large Magellanic cloud (e.g. Gaensler et al., 2005; Mao et al., 2012b) and NGC 4449 (e.g. Chyzy et al., 2000). The strongest magnetic fields of the diffuse ISM (about $50-100\,\mu\mathrm{G}$) are detected in starburst galaxies like M82 (Adebahr et al., 2013) and barred galaxies (Beck et al., 2005). In the Milky Way, a plane parallel magnetic field was detected, wheres towards larger latitudes, some indications of vertical magnetic fields can be seen (e.g. Planck Collaboration et al., 2016).

In spiral galaxies, the formation of *regular* or *coherent* magnetic fields on kpc-scales is attributable to the α-Ω-dynamo, where the α-term describes the influence of turbulence and the Coriolis force, and Ω the effect of differential rotation (Beck et al., 1996). To form

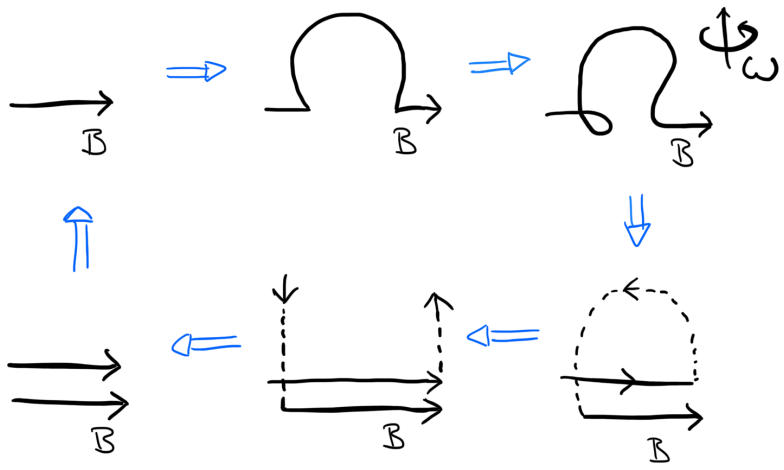

Figure 1.2.2: Simplistic illustration of the α-Ω-dynamo driven by a supernova according to Kulsrud (2005) and Kulsrud (2010).

regular large-scale fields, the α-Ω-dynamo needs ordered rotation of material and hence, in the intra-cluster medium of galaxy clusters it is not working. Figure 1.2.2 shows an illustration of the α-Ω-dynamo effect. According to e.g. Kulsrud (2005) and Kulsrud (2010), considering, for example, a supernova explosion in the disk of a spiral galaxy, the underlying magnetic field can be twisted by the Coriolis force in vertical direction, away from the galactic disk. Due to the differential rotation of the galactic disk and the moment of inertia of the supernova remnant, the rotation of the remnant slows down, which leads to a backward rotation relative to the galactic disk. This leads to an opposite positioning of the foot points of the remnant, so that the magnetic field lines are folded. This process amplifies the initial magnetic field. For real amplification, the supernova explosion must be powerful enough to blow out the magnetic field line entirely out of the gravitational potential of the galaxy, otherwise the remaining magnetic field line would annihilate with the newly generated line. Since differential rotation and star formation processes continue, this effect is highly repetitive and can produce the present day observed μG strengths of regular magnetic fields in spiral galaxies in about 10^9 years (e.g. Rodrigues et al., 2015).

The mean-field approximation of the α-Ω-dynamo equation (Beck et al., 1996; Ruzmaikin et al., 1988; Parker, 1979)

$$\frac{\partial \mathbf{B}}{\partial t} = \nabla \times (\mathbf{v} \times \mathbf{B}) + \nabla \times \alpha \mathbf{B} + \eta \nabla^2 \mathbf{B}\,, \tag{1.2.1}$$

where $\mathbf{B}$ is the strength of the magnetic field, $\mathbf{v}$ the velocity of the gas motion (i.e. rotational velocity and large-scale flows, for example due to galactic winds), and η the magnetic diffusivity can provide solutions with different symmetries, e.g. azimuthal symmetries (usually denoted with m for "modes") and vertical symmetries. Modes m are basically Fourier

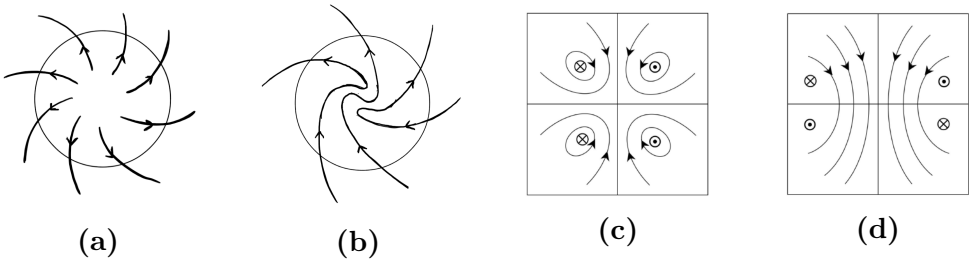

Figure 1.2.3: Possible large-scale magnetic field configurations in disk galaxies: Axisymmetric spiral (a) and bisymmetric spiral (b) field configuration of a face-on galaxy. Even (c) and odd (d) field configuration of an edge-on spiral galaxy (Haverkorn and Heesen, 2012). The illustrations show a simplified view of the magnetic field configurations, whereas in reality the magnetic field structure is more complicated.

expansions of the magnetic field in azimuthal angle. The most simple configurations are *axisymmetric* ($m = 0$) or *bisymmetric* ($m = 1$) in the disk plane and *even parity* or *odd parity* configurations with respect to the plane, as seen in edge-on galaxies (Figure 1.2.3). However, more complicated configurations in therms of higher order or a mix of different modes can be present in spiral galaxies.

1.3 Magnetic Fields in Extragalactic Background Sources

The distribution of the degree of polarization from extragalactic background sources shows a mean value of $\sim 2\,\%$ fractional polarization (Tucci et al., 2004), based on the NRAO VLA Sky Survey (NVSS)[1] catalog conducted by Condon et al. (1998) at 1.4 GHz and 45″ resolution. However, the maximum theoretical degree of polarization amounts to about 70 % (see Section 2.2). This indicates that most of the polarized radiation from EGSs experience strong depolarization (see Section 2.2.2) either intrinsic to the source and/or on the way to the observer as well as within the telescope configuration like the telescope beam and the observing subbands.

Polarized emission of EGSs is most likely produced by powerful AGNs. Magnetic fields in AGNs are present in radio jets, which can reach sizes of Mpc scales, by far larger than the size of the host galaxy. Radio jets originate in the center of AGNs, where the term 'active' refers to galaxies with an extreme energetic central region. The high energy level and the resulting high luminosity of such AGNs can not be attributed to stars of the ISM of the AGNs host galaxy. Instead, the strong luminosity is generated by a supermassive black hole (SMBH) forming an accretion disk which strongly radiates in optical, ultra-violet (UV), and X-ray. In some cases, the luminosity of the central AGN is so high that it can over-shine the emission of the entire host galaxy. The strong luminosity makes AGNs to perfect candidates for studying distant objects in the early Universe. The energy spectrum

[1] http://www.nrao.edu

of AGNs reflects the different emission mechanisms occurring in the source. Compared to galaxies, the energy spectrum shows signatures at a broad range of frequencies: From radio to γ-ray frequencies, emitted from different locations within the AGN. The radio emission is generated by synchrotron radiation processes (see Section 2.1.2) in the radio jets, whereas the optical emission comes from the accretion disk. The X-ray emission is produced by inverse Compton scattering of photons from the accretion disk by a corona of hot electrons located above the central SMBH (Peterson, 1997).

Radio jets are formed close to the accretion disk of the central SMBH driving material into the galactic medium. Typically, two radio jets are formed, pointing in opposite directions from the central nucleus. Jets are made of magnetic fields which can transport charged particles out to large distances into the inter-galactic medium (IGM). The detailed process of jet formation is still poorly understood. A commonly accepted theory is that the jet get launched close to the SMBH, powered by rotation. Instabilities in the magnetic field at the surface of the accretion disk could cause "flares", which are then collimated parallel to the rotation axis of the disk (Longair, 2011).

Radio jets contain CREs and hence they can be observed via synchrotron radiation (see Section 2.1.2). The key-acceleration process of CREs in jets is still under debate (e.g Romero et al., 2017). An observational overview of magnetic fields in AGN jets on pc-scales is given in Hovatta (2017). Observational studies of jets on kpc-scales are very rare. Theoretically, the degree of polarization can reach values up to about 70% if the magnetic field is completely ordered (see Section 2.2). However, such high polarization degree values are not typically seen in AGN jets in the radio (e.g. Aller et al., 2003; Lister and Homan, 2005). Therefore, magnetic fields in jets must be (in general) disordered (or the polarized emission experience strong depolarization within the source or along the line-of-sight). The structure of the magnetic field in radio jets is showing either a parallel or perpendicular orientation relative to the jet axis, depending on the level of helicity (Worrall et al., 2007; Pudritz et al., 2012). RM gradients (see Section 2.2.1) have been observed in some jets, which could be a hint for the jet structure to be helical and collimated along the entire jet (e.g. Gabuzda et al., 2017). A typical magnetic field strength of 200 μG was measured in jets (e.g. Pudritz et al., 2012), whereas close to the core, the magnetic field strength can amount up to 200 mG (O'Sullivan and Gabuzda, 2009).

When the material blown out by the jet reaches a medium with high density, the particles will be decelerated and radio lobes can be formed. Radio lobes often have hot spots with very high intensity in the radio regime. Radio lobes host both turbulent and ordered magnetic fields (Black et al., 1992; Bridle et al., 1994; Leahy et al., 1997) with a strength of about of tens of μG in the lobes, and up to 250 μG in the hot spots (Longair, 2011). One of the most popular examples of an AGN which contains both, radio jets and radio lobes, is shown in Figure 1.3.1. The viewing angle allows the observer to trace both radio jets and lobes, pointing into opposite directions from the central nucleus.

To study the magnetized plasma of EGSs one can analyze their polarization properties. Studying the linear polarization properties of unresolved EGSs at radio wavelengths provides

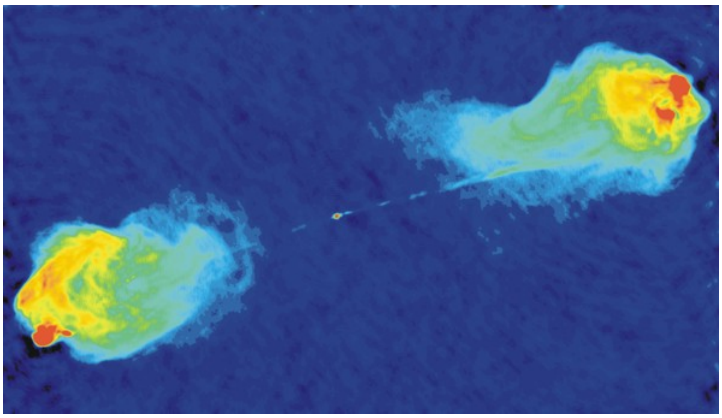

Figure 1.3.1: False color image of the radio jet and lobes in the luminous radio galaxy Cygnus A at 5 GHz with 0.5″ resolution, observed with the VLA. Red color shows regions with the brightest radio emission (hot spots), while blue color shows regions of fainter emission (image from R. Perley, C. Carilli & J. Dreher, NRAO). Original publication: Perley et al. (1984).

a new opportunity to probe the magneto-ionic medium on spatial scales below the resolution limit (e.g. Burn, 1966; Gardner and Whiteoak, 1966; Gaensler et al., 2015) and to learn more about the environment and evolution of radio galaxies and AGNs (e.g. Goodlet and Kaiser, 2005; Bernet et al., 2008). Since EGSs are also used as background probes to study the magnetic properties in intervening systems such as the intra-cluster medium of galaxy clusters (e.g. Bonafede et al., 2010; Pizzo et al., 2011), intervening galaxies along the line of sight (e.g. Gaensler et al., 2005; Mao et al., 2008; Feain et al., 2009) and our own Galaxy (e.g. Taylor et al., 2009; Mao et al., 2010; Harvey-Smith et al., 2011; Van Eck et al., 2011), understanding their polarization and magnetic properties is essential to separate the intrinsic signal from modifications of the signal by intervening systems.

CHAPTER 2

Radio Observations as Tracers of Magnetic Fields

The study of this thesis is based on observation in radio regime. In the following, I provide an overview on radio emission processes. Further, I will explain how magnetic fields are studied using radio observations.

2.1 Radio Continuum Spectrum

Radio continuum emission is separated into thermal and non-thermal radiation. Magnetic fields are traced by non-thermal synchrotron emission while the observed radio continuum emission of galaxies (see observational results on M51 in Chapter 5) contains a fraction of thermal emission as well.

A typical radio continuum spectrum of a nearby star-forming galaxy is shown in Figure 2.1.1. As the diagram shows, thermal emission of free electrons (also known as thermal bremsstrahlung or free-free emission) dominates the spectrum over synchrotron emission only within a small range (in this case between $\sim 30-200\,\mathrm{GHz}$), whereas at lower frequencies (below 30 GHz), non-thermal synchrotron radiation represents the dominant contribution to the total emission. Within a small frequency range of about $10-40\,\mathrm{GHz}$, emission which is believed to originate from rapidly spinning dust grains (also known as anomalous microwave emission (AME)) can dominate the radio spectrum of galaxies (Murphy et al., 2018). Beyond $\sim 200\,\mathrm{GHz}$, the spectrum is dominated by far thermal dust emission.

2.1.1 Thermal Emission – Radiation from a Free Electron

Thermal continuum radiation in the radio regime is produced by free-free emission or thermal bremsstrahlung. Free electrons move in a hyperbolic orbit around an ionized atom (in most cases a proton) and loose part of their energy in form of a photon. The resulting photons

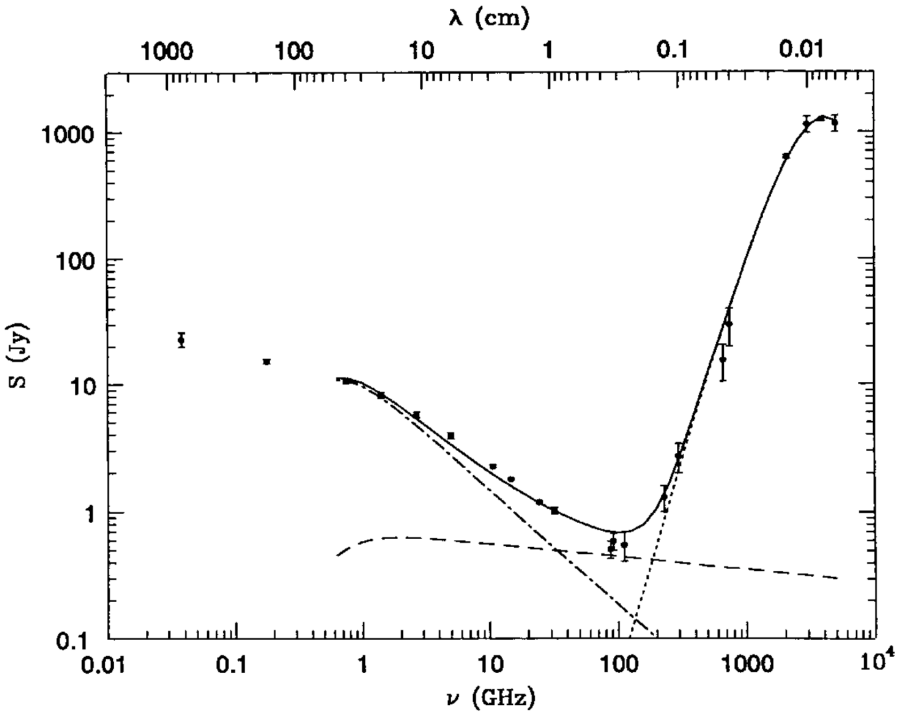

Figure 2.1.1: The observed radio and far infrared (FIR) spectrum of the nearby star-forming spiral galaxy M82 (Klein et al., 1988; Carlstrom and Kronberg, 1991). The total spectrum is the sum (solid line) of synchrotron (dot-dash line), free-free (dashed line), and dust (dotted line) components. The HII regions in this bright starburst galaxy start to become opaque below $\nu \sim 1\,\mathrm{GHz}$: For thermal emission the spectrum becomes optically thick, and absorption of synchrotron emission by thermal gas reduces the synchrotron flux density. The free-free component is largest only in the poorly observed frequency range $30-200\,\mathrm{GHz}$ (Condon, 1992).

form a thermal radiation spectrum. This radiation is produced by an ensemble of free electrons that have random motions and random energies, therefore the resulting spectrum is a continuum and the emission is unpolarized. The typical spectral index of thermal radiation in galaxies amounts to $\alpha_{\mathrm{th}} = -0.1$[1] if the thermal emission is optically thin.

2.1.2 Non-thermal Emission – Synchrotron Radiation

Non-thermal synchrotron radiation is produced by cosmic ray electrons (CREs) that gyrate along magnetic fields in media such as the ISM of galaxies or in the intra-cluster medium of galaxy clusters. Due to the Lorentz force

$$\mathbf{F}_{\mathrm{L}} = \frac{e}{c}\,(\mathbf{v} \times \mathbf{B})\ , \tag{2.1.1}$$

[1]The spectral index is defined as $I_\nu \propto \nu^{\alpha_{\mathrm{th}}}$ in the case of thermal emission.

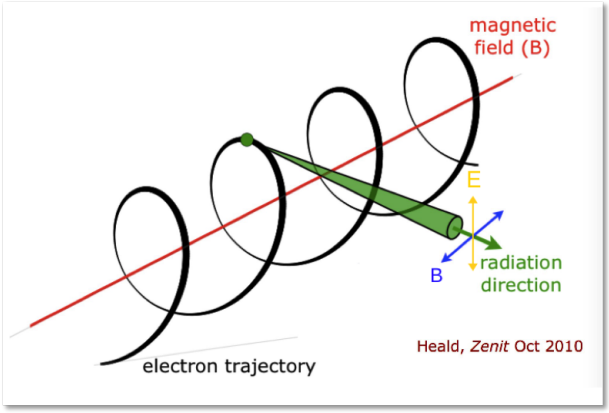

Figure 2.1.2: Schematic of synchrotron radiation produced by a relativistic electron spiraling around a magnetic field line (Credit: Heald & Zenit).

relativistic electrons are constrained to spiral around the magnetic field lines, where e is the electron charge, c the speed of light, $\mathbf{v}$ the velocity of the electron, and $\mathbf{B}$ the magnetic field. The radiation results in a synchrotron spectrum, which occurs in a characteristic frequency range (GHz regime for μG magnetic field strengths). Figure 2.1.2 shows a schematic of synchrotron radiation in case of an electron. The energy distribution of the emitting electrons traveling through a magnetic field may be given by a power-law

$$N(E)\mathrm{d}E \propto E^{g}\mathrm{d}E\,, \tag{2.1.2}$$

where g is the energy spectral index and $N(E)$ the number density of electrons in the energy range $E+\mathrm{d}E$. When the electrons orbit around the magnetic field, they lose energy. The integration over the emission spectra from individual electrons results in a typical synchrotron spectrum seen in Figure 2.1.3, which also shows a power-law

$$I_\nu \propto \nu^{\alpha_{\mathrm{nth}}}\,, \tag{2.1.3}$$

where I_ν is the emitted intensity and $\alpha_{\mathrm{nth}} = \frac{g+1}{2}$ the non-thermal synchrotron spectral index.

The intensity of synchrotron emission is dependent on the number density of CREs n_{CRE} (cm^{-3}), the strength of the magnetic field component perpendicular to the line-of-sight $B_\perp$ (μG) in the emitting region, and the observing frequency ν:

$$I_\nu \propto n_{\mathrm{CRE}} \cdot B_\perp^{1-\alpha_{\mathrm{nth}}} \cdot \nu^{\alpha_{\mathrm{nth}}} \tag{2.1.4}$$

According to Beck and Krause (2005), assuming equipartition[2] of cosmic ray electron energy and the energy of the magnetic field: $E_{\mathrm{CRE}} = E_B = B^2\,/\,8\pi$, it is possible to deduce an expression for the total magnetic field strength B_{tot}, only dependent on the observed

[2]Energy equipartition means that particles in a system which is in thermal equilibrium have on average the same energy density.

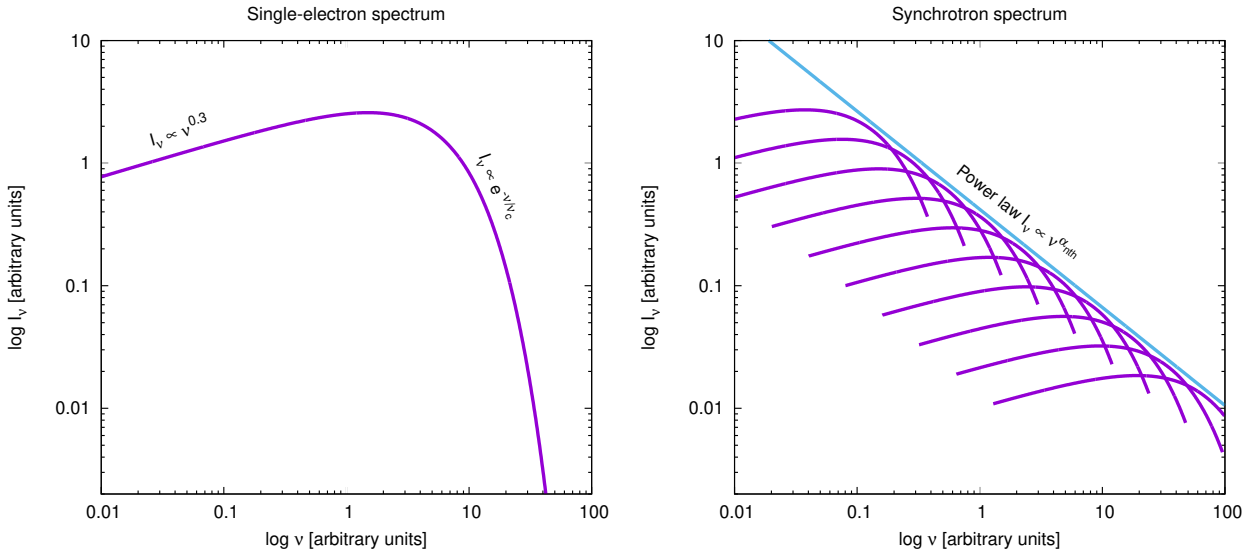

Figure 2.1.3: Spectrum of a single electron (left) and the total synchrotron spectrum (right) which is the sum of emission spectra from individual electrons (Figure credit: Uli Klein, AIfA Bonn).

synchrotron intensity I_ν, the frequency ν, the path length through the synchrotron emitting medium L, and the ratio of proton-to-electron density $K = n_{\mathrm{CR_p}}/n_{\mathrm{CR_e}}$:

$$B_{\mathrm{tot},\perp} \propto \left[(K+1)\, I_\nu\, \nu^{\alpha_{\mathrm{nth}}}/L\right]^{1/(3-\alpha_{\mathrm{nth}})} \tag{2.1.5}$$

The proton-to-electron ratio is uncertain, since it is strongly dependent on the acceleration mechanism of CREs. In disks of spiral galaxies, a proton-to-electron ratio of $K = 100$ is a generally assumed approximation (Bell, 1978). There are several issues with estimating the magnetic field strength using the equipartition formula (Beck, 2016): (1) Equipartition only holds for sources with steep radio spectra where $\alpha_{\mathrm{nth}} < -0.5$. (2) Using the equipartition formula can overestimate the total magnetic field strength if B_{tot} varies along the line-of-sight or within the observing telescope beam. (3) In regions with strong magnetic fields and high gas density (regions with high star formation rate), the ratio of CREs and CR protons is different from the global value, because CREs are much more affected by energy losses compared to protons. Hence, the proton-to-electron density ratio becomes larger in regions with strong star formation.

2.2 Radio Polarization

Considering a distribution of non-relativistic electrons spiraling around magnetic field lines, the radiation is circularly or, in projection to the sky plane, elliptically polarized since the electrons emit radiation in a cone perpendicular to the magnetic field. When the electron

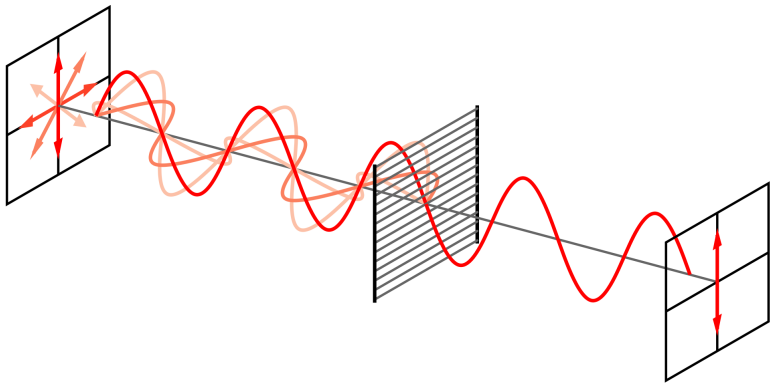

Figure 2.2.1: Illustration of an unpolarized and linearly polarized electro-magnetic wave. Unpolarized radiation is an assemble of electro-magnetic waves with randomly distributed polarization angles as illustrated in the left part of the sketch. In the case of a linearly polarized wave, the angle between a certain axis and the plane of polarization does not change (illustrated in the right part of the sketch). Image Credit: http://physicsopenlab.org/2016/03/13/electromagnetic-waves-polarization/

velocity approaches the speed of light, the emission pattern is sharply collimated forward and appears like a narrow beam. Therefore, only the emission from electrons whose emission direction is pointed directly towards the observer (parallel to the line-of-sight) within the narrow emission cone (see Figure 2.1.2) is visible. The emission from a single relativistic particle is elliptically polarized, while the emission from an assemble of charged relativistic particles moving through a magnetized plasma, is linearly polarized (the elliptical components will cancel out, as emission cones will contribute equally from both sides perpendicular to the line-of-sight – see Chapter 6.5 of Rybicki and Lightman (1986)). This is the reason why we see linearly polarized synchrotron emission. This means that the orientation of oscillation of the transverse electro-magnetic wave does not change along the propagation direction. Figure 2.2.1 illustrates the difference of unpolarized radiation compared to a linearly polarized electro-magnetic wave.

Considering two electro-magnetic polarized waves with different amplitudes E_1 and E_2 moving in z-direction, the electric field (E_x, E_y) can be described by

$$E_x = E_1 \cos(kz - \omega t) \tag{2.2.1}$$
$$E_y = E_2 \cos(kz - \omega t - \delta)\,, \tag{2.2.2}$$

where k is the wave number, ω the frequency and t the time. If there is a phase-shift δ between the transverse and vertical component, the wave is elliptically polarized. The detected wave is then given by the vector sum $\vec{E} = E_x\hat{e}_x + E_y\hat{e}_y$, where $\hat{e}_x$ and $\hat{e}_y$ are the unit vectors in x and y direction. The length of this vector changes depending on the relative phase shift and the amplitudes of the individual components. If the there is no relative phase shift between the two components ($\delta = 0°$ or $\delta = 180°$), the wave will be linearly polarized. The angle of the polarization plane (relative to the y-direction if the wave propagates in z-direction) is

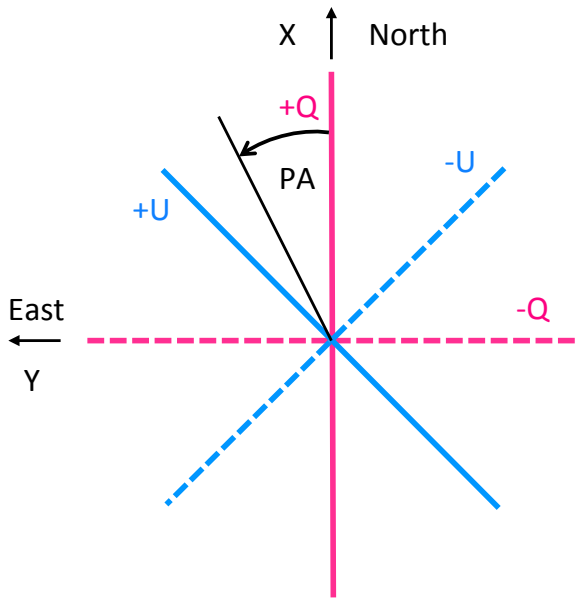

Figure 2.2.2: The polarization convention defined by the International Astronomical Union (IAU). The local x-axis points to the North, the local y-axis points to the East, and the local z-axis points inwards to the observer for a right-handed system.

dependent on the amplitude difference of the two components. For example, if $E_1 = E_2$ and $\delta = 0$, the resulting polarization angle of the linearly polarized electro-magnetic wave is 45°.

To describe the polarization properties of an electro-magnetic wave in a simple way, George Gabriel Stokes in 1852 defined the so-called Stokes parameters I, Q, U and V. The Stokes parameters are connected to the properties of the electro-magnetic wave (on a linearly polarized basis) as:

$$I = E_1^2 + E_2^2 \tag{2.2.3}$$
$$Q = E_1^2 - E_2^2 \tag{2.2.4}$$
$$U = 2\,E_1\,E_2\,\cos(\delta) \tag{2.2.5}$$
$$V = 2\,E_1\,E_2\,\sin(\delta) \tag{2.2.6}$$

The different Stokes parameters provide individual information on the intensity distribution described by Stokes I, the linearly polarized emission described by Stokes Q and U, and on the circular polarization Stokes V. The total power of an observed source is represented by Stokes I. For a completely unpolarized wave, $Q = U = V = 0$ and the entire power of the source is given by its total intensity. For purely linearly polarized waves, only the Stokes parameter V vanishes.

Figure 2.2.2 illustrates the definition of the Stokes parameters Q and U, describing the linear polarization state of the electro-magnetic wave. By definition, Stokes Q and U can have positive and negative values. Changing the polarization angle by 90° changes the sign

of the signal in Stokes Q and U. The linearly polarized intensity $\mathbf{P}$ can be expressed as a complex vector quantity where the observed Stokes parameters Q and U are the vector components of $\mathbf{P}= Q + iU \; = \; p\,I\,e^{i2\psi} \; = \; p\,I \cdot (\cos(2\psi) + i\sin(2\psi))$. The polarization angle ψ which is the angle between the polarization plane and the north-axis (called PA in Figure 2.2.2) is given by:

$$\psi = \frac{1}{2}\tan^{-1}\left(\frac{U}{Q}\right) \tag{2.2.7}$$

The linearly polarized intensity PI is given by the length of the complex polarization vector

$$|\mathbf{P}| = PI = \sqrt{\mathrm{Q}^2 + \mathrm{U}^2}\,. \tag{2.2.8}$$

Since the polarization plane of the electro-magnetic wave is perpendicular to the magnetic field orientation in the emission region (compare Figure 2.1.2), synchrotron emission traces the magnetic field component in the plane of the sky, perpendicular to the line-of-sight $\mathrm{B}_\perp$. Observing synchrotron emission of astronomical objects is a powerful tool to probe the structure of cosmic magnetic fields.

The degree of linear polarization p is given by the ratio of the polarized intensity PI and the total intensity I and can be expressed by the synchrotron (non-thermal) spectral index α_{nth} of the emission region (Le Roux, 1961):

$$p = \frac{PI}{I} = \frac{3 - 3\alpha_{\mathrm{nth}}}{5 - 3\alpha_{\mathrm{nth}}} \tag{2.2.9}$$

For $\alpha_{\mathrm{nth}} = -0.1$ to -1.0 ($I_\nu \propto \nu^{\alpha_{\mathrm{nth}}}$), the maximum observable fractional linear polarization can reach up to 67 % to 75 % for a perfectly ordered magnetic field. The intrinsic polarization fraction can be reduced by different depolarization mechanisms, which are described in Section 2.2.2. Studying these depolarization processes can be used as a powerful probe of the magneto-ionic medium of e.g. the ISM in galaxies.

2.2.1 Faraday Rotation

To get information on the three-dimensional (3D) structure of the magnetic field in the interstellar medium of galaxies or in the intra-cluster medium of galaxy clusters, the third magnetic field component parallel to the line-of-sight is required. This component can be derived from measurements of Faraday rotation: A linearly polarized electro-magnetic wave can be decomposed into two circular (left-handed and right-handed) components with equal amplitude. Since the refractive index of a magnetized medium with thermal electrons is different for the two components, the propagation speeds slightly differ. This causes a difference in phase velocity and from this, a relative phase shift between the two components occurs. As a consequence, in the presence of a magnetized plasma with thermal electrons, the polarization angle. ψ observed at λ of a linearly polarized electro-magnetic wave will be rotated relative to the intrinsic polarization angle ψ_0 of the emission region. The polarization

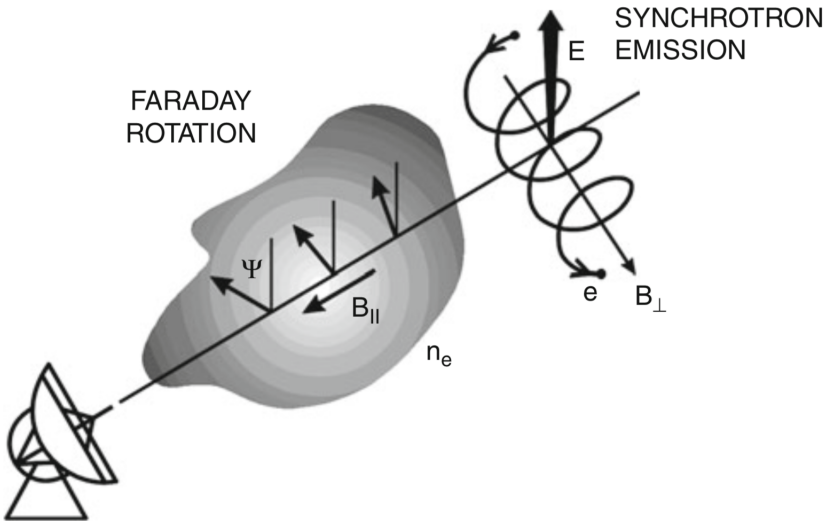

Figure 2.2.3: Illustration of Faraday rotation: A linearly polarized electromagnetic wave at frequency ν passes through a magnetized plasma, and as a consequence the plane of polarization changes by the angle ψ. The schematic shows how synchrotron emission traces the magnetic field component perpendicular to the line-of-sight intrinsic to the synchrotron emitting source, while the parallel component of the magnetic field in a thermal plasma can be traced by Faraday rotation. Both methods together give a 3D picture of the magnetic field along the line-of-sight. Image credit: Beck and Wielebinski (2013).

angle changes proportional to λ^2 where the proportionality constant is the so-called rotation measure (RM):

$$\psi = \psi_0 + \mathrm{RM} \cdot \lambda^2 \tag{2.2.10}$$

An illustration of the effect of Faraday rotation is shown in Figure 2.2.3. RM is measured in $\mathrm{rad\,m^{-2}}$ and is dependent on the charge and mass of the electron e and m_e, the speed of light c, the thermal electron density n_e ($\mathrm{cm^{-3}}$) and on the strength of the magnetic field component $\mathbf{B}_\parallel$ (μG) of the Faraday rotating medium parallel to the line-of-sight $\mathbf{l}$ (pc):

$$\mathrm{RM} = \frac{e^3}{2\pi m_\mathrm{e}^2 c^4} \int_\mathrm{source}^\mathrm{observer} n_\mathrm{e} \mathbf{B}_\parallel \cdot \mathrm{d}\mathbf{l} \tag{2.2.11}$$

RM is positive (negative) for magnetic fields directed towards (away from) the observer. From observations, RM can be determined by plotting the frequency dependence of the observed polarization angle ψ vs. λ^2. The slope of this dependency gives the RM and the intrinsic polarization angle ($\psi_0 = \psi - \mathrm{RM} \cdot \lambda^2$). Since the polarization angle is a quantity which is measured between plus and minus 90° (or between 0° and 180°), measurements at only two frequencies cannot distinguish between ψ and $\psi + n\pi$ ($n \in \mathbb{Z}$) which makes it hard to derive the rotation measure unambiguously (especially when RM is high). This is commonly referred to as the $n\,\pi$ ambiguity. Broadband observations, typically over a range of a few GHz, can solve the ambiguity. Furthermore, it is possible that in a single beam

volume, sources of polarized emission with different RM contributions can be present. The signals from such regions mix, which breaks the linear dependency of the polarization angle and wavelength. In such complex cases, RM is referred as Faraday depth ϕ which is not constant anymore. More details on complex Faraday rotation and how to decompose the signals is given in Section 3.2.

2.2.2 Depolarization

Investigating depolarization effects of linearly polarized synchrotron emission is a powerful tool to put constraints on different magnetic field components in, for example, the ISM of galaxies. To define the different depolarization mechanisms, one distinguishes between media which only rotate the plane of polarization (magnetized medium including thermal electrons) and media which contain synchrotron emitting and Faraday rotating components (magnetized plasma including thermal electrons and cosmic rays). Depending on the intrinsic magnetic field morphology, that is whether the magnetic field has regular or isotropic or anisotropic turbulent character, the main observables of synchrotron emission total intensity (I), polarized intensity (PI), and RM differ (compare Figure 1.1.1). Not only the total amount of these observables tell us something about the underlying magnetic field structure, also studying wavelength-dependent depolarization effects allow us to investigate magnetic fields in the Universe.

The intrinsic degree of polarization (Equation 2.2.9) can be reduced by different effects within the source or along the line-of-sight between the source and the observer, or within the volume traced by the telescope beam. Depolarization mechanisms can be broadly divided into wavelength-independent and wavelength-dependent effects. Besides physical reasons for depolarization caused by Faraday rotation, there are additional depolarization effects caused by properties of the observing instrument such as the beam size and the observing bandwidth. The present day depolarization models are all based on the work of Burn (1966) and Sokoloff et al. (1998), who studied the degree of polarization of radio sources as a function of wavelength with different underlying magnetic field configurations (whether turbulent fields are present or how magnetic fields change the amount of Faraday rotation along the line-of-sight). In the following, different depolarization effects and their conditions are summarized.

Beam depolarization

Beam depolarization occurs when the magnetic field intrinsic to the synchrotron emitting source is tangled on scales smaller than the telescope beam. The polarization fraction then smeared out over the beam size and the measured polarization reduces relative to the intrinsic polarization fraction. This wavelength-independent depolarization effect can modify the intrinsic degree of polarization in the presence of turbulent magnetic fields. Observing with high angular resolution can reduce the effect of beam depolarization. In nearby galaxies, a typical beam size of a few arcsec (when observing with radio interferometers, see Section 3.1) results in linear scales of a few hundred pc up to kpc scales. Since the turbulence

scales in the ISM of galaxies are smaller (typically about 50 pc, e.g. Fletcher et al., 2011; Beck, 2016), the polarized signal observed in nearby galaxies is always attenuated by beam depolarization. On the other hand, for example in radio relics of galaxy clusters, magnetic fields can be well ordered over large-scales (up to Mpc). In such objects, it is possible to directly observe the intrinsic degree of polarization, even with single-dish telescopes as the 100-m Effelsberg radio telescope (e.g. Kierdorf et al., 2017). The same holds for giant radio galaxies whose radio jets and lobes are extended over Mpc scales (e.g. Schoenmakers et al., 2000).

Bandwidth depolarization

Another effect which is connected to the observing instrument that reduces the degree of polarization is bandwidth depolarization. Since the observed polarization angle is dependent on the observing wavelength ($\psi = \psi_0 + \mathrm{RM}\lambda^2$), observations with wide frequency bands can reduce the degree of polarization. Particularly, the plane of polarization Faraday rotates by slightly different angles at different frequencies within the observing frequency band. Averaging over the frequency band entails the reduction of the polarized signal. Mathematically, the degree of polarization reduced by bandwidth depolarization can be expressed as

$$p(\lambda^2) = p_0 \frac{\sin(\Delta\psi)}{\Delta\psi}\,, \tag{2.2.12}$$

where $\Delta\psi = \mathrm{RM} \cdot (\lambda^2_{\mathrm{max}} - \lambda^2_{\mathrm{min}})$, with the observed rotation measure (RM in $\mathrm{rad\,m^{-2}}$) and the smallest (λ_{min} in m) and largest (λ_{max} in m) observing wavelength. p_0 is the intrinsic degree of polarization (e.g. Burn, 1966; Klein and Fletcher, 2015). To reduce bandwidth depolarization, the band can be split into small sub-bands which, however, decreases the image quality due to higher noise level in the sub-band images. To avoid bandwidth depolarization, one can apply the so-called RM-Synthesis technique on the polarization data. A detailed description of this method is given in Section 3.2.

Differential Faraday rotation (DFR) - also known as *Burn slab*

If the synchrotron emitting and Faraday rotating source are present in the same volume, differential Faraday rotation occurs. The polarization plane of electro-magnetic waves emitted from different layers of near and far side regions will be rotated by different amounts of Faraday rotation. This results in a reduced polarized signal after integrating over the entire region along the line-of-sight. If the medium contains a purely coherent (regular) magnetic field and constant electron density, the intrinsic polarization fraction p_0 will be reduced by

$$p(\lambda^2) = p_0 \frac{|\sin(2\mathrm{RM}\lambda^2)|}{|2\mathrm{RM}\lambda^2|}\,, \tag{2.2.13}$$

where RM is the observed rotation measure (Burn, 1966; Sokoloff et al., 1998; Arshakian and Beck, 2011). Differential Faraday rotation occurs, for example, in the ISM of spiral galaxies, where regions with thermal electrons generated by ionizing starlight, CREs accelerated in e.g. supernova remnants, and large-scale regular magnetic fields are mixed.

Internal Faraday dispersion (IFD)
In the case where turbulent magnetic fields are present within the emitting region, the polarized signal will be reduced by internal Faraday dispersion. The plane of polarization gets randomly Faraday rotated along the line-of-sight and after integrating over the emission region (along the line-of-sight) opposite directions cancel out, what reduces the observed polarization degree. For this case, the observed degree of polarization decreases by a relation dependent on the RM dispersion σ_{RM} and the observing wavelength to the power of 4 (Burn, 1966; Sokoloff et al., 1998):

$$p(\lambda^2) = p_0 \frac{1 - e^{-2\sigma_{\mathrm{RM}}^2 \lambda^4}}{2\sigma_{\mathrm{RM}}^2 \lambda^4} \tag{2.2.14}$$

The dispersion of the RM is dependent on the average electron density $\langle n_{\mathrm{e}} \rangle$, the average strength of the turbulent magnetic field $\langle B_{\mathrm{turb}} \rangle$ parallel to the line-of-sight and the turbulence cell size d (given in pc):

$$\sigma_{\mathrm{RM}}^2 = (0.81 \langle n_{\mathrm{e}} \rangle \langle B_{\mathrm{turb}} \rangle)^2 L d / f \tag{2.2.15}$$

$f = \langle n_{\mathrm{e}} \rangle / n_{\mathrm{e}}$ is the filling factor of the turbulent cell and L the path length through the medium (in pc). Since turbulent magnetic fields are present in e.g. the ISM of spiral galaxies, internal Faraday dispersion can be detected in observations of galaxies, especially in star-forming regions where the small-scale dynamo is most efficient and hence the turbulent magnetic field is strong.

External Faraday dispersion (EFD)
If the polarized signal crosses a Faraday rotating region along the line-of-sight, which contains a turbulent magnetic field component, the signal will be depolarized by external Faraday dispersion. For significant depolarization, the turbulent cell size must be smaller than the telescope beam. The same holds if a regular magnetic field changes the strength or direction within the telescope beam. In case of external Faraday dispersion the intrinsic polarization fraction will be reduced by

$$p(\lambda^2) = p_0 e^{-2\sigma_{\mathrm{RM}}^2 \lambda^4} \,. \tag{2.2.16}$$

The Milky Way foreground can cause external Faraday dispersion when observing extragalactic polarized radio sources. At GHz frequencies, this effect decreases when observing targets with high Galactic latitude ($|b| > 20°$) due to less possible confusion with magnetized structures in the Galactic plane (Schnitzeler, 2010).

The above equations can be fitted to the observed degree of polarization as a function of wavelength to get information on the intrinsic magnetic field configuration. Particularly, by fitting different models to multi-frequency polarization data, one can distinguish between regular and turbulent magnetic field configurations as well as whether the depolarization occurs internally or externally of the synchrotron emitting source. A detailed model application on a data set of the nearby spiral galaxy M51 is described in Chapter 6. Besides fitting the observed degree of polarization, one can fit Stokes $Q(\lambda^2)$ and $U(\lambda^2)$ simultaneously. This is considering not only the amplitude of the polarized signal but also the phase between Stokes Q and U which may contain additional information and gives advantages in the error

prediction, since the flux density error of Stokes Q and U is well defined unlike the error in polarized intensity. Sokoloff et al. (1998) summarized different models of depolarization and e.g. O'Sullivan et al. (2012) and Pasetto et al. (2018) applied those models to Stokes Q and U data of extragalactic polarized point sources. Futher broadband depolarization studies can be found in e.g. Goodlet and Kaiser (2005), Laing et al. (2008), Lamee et al. (2016), Anderson et al. (2016), and Vernstrom et al. (2018).

CHAPTER 3

Techniques

In this chapter the main technical methods used for the thesis are described. The data were observed with a radio interferometer which is a radio telescope with features to reach high angular resolution to probe detailed structures in astronomical objects. The concept of radio interferometry and how to obtain images of the radio sky from interferometric data is discussed. In the second part, a modern method to decompose multiple contributions to the polarized signal along the line-of-sight, called rotation measure synthesis, is described.

3.1 The Concept of Radio Interferometry

Radio astronomy is a powerful tool to study various astrophysical mechanism and structures in the Universe. In radio astronomy observations are performed at wavelengths in the centimeter up to meter regime. The resolution of a radio telescope Θ is given by the diameter of the dish D and the observational wavelength λ:

$$\Theta \approx 1.2 \frac{\lambda}{D}$$

Hence, the angular resolution of a radio observation is limited by the physical size of the radio antenna. To accomplish a resolution of arcminutes or even arcseconds, dishes with a diameter of hundreds of meters are necessary. To reach a higher angular resolution than the largest (fully steerable) single-dish radio telescopes ($D \approx 100\,\mathrm{m}$ gives $\Theta \approx 9\,\mathrm{arcmin}$ at $\lambda\,21\,\mathrm{cm}$) the concept of radio interferometry was implemented. Arrays of smaller antennas are used to simulate a large dish to reach higher angular resolution. An interferometer measures the interference pattern produced by multiple apertures. More antennas is like having more slits. With more information, you can produce much more detailed images.

Figure 3.1.1 shows a simple illustration of a 2-element array interferometer. The signals from a certain position the sky where the telescope points to arrive at different antennas at slightly different times, depending on the antenna's location in the array. An interferometer measures the interference pattern produced by pairs of apertures where the interference

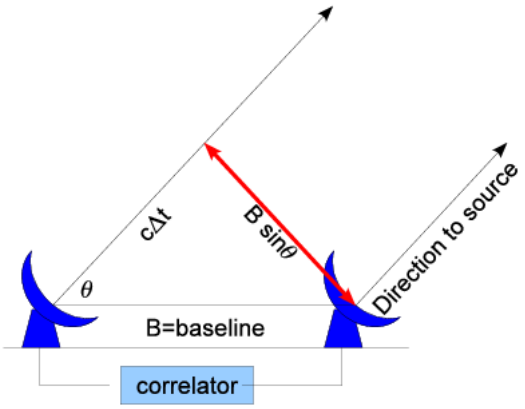

Figure 3.1.1: Simple illustration of a 2-antenna interferometer where B is the baseline between two antennas, Δt the time shift between the signals arriving at two different antennas, c the speed of light and θ in this case is the angle between baseline B and the line-of-sight of the observation. The signals are amplified and digitized at each antenna and then combined in the correlator. Image from Saleem Zaroubi, Caltech.

pattern is related to the source brightness and structure. The raw data achieved by an interferometer are visibilities or measures of the spatial coherence function, formed by correlation of signals from the array's elements. The most common mode of operation will use these data, suitably calibrated, to form images of the radio sky as a function of sky position and frequency. In particular, for small fields of view (FOVs) the complex visibility $V(u,v)$ is the 2D Fourier transformation of the brightness on the sky $T(x,y)$. This means the Fourier transformation relates the interference pattern to the intensity on the sky:

$$V(u,v) = \int\int T(x,y)e^{2\pi i(ux+vy)}\mathrm{d}x\mathrm{d}y \qquad \text{Fourier domain} \qquad (3.1.1)$$

$$T(x,y) = \int\int V(u,v)e^{-2\pi i(ux+vy)}\mathrm{d}u\mathrm{d}v \qquad \text{Image domain} \qquad (3.1.2)$$

xy are the coordinates on the sky plane and uv the corresponding coordinates in the plane of the antennas. To combine the incoming signal of each antenna to an image, each antenna has to measure both the amplitude and the phase of the incoming signal. The result of an interferometric observation has the form of a data "cube" with the source brightness shown in a spatial coordinate system and the frequency as the third dimension. Each pair of antennas (i.e each baseline) will generate a visibility (amplitude and phase). More different baselines (more antennas) gives a better uv-coverage and therefore better image fidelity. The Earth rotation can be used to increase the uv-coverage of an observation. Each radio interferometer has different uv-coverages and different shapes of coverage, depending on the shape of the configuration of the antenna array.

The observations for this thesis were done using the Very Large Array (VLA) in Socorro, New Mexico, conducted by the National Radio Astronomy Observatory (NRAO). The VLA,

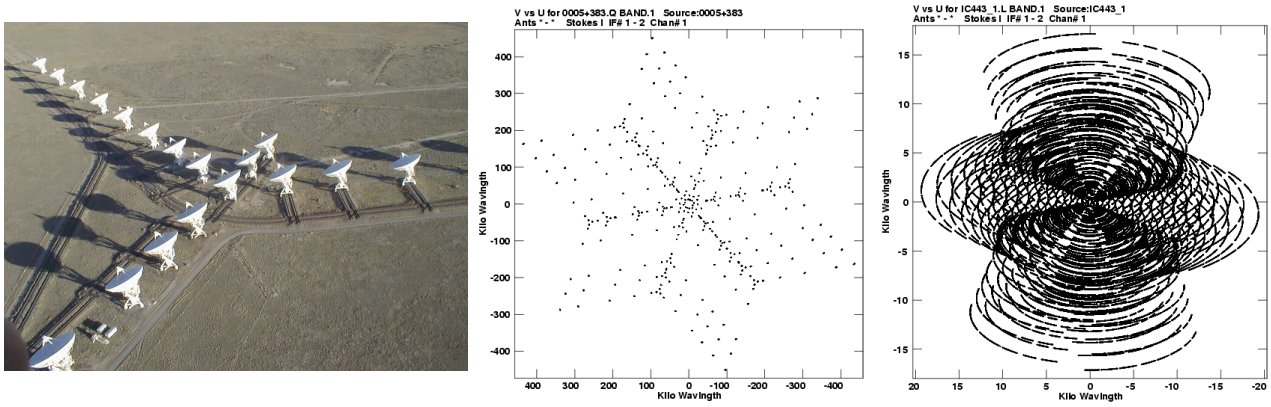

Figure 3.1.2: *Left:* The Very Large Array in Socorro, New Mexico conducted by the National Radio Astronomy Observatory (NRAO). 27 antennas (each with 25 m diameter) with largest separation of 36 km and highest resolution of 0.04″. *Middle: uv*-coverage of the VLA in snapshot mode. *Right: uv*-coverage of the VLA for a long observation. Images from NRAO.

shown in the left panel of Figure 3.1.2, is one of the world's largest radio interferometers, containing 27 radio antennas with 25 m diameter each. There are four basic antenna arrangements, called configurations, whose extends vary from small to large. The antennas are configured in a Y-shape with a maximum antenna separation of 36 km in A-configuration and a separation of 1 km in D-configuration. At the highest central frequency of 43 GHz and the maximum antenna separation the VLA reaches an angular resolution of 0.04″. The VLA has 8 different receivers available, covering a frequency range from 73 MHz up to 50 GHz (24″ up to 0.04″ resolution). The *uv*-coverage of the VLA reflects the shape of the configuration. Figure 3.1.2 (middle and right panel) shows the *uv*-coverage of the VLA without and with Earth rotation (for short and long observations). For radio interferometric observations the FOV is limited by the primary beam of one antenna which is given by $1.2\,\lambda/D_i$ where D_i is the diameter of one antenna element in the array (25 m for the VLA) and λ the observational wavelength.

The theoretical thermal noise $\sigma_{\rm th}$ expected for a synthesized image using natural weighting (see Section 3.1.1) of the visibility data is given by

$$\sigma_{\rm th} = \frac{SEFD}{\eta_c \sqrt{n_{\rm pol} N(N-1) t_{\rm int} \Delta\nu}}\,, \tag{3.1.3}$$

where $SEFD$ is the "system equivalent flux density" (given in Jy) which is equal to 420 Jy at L-band (1 – 2 GHz) and 370 Jy at S-band (2 – 4 GHz) for the VLA. $\eta_c \approx 0.93$ is the efficiency of the correlator, $\eta_{\rm pol} = 2$ is the number of polarizations (equals 2 for observations in Stokes I, Q, U and V), $N = 27$ is the number of antennas, $t_{\rm int}$ the total on source integration time (in seconds) and $\Delta\nu$ the width of the used frequency band (in Hz). The sensitivity of a radio interferometer is given by the electronic properties. To improve the signal-to-noise ratio it is necessary to observe with longer integration times. Using wide frequency bands provides

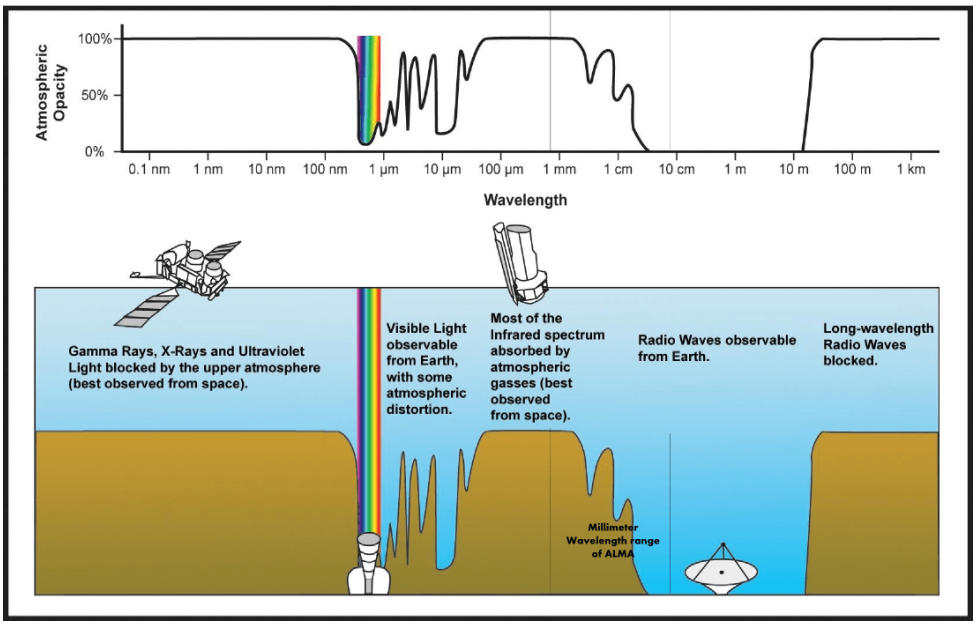

Figure 3.1.3: Spectral range and opacity of observations through the Earth's atmosphere. For radio waves from astronomical objects in cm and m wavelength regime the Earth's atmosphere is transparent. Image from NASA.

better spectral resolution (e.g. for narrow spectral line observations) and additionally increase the *uv*-coverage (compare also Section 3.1.1) and therefore the sensitivity. The VLA has a very good sensitivity compared to other radio interferometric telescopes. In 2011 an upgrade of the 1970s technology was performed and the VLA has evolved into the Expanded Very Large Array (EVLA). The new EVLA has an increased sensitivity by up to an order of magnitude. As the beginning of a new era of radio astronomy the Square Kilometre Array (SKA) will provide the best resolution and sensitivity for future research.

During a radio interferometric observation, the amplitudes and phases of the signal can be corrupted by atmospheric and instrumental effects. Figure 3.1.3 shows a schematic of the opacity of the Earth's atmosphere for a spectral range from γ-rays to long radio waves. Radio waves are ideal to be observed from ground, since the atmosphere is transparent within this spectral window. However, there are several effects which can interrupt the signal and leads to artifacts in the final image (see Section 4.2 for an overview on calibration of data from an interferometric observation). At low radio frequencies ($\nu < 30\,\mathrm{MHz}$, $\lambda > 10\,\mathrm{m}$), signals can increasingly be degraded by variable (in time and across the FOV) ionospheric refraction in the Earth's atmosphere. At high radio frequencies ($\nu > 300\,\mathrm{GHz}$, $\lambda < 1\,\mathrm{mm}$), emission is absorbed by water and oxygen in the Earth's atmosphere. In the vicinity of 1 GHz ($\lambda\,30\,\mathrm{cm}$), man-made Radio Frequency Interference (RFI) is the biggest problem because atmospheric effects can be reduced by calibration procedures at GHz frequencies (see Section 4.2). RFI are strong and rapid changes in amplitude, often much stronger than the astronomical signal, originating from man-made signals, e.g. satellites, radar systems and the Global Positioning System (GPS).

3.1.1 Synthesized Imaging

Imaging of visibilities is a very complex procedure. The visibilities own information on different scales, depending on the length of baselines between the antennas. The longest baselines provide visibilities of the smallest structures and defines the resolution in the final image. The shortest baselines gives information on the largest structures and are crucial for high sensitivity. For visibilities provided by the VLA, synthesis imaging is done using the NRAO *Common Astronomy Software Applications* (CASA) package (McMullin et al., 2007) using the task `clean`, which includes different algorithms for synthesis imaging. `Clean` models the sky visibilities and convolves the model visibilities with a Point Spread Function (PSF) or dirty beam which is given by the Fourier inversion of the visibilities of an unresolved source. The power pattern of the PSF has a similar shape as the shape of a Sinc function, with a main lobe and lower-level side lobes. The full width at half maximum (FWHM) of the main lobe defines the resolution of the synthesized image. The level of the side lobes is strongly dependent on the *uv*-coverage of the observation. An example is shown in Section 4.3.

The clean-algorithm was first developed by Högbom (1974). This algorithm enables the synthesis of complex objects, even if they have relatively poor Fourier *uv*-plane coverage. The first step of cleaning is to Fourier transform the visibilities which forms a so called dirty image (compare Equation 3.1.1). Then, the algorithm searches for the pixel with the highest value in the dirty image, subtracts its PSF and saves the pixel information (position and amplitude) into a model image. In the leftover residual image, the algorithm continues to search for and subtract the highest peak. In case of a single pointing observation, the clean task uses the Cotton-Schwab cleaning algorithm ("cs-clean"). This algorithm breaks the cleaning process into major and minor cycles where the minor circle operates in the image domain. This circle continues until a certain criterion, such as a maximum number of circle iterations or a flux density threshold, is reached. The model image is then (in the major circle) convolved with the PSF and added to the last residual image to form the final synthesized image.

An important choice during the imaging process is how to weight the visibilities, since different weighting algorithms have different influence on the image properties (e.g. sensitivity and angular resolution). The three most common algorithms are:

- **Natural Weighting**: Using natural weighting all visibilities get the same weight given by the inverse of noise variance ($1/\sigma_i^2$). This type of weighting produces a good sensitivity for extended sources in an image but the angular resolution suffers most for this weighting method. Natural weighting was utilized in Chapter 7 to reach the highest possible signal-to-noise ratio for radio continuum images of extra galactic radio sources.

- **Uniform Weighting**: For this method of weighting all visibilities are assigned to a grid and each grid pixel is weighted by the inverse of the number of visibilities assigned to that pixel. This produces noise levels a factor of 2 worse than natural weighting but

minimizes the sidelobe level and thus gives a better angular resolution than natural weighting.

- **Briggs Weighting**: Uniform weighting minimizes sidelobes, whereas natural weighting minimizes the noise level. Briggs weighting provides a compromise between the two, doing so in an optimal way (Briggs, 1995). In this method a "robust" parameter R is given and the scaling of R is such that $R = 0$ gives a good trade-off between resolution and sensitivity. The robust R takes values between -2.0 (close to uniform weighting) to 2.0 (close to natural). For imaging of the nearby galaxy M51 in Chapter 5, we tested different weighting schemes in Section 4.3 and finally utilized the Briggs weighting scheme with a robust parameter $R = 0$.

3.1.2 The Need for Short Spacings

One problem which comes with interferometric observations and imaging is the potential missing of flux density from extended structures. As described in Section 3.1, radio interferometers were developed to simulate huge single dish antennas to reach higher spatial resolution. This method has two limitations: (1) The largest possible distance between antennas is limited by the Earth's diameter, or lately by the maximum diameter of satellite orbits around the Earth. (2) Another important limitation is the shortest separation between antennas. Limited by the size of single elements of an interferometer, the antennas cannot be operated with infinitesimal small spacings. Depending on the observing frequency, the interferometer sees only angular scales smaller than $1.2\,\lambda/D_{\mathrm{min}}$, where D_{min} is the shortest spacing between individual antennas. For the VLA, the largest angular scale at S-band (3 GHz) in D-configuration (this is the array configuration with the shortest distances between the antennas) is about $500''$. For emission structures larger than the detectable angular scale, the VLA is simply blind to the emission; this is a limitation unique to interferometers. For a nearby galaxy like M51 the largest angular structures are represented by the diameter of the galaxy of about $400''$. In this case, the interferometer operated in D-configuration should see the full amount of flux density for a complete *uv*-coverage. However, observers should always check the total integrated flux density detected by the instrument against e.g. single dish observations or observations at other frequencies, since due to flagging of data, i.e. from bad antennas, the *uv*-coverage can be affected in the sense that some angular scales are not recovered in the final image. In Section 2 of Chapter 5 we show an image of M51 obtained from observation in (only) C-configuration. In this image it is clearly visible that some emission on large-scales is missing which comes from a large gap in the visibilities that hampers us from correctly recovering emission from M51 on all scales. New observations at D-configuration (with shorter spacings between individual antennas) fills this gap and enabled us to obtain images covering all scales in M51. This is similar to the strategy of filling the missing spacings by combining interferometric data with single-dish observations. In Section 4.3.1 we compare the total intensity of M51 detected by our new observations at S-band to observations at multiple other frequencies and found a discrepancy which is caused by the in-band spectral index derived by the multi-frequency synthesis algorithm discussed

in Section 4.3.

3.1.3 Polarization Imaging

The main power of radio signals from astronomical sources observed at cm-wavelengths is provided by synchrotron emission. As discussed in Section 2.2, synchrotron emission is linearly polarized. A detailed description of the calibration procedure of polarization data obtained by radio interferometric observations is given in Section 4.1. Synthesized imaging in polarization is different compared to imaging in Stokes I. The FOV in polarization is usually less crowded with neighboring (strong) sources which can cause imaging artifacts. Therefore, and because one combines Stokes Q and U to obtain the polarized intensity, the sensitivity is typically higher in polarization compared to the total intensity (at least by a factor of $1/\sqrt{2}$). However, for observations with wide frequency bands, the polarized signal can suffer from bandwidth depolarization (Section 2.2.2). Because Faraday rotation is wavelength-dependent, the plane of polarization Faraday rotates by slightly different angles at different frequencies within the observing frequency band and after averaging over all frequencies the polarized signal is attenuated. However, bandwidth depolarization can be reduced by dividing the bandwidth into small sub-bands. Anyway, to obtain high signal to noise in polarized intensity one can apply rotation measure (RM)-Synthesis technique on the polarization data. A detailed description of this method is given in the following section 3.2. This method requires data cubes in Stokes Q and U where the polarized signal is recorded at multiple wavelengths (the frequency represents the third axis of the data cube).

3.2 RM-Synthesis

As discussed in Section 2.2.1, the polarization properties of an electro-magnetic radio wave can be affected by Faraday rotation along the line-of-sight. For a Faraday rotating plasma containing magnetic fields and thermal electrons between the source of emission and the observer, the amount of rotation of the polarization angle relative to the intrinsic angle, the RM, can be determined by observing the source at (at least) two separated wavelengths. The slope of ψ vs. λ^2 gives RM. However, the observed polarized signal of a radio wave can be a composition of waves originating from different synchrotron emitting regions within the telescope beam of along the line-of-sigh and can further be influenced by several Faraday rotating regions along the line-of-sight. In this case, the proportionality between the polarization angle and λ^2 is invalid and the RM and therefore the magnetic field components along the line-of-sight must be determined in a different way.

To decompose the different constituents of one signal, a new technique called RM-Synthesis has been developed, first described by Burn (1966) and further extended by Brentjens and de Bruyn (2005). To be able to apply RM-Synthesis on polarization data, the polarized signal must be observed at multiple wavelengths to prepare a 3-dimensional data cube of the polarized sky where the third axis represents the observed wavelength. Broad-

band receivers of modern radio telescopes are ideal to fulfill this requirement. To explain the advantages of RM-Synthesis, it is necessary to consider different kind of sources:

- Source "E" which only emits synchrotron radiation and does not contain thermal electrons and therefore no Faraday rotation intrinsic to the source occurs. Source "E" contains cosmic rays and a magnetic field component in the sky plane.
- Source "R" which only Faraday rotates the polarization plane of a linearly polarized electro-magnetic wave. Source "R" contains thermal electrons and a magnetic field component parallel to the line-of-sight. A Faraday rotating region between the source of synchrotron emission and the observer is often referred as a *Faraday screen* (Burn, 1966).
- Source "ER" which emits synchrotron radiation and Faraday-rotates the plane of polarization simultaneously. This is the case for e.g. the ISM of galaxies, where magnetic fields, thermal electrons, and cosmic rays are mixed within the same spatial volume.

If the polarization angle is a linear function of λ^2, RM is constant. This is only the case if the synchrotron emitting source is not Faraday rotating (i.e. for source "E") and if one or more Faraday rotating sources ("R") are located between the synchrotron emitting source and the observer (one or multiple Faraday screens). In this case RM is the sum of all Faraday screens. In the case of a complex source which both emits and rotates ("ER") RM needs to be replaced by the *Faraday depth* ϕ which is not constant anymore ($\phi \rightarrow \phi(\lambda^2)$):

$$\psi = \psi_0 + \phi \cdot \lambda^2 \,, \tag{3.2.1}$$

with

$$\phi = \frac{e^3}{2\pi m^2 c^4} \int_{\text{source}}^{\text{observer}} n_\text{e} \mathbf{B}_\parallel \cdot \mathrm{d}\mathbf{l} \,. \tag{3.2.2}$$

ϕ is measured in $\mathrm{rad\,m^{-2}}$ and is dependent on the thermal electron density n_e ($\mathrm{cm^{-3}}$) and on the magnetic field component $\mathbf{B}_\parallel$ (μG) of the Faraday rotating medium parallel to the line-of-sight $\mathbf{l}$ (pc). Each synchrotron emitting source along the line-of-sight will produce a separate polarized signal.

Figure 3.2.1, taken from Heald (2009), illustrates an example of different complex lines of sight with emitting ("E"), Faraday rotating ("R"), and emitting plus Faraday rotating ("ER") sources. The background source has an intrinsic Faraday depth of $100\,\mathrm{rad\,m^{-2}}$, seen as a δ-function in the Faraday spectrum (see Section 3.2.1) of the top panel. In case of a Faraday screen located between the source of emission and the observer (middle panel), the observed Faraday depth is shifted by rotation within the intervening plasma. The bottom panel shows a complex case where the intervening plasma contains its own synchrotron emitting conditions. Each layer in this plasma emits a new electro-magnetic wave which however gets Faraday rotated. The resulting Faraday spectrum shows a broad component with different Faraday depths for different layers of the intervening plasma.

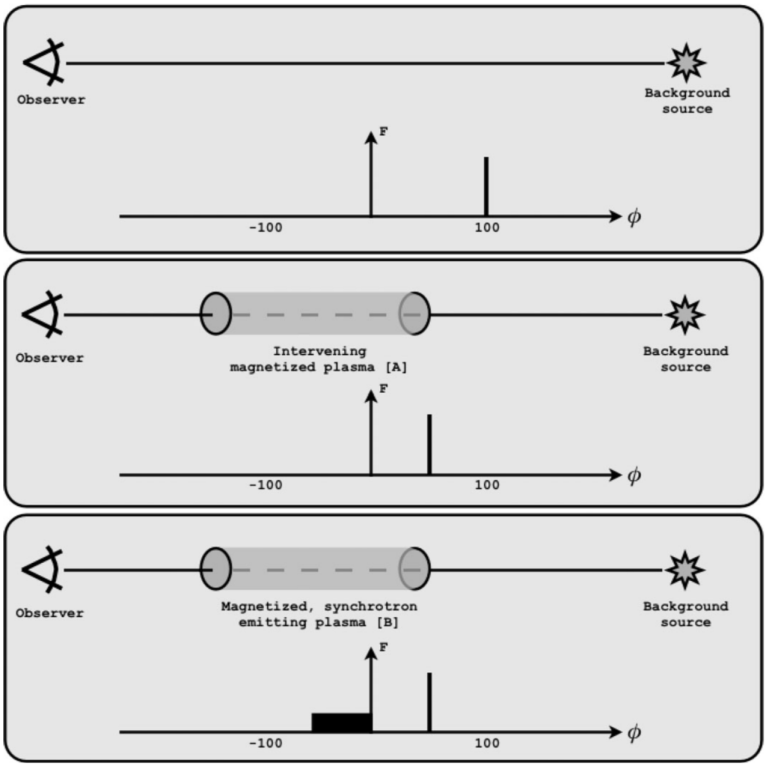

Figure 3.2.1: Simplistic illustration of different lines of sight with a synchrotron emitting source only (top panel), a Faraday rotating source ("R") between the source of emission and the observer (middle panel) and with an intervening source which contains both, synchrotron emitting and Faraday rotating components ("ER"). Also shown are the corresponding *Faraday depths* ϕ in the *Faraday spectra*. Note that the background source has an intrinsic Faraday depth of 100 rad m^{-2}. Image taken from Heald (2009).

3.2.1 Mathematical Derivation

In this section we explain the details of RM-Synthesis technique. As discussed above, the requirements for applying RM-Synthesis are Stokes Q and U measurements at a large number of connected frequencies. Starting with the observed complex polarization vector $p\,I\,e^{2\,i\,\psi(\lambda^2)}$ (where I is the total intensity and $p = |\mathbf{P}|/I$ is the fractional polarization, see Section 2.2) and consider a vector which can originate from emission over the *whole range of* ϕ, the observed quantity $\mathbf{P}(\lambda^2)$ can be written as (Heald, 2009)

$$\mathbf{P}(\lambda^2) = \int_{-\infty}^{+\infty} \mathbf{F}(\phi)\, e^{2\,i\,\phi\lambda^2}\, \mathrm{d}\phi\,, \tag{3.2.3}$$

where $\mathbf{F}(\phi)$ is the Faraday dispersion function or *Faraday spectrum* which describes the intrinsic polarized flux density as a function of Faraday depth ϕ. Equation 3.2.3 relates the intrinsic polarized radiation along the line-of-sight $\mathbf{F}(\phi)$ to the observed quantity $\mathbf{P}(\lambda^2)$. Because this Equation takes the form of a Fourier transformation, one can easily express the

intrinsic polarization in terms of the observable quantity:

$$\mathbf{F}(\phi) = \int_{-\infty}^{+\infty} \mathbf{P}(\lambda^2)\, e^{-2\,i\,\phi\lambda^2}\, \mathrm{d}\lambda^2 \tag{3.2.4}$$

From the observed polarized flux density $\mathbf{P}(\lambda^2)$ one can determine the Faraday spectrum $\mathbf{F}(\phi)$ and therefore the intrinsic polarized flux density.

This method has physical boundaries, given by the observation: It is impossible to observe in an infinite wavelength range. First we do not observe at wavelength $\lambda^2 < 0$. Secondly, modern radio telescopes have limited bandwidths which are not sensitive to all values $\lambda^2 > 0$. To circumvent this problem Brentjens and de Bruyn (2005) introduced a window function $W(\lambda^2)$ which only gives contributions ($\neq 0$) at values of λ^2 where the telescope is able to observe. From this follows the so-called *Rotation Measure Spread Function* (RMSF)

$$R(\phi) \equiv K \int_{-\infty}^{+\infty} W(\lambda^2)\, e^{-2\,i\,\phi(\lambda^2 - \lambda_0^2)}\, \mathrm{d}\lambda^2\,, \tag{3.2.5}$$

where K is the inverse of the integral over $W(\lambda^2)$. RMSF is the analogous to the 'dirty beam' pattern of a telescope in synthesis imaging (see Section 3.1.1). The RMSF has the form of a Sinc function which is the Fourier transformation of a box function, given by the observing frequency band. Therefore, analogous to the beam pattern of a radio telescope (i.e. the PSF) which is strongly dependent on the *uv*-coverage, the RMFS is strongly dependent on the properties of the instrument and the observation (i.e. the λ^2-coverage). Details on instrumental and observational specifications and limitations are given in Section 3.2.3.

3.2.2 Application

To perform RM-Synthesis on polarization data it is best to observe with large bandwidths, consistent of many small individual frequency channels, resulting in frequency cubes of Stokes I, Q, and U. Due to Faraday rotation, the polarization angle can change significantly within the observed bandwidth of the telescope (see Section 2.2.2 about bandwidth depolarization). Splitting the observational bandwidth into many individual frequency channels will reduce but not prevent this effect. The polarization angles for each frequency of each channel have to be corrected for the physical Faraday depth of every source between the emitting source and the observer. The RM-Synthesis technique compares the polarized signal from different frequency channels given by a series of Faraday depths and finds the Faraday depth which maximizes the polarization signal after adding all frequency channels together. This algorithm works well, since with a 'wrong' Faraday depth, the angles ($\psi \propto \phi\lambda^2$) may not produce the highest polarization signal when added over the entire band. The final maximum signal shows a peak at the Faraday depth ϕ of each Faraday rotating source along the line-of-sight. While the inputs for RM-Synthesis are data cubes of Stokes Q and U where the third axis is the frequency, the algorithm give out cubes of the polarized intensity, Stokes Q,

and Stokes U where the third axis represents the Faraday depth. Additionally, maps of the polarized intensity, and RM at the Faraday depth of the most significant peak are generated. An application to an observational data set is explained in detail in Section 5.3.1 of Chapter 5.

If the radiation of a background polarized source propagates through a foreground medium which both Faraday rotates and produces its own synchrotron emission in the same volume ("ER"), the peak in Faraday depth space will spread out and turns into a *Faraday thick* source. In an ideal case the Faraday spectrum will show a 'perfect' box which means the polarized flux density will appear at different values of ϕ_i as illustrated in the bottom panel of Figure 3.2.1. In reality those boxes are radiused because of the form of the RMSF. If the observational wavelength range would extend from minus to plus infinity with no gaps, the resulting RMSF would be a δ-function and the observed Faraday spectrum would show a perfect box shape (the Fourier transform of a δ-function is a box function). However, in reality, an extended source in the Faraday spectrum would show up like a double source with two "horns" (see next Section 3.2.3). Examples for sources which both emits synchrotron radiation and contains Faraday rotating plasma are our own Milky Way, intervening galaxies, and galaxy clusters.

3.2.3 RM-Synthesis Specifications

Even if RM-Synthesis technique is able to decompose the polarized signal of an observation along the line-of-sight, its results are limited by the observational setup. An overview of the bounding instrumental parameters is shown in Figure 3.2.2.

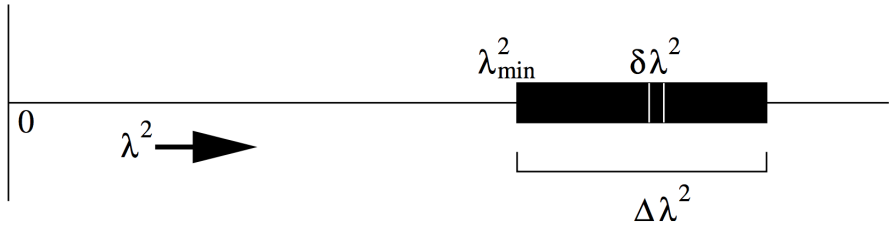

Figure 3.2.2: The three instrumental parameters that determine the output of RM-Synthesis. The black bar illustrates the observing frequency band. $\lambda^2_{\rm min}$ is the shortest wavelength of the observation, $\delta\lambda^2$ the channel width and $\Delta\lambda^2$ gives the λ^2-coverage of the observing band. Image from Brentjens and de Bruyn (2005).

Resolution in ϕ space

The resolution $\delta\phi$ in ϕ space is determined by the full width of the λ^2-coverage $\Delta\lambda^2$ of the observing frequency band

$$\delta\phi \approx \frac{2\sqrt{3}}{\Delta\lambda^2}. \tag{3.2.6}$$

This corresponds to the FWHM of the RMSF (Equation 3.2.5) in ϕ space. The FWHM of the RMSF determines the precision with which one is able to distinguish different ϕ components (also dependent on the signal-to-noise ratio of the peaks) and is the equivalent to the spatial resolution of a radio interferometer (see Section 3.1). In reality, due to RFI the λ^2-coverage of an observation contains gaps which causes side lobes in the RMSF. If the side-lobe level or rms noise is too high it is not possible to distinguish real signals and artificial peaks in the Faraday spectrum. The theoretical resolutions $\delta\phi$ of the broadband receivers used for this thesis, i.e. S-band (2 – 4 GHz) and L-band (1 – 2 GHz) receivers of the VLA, are $\approx$ 205 rad m^{-2} and $\approx$ 51 rad m^{-2}, respectively. Unfortunately, a significant fraction of the observational bandwidth is useless due to RFI. Therefore, the actual resolution reduces to $\approx$ 522 rad m^{-2} and $\approx$ 126 rad m^{-2} for S-band and L-band, respectively.

Maximum Scale

Applying RM-Synthesis on polarization data of a region that is emitting synchrotron radiation and contains Faraday rotating plasma ("ER") reveals an extended component in the Faraday spectrum. However, sources broader than

$$\text{max-scale} \approx \frac{\pi}{\lambda^2_{\text{min}}} \tag{3.2.7}$$

cannot be recovered, where λ_{min} is the shortest wavelength of the observation. That means the larger λ_{min} the smaller the Faraday rotating regions has to be to recover them. In the case of a region which is larger than "max-scale" only two "horns" remain at the edges of the structure in the Faraday spectrum (Beck et al., 2012), related to the emitting and rotating layers at the front and the back (relative to the line-of-sight) of the structure. This problem is similar to the missing short baselines in synthesis imaging (Section 3.1.2) where sources larger than the largest detectable scales are "resolved out". To resolve Faraday "thick" sources (which are spread out in Faraday space) the FWHM of the main peak in the RMSF should be narrower than the maximum scale one wish to observe (again in Faraday depth space - not physical scale). This is equivalent to the beam/resolution of a telescope which should be smaller than the largest detectable scale. From Equation 3.2.6 and 3.2.7 it follows

$$\lambda^2_{\text{min}} < \Delta\lambda^2 \tag{3.2.8}$$

as a requirement for resolving Faraday "thick" structures. Theoretically, observations at S-band and L-band fulfill this requirement. However, due to RFI, the effective bandwidth reduces and prevent us from detecting extended components in the Faraday spectrum at S-band. At L-band, even after flagging of bad channels due to RFI, the effective bandwidth is sufficient to fulfill the requirement of detecting Faraday thick sources. Compared to synthesis imaging, in RM-Synthesis it is also possible that a source is unresolved in ϕ space in the sense that its extent in ϕ is less than the width of the RMSF.

Maximum ϕ

The maximum detectable magnitude of ϕ is limited by the spectral resolution of the instru-

ment i.e. the channel width of the observing frequency band and is given by:

$$||\phi_{\max}|| \approx \frac{\sqrt{3}}{\delta\lambda^2} \tag{3.2.9}$$

The S-band and L-band receivers used to observe the data for this thesis, provides a channel width of 2 MHz and 1 MHz, respectively. This gives a theoretical maximum detectable Faraday depth of $\sim 40\,000\,\mathrm{rad\,m^{-2}}$ and $\sim 10\,000\,\mathrm{rad\,m^{-2}}$ for S-band and L-band, respectively. Since, the maximum amplitude of Faraday depth in galaxies and AGNs is by far smaller than those values, we averaged frequency channels together, which reduces the computing time when applying RM-Synthesis.

All parameters and limitations given by the observations obtained for this thesis are summarized in Table 5.1 and 7.4 for S-band and L-band, respectively. RM-Synthesis is a powerful tool to decompose different sources of polarized emission along the line-of-sight or within the telescope beam. If the resolution in ϕ-space is not sufficient enough to resolve different components, is is still advised to apply RM-Synthesis to broadband Stokes Q and U data to prevent bandwidth depolarization.

CHAPTER 4

Analyzing Wideband Polarimetry Data

In this chapter, we describe the observation and data reduction of the new radio polarimetric wideband data of M51 in detail. Especially, finding the right synthesis imaging parameters for large extended sources is anything but trivial. Section 4.1 gives details on the observation with the Very Large Array (VLA) interferometer. Section 4.2 describes the data reduction procedure including flagging and calibration of the new wideband S-band data. In Section 4.3 we discuss different imaging parameters and present the parameter values we used to create synthesized images of M51 using the new broadband S-band data. We close this chapter in Section 4.4 with a summary of the whole radio polarimetric data set for M51 used in our scientific analysis.

4.1 Observation

The observations were taken at S-band (2 – 4 GHz, λ 7.5 – 15 cm) in continuum mode in full polarization. A brief summary of the observational parameters is given in Table 4.1. The VLA was the instrument of choice because of its high sensitivity wide-band receiver capability and the large antenna separation, resulting in high spatial resolution. The first two observing blocks were performed in C-configuration with a maximum antenna separation of 3.4 km and a resulting angular resolution of 7″ at S-band. This corresponds to a physical scale of about 300 kpc at the distance of M51. To reach a theoretical image noise of $\sim 4\,\mu$Jy in total intensity, 3 hours of on-source time was necessary in C-configuration. This results in 2 separate observations of 2 hours (including telescope overhead and calibrator pointing), taken in November and December 2014. 3C 286 was observed as flux density and polarization angle calibrator, with a polarization angle of +33°. As phase calibrator J1313+5458 was observed once at the beginning, middle and end of the target observation. J1407+2827 was observed as leakage calibrator. The measurement sets (MSs) consist of 16 spectral windows with 64 channels with 2 MHz channel width.

Unfortunately, there exists a large *uv*-gap in the C-configuration data. As discussed in

Table 4.1: Radio Continuum Observational Parameters of M51.

Frequency (GHz)	2 – 4 (reduced to 2.6 – 3.6 after flagging)
Bandwidth (MHz)	2000 (reduced to 1000 after flagging)
No. of spectral widows	16 (reduced to 9 after flagging)
Total no. of channels	1024
Central Frequency (GHz)	3.06
Array Configuration	C; D
Observing dates	26 Nov /14 Dec 2014; 09/10 Oct 2015
Total Flux Density Calibrator	3C 286
Polarization Angle Calibrator	3C 286

Section 3.1.2, missing spacings prevent us from correctly recovering the full extended emission in M51 in all Stokes parameters. As an example, the left panel of Figure 4.1.1 shows an amplitude vs. *uv*-distance plot of the M51 C-configuration observation at 3 GHz. Note that the huge gap towards small *uv*-distances ($< 600\,\lambda$) results from the minimum spacing between individual antennas, already mentioned in Section 3.1.2, which is unavoidable. However, a large gap between 40 – 70 m (700 – 900 λ) is conspicuous. This gap produces artifacts as obviously visible in a preliminary total intensity image of M51 produced using the C-configuration data in the right panel of Figure 4.1.1. The large stripe-like artifacts leads to non-uniform background and obvious systematics that results in wrong flux density estimates and missing real emission on scales of 4.9′ – 8.6′ from M51 itself at 3 GHz (M51 has an angular diameter of about 7.6′). Note that the range of scales of emission that this gap in the *uv*-plane corresponds to is smaller at higher frequencies (between 3.9′-6.9′ at 4 GHz). In particular for polarization analysis, missing emission on certain spatial scales in Stokes Q and U maps will result in finding incorrect polarization angles and hence, incorrect properties of the magneto-ionic medium including the polarized intensity, the Faraday depth, and the intrinsic polarization angle (e.g., Gaensler et al., 2001). Therefore, data from the VLA in D-configuration were required to densely sample the missing *uv*-range (40 – 70 m; 700 – 900 λ) to reliably image M51 and to estimate the real flux density of the observed structures.

To fill the missing spacings of the data in C-configuration, additional observations in D-configuration were performed in October 2015. To achieve the same surface brightness sensitivity as for the C-configuration data, 1.5 hours of on-source time were required, 2 hours including overhead. The same flux density, phase, and leakage calibrator sources as for C-configuration were observed. Table 4.2 shows a summary of the observations.

4.2 Flagging and Calibration

Calibration and data reduction were done using the NRAO *Common Astronomy Software Applications* (CASA) package (McMullin et al., 2007). After automatic flagging of the beginning and end of each spectral window due to decreasing sensitivity towards the edges and

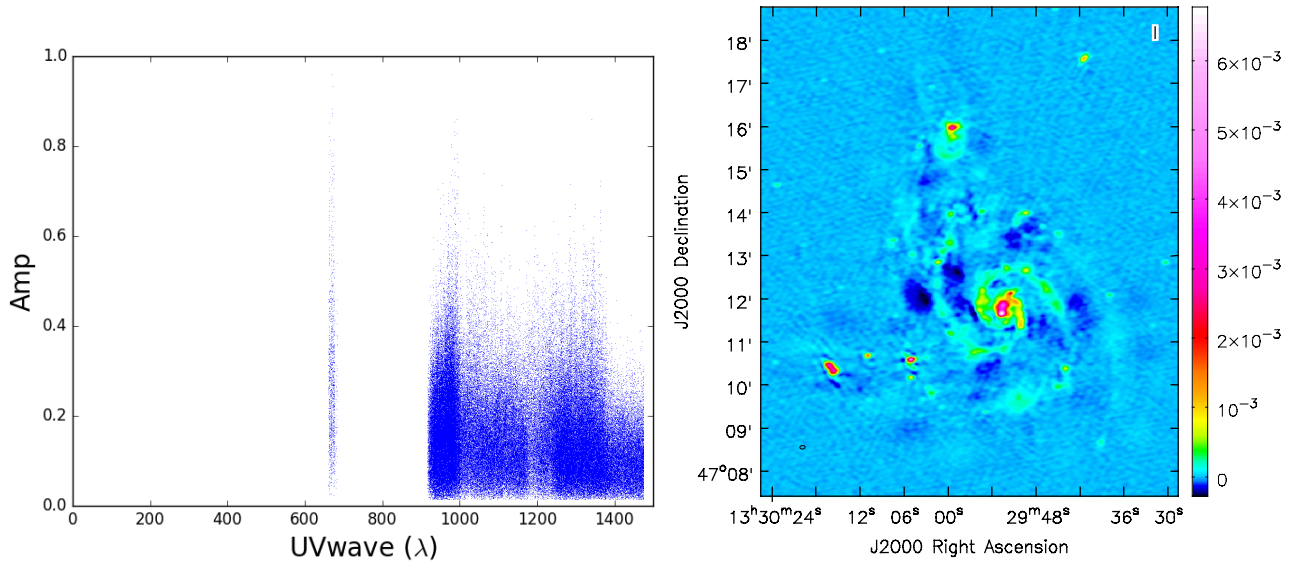

Figure 4.1.1: *Left:* The *uv*-coverage for C-configuration data at 3 GHz. The gap in the *uv*-plane between $700-900\,\lambda$ corresponds to angular scales of $4.9'-8.6'$ at 3 GHz. *Right:* Total intensity map of M51 at S-band using C-configuration data only after preliminary data reduction. The color scale is in Jy beam^{-1}. The image clearly contains stripe-like artifacts and regions of missing flux density (negative bowls).

the first 10 seconds of each scan, Hanning smoothing was applied to smooth the side lobes of the Sinc function, resulting from the Fourier transformation of a box function (the visibilities in frequency space are present at separate frequency channels with 1 – 2 MHz channel width, causing a box-function like distribution). Then, an initial bandpass calibration was applied on the flux density calibrator to improve the detection rate of RFIs using the automatic flagging algorithm RFlag. After applying RFlag, the visibilities of the calibrators and the science target in the MSs were carefully inspected for further RFI excisions manually. Due to flagging of RFI, and flagging the beginning and end of each spectral window, the effective frequency band is reduced to 1000 MHz (2.56 GHz – 3.56 GHz), divided into nine spectral windows.

Individual antennas are moved on rails and thus, it is physically impossible to move them on the exact right position (with sufficient accuracy). Because the visibilities u and v are a function of position, to use the right baseline positions is crucial for a good image quality with no artifacts. Therefore, as a first step of calibration, the task `gencal` was used for an a priori antenna position correction. Then, the CASA task `setjy`, using the standard Perley and Butler (2013a) flux density scale, was used to determine the absolute flux density of the total flux density calibrator 3C 286 by placing the correct visibilities of the flux density calibrator into the model column of the data set. For M51 3C 286 was used, a strong quasar with well-known and stable total flux density scale of 10.9 Jy at 2.565 GHz (Perley and Butler, 2013a). To prevent small atmospheric and instrumental time variations of the phase, an initial phase calibration was done using the task `gaincal`, averaging over 30 second intervals within the

Table 4.2: Detailed Observational Parameters of Different Array Configurations of M51.

Source	Config	t_{int} min	θ arcsec	σ_{th} μJy beam^{-1}
(1)	(2)	(3)	(4)	(5)
M51	C	2×90	7.4×4.7	~ 4
M51	D	90	24.4×17.5	~ 13

Notes. (1) Name of the source; (2) Array configuration; (3) Total on-source integration time; (4) Full resolution in the synthesized image; (5) Theoretical rms noise (Equation 3.1.3).

bandpass. For phase calibration, a bright unresolved source near the since target was used (J1313+5458 in case of M51). The next step is to solve for antenna-based delays of the signal of each antenna relative to a reference antenna. The reference antenna can be chosen by the user, taking care to use one which is located near the center of the antenna array. For this observation antenna ea25 was used as reference antenna. To solve for variations with frequency, a bandpass calibration of the total flux density calibrator is needed. The variations are caused by slightly different antenna bandpasses. Bandpass calibration was done for both amplitude and phase for each spectral window. Then, `gaincal` was used to calibrate for the complex gain (amplitude and phase) for all calibrators and since targets. Because the flux density scale of the flux density calibrator is known, the task `fluxscale` can then be used to set the right flux density scale to all other sources, comparing the complex gains of each source with those of the flux density calibrator.

The previous run of `setjy` only sets the total intensity level of the flux density calibrator. Because 3C 286 has a well-known and stable polarization angle of +33° (Perley and Butler, 2013b), the flux density calibrator is also suitable for polarization calibration. Using the manual mode in `setjy`, the polarized flux density model can be generated using the known polarization angle and fractional polarization of 3C 286 (Perley and Butler, 2013b). The polarization fraction is known with accuracy of 0.03 % while the polarization angle has an uncertainty of only 1° at 5 GHz. Both quantities are very stable over the past 20 years. As it was necessary to solve for antenna-based delays in total intensity, one needs to solve for the cross-hand delays due to delay differences between right-handed and left-handed circular polarization. This was done using `gaincal` with gaintype KCROSS. Another important step of polarization calibration is to solve for instrumental polarization. Mechanical and electronical effects (e.g. spillover between clouds on the sky above the antennas) can result in an artificial polarized signal in the data measured by a radio telescope. Thus an unpolarized source can appear to be polarized and the level of polarization in a polarized source can be erroneous. For this purpose an unpolarized calibrator needs to be observed (J1407+2827 in case of M51). Leakage polarization calibration was done using the CASA task `polcal` which derives the level of leakage polarization from the unpolarized calibrator which can later be subtracted from all observed sources (including calibrators and target sources). As a last step of calibration, one needs to set the right polarization position angle into the model column of

the calibrator 3C 286. To do so, the task `polcal` was used with the parameter poltype='Xf' for position angle (X) and frequency-dependent (f) calibration. The polarization calibrator 3C 286 has a well-known RM of 0 rad m^{-2} (Perley and Butler, 2013b). We have verified that, after calibration, 3C 286 has a RM consistent with zero (using RM-Synthesis).

All the tasks and steps described above generate calibration tables. The calibration solutions in those tables must be applied to the raw data column of each source. This was done by CASAs task `applycal`, which writes the calibration results into the corrected data column, which can then be used for further scientific analysis. When applying the calibration solutions to the data, the solutions were linearly interpolated. Calibration was performed for each observation separately. For imaging, the calibrated visibilities of the target source M51 from each configuration observation were combined using the task `concat`.

Despite calibration of the since target, small phase (and sometimes amplitude) errors can remain in the data. To reduce the errors, self-calibration was applied to the data. For the process of self-calibration, primary images are formed for each spectral window separately using the CORRECTED_DATA column of the MS. The cleaning threshold of the flux density for the primary images should be high enough to make sure that no artifacts from bad phase/amplitude solutions are erroneously interpreted as real signal and modeled during the imaging process. The model image formed during this imaging process is then used as a new model for calibration which in particular means one uses the target source as a new calibrator. Self-calibration can be used to eliminate phase and amplitude errors. We tested self-calibration for amplitude only, phase only, and a combination of phase and amplitude. Furthermore, we applied self-calibration multiple times. This test has shown that only one circle of self-calibration of the phase improved the dataset (such as reduction of imaging artifacts), whereas multiple circles and amplitude corrections show no improvements. Therefore, our final calibrated dataset was only self-calibrated for phase errors.

4.3 Imaging

Images of Stokes I, Q, and U were created using the `clean` algorithm in CASA (Högbom, 1974). Details on the synthesized imaging procedure are given in Section 3.1.1. The NRAO CASA team is currently developing a new version of `clean`, called `tclean`, where the "t" stands for test-version[1]. Since the test version provides more combinations of different algorithms such as multi-scale (see below) together with wideband image reconstruction `tclean` was used for imaging. The observations were done using a wide-band receiver, covering a frequency range of 2 GHz (2 – 4 GHz). Observing with wide frequency bands not only provides simultaneous analysis of science targets at multiple frequencies but also improves the *uv*-coverage and therefore the sensitivity in the final wideband image. Figure 4.3.1 shows the different *uv*-coverages of one single spectral window (left panel) and the full observing band using only the effective bandwidth after flagging of bad spectral windows and channels (right panel). It is clearly shown that using the full frequency band the density in *uv*-coverage

[1] https://casa.nrao.edu/casadocs/casa-5.0.0/global-task-list/task_tclean/about

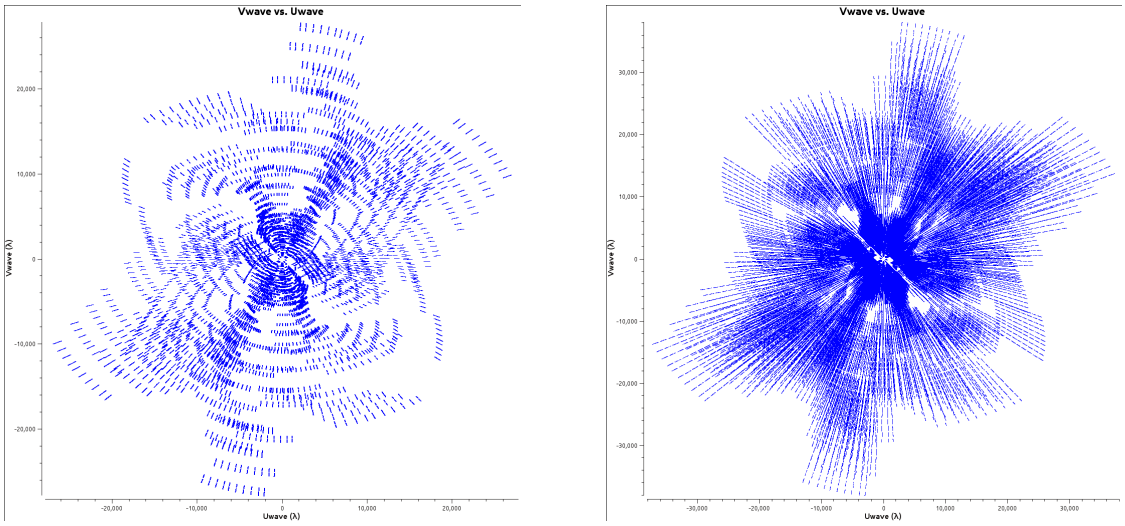

Figure 4.3.1: *Left: uv*-coverage of spectral window 0 with about 128 MHz bandwidth (2.560 – 2.688 GHz). *Right: uv*-coverage of the full observation with about 1000 MHz bandwidth (2.56 – 3.56 GHz).

highly improved.

Applying a Fourier transformation to the calibrated visibilities forms a dirty image, which is the first step of imaging. The dirty image is the true image on the sky, convolved with the dirty beam, also known as the Point Spread Function (PSF). One can create a dirty image by imaging with zero iterations. For more details on synthesized imaging see Section 3.1.1. The dirty image can be used to check how strong the artifacts of the PSF can influence the final image and how high the level of sidelobes is compared to the main lobe. Figure 4.3.2 (left) shows the dirty image of the concatenated visibilities of all configuration observations. The sidelobes seen in the image do not exceed a level of about $\pm 7\,\%$ of the main peak, measured using CASA `viewer`.

The field of view of an interferometric observation, also referred as primary beam, is defined by the antenna size and the observing wavelength. At 3 GHz, the primary beam of the VLA antennas amounts to 0.25 degrees or 15.5 arcmin (shown in the right panel of Figure 4.3.2). Away from the phase center, the antenna response decreases by a factor of two at the Half Power Beam Width (HPBW). To correct for this, the image's flux density levels need to be corrected for the primary beam attenuation. This is especially important for extended sources, since the antenna response is different for different parts of the source itself. The primary beam has an approximately Gaussian shape whose size is frequency dependent. When observing with wide frequency bands, the primary beam shape varies by a factor of $\nu_{\rm max}/\nu_{\rm min}$ across the band (factor of two at S-band) which results in apparent steepening of spectral indices of sources away from the phase center (or the outer regions of an extended source). To correct for this, one can either use the option pbcor = True in `tclean` (only for nterms = 1, see below) or apply the task `impbcor` (for nterms > 1). The task `impbcor` needs a primary beam pattern image, produced during the bevorhand `tclean` run. For wideband

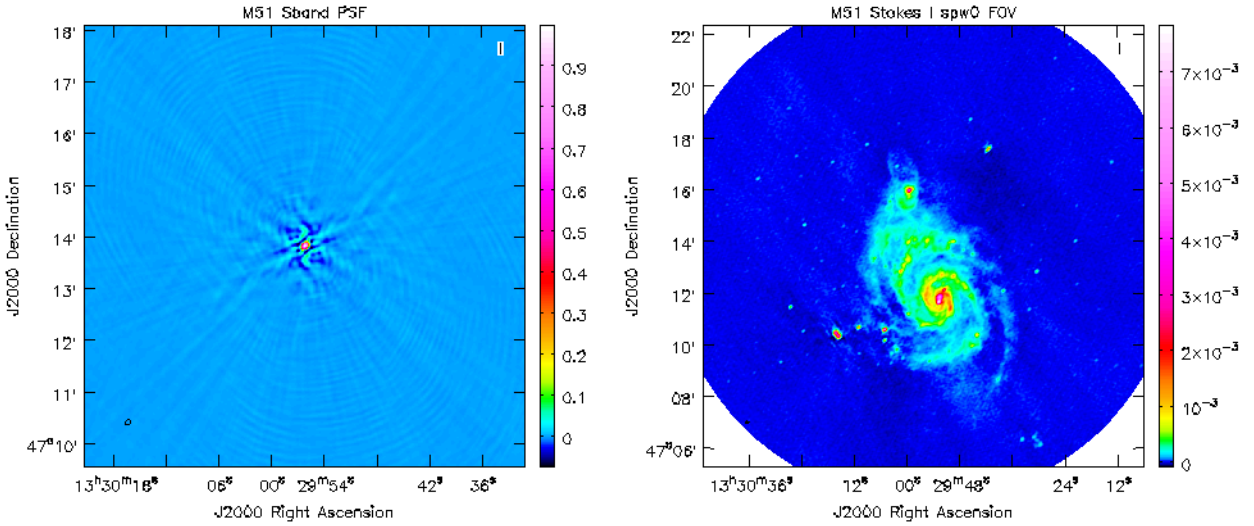

Figure 4.3.2: *Left:* Dirty beam also called Point Spread Function (PSF). *Right:* Preliminary Stokes I image to visualize the field of view and size of the primary beam (with unit Jy beam^{-1}).

imaging, the new task `widebandpbcor` was used, which computes a set of primary beams at different frequencies across the observing frequency band and calculates a primary beam spectrum to apply the right correction of the flux density scale at each frequency. The frequency chunks can be specified giving a list of spectral windows and channels therein. Further, one can give relative weights to the frequencies selected using the spectral window and channel lists. Since for the M51 data all nine spectral widows show the same quality (in terms of e.g. occurring RFI), equal weights were given to the frequencies.

Since the total flux density of a radio source changes with frequency (see Section 2), for observations with wide frequency bands variations of the total flux density level across the band needs to be taken into account. Using the multi-frequency synthesis (*mfs*) algorithm in `tclean` (Rau and Cornwell, 2011), the spectral dependency of the sky's flux density across the band is fitted by a polynomial Taylor expansion

$$I_\nu = \sum_{t=0}^{N_t-1} I_t \cdot \left(\frac{\nu - \nu_0}{\nu_0}\right)^t , \tag{4.3.1}$$

where I_t is the sky's flux density at the t-th order of Taylor expansion and N_t the user specified number of Taylor terms used and ν_0 a reference frequency (given by the midpoint between the highest and lowest frequency). One can choose the number of terms for the expansion using the parameter "nterms" in `tclean`. nterms = 1 is the default, generating an image assuming a spectrum with zero spectral index, i.e. no frequency dependency of the sky's flux density. In radio-frequency regime, the emission of M51 is mainly produced by synchrotron radiation whose spectral dependency is given by a power law. Using nterms = 2, `tclean` fits a constant spectral index to the visibilities across the frequency band. In this

case, the total intensity is given by

$$I_\nu = I_{\nu_0} \cdot \left(\frac{\nu}{\nu_0}\right)^{\alpha_{\text{tot}}} , \tag{4.3.2}$$

where I_{ν_0} is the total intensity at the reference frequency ν_0 and α_{tot} is the spectral index of the total flux density. Using `tclean` with nterms = 2 produces an image at the central frequency of the frequency band. Additionally, a spectral index map is generated which shows the spatial distribution of the in-band spectral index across the galaxy. Details about the in-band spectral index and problems that arise by computing the in-band spectral index using multi-frequency synthesis imaging are described in Section 4.3.1. To correct for the spectral dependency of the primary beam, `widebandpbcor` was applied to the *mfs* total intensity image, which also fits Taylor polynomials to the primary beam response within the observing band. Further, the option "calcalpha" can be chosen in `widebandpbcor` to correct the spectral index map for the primary beam.

To find the optimal input parameters for deconvolution, different input parameters were tested. One important parameter is the stopping threshold until `tclean` should search for peaks in the residual image (a detailed description on synthesized imaging is given in Section 3.1.1). The root mean square (rms) noise σ in the image gives a good estimate for the cleaning threshold. To check the image quality, a threshold of $\sim 3\,\sigma_{\text{th}}$ using the theoretical rms noise given by Equation 3.1.3 was used. The threshold needs to be low enough to make sure the entire flux density of the source is recovered, but if the threshold is too low, doubtful features due to calibration errors or clean artifacts might be treated as real signal. If the image quality is satisfying, hence no clean artifacts and questionable features (e.g. no rings or stripes) are visible in the image, one can clean down to the image rms noise. In case of our M51 measurements, the rms noise in the images is measured in a box with the size of about 20 beams at a region free of emission towards the north-west of the galaxy. Since the synthesized beam should be sampled by about 5 pixels across its minor axis, for the beam size of the current data set of about 6″ (minor axis), a cell size of 1″ was used for imaging.

During cleaning, the sources in the field are represented by point sources and the final image is the sum of these point source components (Dirac delta functions) convolved with the PSF. To improve imaging of extended sources, different extensions of the classical `clean` algorithm for handling extended sources are available. One example is multi-scale cleaning where the emission on the sky is decomposed into scales with different angular sizes (Cornwell, 2008). During multi-scale cleaning the residual image (see Section 3.1.1) gets smoothed to different user-specified scale sizes. To image extended sources it is recommended to select different scales which represent the scales existent in the data, including the zero-scale for point sources, one scale of about the beam size and some larger scales. The largest scale should represent half of the largest extent of the source. M51 has an apparent diameter of about 400″ at 3 GHz and the minor axis of the synthesized beam is about 6″. This results in a scale sample of 0, 6, 9, 18, 30, 45, 60, 100, and 200 pixels. The scales are given in pixels and since the cell size (or pixel size) is chosen to be 1″, the scales correspond to the angular size on the sky in arcsec.

Another important imaging parameter to choose is the right weighting algorithm to be

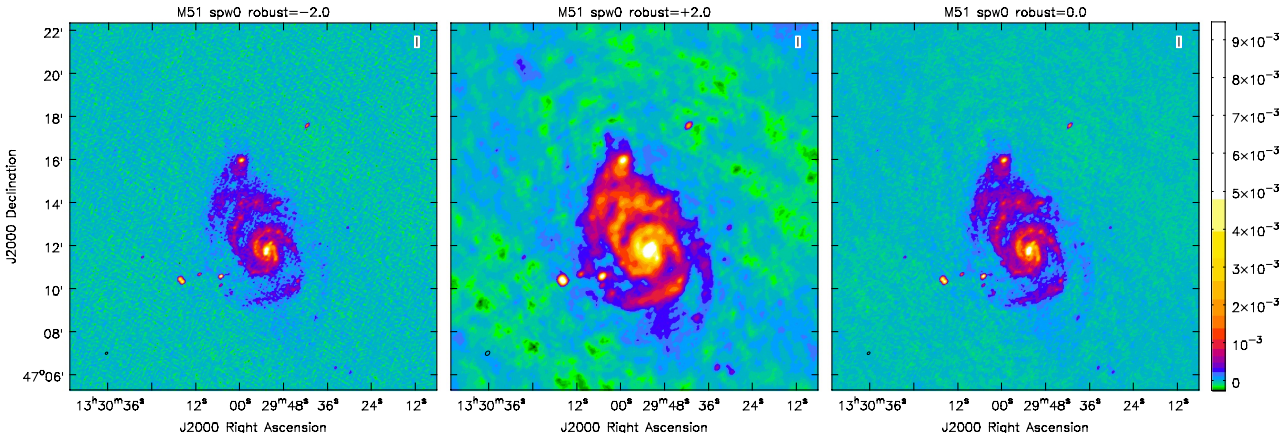

Figure 4.3.3: Stokes I images of M51 using spectral window zero only (at 2.56 GHz). For each image different weighting algorithms were applied. The left panel shows the synthesized image with uniform weighting (robust $= -2$), the middle panel the image with natural weighting (robust $= +2$) and the right panel with a compromise between natural and uniform weighting (robust $= 0$). The unit of the flux density is Jy beam^{-1} and all images have the same scale.

applied to the data. The most common weighting schemes for interferometric data are listed in Section 3.1.1. Figure 4.3.3 shows Stokes I images of M51 after applying different weighting schemes using only the first spectral window. There are differences in the image sensitivity and synthesized beam sizes: Uniform weighting gives the highest resolution but there is some missing flux density in the left image of Figure 4.3.3 (compared to the middle one). Natural weighting gives the highest flux density with slightly larger rms noise, but the synthesized beam size is large. Also the natural weighted images contains strong artifacts across the entire image. Giving a Briggs parameter (see Section 3.1.1) between the two extremes gives the highest signal-to-noise ratio (factor 2 larger compared to robust $= \pm 2$). Table 4.3 summarizes the differences in image parameters after applying different weighting algorithms. To archive a good balance between high resolution and good flux density coverage and high signal-to-noise ratio, robust-weighting with a robust parameter of 0 was used for the final images.

Because of the in-band spectral index problem (discussed in the next section) and the effect of bandwidth depolarization we divided the frequency band into nine spectral windows and created individual images for each spectral window in Stokes I, Q, and U. For the final synthesized images of M51 we used the following set of parameters in `tclean`:

- As a stopping threshold we used 1σ of the rms noise in the corresponding images, measured in a box with size of about 20 times the beam size at a source-free location towards the north-west of M51.

- We used only a single Taylor expansion term, assuming no frequency dependence of the flux density within a single spectral window (nterms $= 1$).

Table 4.3: Image Parameters at 2.56 GHz After Applying Different Weightings.

robust	close to	beam arcsec	σ μJy beam^{-1}	I_{int} mJy	S/N
(1)	(2)	(3)	(4)	(5)	(6)
-2.0	uniform	7.73 × 5.48	50	680	14
+2.0	natural	14.05 × 10.14	60	730	12
0.0	compromise	8.91 × 6.10	30	690	23

Notes. All parameters given in this table are obtained from the test images in Figure 4.3.3. (1) Briggs's robust parameter; (2) Weighting scheme the briggs parameter corresponds to; (3) Synthesized beam size; (4) rms noise; (5) Total integrated flux density; (6) Signal-to-noise ratio.

Table 4.4: Final Image Parameters of M51.

Stokes	threshold μJy beam^{-1}	ν_c GHz	nterms	beam arcsec	cell arcsec	σ μJy beam^{-1}
(1)	(2)	(3)	(4)	(5)	(6)	(7)
I^{mfs}	20	3.06	2	7.2 × 5.2	1	25
I^{spw}	30	2.624 – 3.624	1	7.0 × 4.5 – 8.9 × 6.1	1	15 – 25
Q,U^{spw}	20	2.624 – 3.624	1	7.0 × 4.5 – 8.9 × 6.1	1	15 – 22

Notes. (1) Stokes parameter where 'mfs' stands for multi-frequency synthesis and 'spw' for spectral window; (2) `tclean` stopping threshold; (3) Central frequency of the final image; (4) Number of Taylor coefficients; (5) Synthesized beam size; (6) Cell size of each pixel in the final image; (7) rms noise in the final image (without primary beam correction - with pbcorr the rms noise is about 20 % larger).

- For multi-scale cleaning we used a scale sample of 0, 6, 9, 18, 30, 45, 60, 100, and 200 arcseconds, which corresponds to about 360 – 7400 pc.
- For all images we used Briggs-weighting with a robust parameter of 0.0 as a compromise between natural and uniform weighting, hence a compromise between high resolution and good sensitivity.

The final image parameters are listed in Table 4.4.

4.3.1 In-band Spectral Index

For imaging of wideband observations, the total intensity spectral index must be taken into account (see Section 2.1.2). For observations with wide frequency band receivers, the

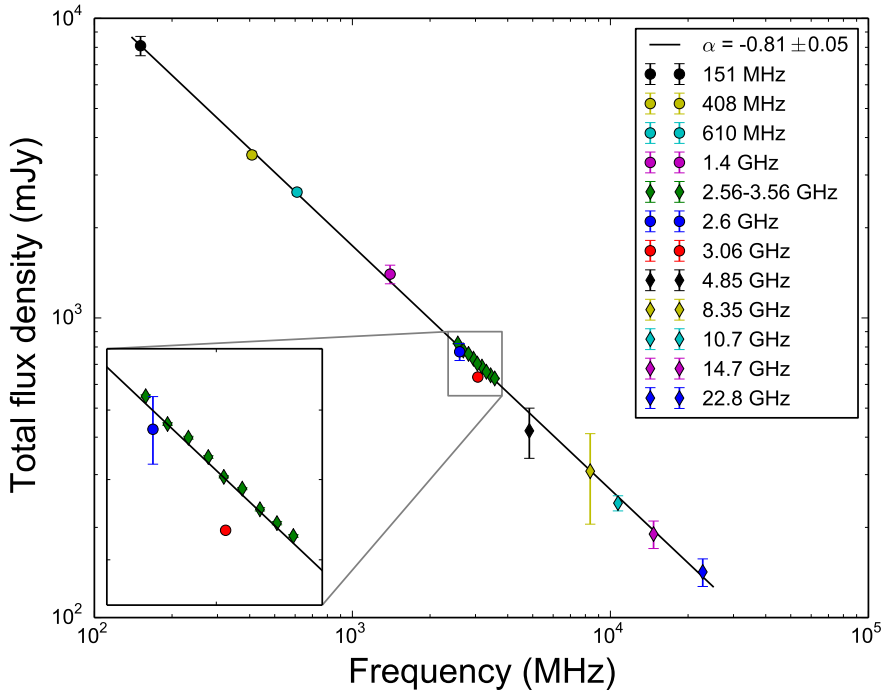

Figure 4.3.4: Total integrated radio continuum spectrum of M51 with a fitted power law giving a total spectral index $\alpha_{\rm tot} = -0.81 \pm 0.05$. The flux densities and references are listed in Table 4.5. In the bottom left, a zoom in to the S-band frequency range with the integrated flux densities of the spectral window images is shown. The red data point at 3.06 GHz shows the total flux density level obtained from the *mfs* Stokes *I* image (using nterms = 2) which is underestimated by about 10 %. The blue data point which lies within the S-band range comes from single-dish observations (Klein et al., 1984) and is in agreement within the errorbars with our observation.

synthesized imaging algorithm `clean` (Högbom, 1974) has implemented a procedure called multi-frequency synthesis. Using this algorithm gives the possibility to chose the number of Taylor coefficients to model the frequency dependence of the sky's brightness (see Rau and Cornwell, 2011 and Equation 4.3.1 and 4.3.2 in Section 4.3). This method revealed a problem of not recovering the right amount of flux density for extended sources. For regions with low signal-to-noise ratio (especially in the outskirts of M51, where most of the extended emission is located) `tclean` (the same holds for `clean`) gives a spectral index which is too steep.

Figure 4.3.4 shows the total integrated radio continuum spectrum of M51 at frequencies ranging from 151 MHz up to 23 GHz, showing data points from previous observations of several authors. The corresponding flux densities and references are listed in Table 4.5. The red data point at 3.06 GHz shows the integrated flux density of the new S-band observation at $I^{\rm mfs} = 635 \pm 2$ mJy (the errors is dominated by the noise contribution in the images:

Table 4.5: Integrated Total Radio Continuum Flux Densities of M51.

Frequency GHz	Flux density Jy	Reference
0.151	8.1 ± 0.6	Mulcahy et al. (2014)
0.408	3.5 ± 0.1	Gioia and Gregorini (1980)
0.610	2.63 ± 0.06	Segalovitz (1977)
1.4	1.4 ± 0.1	Dumas et al. (2011)
2.6	0.771 ± 0.05	Klein et al. (1984)
3.06	0.635 ± 0.002	I^{mfs} This work
2.56	0.822 ± 0.002	I^{spw} This work
2.69	0.779 ± 0.002	I^{spw} This work
2.82	0.759 ± 0.002	I^{spw} This work
2.95	0.731 ± 0.002	I^{spw} This work
3.06	0.704 ± 0.001	I^{spw} This work
3.18	0.688 ± 0.001	I^{spw} This work
3.31	0.661 ± 0.002	I^{spw} This work
3.43	0.644 ± 0.002	I^{spw} This work
3.56	0.628 ± 0.002	I^{spw} This work
4.85	0.420 ± 0.080	Stil et al. (2009)
8.35	0.308 ± 0.103	Dumas et al. (2011)
10.7	0.241 ± 0.014	Klein and Emerson (1981)
14.7	0.190 ± 0.020	Klein et al. (1984)
22.8	0.142 ± 0.015	Klein et al. (1984)

Notes. The listed flux densities are plotted in Figure 4.3.4. The errors reported for our S-band flux densities are dominated by the noise contribution in the individual images: $\Delta I = \sigma_I \cdot \sqrt{N_{\mathrm{beams}}}$.

$\Delta I = \sigma_I \cdot \sqrt{N_{\mathrm{beams}}}$, where N_{beams} is the number of beams within the integration area). The power-law fit to the flux densities from 151 MHz to 23 GHz gives a total integrated spectral index of $\alpha_{\mathrm{tot}} = -0.81 \pm 0.05$. By comparing the integrated flux density at S-band with the power-law fit, the missing flux density in the *mfs* Stokes I image amounts to about 70 mJy (10 %). To obtain the right amount of flux density, we produced spectral window images applying nterms = 1 in `tclean` which corresponds to a spectral index of zero within the sub-bands of about 128 MHz bandwidth. This results in spectral window images with the right level of total flux density. The integrated flux densities of M51 from the spectral window images are shown as green diamonds in Figure 4.3.4. To better compare the flux density level with the power law fit, a zoom-in version of the plot is shown in the bottom left corner of Figure 4.3.4. The total intensity measurements of the new spectral window images are in excellent agreement with the power-law fit performed using the archival Stokes I data at multiple frequencies. This shows that our observations cover the right flux density level and thus, the data are most likely do not suffer from missing short spacings (see Section 3.1.2).

We only show the total integrated radio continuum spectrum for the purpose to validate if the right amount of flux density was detected by our observations. For a detailed discussion of the spectrum, please see Mulcahy et al. (2014).

Figure 4.3.5 shows the spectral index distribution of M51. The left panel shows the spectral index distribution evaluated by fitting a power law to the spectral window images on a pixel basis. The right panel shows the spectral index map formed by `tclean`. To compare both results, the color scale is identical. The spectral index comparison shows that the multi-frequency synthesis algorithm computes spectral indices which are steeper on average by a factor of almost 3, compared to the spectral indices computed by a power law fit to the spectral window images. To quantify this statement, Figure 4.3.6 shows the histogram of the spectral index distribution for both cases. The power-law fit spectral index distribution shows a mean of -0.92 with a standard deviation of 0.69. Using

$$I^{\mathrm{mfs}} = I_{\nu_0} \cdot \left(\frac{\nu}{\nu_0}\right)^{\alpha_{\mathrm{tot}}} \tag{4.3.3}$$

with a reference frequency $\nu_0 = 2.56\,\mathrm{GHz}$ at the beginning of S-band and a reference flux density of $I_{\nu_0} = 822\,\mathrm{mJy}$, an average spectral index of -0.92 would give rise to a total integrated flux density of 698 mJy at 3.06 GHz, which is very close to the flux density measured in the spectral window image ($I^{\mathrm{spw}}_{3.06\,\mathrm{GHz}} = 704 \pm 1\,\mathrm{mJy}$). However, the spectral index distribution computed by `tclean` has a mean of -2.55 with standard deviation of 2.37 which gives a flux density of only 522 mJy at 3.06 GHz. Furthermore, the histogram of the spectral index from `tclean` shows a skewness of the distribution towards steeper spectral indices. In this case, the distribution deviates significantly from a Gaussian distribution (expected from the image noise), whereas the distribution of spectral indices from power-law fit shows a shape close to a Gaussian distribution. This analysis shows once again that the in-band spectral index computed by the `clean` algorithm is too steep and thus, is unsuitable for further analysis. Furthermore, the total flux density level in the Stokes I image computed using multi-frequency synthesis suffers from the wrong spectral index computation. For further analysis (e.g. for computing the map of the degree of polarization) we used the Stokes I map of the central spectral window at 3.06 GHz instead of the *mfs* Stokes I image.

A too steep spectral index computed by CASA's `clean` task was also found by other authors, e.g. Basu et al. (2017) and Condon (2015). The reason for the computation of the too steep spectral indices is beyond our current knowledge. For the multi-frequency synthesized image, this results in an integrated flux density level which is below the flux density extrapolated from other frequencies (assuming a constant spectral index across the referred frequency range).

4.3.2 Separation of Thermal and Non-thermal Emission

Polarized emission is generated by non-thermal synchrotron radiation. As it was discussed in Section 2.1, the observed total intensity emission of galaxies is a superposition of thermal + non-thermal radio emission. Therefore, to calculate an accurate (non-thermal) fractional

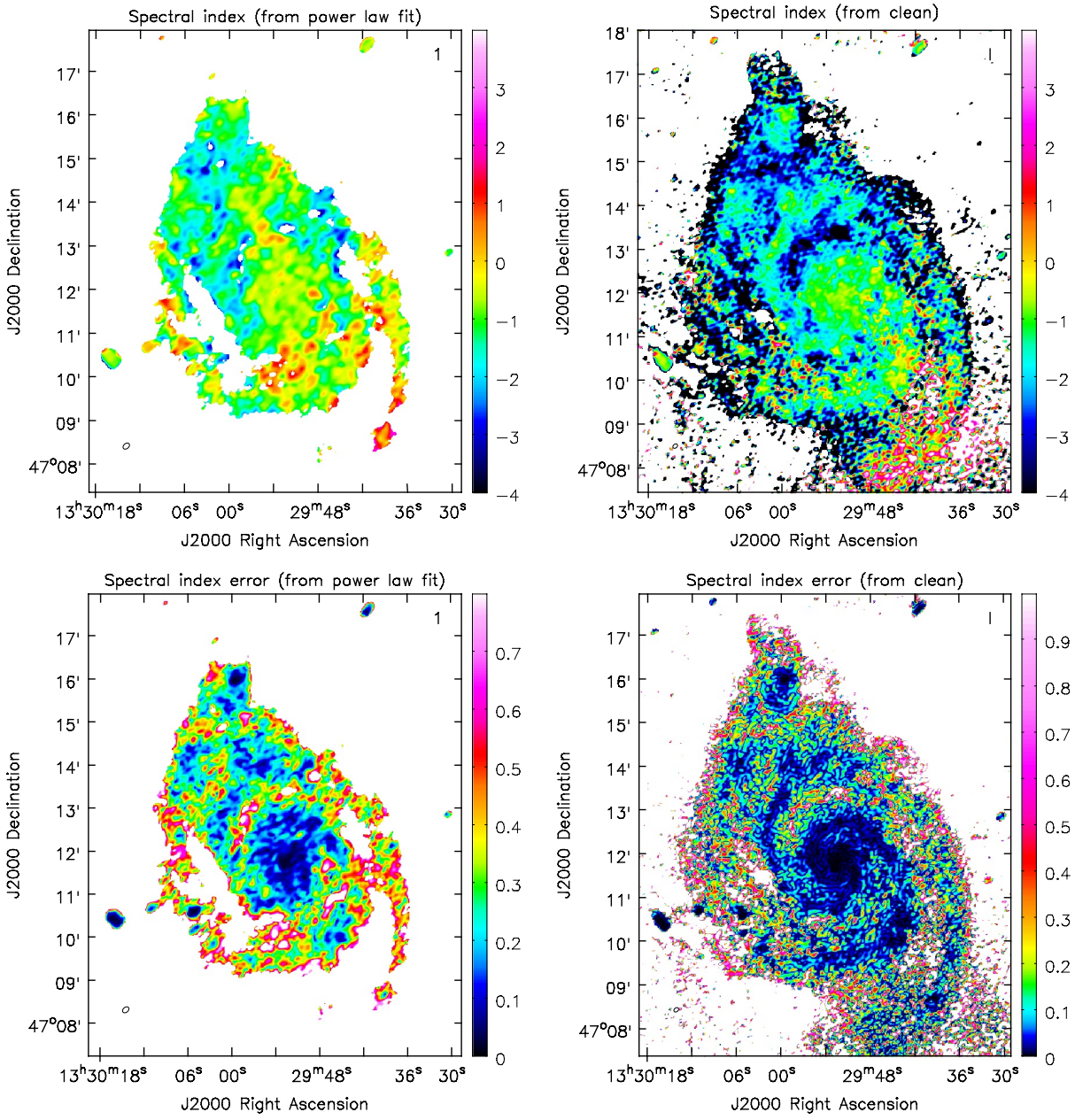

Figure 4.3.5: Spectral index maps of M51. The left images show the spectral index map from pixel-wise power law fitting of total intensity images of each spectral window (error map at the bottom). The right images show the spectral index map computed by CASA's `tclean` at the same color scale.

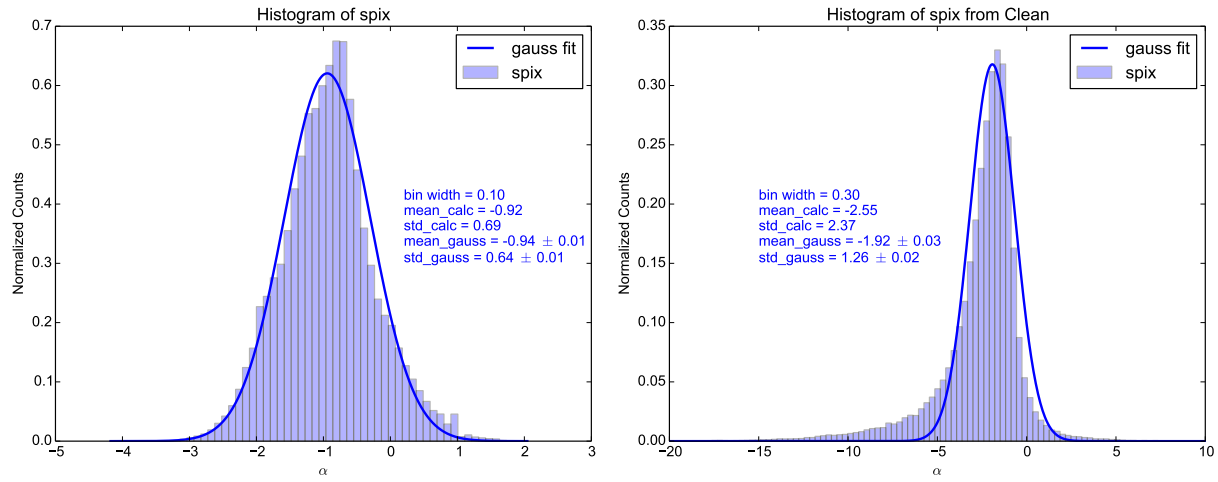

Figure 4.3.6: Histogram of the spectral index maps in M51. The left plot shows the spectral index distribution from a pixel-wise power law fit of total intensity images of each spectral window. The right plot shows the spectral index distribution computed by CASA's `tclean`. Data were only used where the signal to noise in total intensity exceeds three. The solid line is the best-fitting Gaussian to the histogram. The calculated mean and standard deviation from the data and the mean and standard deviation from the Gaussian fit are shown, respectively.

polarization and total magnetic field strength, the thermal fraction of the total intensity map of M51 must be subtracted from the Stokes I map. Thermal radiation is produced by free-free emission or bremsstrahlung of free electrons (see Chapter 2). Free electrons in the interstellar medium (ISM) of spiral galaxies are generated by ionization of neutral atoms (mainly hydrogen) where star formation processes such as supernova explosions and stellar winds are the most prominent ionization processes. Regions of recent star formation are the strongest sources of thermal emission in the ISM of galaxies. Star forming regions, such as molecular clouds, can be observed in infrared (IR) which traces stars and their environment, and in millimeter and sub-millimeter range which traces continuum dust emission and transitions in molecules. A good tracer of ionized hydrogen in the ISM of galaxies is the Hα emission line. It is generated by electrons of hydrogen atoms, falling from the third down to the second lowest energy level. This transition has a characteristic wavelength of 656 nm (Cox, 2000) and is therefore visible in the red part of the optical spectrum. However, Hα emission can be attenuated by dust absorption within the ISM. To correct for this, the absorbed and then re-radiated photons can be observed in IR emission. A detailed method of subtracting the thermal emission from radio continuum observations was developed by e.g. Tabatabaei et al. (2007) and Tabatabaei et al. (2018). Using this method, a Hα map is used as a tracer for the thermal radio emission. However, this method uses several assumptions which can cause erroneous thermal fractions and hence wrong polarization fractions.

For the purpose of our study, instead of correcting each pixel of the total intensity map

Table 4.6: Total Flux Densities and Thermal Fractions of M51.

Total Flux Density	Value	Reference
$S_{4.85\mathrm{GHz}}$	$420 \pm 80\,\mathrm{mJy}$	Stil et al. (2009)
$S_{1.4\mathrm{GHz}}$	$1400 \pm 100\,\mathrm{mJy}$	Dumas et al. (2011)
$S_{3.06\mathrm{GHz}}$	$704 \pm 1\,\mathrm{mJy}$	This work
Thermal Fraction	**Value**	**Reference**
$f^{\mathrm{th}}_{4.85\mathrm{GHz}}$	$0.15^{+0.12}_{-0.14}$	Tabatabaei et al. (2017)
$f^{\mathrm{th}}_{1.4\mathrm{GHz}}$	$0.05^{+0.05}_{-0.04}$	Tabatabaei et al. (2017)
$f^{\mathrm{th}}_{3.06\mathrm{GHz}}$	$0.09^{+0.08}_{-0.08}$	This work

Notes. The thermal fraction at 3.06 GHz was obtained using Equation 4.3.5.

for thermal emission (using e.g. a Hα map) we assume a constant thermal fraction across the entire galaxy. For this method, only a few data points at different radio frequencies are needed. Tabatabaei et al. (2017) fitted the radio continuum spectrum of a sample of nearby galaxies, including M51, using a Bayesian Markov Chain Monte Carlo (MCMC) interface. The data points of the spectrum are taken from Effelsberg observations and archival data in a frequency range of 1 – 10 GHz. The total radio continuum spectrum can be expressed as

$$S^{\mathrm{tot}}_{\nu} = S^{\mathrm{th}}_{\nu} + S^{\mathrm{nth}}_{\nu} = A_1\,\nu^{-0.1} + A_2\,\nu^{\alpha_{\mathrm{nth}}}\,, \tag{4.3.4}$$

where A_1 and A_2 are constant scaling factors and α_{nth} is the non-thermal spectral index which is assumed to be constant across the chosen frequency range (Tabatabaei et al., 2017). With this method, a mean thermal fraction across the galaxy is generated. The thermal fractions computed by Tabatabaei et al. (2017) are given in Table 4.6. Assuming a constant thermal spectral index of $\alpha_{\mathrm{th}} = -0.1$ and using the relation

$$f_{\mathrm{th}}(\nu) = \frac{S^{\mathrm{th}}_{\nu}}{S^{\mathrm{tot}}_{\nu}} = S_{\nu_0} \cdot f^{\mathrm{th}}_{\nu_0} \left(\frac{\nu}{\nu_0}\right)^{-0.1} / S^{\mathrm{tot}}_{\nu}\,, \tag{4.3.5}$$

with the numbers given in Table 4.6, the thermal fraction of M51 at $\nu = 3.06\,\mathrm{GHz}$, which is the central frequency of S-band, amounts to 9 %. This method gives a good approximation for the mean thermal fraction of M51 at S-band. Note that we did not correct the Stokes I map for thermal emission on a pixel-by-pixel basis. Instead we integrated the total intensity in particular regions for scientific analysis and subtracted the thermal fraction from the integrated total flux density: in Section 5.3.3 we investigate the degree of polarization as a function of radius where the thermal fraction was subtracted from individual data points of Stokes I to obtain the degree of non-thermal polarization. In Section 6.1.3 of Chapter 6, we compare different depolarization models to the observed degree of (non-thermal) polarization as a function of wavelength and applied the above described method to subtract the thermal fraction from Stokes I at all available wavelengths. In this method, the associated uncertainties of the thermal fraction were not taken into account.

In reality, the thermal fraction can have spatial variations across the galaxy. Mulcahy et al. (2017) performed a detailed thermal separation of their broadband S-band data of the face-on spiral galaxy NGC 628. They found a thermal fraction of 10 – 20 % in the spiral arms, 20 – 30 % at locations coinciding with HII regions and up to 47 % in the central part of the galaxy. The spatial variations in the thermal fraction in NGC 628 are lower limits to those in M51, because M51 has a higher star formation rate but similar size as NGC 628 (Heesen et al., 2014).

4.4 Summary of the Radio Polarization Dataset of M51

One important result of our analysis of wideband interferometric data shows that the in-band spectral index at S-band derived by the multi-frequency synthesis application in CASA's task `clean` is unreliable that is, the in-band spectral indices are too steep by about a factor of two. Note that this is only true when applying multi-frequency synthesis with number of Taylor coefficients > 1. Not only the spectral index distribution is unreliable, due to a strong bias towards steeper spectral indices also the total integrated flux density at S-band is too low by about 10 % (when using nterms $= 2$ in `clean`). Hence, the flux densities observed by the broadband S-band receiver of the VLA and analyzed by CASA's `clean` task must be taken with caution. For this reason, we used images in Stokes I, computed across the nine spectral windows of the effective frequency band, assuming no frequency dependence of the sky's brightness across those sub-bands. Comparing the flux density with the total integrated radio spectrum at other frequencies (if available) provides a trustful test whether the right amount of flux density was detected (as it is the case for all Stokes I spectral window images of our study). Details on the in-band spectral index problem are given in Section 4.3.1.

For the polarization study, we generated maps in Stokes Q and U for each spectral window and applied RM-Synthesis to obtain maps of the linearly polarized intensity, the polarization angle, and the RM. In Section 5.3 of Chapter 5 we describe the RM-Synthesis procedure in detail and give the chosen RM-Synthesis parameters used to generate the polarized intensity map.

Additionally, the maps of Stokes I (at the central spectral window), Q, and U (the maps of all spectral windows) were smoothed to 15″ resolution to be able to compare the results of our new S-band observations with VLA data at higher frequencies in C- and X-band at 4.85 GHz and 8.35 GHz (Fletcher et al., 2011) which are available at a resolution of 15″. To compare this to data at lower frequencies, we also smoothed the broadband L-band (1 – 2 GHz) VLA data set (Mao et al., 2015) to 15″ resolution in Stokes I, Q, and U. This provides us with a powerful radio polarization data set between 1 – 8 GHz to investigate in Chapter 6 the magneto-ionic medium of M51 at different physical depths and to investigate wavelength-dependent depolarization across the widest wavelength coverage in polarization of a nearby spiral galaxy to date. Table 4.7 gives an overview of the combined data set.

To ensure that the polarization analysis is not affected by bandwidth depolarization, we

Table 4.7: Combined Radio Polarization Dataset of M51.

Band GHz (1)	$\Delta\nu$ MHz (2)	$\delta\nu$ MHz (3)	N_{maps} (4)	σ_I μJy beam^{-1} (5)	σ_{QU} μJy beam^{-1} (6)	Reference (7)
L (1 – 2)	400 (1.12 – 1.84 GHz)	8	44	35	8	*A*
S (2 – 4)*	1000 (2.56 – 3.56 GHz)	128	9	30	6	This work
S (2 – 4)	1000 (2.56 – 3.56 GHz)	128	9	60	9	This work
C (4.85)	500	-	1	30	10	*B*
X (8.35)	1100	-	1	20	8	*B*

Notes. All maps have a resolution of 15″ except the with * marked S-band maps with a resolution of 10″ × 7″; (1) Frequency band; (2) Effective bandwidth (after flagging); (3) Channel width; (4) Number of maps given the effective bandwidth and the channel width; (5) rms noise in the total intensity map (across the band for L-band); (6) average rms noise in the Stokes Q and U maps; (7) References of the maps: *A* from Mao et al. (2015) and *B* from Fletcher et al. (2011). At S-band we give the rms noise values of the total intensity map of the central spectral window only since this map was used for analysis (see discussion of the in-band spectral index in Section 4.3.1).

examined the amount of depolarization within the observational frequency bands (1100 MHz at X-band, 500 MHz at C-band, 1000 MHz at S-band, and 400 MHz at L-band, also listed in Table 4.7). The reduction of the degree of polarization by bandwidth depolarization is dependent on the amplitude of the observed RM and the observational frequency and bandwidth (compare Equation 2.2.12). The effect is strongest at low frequencies. In fact, the degree of polarization would reduce by more than 5 % at L-band (given a bandwidth of 8 MHz) if |RM| is greater than about 300 rad m^{-2}. The maximum amplitude of RM observed at L-band in M51 amounts to only about 30 rad m^{-2}. For S-band (with subbands of 128 MHz width), a |RM| of 500 rad m^{-2} would reduce the degree of polarization by 5 %, but the maximum observed |RM| at S-band is a factor of about two smaller. Also at higher frequencies (at X and C-band) the amplitude in |RM| does not exceed the limit which reduces the degree of polarization by more than 1 %. Therefore, bandwidth depolarization does not affect our subsequent analysis.

CHAPTER 5

The Magnetized Disk-halo Transition Region in M51

5.1 Introduction

Observations show that large-scale magnetic fields exist not only in disks of galaxies, but also in galactic halos (e.g. Krause, 2014; Beck and Wielebinski, 2013; Mao et al., 2012c; Irwin et al., 2012). Due to the lack of simultaneous measurements of both disk and halo field structures in galaxies, the origin of large-scale halo fields and how they are connected to the underlying galactic disk remains poorly understood.

The grand design face-on spiral galaxy M51 provides a perfect laboratory for magnetic field studies in galaxies. Figure 5.1.1 shows an optical image of M51, overlaid with radio contours and a table with parameters of the galaxy. It has two clearly separated spiral arms where star formation takes place. The bright source located at the northern outskirts of M51 is its irregular companion dwarf galaxy NGC 5195.

M51 is well studied at multiple radio frequencies but observations of the linearly polarized emission in the vicinity of the frequency range of S-band (2 – 4 GHz) was only performed with the Effelsberg 100-m single-dish radio telescope at a limited resolution of about 4.5′ and with a narrow frequency band (Mulcahy, 2011). Why is this particular frequency range interesting? This question can be answered by considering wavelength-dependent Faraday depolarization: The polarized emission of M51 at different frequencies seems to originate from different layers of the face-on galaxy, that is from different physical depths. At high radio frequencies (5 – 8 GHz) the linearly polarized emission from the disk of the galaxy experiences low Faraday depolarization whereas at low radio frequencies (at around 1 GHz), the polarized signal from the disk is almost completely depolarized. Figure 5.1.2 shows the observed degree of polarization of M51 at frequencies between 1 – 8 GHz at the same angular resolution and the same color scale. One can see that the degree of polarization decreases with increasing wavelength (from bottom to top). Especially at L-band (top panel

Alternative Name	NGC 5194
Hubble Type	SAbc
Redshift	0.001544
Distance[a]	7.6 Mpc ($1'' \approx 37$ pc)
Position of center[b]	$13^h29^m52^s.709$
	$+47°11'42''.59$
Apparent Size (3 GHz)	$\sim 7.6'$
Linear size (3 GHz)	~ 17 kpc
Galactic Latitude	$+47°$
Galactic Longitude	$+202°$
Inclination[c]	$-20°$
Position Angle[c]	$-10°$
SFR[d]	$\sim$ 3.9 $M_\odot$ yr^{-1}

Figure 5.1.1: The Whirlpool spiral galaxy M51. Shown are the contours of total radio emission at λ 6 cm (VLA+Effelsberg) and magnetic field lines, overlaid on an optical image (Fletcher et al., 2011). The Table on the right summarizes physical parameters of M51.
Notes: [a] from Ciardullo et al. (2002); [b] RA and DEC in J2000 coordinate system from Ford et al. (1985); [c] Inclination of 0° is face-on, position angle of 0° is north, from Tully (1974); [d] Star formation rate from Heesen et al. (2014).

of Figure 5.1.2) the central region of M51 is strongly depolarized. Therefore, filling in the gap of polarization observations between high and low radio frequencies, allows us to probe an unknown physical layer of M51. Berkhuijsen et al. (1997) and Fletcher et al. (2011) proposed to probe a thick polarized disk of M51 at high frequencies (4.85 and 8.35 GHz) and the halo of M51 at low frequencies (1 GHz). At S-band, we hope to probe the layer in between the disk and the halo and we hope to learn something about the transition or possible interaction between the disk and halo of M51.

To investigate the transition between the disk and halo seen in polarized emission, we observed M51 with the Very Large Array (VLA) at S-band (2 – 4 GHz). Our new broadband S-band polarization data fill the gap between data observed with the VLA at L-band (1 – 2 GHz) by Mao et al. (2015), and C-band (4.85 GHz) and X-band (8.35 GHz) by Fletcher et al. (2011). With this combined high quality and broad frequency coverage data set we are able to investigate the magneto-ionic properties in different layers of M51. Preliminary results of this were already presented in conference proceedings (Kierdorf et al., 2018).

Polarization studies of M51 show that different configurations of the regular magnetic field exist in the disk and in the halo (e.g., Fletcher et al., 2011). According to Fletcher et al. (2011), the regular field in the disk is best described by a superposition of two azimuthal modes (axisymmetric plus quadrisymmetric), whereas the halo field has a dominating bisymmetric azimuthal mode (see Section 1.2 in Chapter 1). The difference in the magnetic field

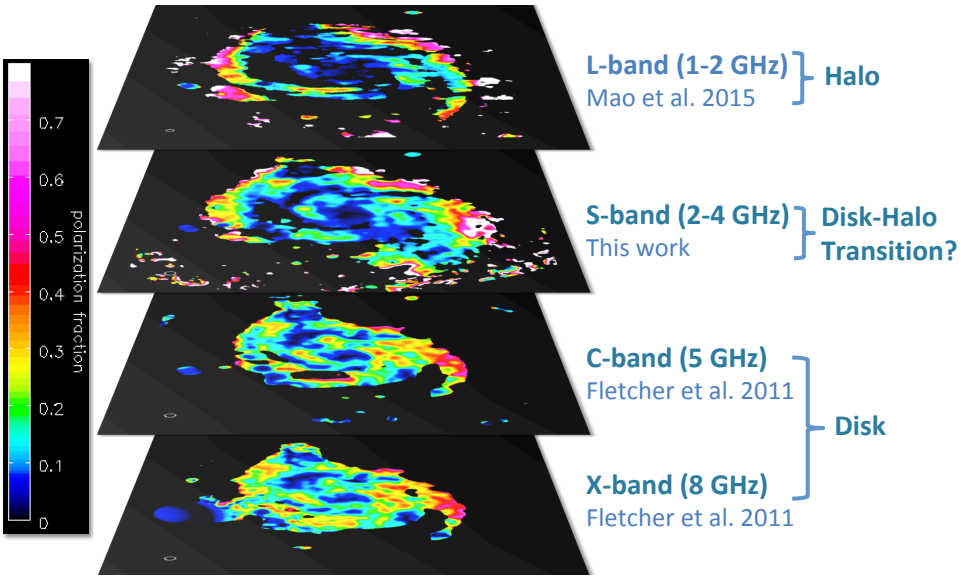

Figure 5.1.2: Observed degree of polarization of M51 at different frequencies. All images have the same color scale and are smoothed to the same resolution of 15″ (which corresponds to about 550 pc at the distance of M51). Note that the total intensity images used to calculate the degree of polarization were not corrected for thermal emission.

configuration between the disk and the halo of M51 is still poorly understood. A better understanding will come from observations of the transition region between the disk and the halo, thus with our new S-band data.

Additionally, the new broadband observations offer the possibility to perform RM-Synthesis to develop detailed models for the RM structure and therefore to see whether M51 shows a complex behavior in Faraday depth and to resolve any different Faraday rotating components from the different transition layers of the galaxy. The RM distribution computed by RM-Synthesis has the strong advantage to generate RM values unambiguously compared to the traditional method of measuring the polarization angles at (at least) two separated frequencies in narrow frequency bands (see Section 3.2). Another strong advantage of RM-Synthesis is the reduction of bandwidth depolarization.

The structure of this Chapter is as follows. Section 5.2 discusses the total intensity map of M51 at 3 GHz while in Section 5.3, we discuss the observed magnetic field component in the plane of the sky at S-band, specifically the linearly polarized intensity map, the magnetic field structure shown by the polarization angles, and the map of the degree of polarization (to analyze the field regularity). Details on the RM-Synthesis application are given in Section 5.3.1. Section 5.4 treats the magnetic field component parallel to the line-of-sight, given by the RM map observed at S-band. We discuss the global distribution of RM including a structure function analysis as well as local features of RM. Section 5.5 gives a summary of the scientific results.

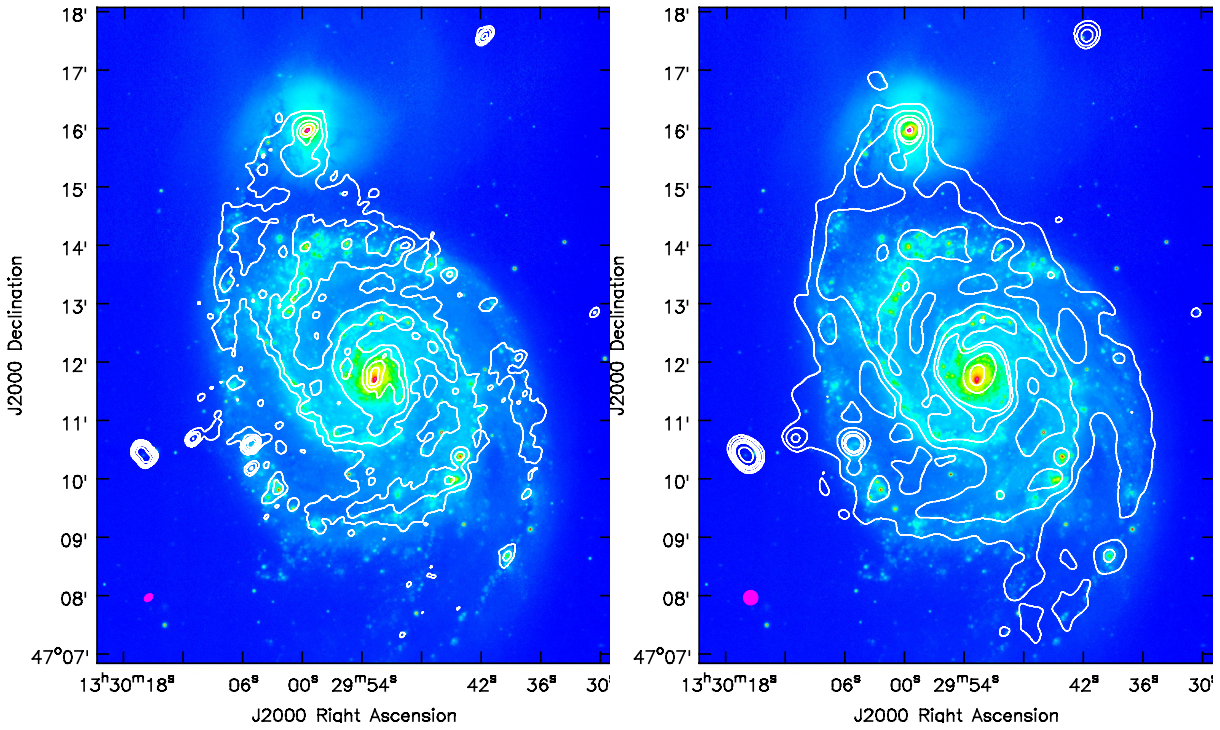

Figure 5.2.1: Total intensity of M51 at 3 GHz with a resolution of $10'' \times 7''$ (left) and $15''$ (right), overlaid onto a Hα image (Kennicutt et al., 2003). The contours are drawn at [8, 16, 32, 64, 128, 256, 512] $\times$ 30 μJy beam^{-1} (left) and [8, 16, 32, 64, 128, 256, 512] $\times$ 60 μJy beam^{-1} (right). The beam size is shown in the bottom left corner.

5.2 Total Intensity at S-band

In this section, the total intensity radio continuum emission in M51 at S-band is described and interpreted. We show Stokes I images at our highest resolution ($10'' \times 7''$) and images smoothed to $15''$ resolution. The S-band maps discussed in this section are listed in Table 4.7 along with the rms noises for both resolutions.

The radio continuum images of M51 at S-band are shown in Figure 5.2.1. Shown are the total intensity contours at S-band at $10'' \times 7''$ resolution (left) and $15''$ resolution (right). The $7''$ beam corresponds to a physical scale of about 360 pc at the distance of M51, whereas $15''$ corresponds to a physical scale of about 550 pc. Due to smoothing, the signal-to-noise ratio in the $15''$ resolution Stokes I image is by a factor of about 1.5 – 2 higher compared to the high resolution image (Table 4.7). Note that for S-band we report the total intensity rms noise of the spectral window image used for analysis. All images are overlaid to the optical image in Hα of Kennicutt et al. (2003)[1]. The two prominent spiral arms as well

[1]Hα emission is generated when electrons of hydrogen atoms falling from the third down to the second lowest energy level. This transition has a characteristic wavelength of 656 nm (Cox, 2000), is visible in the red part of the optical spectrum and is a good tracer of star formation activity (see Section 4.3.2).

as the small irregular companion dwarf galaxy NGC 5195 at the northern end of M51 are well visible in total intensity radio continuum emission at S-band (Figure 5.2.1). In the high resolution image, detailed structures of the gas are visible, especially spiral arms and peaks from HII regions, whereas in the smoothed version with 15″ resolution, the emission is detected towards slightly larger radii. The total intensity shows a close correspondence with the optical spiral arms and central region of M51, where the majority of star formation takes place. The results of the total intensity observations such as the appearance at S-band are consistent with radio synchrotron observations at other frequencies, specifically at C and X-band (Fletcher et al., 2011) and L-band (Mao et al., 2015).

Supernova remnants and strong stellar winds are the major sources of particle acceleration and therefore for the production of CREs in the ISM of spiral galaxies (e.g. Blasi, 2013). Hence, the spiral arms are well visible in total intensity (with a signal-to-noise ratio of 20 – 40 in our new S-band observation), tracing synchrotron radiation generated by CREs traveling through magnetized plasma (see Section 2.1.2). In the high resolution total intensity image one can ascertain some peaks of emission, e.g. at RA(J2000)= $13^{h}29^{m}44^{s}$ and Dec(J2000)= $+47°10'23''$, which well coincide with HII regions (Hill et al., 1997), visible as strong emission in the Hα image. This is expected since synchrotron emission and thermal bremsstrahlung, the main contribution to the total radio continuum emission, are attributed to star formation processes which most efficiently takes place in HII regions (e.g. Draine, 2011).

Total intensity synchrotron emission mainly traces isotropic random magnetic fields generated by the small-scale dynamo. The small-scale dynamo works most efficiently in regions with strong turbulence driven by star formation processes (e.g. Moss et al., 2012, see also Section 1.1).

5.3 M51's Magnetic Field in the Plane of the Sky at S-band

This section treats the properties of M51's magnetic field component in the plane of the sky perpendicular to the line-of-sight. Information on this component are given by the polarized intensity PI and the polarization angle ψ maps. To obtain maps of PI and ψ at S-band we applied RM-Synthesis to the polarization Stokes Q and U data. Details on the RM-Synthesis application are given in Section 5.3.1. The results of the polarized intensity and structure of the magnetic field (the PI and ψ maps) are discussed in Section 5.3.2. Using the PI and Stokes I maps one can generate a map of the observed degree of polarization which will be discussed in Section 5.3.3.

5.3.1 RM-Synthesis Application

To obtain the polarized intensity, RM and polarization angle map at S-band, we applied RM-Synthesis to the polarization Stokes Q and U data. First, images in Stokes Q and U were produced for each spectral window using `tclean`, which were concatenated to Stokes Q

Table 5.1: RM-Synthesis Parameters and Specifications at S-band.

Parameter	Value (Unit)	Explanation
$\phi_{\rm min}$	-2000 (rad m^{-2})	Minimum Faraday depth
N_ϕ	2000 (rad m^{-2})	Number of steps
$d\phi$	2 (rad m^{-2})	Step size
cutoff	$6\sigma_{\rm QU}$ (Jy)	RM-Clean cutoff
$\lambda^2_{\rm min}$	0.0137 (m^2)	Minimum wavelength
$\delta\lambda^2$	0.0013 (m^2)	Channel width
$\Delta\lambda^2$	0.0066 (m^2)	Wavelength-coverage
$\delta\phi$	522 (rad m^{-2})	Resolution in ϕ-space
$\|\|\phi_{\rm max}\|\|$	1357 (rad m^{-2})	Maximum detectable ϕ
max-scale	229 (rad m^{-2})	Maximum detectable scale

Notes. $\sigma_{\rm QU}$ is the average rms noise in the spectral window Stokes Q and U maps.

and U data cubes. The cleaning threshold and other imaging parameters are summarized in Table 4.4. Then, RM-Synthesis was performed by applying the python-based code developed by Michael Bell[2], based on RM-Synthesis techniques of Brentjens and de Bruyn (2005), on the data cubes. Details on the concept of RM-Synthesis are given in Section 3.2. RM-clean, a technique to deconvolve the complex polarization from clean models, similar to the clean algorithm used in interferometric imaging (e.g. Heald et al., 2009, see also Section 3.1.1) is included in this package and was applied to the data cubes as well. The parameters used to generate the polarized intensity and RM map of M51 as well as its limitations given by the instrument setting (see Section 3.2.3) are summarized in Table 5.1. RM-Synthesis produces cubes of Stokes Q, U, and polarized intensity with the Faraday depth on the third axis. The Faraday depth was chosen to range from -2000 to $+2000\,\mathrm{rad\,m^{-2}}$, to be able to detect possible contributions at large Faraday depths but not larger than the maximum detectable Faraday depth of $1357\,\mathrm{rad\,m^{-2}}$ given by the frequency configuration of the observation (see Table 5.1). Additionally, a Faraday depth and polarized intensity map of M51 at the Faraday depth of the main peak in the Faraday spectrum was generated. The rms noise in the polarized intensity map is given in Table 4.7. The rms noise in polarized intensity $\sigma_{QU} = (\sigma_Q + \sigma_U)/2$ at S-band was measured in a region at a source free location in the Stokes Q and U Faraday cubes, taking the average rms noise from all Faraday depth channels (at all Faraday depths within the cube).

The peak polarized intensity map together with Faraday spectra from different locations across M51 is shown in Figure 5.3.1. The resolution in Faraday depth, obtained from the wavelength coverage of the observation (Equation 3.2.6), amounts to $522\,\mathrm{rad\,m^{-2}}$. Given the poor resolution in Faraday space, no Faraday spectrum shows a complex behavior (multiple peaks or broad features, see Section 3.2 in Chapter 3). In case of only detecting a single unresolved Faraday depth feature in Faraday spectrum, RM $\approx \phi$ can be assumed. Therefore,

[2] http://www.github.com/mrbell/pyrmsynth

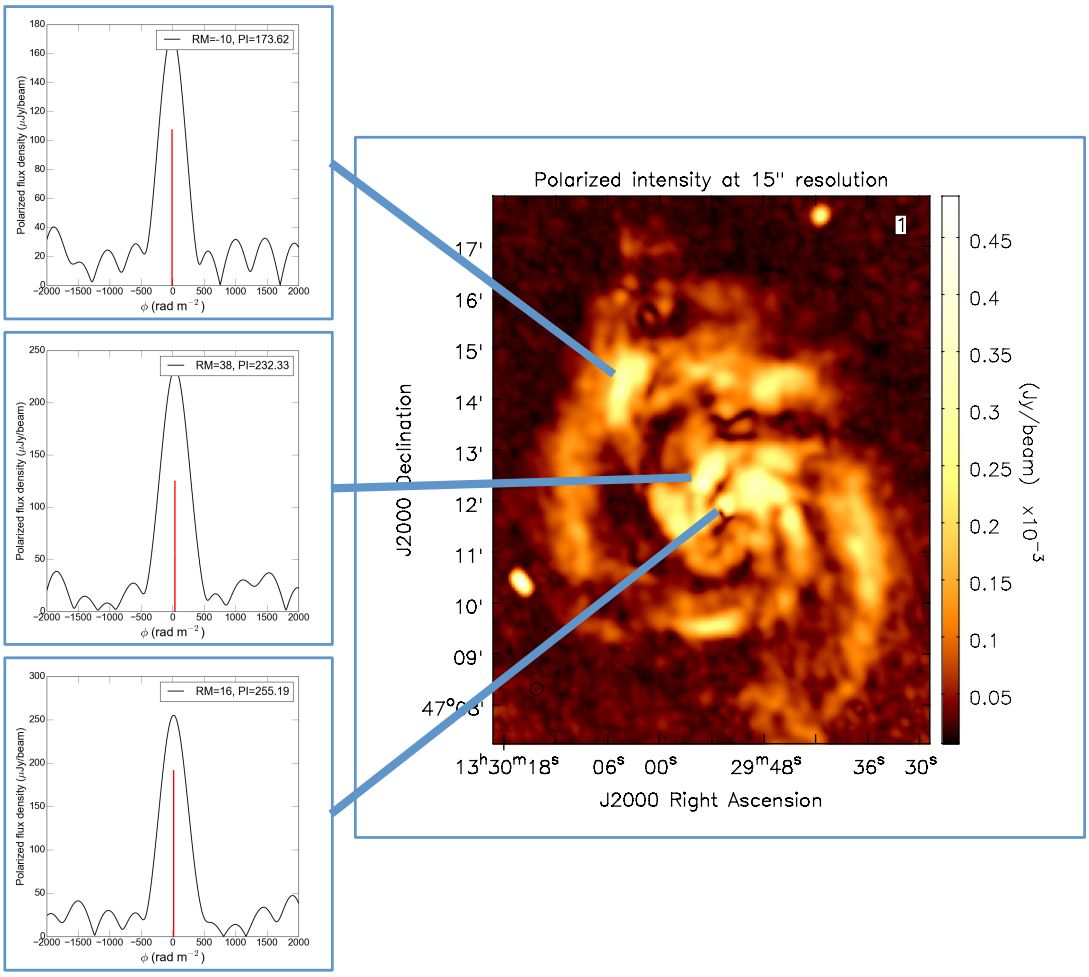

Figure 5.3.1: Linearly polarized intensity of M51 at 15″ resolution observed at S-band (right panel). The three panels on the left show Faraday spectra computed at three different locations in M51 (from a single pixel). With the resolution in Faraday depth of 522 rad m^{-2}, the Faraday spectra show no complex behavior because only one single peak is visible.

for the Faraday depth at the highest peak in polarized intensity we adopt the notation "peak RM" (or just "RM") in this thesis. Combining L- and S-band and applying RM-Synthesis will be part of a future project.

5.3.2 Polarized Intensity and Magnetic Field Structure

Figure 5.3.2 shows the contours of polarized intensity (obtained from RM-Synthesis, see Section 5.3.1) at 10″×7″ resolution (left) and 15″ resolution (right), overlaid with polarization $E + 90°$-orientations, representing the plane of polarization rotated by 90° to show the magnetic field structure. The contours are again overlaid to a Hα image from Kennicutt et al. (2003). Due to smoothing, the signal-to-noise ratio in the 15″ resolution Stokes Q and

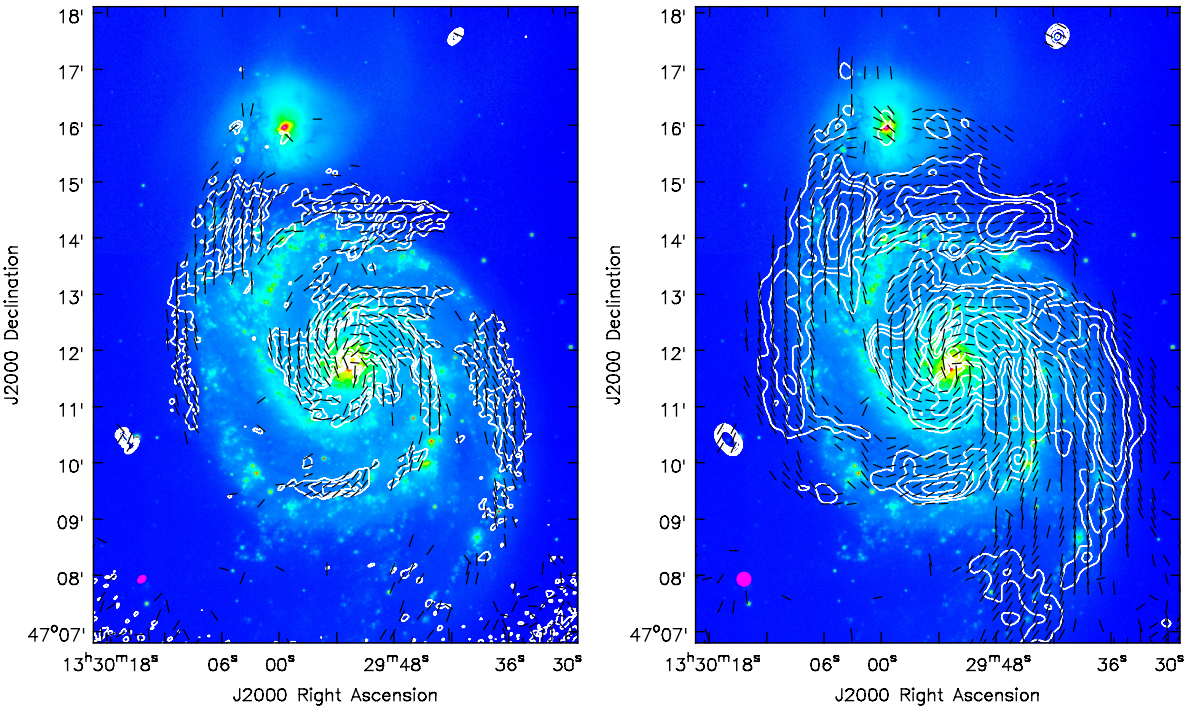

Figure 5.3.2: Linearly polarized intensity of M51 at 3 GHz with a resolution of $10'' \times 7''$ (left) and $15''$ (right), overlaid onto a Hα image (Kennicutt et al., 2003). The contours are drawn at [8, 12, 16, 24, 32, 64, 128, 256, 512] $\times$ 6 μJy beam^{-1} (left) and [8, 12, 16, 24, 32, 64, 128, 256, 512] $\times$ 9 μJy beam^{-1} (right). The polarized intensity maps are overlaid with the polarization $E + 90°$-orientations, not corrected for Faraday rotation to show the magnetic field structure. The beam size is shown in the bottom left corner.

U images increases by a factor of about 1.5 – 2 compared to the high resolution images. The magnetic field structure observed at S-band shown by the polarization $E + 90°$-orientations has a spiral pattern. The magnetic field orientations are not corrected for Faraday rotation, thus the displayed line segments are not the angles of the intrinsic magnetic field ψ_0. To derive the intrinsic magnetic field orientation one has to correct for Faraday rotation using $\psi_0 = \psi - \mathrm{RM} \cdot \lambda^2$ (see Section 2.2.1). However, the average error of about 20 rad m^{-2} in the observed RM leads to an error in the polarization angle of about $\pm 10°$. Hence, the corrected angles show some scatter across the galaxy. Because of this illustration issue, we only show the observed, not corrected angles. Anyway, the plotted orientations are close to the intrinsic one (they differ only by about $\pm 10°$) and thus illustrate the magnetic field structure in the galaxy sufficiently. The magnetic field structure observed at S-band is consistent with observations at C and X-band (Fletcher et al., 2011), and L-band (Mao et al., 2015), that is the polarization angles are arranged as spiral patterns at all frequencies. However, a closer look shows that the angles slightly differ which is caused by Faraday rotation between the bands.

Compared to the total intensity map, which shows a strong correspondence with the

optical spiral arms, the polarized intensity map is more complicated. Some parts of polarized emission coincides well with the optical spiral arms, but at some locations the peak of polarized emission is seen in the inter-arm regions. Such "magnetic arms" are observed in other face-on galaxies as well, for example in NGC 6946 (Beck and Hoernes, 1996) and IC 342 (Beck, 2015). In NGC 6946, the magnetic arms are well separated from the gas spiral arms but in M51, the situation is more complicated: At some locations, the inter-arm region shows a strong polarized signal (near the eastern inner spiral arm at RA(J2000)= $13^{h}29^{m}58^{s}$ and Dec(J2000)= $+47°11'33''$). However, at other inter-arm locations, only weak or even no polarized signal is detected. For example between the inner and outer eastern spiral arm (at RA(J2000)= $13^{h}30^{m}02^{s}$ and Dec(J2000)= $+47°11'00''$), a large region is located where the signal is completely depolarized. The formation of gas spiral arms in M51 is believed to be initiated by density waves (Lin and Shu, 1964; Kaplan and Pikelner, 1974; Byrd and Howard, 1990, see also Beck, 2016), which can also explain the formation of magnetic arms: quasi-static waves of high density compress the gas and magnetic fields during their galactic orbit. Compressed magnetic fields show up as strong polarized signals. Due to the compression of the gas, molecular clouds can be formed. The formation of stars is initiated, which is followed by evolution processes (stellar winds and supernova explosions/remnants) that generate thermal emission, turbulent magnetic fields and CREs. During the process of compression and star formation, the gas continues to rotate through the disk around the center of the galaxy. Hence, the processes of compression and star formation happen after each other in time and due to the continuous rotation also spatially. Therefore, the peak in polarized intensity should be located at the inner edge of the gas spiral arms (when the gas rotates counter-clockwise as it is the case in M51, Walter et al., 2008) as it was shown by Patrikeev et al. (2006) using maps of the CO, infrared and radio continuum emission. However, in M51 the peak polarized intensity seems to appear at arbitrary locations relative to the gas spiral arms at S-band. Consistently this was also found at other radio frequencies (see Fletcher et al. (2011) for a detailed description of total and polarized intensity in M51 seen at X and C-band). The relative locations of the magnetic and material arms traced by different observations were investigated in details in Patrikeev et al. (2006). The discrepancy of the location of the peak polarized intensity relative to the gas spiral arms could originate from tidal interactions with the small irregular companion galaxy NGC 5195, located at the northern end of M51, which could result in spiral arms showing considerable structures in the form of short-lived kinks and bifurcations (Dobbs et al., 2010).

Another explanation for the presence of "magnetic arms" is that turbulent gas motions in star forming regions causes an only weakly polarized signal, whereas in more quiescent regions such as the inter-arm regions, the magnetic field is not disrupted and the large-scale dynamo has sufficient time to generate regular magnetic fields without suppression by continues injection and amplification of turbulent fields by supernova shocks and/or stellar winds (as it is the case in the gas spiral arms). However, magnetic arms do not occur in all inter-arm regions in M51 and also not in all nearby face-on spiral galaxies. Hence, the formation of magnetic arms is still under debate. See Chapter 4.9 in Beck (2016) as a review on magnetic arms in nearby spiral galaxies.

The arbitrary locations of magnetic arms compared to the gas spiral arms has been observed at other radio frequencies as well (at C and X-band, Fletcher et al., 2011, and L-band, Mao et al., 2015). In other words, the polarized intensity spatial distributions across the galaxy are very similar at different frequencies, and therefore in different layers (see also Figure 5.1.2 in Section 5.1). As a future project, we will perform a detailed analysis of the structure in polarized intensity at different frequencies using a wavelet analysis of the relative positions and amplitudes of spiral structures as it was done for M83 in Frick et al. (2016).

5.3.3 Field Regularity

By dividing the linearly polarized intensity by the (non-thermal) total intensity one can generate a distribution of the observed degree of polarization in M51 (see Section 2.2 in Chapter 1). The observed distribution of the degree of polarization in M51 is shown in the top panels of Figure 5.3.3. Again we show images with different resolutions: The left panel shows the full resolution image with $10'' \times 7''$ beam size and the right panel shows the degree of polarization at $15''$ resolution computed using the smoothed versions of polarized and total intensity images. The degree of polarization map was clipped by the polarized intensity map using five times rms noise in polarized intensity (σ_{PI}, see Table 4.7) as a clipping threshold. To compute the non-thermal degree of polarization one should divide the polarized intensity only by the non-thermal contribution to the total emission. However, the total intensity map used to compute the degree of polarization map was *not* corrected for thermal emission on a pixel-by-pixel basis. Thus, the degree of polarization values shown in the maps are lower limits of the real (non-thermal) degree of polarization and are especially underestimated in regions where strong thermal emission contributes to the total radio continuum. More details on the procedure of separating the thermal contribution from the total radio continuum emission are given in Section 4.3.2. Also, as discussed in Section 4.3.1, the total intensity image obtained by multi-frequency synthesis (*mfs*) cannot recover the right amount of total flux density and hence, for computing the degree of polarization across M51 the total intensity spectral window image at 3 GHz was used. The polarized intensity map was generated by RM-Synthesis and hence produces PI at the central frequency of 3 GHz in the effective S-band range. The error map of the polarization fraction contributed from the image rms noise in total and polarized intensity was computed by Gaussian error propagation

$$\Delta p = \sqrt{\left(\frac{\sigma_{QU}}{I}\right)^2 + \left(\frac{PI \cdot \sigma_I}{I^2}\right)^2}\,, \tag{5.3.1}$$

where σ_I is the rms noises in Stokes I, σ_{QU} is the average rms noise in Stokes Q and U, and PI and I are the pixel-wise polarized intensity and total intensity values. To use Equation 5.3.1, we assume a Gaussian distribution of the noise in Stokes I, Q, and U. The error maps are shown in Figure 5.3.3. The typical error of the degree of polarization at $15''$ resolution amounts to about 1 % at high signal-to-noise ratio regions and up to about 8 % at locations with low signal-to-noise ratio. The degree of polarization is a measure of the ordering of the magnetic field responsible for the synchrotron emission: The higher the intrinsic degree of polarization, the more aligned or ordered are the magnetic field lines. However, the observed

degree of polarization can be attenuated by depolarization effects within the beam and along the line-of-sight. Different depolarization effects are summarized in Section 2.2.2.

At the locations of the gas spiral arms, the degree of polarization is low ($< 10\,\%$) which originates from tangled and/or turbulent magnetic fields due to star-forming activity, whereas at some inter-arm locations, the degree of polarization is high (up to about $40\,\%$), resulting from ordered or undisrupted magnetic fields. The global distribution of the degree of polarization in Figure 5.3.3 shows a clear radial increase from about $2\,\%$ in the center up to about $40\,\%$ at the outer spiral arms at S-band. To better illustrate this, we computed the degree of polarization as a function of the radius of the galaxy determined from the average total and polarized intensities at $15''$ resolution in radial rings. Note that we did not subtract thermal emission from the total intensity map. To get an estimate of the non-thermal emission in each ring, we assumed an exponentially decreasing radial profile of the thermal flux density[3]

$$S_\nu^{\mathrm{th}}(r) = S_\nu(0) \cdot \exp\left(-\frac{r}{l_s}\right) , \tag{5.3.2}$$

where r is the radius, $S_\nu(0)$ is the thermal flux density at the center of M51 (at radius $r = 0$), and l_s the scale length which is the radius at which the thermal flux density of the galaxy has decreased by a factor of e from the center. The scale length of $l_s = 40''$ was extracted from the Hα surface brightness in M51 as a function of radius (Figure 2 in Kennicutt, 1989). The slope of this dependency gives the scale length. To determine the thermal flux density at the center of M51 $S_\nu(0)$, we integrated the thermal flux density over radius

$$S_\nu^{\mathrm{th}} = \int_0^{r_{\mathrm{max}}} S_\nu(0) \cdot \exp\left(-\frac{r}{l_s}\right) \mathrm{d}r \qquad \Leftrightarrow \qquad S_\nu(0) = \frac{S_\nu^{\mathrm{th}}}{l_s\left(1 - \exp\left(-\frac{r_{\mathrm{max}}}{l_s}\right)\right)} , \tag{5.3.3}$$

where $S_\nu^{\mathrm{th}} = f_\nu^{\mathrm{th}} \cdot S_\nu^{\mathrm{tot}}$ was calculated using an average thermal fraction $f_\nu^{\mathrm{th}} = 9\,\%$, derived by Tabatabaei et al. (2017) (including dust-extinction correction) and the total integrated flux density S_ν^{tot} at the central spectral window (at 3.06 GHz) from Table 4.6 in Section 4.3.2. Note that this assumption ignores local spatial variations (by a factor of 2 – 4) of the thermal fraction as discussed in Section 4.3.2. The thermal flux density $S_\nu^{\mathrm{th}}(r)$ estimated via Equation 5.3.2 was then subtracted from the total averaged flux density in each ring.

The degree of (non-thermal) polarization as a function of radius at S-band is shown in Figure 5.3.4. The plotted error bars in Figure 5.3.4 are derived from the rms noise in the maps in Stokes I, Q, and U via Gaussian error propagation (compare Equation 5.3.1). The degree of polarization increases from a few percent at small radii up to about $20\,\%$ at larger radii. Additionally, we show the degree of (non-thermal) polarization as a function of radius at higher (X- and C-band) and lower (L-band) frequencies. The trend of an increasing degree of polarization towards larger radii is similar at all frequencies, whereas the amplitudes are significantly different (about a factor of three larger at higher frequencies and a factor of two lower at L-band compared to S-band). There are two bumps in the degree of polarization as

[3] Assuming an exponential decrease of the thermal emission in a spiral galaxy is valid as it was shown in e.g. NGC 6946 (Figure 10 in Walsh et al., 2002). Evidences of an exponential decrease of the SFR and therefore of the thermal emission in M51 is given Mulcahy et al. (2016)

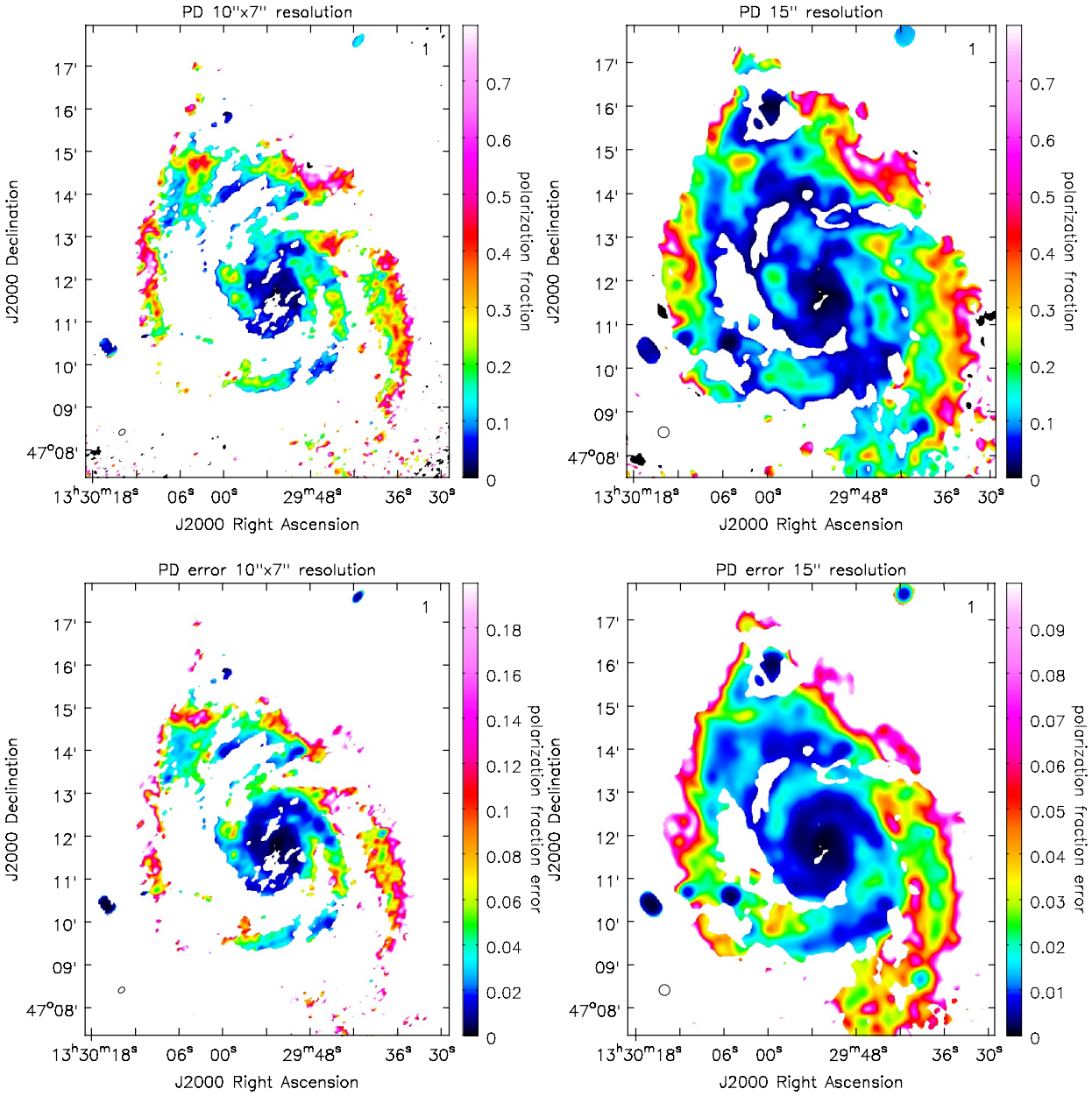

Figure 5.3.3: Observed degree of polarization at 3 GHz (top panels) at $10'' \times 7''$ resolution (left) and $15''$ resolution (right) and the corresponding error map (bottom panels). The beam circle is shown in the bottom left corner. Note that the total intensity image used to calculate the degree of polarization was not corrected for thermal emission and hence, the observed degree of polarization is underestimated in regions where strong thermal emission contributes to the total radio continuum.

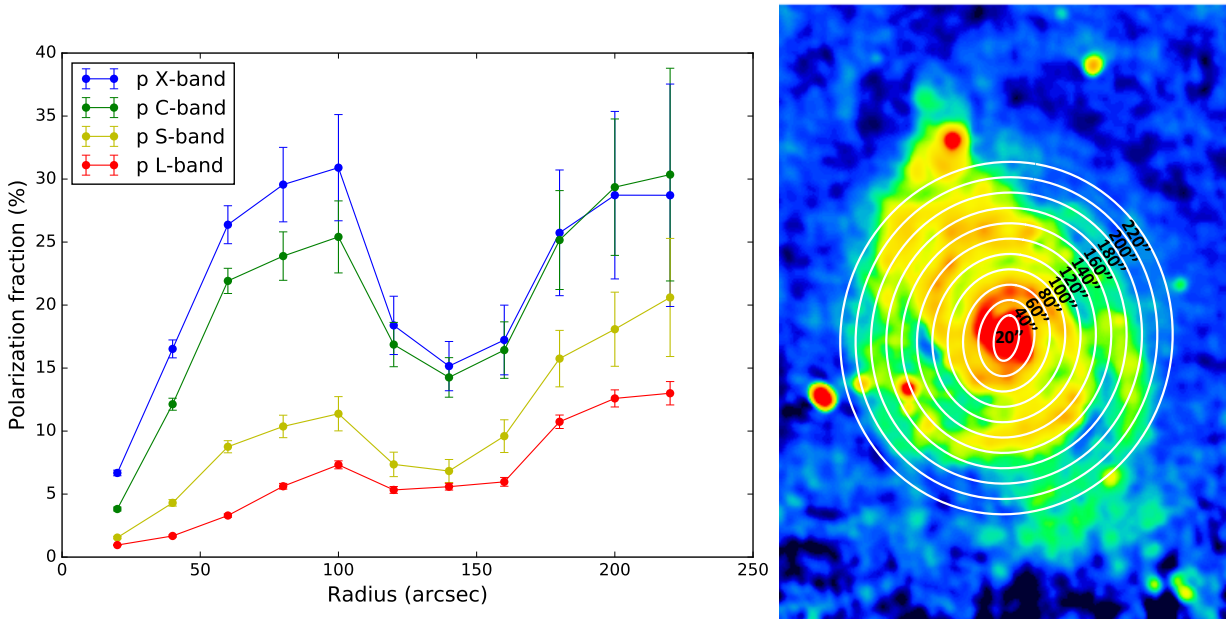

Figure 5.3.4: Degree of non-thermal polarization as a function of radius in M51. The rings are displayed in the right panel, overlaid to the total intensity distribution in M51 at S-band with 15″ resolution in rings of 20″ radial width in the plane of the galaxy (with inclination $l = -20°$ and position angle PA$= -10°$) out to a maximum radius of 220″ (this refers to the middle of the ring). The error bars are calculated from the rms noise in the maps from which the degrees of polarization are derived.

a function of radius at 100″ ($\sim$3.7 kpc) and about 200″ ($\sim$7.4 kpc). The rings at those radii are well coinciding with the radius of the inter-arm regions between the two well pronounced gas spiral arms in M51. As discussed above, the inter-arm regions are believed to host well-ordered magnetic fields which results in a high degree of polarization. If this is the case, then we expect the minima to appear at the position of the gas spiral arms where the magnetic field is disturbed by turbulence and hence, the degree of polarization is lower. Indeed, the minima in Figure 5.3.4 occurs at the galaxy center and at a radius of about 140″ ($\sim$5.2 kpc), which is exactly the radius at which both spiral arms are located. The degree of polarization changes by almost a factor of two between the arm and inter-arm regions. Note that the rings are not perfectly coinciding with the spiral arms – due to some pitch angles[4] one can only approximately assume circular shaped spiral arms. However, because the strongest/weakest emission of both prominent spiral arms/inter arms appears within the same rings, this approximation is sufficient for the purpose of this study.

The higher fractional polarization at larger radii could be caused by a decrease of Faraday depolarization as a function of radius. To verify that this is indeed the case, we calculated the depolarization between different bands. Figure 5.3.5 shows the depolarization (DP) between

[4]The pitch angle is defined as the angle between the tangent to the spiral arm and the tangent to a perfect circle, measured at the point where the arm and the circle intersect (e.g. Carroll and Ostlie, 1996).

S-band (2 – 4 GHz) and X-band (8.35 GHz) and L-band (1 – 2 GHz) and X-band, where DP = 1 means no depolarization and DP = 0 means total depolarization. Indeed, DP increases towards larger radii (from 0.1 – 0.4 between X- and L-band and from 0.2 – 0.7 between X- and S-band), which shows that the depolarization gets weaker at larger radii. A decreasing Faraday depolarization towards larger radii implies a decreasing turbulent magnetic field strength probably accompanied by a decreasing electron density towards larger radii (compare Equation 2.2.15). One can use the relationship between the degree of polarization and the ordered $B_{\rm ord}$ and turbulent $B_{\rm turb}$ magnetic field strength (Burn, 1966, corrected by Heiles, 1996):

$$\frac{p_{\rm obs}}{p_{\rm max}} = \frac{B_{\rm ord}^2}{B_{\rm ord}^2 + \frac{2}{3}B_{\rm turb}^2}\,, \tag{5.3.4}$$

with $p_{\rm obs}$ and $p_{\rm max}$ are the observed and maximum degrees of polarization, to determine the ratio of the isotropic turbulent field compared to the ordered field (regular plus anisotropic random):

$$\frac{B_{\rm turb}}{B_{\rm ord}} = \sqrt{\frac{3}{2}\left(\frac{p_{\rm max}}{p_{\rm obs}} - 1\right)} \tag{5.3.5}$$

Assuming a theoretical maximum degree of polarization 70 %[5] and using a typical degree of polarization in the inter-arm regions (at small radii up to $\sim$ 100″, $\sim$3.7 kpc) of about 20 % gives a turbulent field by a factor of 2 larger than the ordered field. With a degree of polarization of about 40 % observed at larger radii (compare Figure 5.3.3) this ratio of the ordered and turbulent field shrinks and the strengths become about equal.

5.4 M51's Magnetic Field Along the Line-of-sight at S-band

In this section, the component of the magnetic field parallel to the line-of-sight in M51 is discussed. By analyzing the RM map (obtained by RM-Synthesis, see Section 5.3.1) at S-band, a possible connection of the magnetic field in the disk and in the halo is investigated. The RM map obtained from RM-Synthesis is the first RM map of M51 at S-band.

5.4.1 Global RM Distribution

The RM map of M51 at S-band is shown in the top panels of Figure 5.4.1 at 10″×7″ resolution (left) and 15″ resolution (right). The RM map was clipped by the polarized intensity image using five times the average rms noise in Stokes Q and U σ_{QU} (Table 4.7) as a clipping threshold. The error in RM can be obtained by

$$\sigma_\phi = \frac{0.5\,\delta\phi}{\mathrm{S/N}_{PI}}\,, \tag{5.4.1}$$

[5] Assuming a typical synchrotron spectral index of $\alpha_{\rm syn} = -1.1$ at the inter-arm regions (Fletcher et al., 2011).

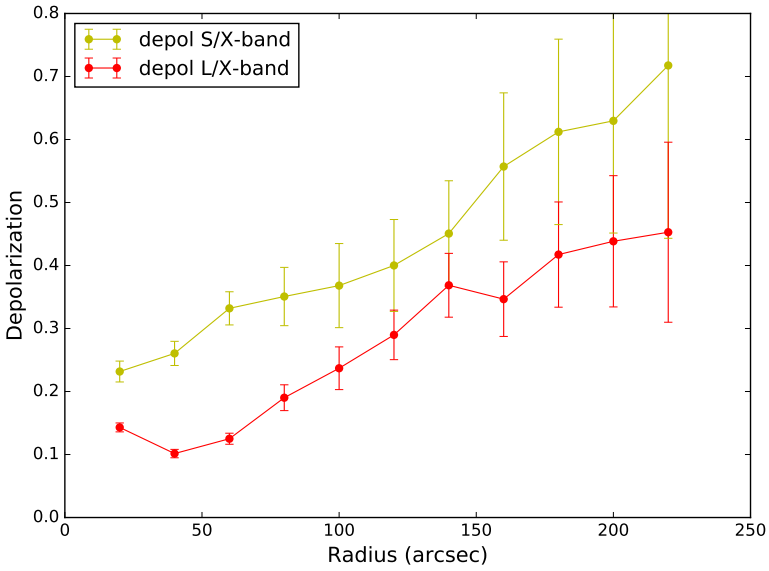

Figure 5.3.5: Faraday depolarization between S-band (2 – 4 GHz) and X-band (8.35 GHz) and L-band (1 – 2 GHz) and X-band in M51 as a function of radius in rings of 20″ radial width. The depolarization was calculated by the ratio of the degrees of polarization at the corresponding frequencies, where DP = 1 means no depolarization and DP = 0 means total depolarization.

where S/N_{PI} is the signal-to-noise ratio in polarized intensity and $\delta\phi$ is the resolution in Faraday depth (e.g. Iacobelli et al., 2013). The RM error across M51 is shown in the bottom panels of Figure 5.4.5 with a typical value of about $20 - 30\,\mathrm{rad\,m^{-2}}$.

The observed RM at S-band ranges from $\sim -150\,\mathrm{rad\,m^{-2}}$ to $\sim +150\,\mathrm{rad\,m^{-2}}$, which is much larger compared to the magnitudes found at L-band by Mao et al. (2015) of only $\pm 30\,\mathrm{rad\,m^{-2}}$. Fletcher et al. (2011) found magnitudes of $\pm 200\,\mathrm{rad\,m^{-2}}$ between $\lambda\,3 - 6$ cm. The varying amplitudes in RM found at different wavelengths results from the fact that the polarized emission from different layers in M51 experiences different amount of Faraday rotation: The polarized signal at short wavelengths (3 and 6 cm) originates from the disk and experiences Faraday rotation from all upper layers above the disk and the disk itself which are contributing to the observed RM. At S-band (around $\lambda = 10$ cm) the polarized signal from the disk is partly depolarized and the remaining signal experiences less Faraday rotation on the way to the observer which leads to a smaller amplitude in RM. At long wavelengths (around 20 cm) the signal from the disk is almost completely depolarized which is also reflected in the small amplitude of RM detected at L-band (see also Figure 5.1.2 in Section 5.1).

Thanks to M51's mild inclination of $l = -20°$, the RM map at S-band can detect signatures of the disk-halo magnetic field structure. Since the magnetic field orientations at S-band show a spiral pattern over large scales (compare Figure 5.3.2), one expects to see an obvious pattern also in RM across the galaxy if there exists a large scale regular magnetic

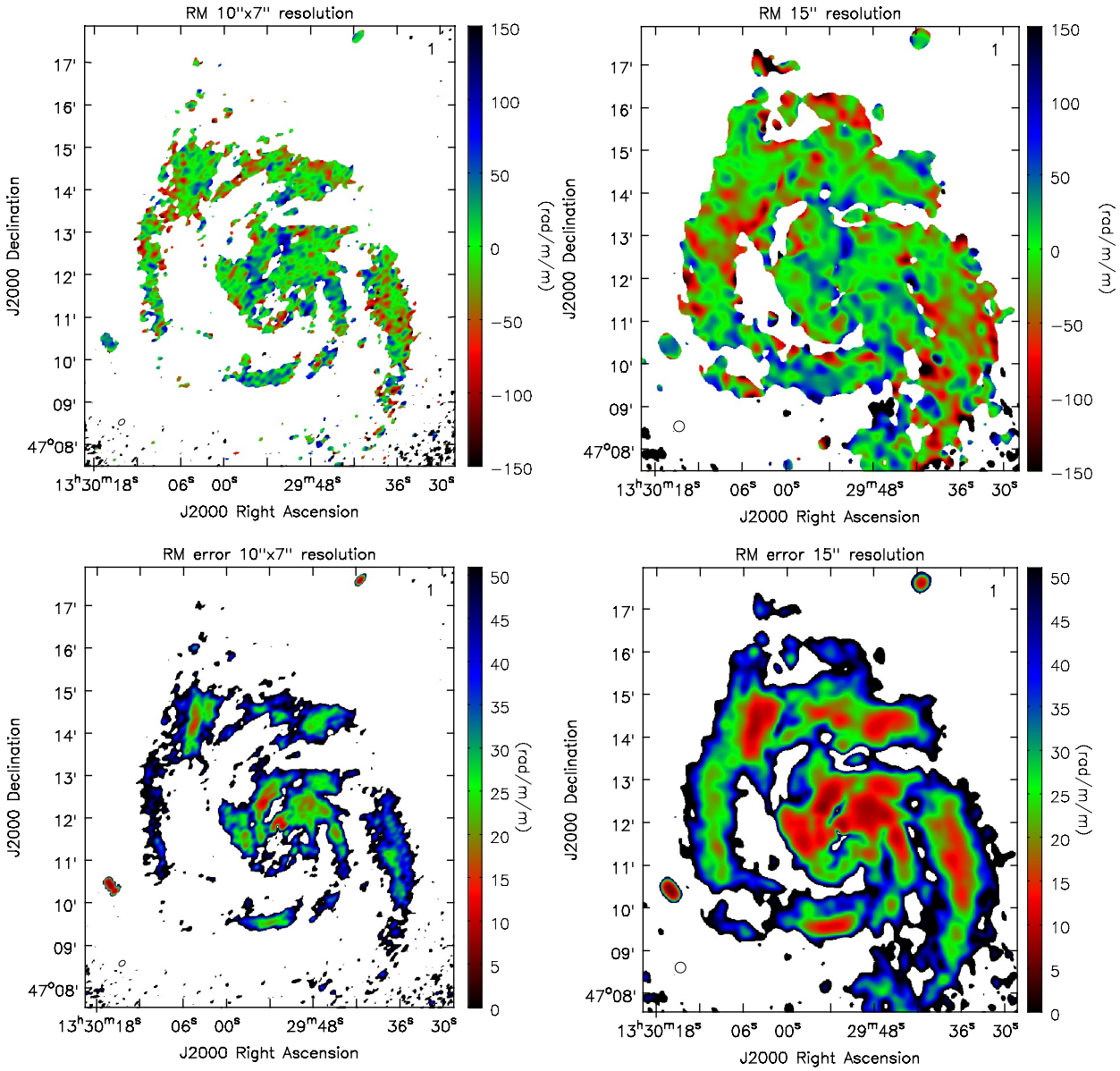

Figure 5.4.1: RM map of M51 (top panels) at $10'' \times 7''$ (left) and $15''$ (right) resolution. The bottom panels show the corresponding error maps, calculated using Equation 5.4.1. The beam ellipse is shown in the bottom left corner of each image.

field (as it was observed in e.g. M31 by Berkhuijsen et al., 2003). The RM maps in the top left panels of Figure 5.4.1 are dominated by fluctuations with no obvious large-scale signatures of a coherent field structure. This shows that the line-of-sight magnetic field component has a disordered structure across the galaxy. Therefore, the magnetic field in the disk-halo transition region of M51 seems to be dominated by magnetic fields with many reversals. This appears to be contradictory because the magnetic field orientations indicated by the polarization angles show an obvious systematic pattern along the spiral arms. However, the RM map shows many small patterns and fluctuations with changing sign. This contradiction is difficult to resolve. Anisotropic random fields could be one possibility. However, the large amplitudes of RM of $\pm\,150\,\mathrm{rad\,m^{-2}}$ indicate regular magnetic fields because for a purely anisotropic random magnetic field one would see only small amplitudes in RM. One explanation for the fluctuating nature of the RM could be provided by significant vertical magnetic field components perpendicular to the galaxy plane. Those vertical components could dominate the signal in Faraday rotation and could remove any large-scale pattern from a regular field in the disk-halo transition region. A detailed comparison of the structures appearing in the RM maps at S-band and between $\lambda\,3-6\,\mathrm{cm}$ by Fletcher et al. (2011) is provided by a structure function analysis in Section 5.4.2. Local features of regular magnetic fields which are transported from the disk into the halo, as another possible explanation for the fluctuating character of the RM, are investigated in Section 5.4.3.

In other face-on spiral galaxies (e.g. NGC 6946, IC 342, and M31) strong regular magnetic field components were found, shown by a clear north-south asymmetry in the RM map in the case of NGC 6946 (Beck, 2007). Fletcher et al. (2011) have found a large-scale pattern in the RM map of M51 after smoothing their data to 30″ which corresponds to $\approx$ 1.1 kpc (left panel of Figure 5.4.2). The visible pattern of large regions where RM changes sign is still rather complicated and difficult to interpret. An axisymmetric or bisymmetric spiral magnetic field in the disk would produce a single or double periodic azimuthal variation in the RM map. To test whether we can see a pattern in the RM map on larger scales in our S-band data, we created a RM map at 30″ resolution (right panel of Figure 5.4.2). There seems to be a dominant negative RM pattern at the north-east and south-west of the galaxy, which is difficult to explain by a simple axisymmetric or bisymmetric spiral field in the disk. Instead, a quadrisymmetric azimuthal spiral field (with mode $m = 2$) could be responsible for the pattern found at S-band with dominantly negative RM in the north-east and south-west and positive RM in the north-west and south-east. However, for a proper analysis of the RM map towards detecting signatures of a large scale RM pattern, one needs to apply a Fourier mode analysis (e.g. Fletcher et al., 2011).

A histogram of the RM map is shown in Figure 5.4.3. One can obtain the RM dispersion $\sigma_{\mathrm{RM},\perp}$, i.e. the dispersion from fluctuations of the magnetic field and thermal electron density in the sky plane on scales larger than the beam size, from the standard deviation of the RM distribution. The standard deviation given by the RM distribution in M51 at S-band at $10'' \times 7''$ and 15″ resolution amounts to about $38\,\mathrm{rad\,m^{-2}}$. Note that this RM dispersion should not be confused with the σ_{RM} caused by turbulent magnetic fields and fluctuations in the electron density within the telescope beam (Section 2.2.2). $\sigma_{\mathrm{RM},\perp}$ is basically the

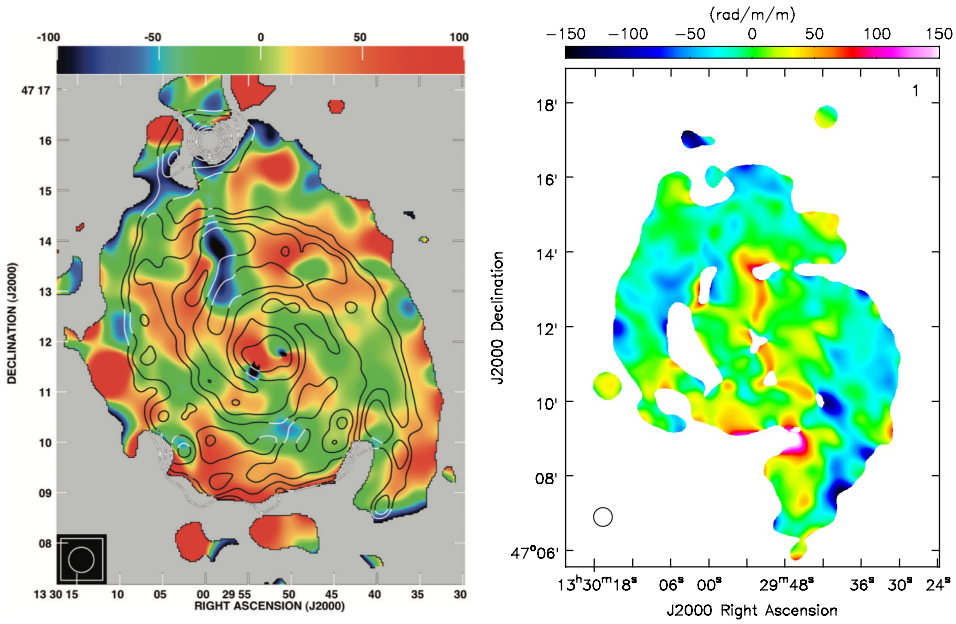

Figure 5.4.2: RM map of M51 at 30″ between $\lambda\lambda\,3$ and 6 cm (left panel) (Fletcher et al., 2011) and at S-band (right panel). The beam ellipse is shown in the bottom left corner of the image.

dispersion of RM *between* the beams. Therefore, $\sigma_{\mathrm{RM},\perp}$ is a lower limit for the RM dispersion within the beam σ_{RM}.

In the ISM of galaxies, sources of turbulence appear on different scales: Disruption in density waves, shearing regions, and superbubbles appear at kpc scales, whereas supernova remnants can reach sizes up to 100 pc. HII regions and winds of massive stars can interfere with the ISM on pc-scales (e.g. Elmegreen and Scalo, 2004). From the dispersion in RM across the galaxy, Fletcher et al. (2011) derived a turbulence cell size of 50 pc for the ISM in M51 (assuming a linear diameter of the beam of 600 pc, a RM dispersion $\sigma_{\mathrm{RM},\perp}$ of 15 rad m^{-2}, an average electron density of 0.1 cm^{-3}, a path length through the disk of 1 kpc, and a magnetic field strength of 20 μG). This is a typical turbulent cell size in spiral galaxies, which is by a factor of 6 – 12 (in linear scale) smaller than the physical size of our telescope beam of 330 pc at 7″ resolution and 550 pc at 15″ resolution. Therefore, all our observations are affected by beam depolarization, which originates from turbulent magnetic fields and fluctuating electron densities on scales smaller than the telescope beam (Section 2.2.2). To investigate the appearance of different scales from a turbulent magnetic field in the RM map and their correlations we generated a RM structure function which is discussed in Section 5.4.2.

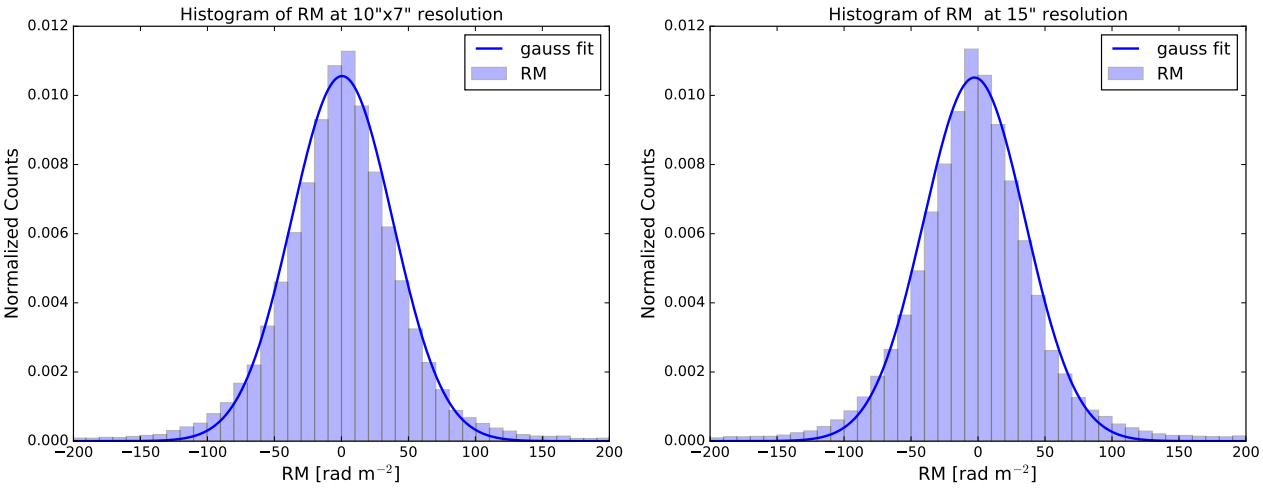

Figure 5.4.3: Histogram of the RM map at $10'' \times 7''$ (left panel) and $15''$ (right panel), shown in Figure 5.4.1. Data were only used where the signal-to-noise ratio in polarized intensity exceeds five. The solid line is the best-fitting Gaussian to the histogram with means of 0.5 and -2.7 rad m^{-2} and standard deviations of 37.8 and 37.9 rad m^{-2}, respectively.

5.4.2 Rotation Measure Structure Function

The statistics of fluctuations in RM can tell us about the magnetic field amplification by turbulence in the ISM on different scales. However, RM is a quantity not only dependent on the magnetic field component parallel to the line-of-sight but also on the electron density as well as the path length through the magnetized medium. In other words, features in the RM structure function could reflect fluctuation of the electron density, the magnetic field component along the line-of-sight and/or the path length and a combination of those quantities.

The second order structure function in RM is defined as (Simonetti et al., 1984; Haverkorn et al., 2004; Mao et al., 2015)

$$SF_{\mathrm{RM}}(\delta d)_{\mathrm{obs}} = \left\langle [\mathrm{RM}(d) - \mathrm{RM}(d+\delta d)]^2 \right\rangle , \tag{5.4.2}$$

where d is the position of a pixel in the RM map and $d+\delta d$ is the position of any neighboring pixel with distance δd to the reference pixel at position d. The brackets $\langle \ldots \rangle$ denote the average. Using Equation 5.4.4 we calculate the observed structure function of RM for any distance within the galaxy obtained from the RM map. Note that we excluded polarized background sources from the RM map to compute the structure function. The contribution of uncertainties of the observed RM by the rms noise in the Stokes Q and U images can be taken into account by subtracting a DC offset from the observed structure function (Haverkorn et al., 2004; Mao et al., 2015)

$$\Delta SF_{\mathrm{RM}}(\delta d) = \left\langle \Delta\mathrm{RM}(d)^2 + \Delta\mathrm{RM}(d+\delta d)^2 \right\rangle . \tag{5.4.3}$$

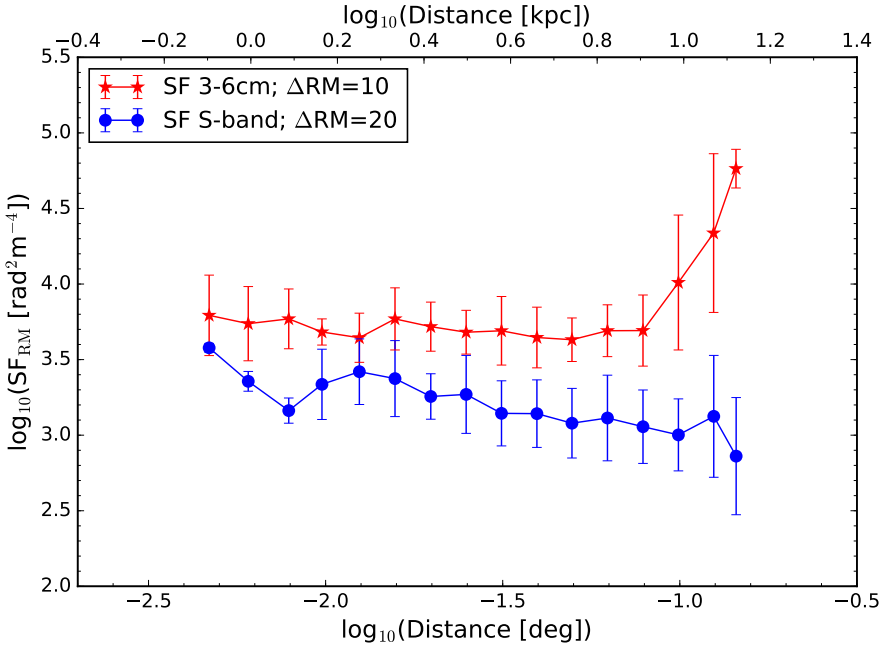

Figure 5.4.4: RM structure function of M51 constructed from the RM map at S-band (blue) and from the RM map computed from narrow band observations at 3.6 cm and 6.2 cm wavelength (red) (Fletcher et al., 2011). The structure functions were binned in equal log intervals of 0.1. The errors bars denote the standard deviation in each bin interval. Note that for computation of the structure function at S-band, a RM map with a 5σ clipping threshold in polarized intensity was used.

With

$$SF_{\rm RM}(\delta d) = SF_{\rm RM}(\delta d)_{\rm obs} - \Delta SF_{\rm RM}(\delta d)\,, \tag{5.4.4}$$

where $\Delta SF_{\rm RM}$ is the typical error in the corresponding RM map, we obtain the structure function of the RM map in M51 $SF_{\rm RM}(\delta d)$ (Haverkorn et al., 2004).

We computed the structure function from our new S-band RM map which has an average RM error of $+20\,\mathrm{rad\,m^{-2}}$. For a direct comparison we also computed the structure function using the RM map derived from $\lambda\lambda\,3$ and 6 cm VLA data by Fletcher et al. (2011), which has an average RM error of $+10\,\mathrm{rad\,m^{-2}}$. Figure 5.4.4 shows the structure function of the RM map across M51 obtained from RM-Synthesis applied on the S-band Stokes Q and U data at $15''$ resolution and from the RM map between $\lambda\,3.6-6.2$ cm (Fletcher et al., 2011). We only show the structure functions up to scales equal to the galaxy diameter ($7'$ or 17 kpc). At large scales ($\log(\delta d) > -1.1$; $\delta d > 4.7'$) the structure function from $\lambda\,3-6$ cm shows a strong increase also found by Mao et al. (2015). They interpreted the rise at large scales as a signature of a large-scale RM gradient produced by coherent fields in magnetic arms of M51. In the structure function from the RM map at S-band no such increase at larger scales is detected, likely because the magnetic field at S-band (in the disk-halo transition region) is dominated by vertical fields with many field reversals.

The amplitude of the flat part of the structure function at S-band at about 10 cm observing wavelength ($\log(SF_{\rm RM})_{\rm S\text{-}band} \approx 3.2^{+0.2}_{-0.2}$) is significantly smaller compared to the amplitude of the structure function obtained from data at shorter wavelength between $\lambda\,3-6$ cm ($\log(SF_{\rm RM})_{3-6\,\rm cm} \approx 3.7$). The amplitude of the structure function obtained from L-band (around $\lambda\,20$ cm) lies below the S-band structure function ($\log(SF_{\rm RM})_{\rm L\text{-}band} \approx 2.2$) (Mao et al., 2015). From the amplitude of the flat part of the structure function one can calculate the RM dispersion (amplitude $\approx 2\,\sigma^2_{\rm RM}$). From this, we computed a RM dispersion at S-band of $\sigma_{\rm RM} \approx 28^{+7}_{-6}\,\mathrm{rad\,m^{-2}}$. This value is smaller than the standard deviation obtained from the histogram of the RM map at S-band ($38\,\mathrm{rad\,m^{-2}}$, compare Figure 5.4.3). The reason why the $\sigma_{\rm RM}$ computed from the saturation level of the structure function from S-band observations is smaller, compared to the standard deviation of the histogram is as follows: When computing the structure function via Equation 5.4.4, we subtract the typical error of the observed RM. This decreases the amplitude of the structure function and yields a smaller value of $\sigma_{\rm RM}$. To test this, we computed the structure function only from the observed RMs which gives a RM dispersion of about $35\,\mathrm{rad\,m^{-2}}$. This is consistent with the standard deviation from the histogram. We tested also if the saturation level of the structure function and the histogram gives the same value of $\sigma_{\rm RM}$: We generated a Mock RM map with a Gaussian distribution with a mean of zero and a standard deviation of $50\,\mathrm{rad\,m^{-2}}$ and $25\,\mathrm{rad\,m^{-2}}$. From this, we computed a structure function and indeed, the level of saturation gives exactly $2\sigma^2_{\rm RM,Mock}$, where $\sigma_{\rm RM,Mock}$ is the standard deviation of the Mock RM map.

For the structure function between $\lambda\,3-6$ cm and at L-band (the amplitude of the structure function at L-band is given in Mao et al., 2015) we computed a RM dispersion of $50\,\mathrm{rad\,m^{-2}}$ ($60\,\mathrm{rad\,m^{-2}}$) and $9\,\mathrm{rad\,m^{-2}}$ ($14\,\mathrm{rad\,m^{-2}}$), with (without) error subtraction. Both are in excellent agreement with the standard deviation computed from the histogram of the observed RM (60.4 and $13.7\,\mathrm{rad\,m^{-2}}$, respectively). The $\sigma_{\rm RM}$ at L-band is by a factor of five smaller than the one at short wavelengths. The observations at L-band are taken at similar resolutions (about $11''$) and hence, the different values reflects once again that we observe different polarization layers of the face-on galaxy at different wavelengths: The RM dispersion at long wavelengths is smaller because the contribution from the turbulent magnetic field and fluctuations in thermal electron densities is lower in the layer closer to the observer (the near-side halo).

5.4.3 Local RM Features

Magnetic fields in spiral galaxies are believed to be transported into the halo by galactic winds or fountains, supernova remnants, and so-called Parker instabilities (Parker, 1966; Rodrigues et al., 2016; Moss et al., 2010; Braun et al., 2010). Also observations of edge-on spiral galaxies provide evidence to expect vertical magnetic fields (e.g. Krause, 2014). Evidences for such vertical field components is given by the RM map of a face-on galaxy such as M51, since RM is tracing the magnetic field component along the line-of-sight. Heald (2012) found a co-location of a gradient in RM of $38.2\,\mathrm{rad\,m^{-2}}$ (ranging from +18.8 to $+57.0\,\mathrm{rad\,m^{-2}}$) and a hole observed in neutral Hydrogen (HI) in the face-on nearby spiral

galaxy NGC 6946. The data are part of the Westerbork Spitzer Infrared Nearby Galaxies Survey (SINGS) conducted by Heald et al. (2009). The uncertainty in RM is stated as about $5\,\mathrm{rad\,m^{-2}}$. The HI hole is formed by star formation driven flows, transporting the local magnetic field from the disk into the halo. Note that the variation of RM across the HI hole shows a sinusoidal variation, erroneously referred to as a gradient in the literature. Also Mulcahy et al. (2017) found one RM variation coinciding with a HI hole in the face-on spiral galaxy NGC 628 at S-band. In this case the RM ranges from $-20\,\mathrm{rad\,m^{-2}}$ to $-130\,\mathrm{rad\,m^{-2}}$ with an uncertainty of about $30-40\,\mathrm{rad\,m^{-2}}$ (read off from the error map in Figure 18 of Mulcahy et al., 2017). Mao et al. (2015) found no coincidence between HI holes and RM variations in M51 observed at L-band. Physically, it means at L-band deep layers through the galaxy cannot be probed and thus, we are only probing a layer which lie above the polarized emission generating disk.

M51 was observed in HI as part of the THINGS (The HI Nearby Galaxy Survey) project (Walter et al., 2008). Bagetakos et al. (2011) provided a catalog of HI holes in nearby galaxies, detecting them by visually inspecting the HI maps. Details on the selection criteria of the HI hole detections are given in Bagetakos et al. (2011). To compare the HI hole detections with the RM map seen in M51 at S-band, in Figure 5.4.5 the ellipses associated with HI hole detections are overlaid to the RM map. Shown are the RM maps for both, the full resolution of $10'' \times 7''$ and the version smoothed to $15''$ resolution. One can clearly see that the $15''$ map has a better signal-to-noise ratio compared to the high resolution version. In the high resolution image a large fraction of HI holes lie outside regions with high signal-to-noise ratio.

By comparing the position of HI hole detections with the RM map at $15''$ visually, a RM variation of $\Delta\mathrm{RM} = 124\,\mathrm{rad\,m^{-2}}$ coinciding with a HI hole was detected, with RM increasing from $-94 \pm 46\,\mathrm{rad\,m^{-2}}$ at the northern edge of the HI hole to $+30 \pm 40\,\mathrm{rad\,m^{-2}}$ at the southern edge. The HI hole is located at RA(J2000)= $13^{\mathrm{h}}29^{\mathrm{m}}49^{\mathrm{s}}$ and Dec(J2000)= $+47°10'02''$ with an expansion velocity of $14\,\mathrm{km\,s^{-1}}$ and a kinetic age of 29 Myr (Bagetakos et al., 2011). The location is indicated by a square in the right hand panel of Figure 5.4.5. A zoom in to this region is shown in Figure 5.4.6. The midpoint of the RM variation is close to the typical RM value in the surrounding area of the disk of about $-20\,\mathrm{rad\,m^{-2}}$. The RM variation has a scale with a linear size of 600 pc, while the HI hole itself has a linear scale of about 800 pc in diameter. Not only the RM variation but also the orientation of the surrounding magnetic field matches with the orientation of the HI hole (south-east to north-west). The RM variation and matching magnetic field orientation are indications that at this location the regular magnetic field was transported into the halo by star formation driven processes (shocks in supernova remnants), forming a large loop of magnetic field lines along the regular mean field direction.

No other RM variations coinciding with HI holes across the galaxy were found. There are several possible reasons why only one coincidence of HI holes and RM variations was detected in M51 at S-band. (1) HI holes need to have a certain age since they must be old enough to have build up a vertical offset from the mean field, and young enough so that shearing effects (e.g. from differential rotation) are not destroying the signatures in

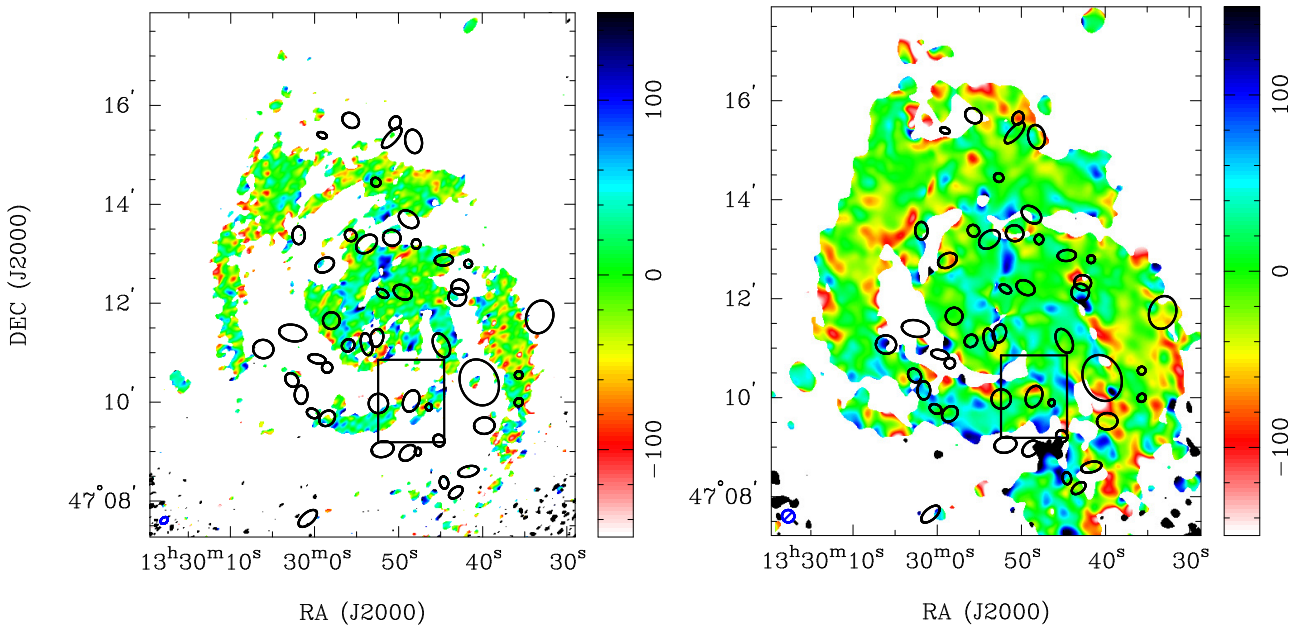

Figure 5.4.5: RM map of M51 at $10'' \times 7''$ (left) and $15''$ (right) resolution, overlaid with the position of the HI holes from Bagetakos et al. (2011). Both images have the same color scale, ranging from $-150\,\mathrm{rad\,m^{-2}}$ to $+150\,\mathrm{rad\,m^{-2}}$. The beam ellipse is shown in the bottom left corner of each image. The black square in the right panel shows the frame of the zoom in to the HI hole coinciding with a RM variation shown in Figure 5.4.6.

RM. (2) HI holes are formed by multiple supernova explosions and stellar wind activities. Therefore, the feature must appear in an ideal geometrical situation to be detectable. The probability to find an undistorted magnetic field loop, observable as a RM variation across the entire extend of the hole, could be small. (3) A simple reason for non-detections of RM variations coinciding with HI holes (at least in M51) could be the weak regular magnetic field component in the disk an thus, that the field is dominated by anisotropic random fluctuations. For anisotropic random fields we do not expect to see a variation in RM even if a magnetic field loop is formed and coincides with the HI hole because the randomly occurring field reversals along the loop of anisotropic random fields would cancel out each other. Hence, a RM variation can only be observed in case of a regular/coherent magnetic field. If the total magnetic field in M51 is indeed dominated by anisotropic random fields, the RM variation found in our S-band data could be an exceptional case where the magnetic field is only regular/coherent locally at the position of the corresponding HI hole. However, Heald (2012) and Mulcahy et al. (2017) found also only one RM variation coinciding with a HI hole in the face-on nearby spiral galaxies NGC 6946 and NGC 628, respectively, even though these galaxies have a strong regular magnetic field component. The fact of the rare number of detections of HI holes coinciding with RM features in three nearby face-on spiral galaxies leaves open the question whether the detections are coincidental or not.

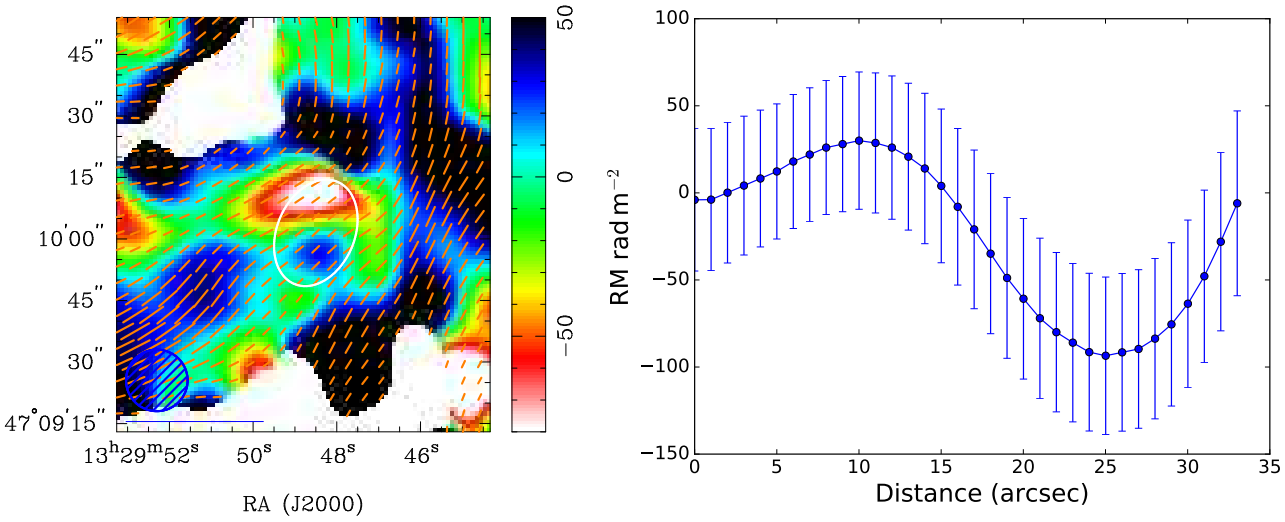

Figure 5.4.6: Region of M51 with a RM variation of $\Delta\mathrm{RM} = 124\,\mathrm{rad\,m^{-2}}$ coinciding with a known HI hole marked by an ellipse. The left hand panel shows the RM map in $\mathrm{rad\,m^{-2}}$ overlaid with the polarization $E + 90°$-orientations to show the magnetic field structure, not corrected for Faraday rotation. The RM increases from $-94 \pm 46\,\mathrm{rad\,m^{-2}}$ at the northern edge of the HI hole to $+30 \pm 40\,\mathrm{rad\,m^{-2}}$ at the southern edge. The 15″ beam is shown in the bottom left corner. The selected region is indicated as a black square in Figure 5.4.5. The right hand panel shows the RM values and the corresponding errors across the variation (from south to north).

5.5 Summary

We studied the nearby face-on spiral galaxy M51 at S-band (2 – 4 GHz) where no polarization data of M51 existed before. The goal was to probe a so far unknown physical layer between the disk and halo of M51 to investigate the transition region. In the following, we summarize the results.

Total intensity The total intensity distribution in M51 at S-band shown in Figure 5.2.1 follows the optical spiral arms in the Hα image. This shows that the total magnetic field gets mostly amplified in star-forming regions, related to the small-scale dynamo. The results of the total intensity observations at S-band are consistent with radio synchrotron observations at other frequencies at C and X-band (Fletcher et al., 2011) and L-band (Mao et al., 2015).

Polarized intensity The polarized intensity distribution in M51 at S-band (Figure 5.3.2) shows a complicated structure. The peak polarized intensity (magnetic arms) seems to appear at arbitrary locations relative to the gas spiral arms. The discrepancy could originate from tidal interactions with the small irregular companion galaxy NGC 5195. Another explanation is that in the inter-arm regions the large-scale dynamo has sufficient time to generate

regular magnetic fields without weakening by continues injection and amplification of turbulent fields by supernova shocks and/or stellar winds (as it is the case in the gas spiral arms). Interestingly, the structure of the emission seen in polarized intensity seems to be similar at different frequency bands (in different layers). In Section 5.3.2 we discuss possible explanations. However, as a future project it would be interesting to perform a detailed analysis of the structure in polarized intensity at different frequencies using e.g. a wavelet analysis as it was done for M83 in Frick et al. (2016).

Degree of polarization At the locations of the gas spiral arms, the degree of polarization shown in Figure 5.3.3 is low ($< 10\,\%$) which originates from tangled and/or turbulent magnetic fields due to star-forming activity, whereas at some inter-arm locations, the degree of polarization is high (up to about $40\,\%$), resulting from ordered or undisrupted magnetic fields. The global distribution of the degree of (non-thermal) polarization in M51 shows a clear radial increase which indicates that the total magnetic field must be more ordered at larger radii and thus, the ordered field decreases more slowly than the turbulent field. Because we have polarization data at multiple radio frequencies, we were able to investigate the radial trend of the depolarization between different frequencies (between S-band ($2-4\,\mathrm{GHz}$) and X-band ($8.35\,\mathrm{GHz}$) and L-band ($1-2\,\mathrm{GHz}$) and X-band). We found that the depolarization gets weaker towards larger radii (compare Figure 5.3.5). This is porbably caused by a decreasing turbulent magnetic field strength towards larger radii.

Global RM distribution No obvious large-scale RM pattern in our new S-band data was found at a resolution of $15''$ (without any smoothing or spatial filtering). Due to the inclination of the galaxy one would expect to see a pattern in the RM map if a (strong) regular magnetic field is present because the magnetic field orientations indicated by the polarization angles show a systematic pattern across the spiral arms. Also the high amplitudes of the observed RM of $\pm\,150\,\mathrm{rad\,m^{-2}}$ indicates the presence of regular fields. Instead, the RM map at S-band (Figure 5.4.1) is dominated by fluctuations. This suggests that vertical components could dominate the signal in Faraday rotation and could remove any large-scale pattern from a regular field in the disk-halo transition region. The RM structure function at S-band in Figure 5.4.4 shows a flat trend across all scales, resulting from uncorrelated field structures on all scales probably because the magnetic field at S-band (in the disk-halo transition region) is dominated by turbulence. However, after smoothing the data to a lower resolution of $30''$ ($1\,\mathrm{kpc}$ physical size), the RM map shows some hint of a quadrisymmetric spiral pattern (with mode $m = 2$) at S-band (compare Figure 5.4.2). The underlying $m = 2$ field indicated in our $30''$ resolution RM map may be too weak to be seen in the structure function. From the RM structure function, we extracted a RM dispersion of $\sigma_{\mathrm{RM}} \approx 28\,\mathrm{rad\,m^{-2}}$ at S-band.

Local RM features We investigated the RM map for features from vertical magnetic field components. They are believed to originate from regular fields from the disk being transported into the halo via galactic winds and/or supernova remnants, creating a positive and negative RM feature which can possibly lie at the location of a HI hole. We found only

one such RM feature coinciding with a HI hole in M51 at S-band shown in Figure 5.4.6. One reason for having only one feature could be that the magnetic field in the disk is dominated by anisotropic random fields. In other nearby face-on galaxies (with strong regular magnetic fields in the disk) the detections of RM features coinciding with HI holes are also rare (only two detections in two galaxies), thus it remains an open question whether the detections are coincidental or not.

CHAPTER 6

The Mystery of M51's Multi-layer Magneto-Ionic Medium: Application of an Analytical Depolarization Model

In this chapter, the wavelength-dependent depolarization in M51 is discussed and compared to depolarization models, of the degree of polarization as a function of wavelength. We combine our new S-band polarization data with those at C- and X-band at 4.85 GHz and 8.35 GHz (Fletcher et al., 2011) and with the broadband L-band (1 – 2 GHz) VLA data from Mao et al. (2015). These data provide us with the widest wavelength coverage polarization data set for a nearby face-on spiral galaxy. Details on the complete data set are given in Section 4.4 in Chapter 4. Preliminary results of the analysis in this chapter were published as a short International Astronomical Union (IAU) conference proceeding (Kierdorf et al., 2018).

6.1 Wavelength-dependent Depolarization between 1 – 8 GHz

In the ISM of spiral galaxies, cosmic ray electrons (CREs), thermal electrons, and magnetic fields are mixed in the same spatial volume (e.g Longair, 2011). The CREs together with the perpendicular to the line-of-sight component of the magnetic field produce synchrotron radiation, while the thermal electrons together with the parallel to the line-of-sight component of the magnetic field cause Faraday rotation of the plane of linear polarization. In such a case, the observed degree of polarization changes as a function of wavelength (Burn, 1966).

In general, the degree of polarization as a function of wavelength decreases. However, in a slab with a uniform layer in terms of regular magnetic fields, constant thermal and CRE densities, the degree of polarization varies like a Sinc function (by differential Faraday rotation, also known as 'Burn slab'). A simple case of depolarization by differential Faraday rotation in a Burn slab is shown in Figure 6.1.1. Depending on the considered wavelength-range, the

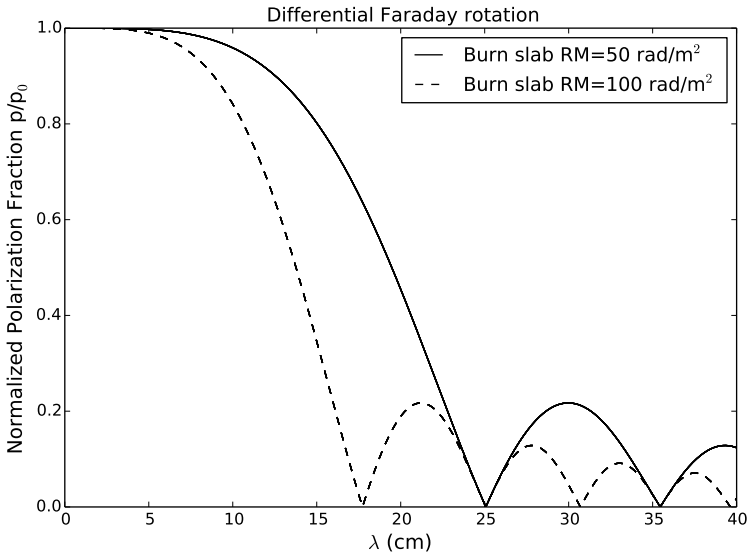

Figure 6.1.1: Degree of polarization as a function of wavelength depolarized by differential Faraday rotation (in a uniform layer with constant thermal electron and CRE density and a purely regular magnetic field). The different curves show the degree of polarization resulting from a Burn slab with RM of 50 rad m^{-2} (solid line) and 100 rad m^{-2} (dashed line).

degree of polarization may increase as a function of wavelength. To understand this, we need to consider a purely regular magnetic field, in which the plane of polarization gets Faraday rotated by different amounts, depending on the location relative to the observer (see the discussion of differential Faraday rotation in Section 2.2.2). Because thermal electrons and CREs are present in each layer, both Faraday rotation and emission of linearly polarized radiation occur at each point along the line-of-sight. If the polarized emission from each layer is cancelled by emission from another layer (which is the case when their polarization angles differ by 90°) the observed degree of polarization drops to zero. Those nulls appear when $\mathrm{RM}\lambda^2 = n\pi$ with $n \in \mathbb{Z}, n \neq 0$, where RM is the total rotation measure of the emission region. If the wavelength increases further, the polarization angles change again and let the polarization signal appear again and thus, the degree of polarization increases with increasing wavelength.

Due to the general trend of a decreasing polarization fraction as a function of wavelength, if a galaxy has a face-on orientation relative to the observer, linearly polarized emission at different wavelengths probe the ISM at different physical depths: Short radio wavelengths probe the polarized emission through the entire disk of the galaxy because at short wavelengths the signal experiences low Faraday depolarization on the way to the observer. At long radio wavelengths, the polarized signal from the disk (and a possible far-side halo) experiences strong Faraday depolarization and the remaining signal probes the polarized emission from the upper disk and/or the halo. Note that in perfectly face-on galaxies (with 0° inclination), only vertical components of regular fields and/or of turbulent fields are able to depolarize. However, if the galaxy is only nearly face-on with a mild inclination, regular fields parallel to

the disk can also contribute to depolarization. Summarizing, due to wavelength-dependent Faraday depolarization, polarized signals at different wavelengths probe layers of different physical depths of a face-on galaxy. With this, one can constrain the intrinsic regular and turbulent magnetic field strengths in different polarization layers by comparing the observed degree of polarization as a function of wavelength with models of depolarization mechanisms (such as differential Faraday rotation, internal or external Faraday dispersion).

6.1.1 The Mystery of M51's Multi-layer Magnetic Field Configuration

An excellent laboratory for studying depolarization effects in a multi-layer magneto-ionic medium is the grand design face-on spiral galaxy M51. This galaxy is well studied at many radio frequencies, but observations in polarization has only been performed at two widely separated radio windows of short (3 and 6 cm) and long (around 20 cm) wavelengths (Beck et al., 1987; Horellou et al., 1992; Berkhuijsen et al., 1997; Fletcher et al., 2011; Mao et al., 2015). No high resolution polarization observations were performed at the intermediate wavelengths in the vicinity of 10 cm[1]. Berkhuijsen et al. (1997) studied M51's polarization layers at 2.8, 6.2, 18.0, and 20.5 cm wavelength, where the λ 2.8 cm data were taken with the Effelsberg 100-m radio telescope and the rest obtained using the VLA. Surprisingly, they found different polarization patterns at high and low frequencies, which implies different magnetic field configurations at different frequencies, concluding that this is caused by different configurations of the regular magnetic field in the disk and in the halo.

Since the data taken by Berkhuijsen et al. (1997) had limited resolution due to the Effelsberg beam at λ 2.8 cm (about 70″) and the λ 6 cm data suffered from missing flux density from extended angular structures because no single-dish map to correct for was available at that time, Fletcher et al. (2011) performed new observations at λ 3.6 and λ 6.2 cm, combining VLA and Effelsberg observations to obtain high angular resolution (15″) and high sensitivity. With the new data, Fletcher et al. (2011) confirmed the findings by Berkhuijsen et al. (1997) of different magnetic field configurations in the disk and in the halo. They found that the regular field in the disk can be described by a superposition of an axisymmetric and quadrisymmetric azimuthal mode ($m = 0, 2$). In contrast, the regular magnetic field in the halo shows a strong bisymmetric azimuthal mode ($m = 1$). According to Fletcher et al. (2011), the radial component of the disk is directed outwards from the galaxy centre, whereas in the halo the radial component is directed inwards in the north, opposite to the direction of the disk field, and outwards in the south, same as the disk field (compare Figure 14 in Fletcher et al., 2011).

The difference in the magnetic field configuration between the disk and the halo of M51 is still not understood. Fletcher et al. (2011) offered some speculative suggestions according to which (1) interactions with M51's companion galaxy NGC 5195 could be responsible for the configuration in the halo by driving a different mean field dynamo action e.g through tidal forces resulting in a $m = 1$ mode. (2) Another possibility is that the halo field could be

[1] Polarization observations at λ 11 cm were performed with the Effelsberg 100-m single-dish radio telescope at a poor resolution of about 4.5′ and with a narrow frequency band by Mulcahy (2011).

a field generated during early evolutionary stages of M51 in the disk, and later transported from the disk into the halo while different dynamo action built the present day disk field. (3) Also, a velocity field that is different compared to the one in the disk could modify the magnetic field pattern in the halo after the magnetic field has been transported from the disk into the halo. However, Moss et al. (2010) argued that in case of an active galactic wind the halo component of the field may enslave that of the disk, making separate field patterns improbable (under the condition that the disk and halo fields are generated by a standard mean-field α-Ω-dynamo, i.e. based on differential rotation and turbulence, see Section 1.2). A better understanding of what causes the different modes comes with observation of the transition region between the disk and the halo.

Shneider et al. (2014a) developed a model of the depolarization of synchrotron radiation in a multi-layer magneto-ionic medium, applied specifically to M51. They developed model predictions for the degree of polarization as a function of wavelength and distinguished between a two-layer system with a disk and a halo and a three-layer system with a far-side halo, a disk and a near-side halo. Details are given in Section 6.1.2. The advantage of this model, compared to the depolarization models described in Section 2.2.2, is that it contains multiple layers, whereas the 'classical' depolarization models only considering different magnetic field configurations within a single resolution element and for only one layer (QU-fitting deals with multiple components by putting them into the sky plane instead of stacking them along the line-of-sight). Another speciality of the models is the differentiation between isotropic and anisotropic random magnetic fields.

In Shneider et al. (2014a) the models were compared to the observed degree of polarization at the three wavelengths 3.6, 6.2, and 20.5 cm obtained by Fletcher et al. (2011). Figure 6.1.2 shows the model predictions of the normalized degree of polarization (p/p_0) for a two-layer and three-layer system. Details on the models will be explained in Section 6.1.2. With the data points at $\lambda\lambda$ 3.6, 6.2, and λ 20.5 cm only it is not possible to distinguish between different model predictions of a two-layer or three-layer system. As Figure 6.1.2 shows, our new S-band data (the boundaries of S-band are indicated with the vertical red lines) provide the crucial λ range to clarify which model fits the data best and therefore which system is more likely for M51.

In Section 4.4 we summarize the observations at all available frequencies. With our combined high quality and broad frequency coverage data set the depolarization curves shown in Figure 6.1.2 can be sampled extremely well in wavelength space, with high sensitivity, thus allowing actual tracing of these depolarization curves and figuring out what kind of magnetic field configurations causes the depolarization in different layers of M51.

6.1.2 The Shneider et al. (2014a) Multi-layer Depolarization Model

Shneider et al. (2014a) modeled a nearly face-on (with 20° inclination) spiral galaxy with a magnetized disk and a halo. They performed a multi-layer decomposition along the line-of-sight for a two-layer (disk – halo) and a three-layer (halo – disk – halo) system separately. A

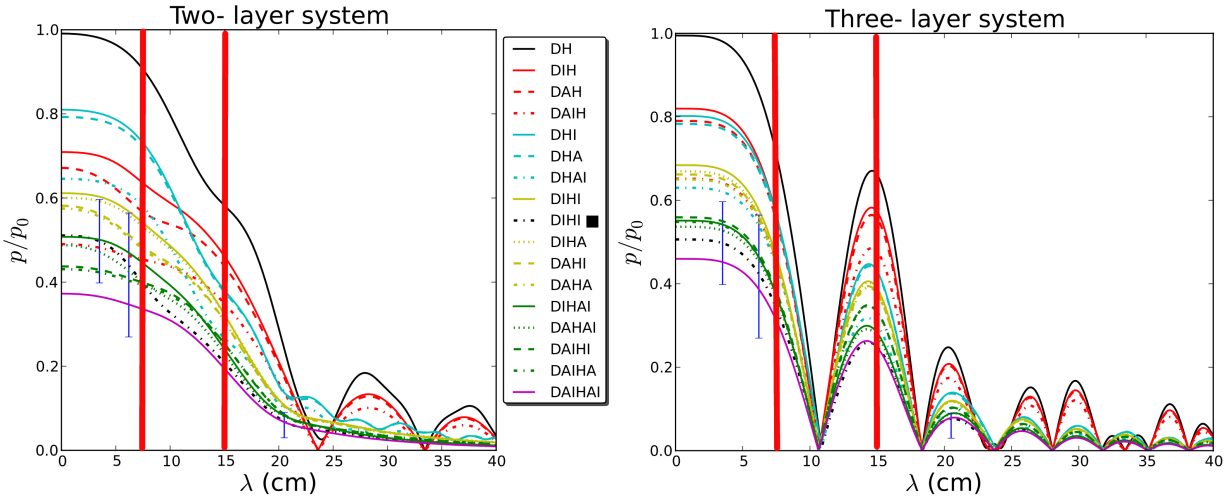

Figure 6.1.2: Normalized degree of polarization as a function of wavelength for a two-layer system (left) with a disk and a halo and a three-layer system (right) with a far-side halo, a disk and a near-side halo in M51. The measured polarization values at the three observed wavelengths 3.6, 6.2, and 20.5 cm (Fletcher et al., 2011) are displayed with error bars. The images were taken from Shneider et al. (2014a). For this thesis, we observed M51 at wavelengths between 7.5 – 15 cm (S-band) indicated with vertical red lines to distinguish between different models of depolarization with different underlying magnetic field configuration in this galaxy. The nomenclature of the different models is as follows: Capital letters 'D' and 'H' stands for regular fields in the disk and halo. Capital letters 'I' and 'A' denotes isotropic and anisotropic turbulent fields. Details on the different models are given in the next Section 6.1.2.

detailed schematic of the two-layer and three-layer system is shown in Figure 6.1.3. Since the properties of the near and far side halo are assumed to be identical, including a third layer (a far-side halo) is done by mirror *reflection* of the near-side halo, essentially a signature of a symmetric quadrupolar field that is excited by the large-scale dynamo most easily (Beck et al., 1996). Note that for a quadrupolar magnetic field configuration, vertical magnetic field lines (with respect to the disk plane) are required (compare Figure 1.2.3 (c) in Section 1.2).

In the following, all equations to model the degree of polarization as a function of wavelength in a multi-layer magneto-ionic medium are given. The equations are duplicated (with some minor corrections) from Shneider et al. (2014a) for ease of subsequent discussion. For detailed derivations of the equations please see Shneider et al. (2014a), and Sokoloff et al. (1998) and Berkhuijsen et al. (1997). The degree of polarization for a two-layer and three-layer system is given in normalized form (p/p_0). The following assumptions were used to model the degree of polarization as a function of wavelength in M51:

- The intrinsic degree of polarization at $\lambda = 0$ is assumed to be $p_0 = 0.7$ everywhere in the galaxy. This corresponds to the theoretical injection spectrum for electrons

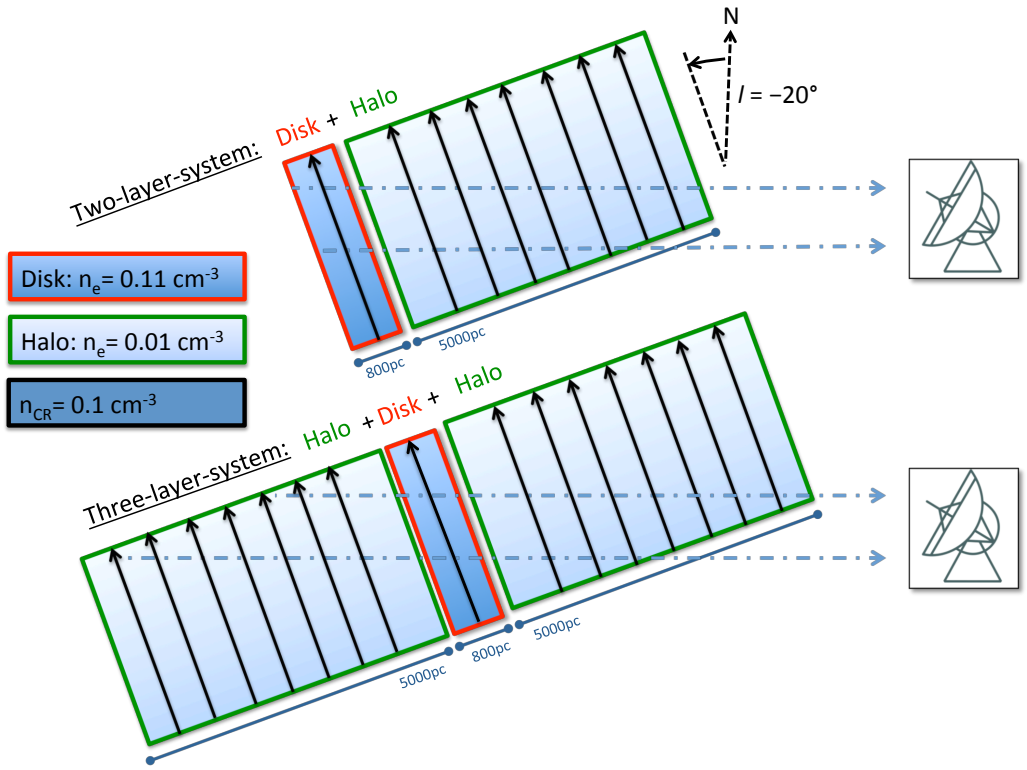

Figure 6.1.3: Graphical illustration of a two-layer system with a disk and a halo and a three-layer system with a far-side halo a disk and a near-side halo (with respect to the observer on the right side) illustrated with an inclination of $l = -20°$. The properties of the near and far-side halo are assumed to be identical, which in terms of a regular magnetic field means a reflection of the physical system. Note that the vertical component of the regular field is assumed to be zero which means that only the line-of-sight component of the plane parallel field causes Faraday rotation. The ratio of the path length through the illustrated disk and halo layer conforms the assumed ratio in the model.

accelerated in supernova remnants with $\alpha_{\rm syn} = -0.5$ (compare Equation 2.2.9). The synchrotron spectral index of -0.5 was observed by Fletcher et al. (2011) at the spiral arms where supernova explosions take place and where the particles get accelerated in supernova remnants. In inter-arm regions, Fletcher et al. (2011) estimated an average $\alpha_{\rm syn}$ of -1.1 which gives an intrinsic degree of polarization of $p_0 = 76\,\%$. Therefore, if assuming $p_0 = 0.7$ would give an overestimation of (p/p_0) by about $8\,\%$. At S-band we observed the same synchrotron spectral index. For synchrotron spectral indices between -0.1 and -1.7, the theoretical maximum intrinsic polarization fraction amounts to $60-80\,\%$. For this range, the assumed intrinsic polarization fraction of $p_0 = 0.7$ would give a maximum error of (p/p_0) of $\pm\,0.15$.

- The degree of polarization p and the polarization angle ψ are affected exclusively by depolarization mechanisms in the ISM *within* the galaxy (depolarization effects from the Galactic foreground are assumed to be negligible).

- The disk and halo layers are considered to satisfy conditions for emitting synchrotron emission and cause Faraday rotation in the same volume and thus, they both are assumed to contain thermal electrons, CREs and magnetic fields.

- The model is based on the magnetic field modes found in M51 by Fletcher et al. (2011) and hence it *completely neglects the vertical components* of the regular fields in the disk and the halo. In Section 6.1.3 we compare the depolarization models with the observed degree of polarization in a particular sector in M51. For the considered sector, this assumption is valid because the observed RM (at S-band) amounts to only about $2\,\mathrm{rad\,m^{-2}}$ and therefore, the depolarization effects are dominated by projection of the plane-parallel magnetic field. However, in Section 6.1.4 we will discuss problems and possible consequences which comes with this assumption.

- All models considered in our discussion are constructed under the assumption that regular magnetic fields are present in the disk and halo.

- The scale height and the density of thermal electrons in the disk and halo are those proposed by Berkhuijsen et al. (1997): $n_\mathrm{e} = 0.11\,\mathrm{cm^{-3}}$ and $L = 800\,\mathrm{pc}$ in the disk and $n_\mathrm{e} = 0.01\,\mathrm{cm^{-3}}$ (assumed as a tenth of the value in the disk) and $L = 5\,\mathrm{kpc}$ in the halo.

- The number of turbulent cells within the observational telescope beam is assumed to be large enough to have a number of independent cells to be deterministic.

- Anisotropy of random magnetic fields is considered to be caused by compression in the spiral arms and by shear from differential rotation, hence not in vertical direction.

- The case of depolarization caused by gradients of RM across the observational telescope beam is not taken into account (Sokoloff et al., 1998).

All symbols used in the equations are summarized in Table 6.1.

The total magnetic field in spiral galaxies can be described as a superposition of a regular mean field and a turbulent random field component $\boldsymbol{B} = \boldsymbol{B}_\mathrm{reg} + \boldsymbol{b}_\mathrm{turb}$. To derive the degree of polarization as a function of wavelength for a two-layer and three-layer system, we start with the regular disk and halo magnetic field components. According to Fletcher et al. (2011), the regular field in the disk of M51 can be described by a superposition of an axisymmetric ($m = 0$) and quadrisymmetric ($m = 2$) azimuthal Fourier mode and the regular field in the halo is best described by an axisymmetric, together with a bisymmetric azimuthal mode with $m = 1$. In cylindrical polar coordinates (B_r, B_ϕ, B_z), where (r, ϕ) are the radial and azimuthal directions in the galaxy plane and z is the vertical component, the regular

Table 6.1: Symbols used in the Equations.

Symbol (Unit)	Description
$B_{\rm tot}$ (μG)	Total regular magnetic field
$b_{\rm tot}$ (μG)	Total random magnetic field
B_r	Radial component of the magnetic field in the galaxy plane
B_ϕ	Azimuthal component of the magnetic field in the galaxy plane
B_z	Vertical component of the magnetic field in the galaxy plane
B_0	Amplitude of the horizontal magnetic field with mode $m = 0$ in the disk
B_2	Amplitude of the horizontal magnetic field with mode $m = 2$ in the disk
$B_{\rm h0}$	Amplitude of the horizontal magnetic field with mode $m = 0$ in the halo
$B_{\rm h1}$	Amplitude of the horizontal magnetic field with mode $m = 1$ in the halo
pa_0 (°)	Pitch angle of the horizontal magnetic field with mode $m = 0$ in the disk
pa_2 (°)	Pitch angle of the horizontal magnetic field with mode $m = 2$ in the disk
$pa_{\rm h0}$ (°)	Pitch angle of the horizontal magnetic field with mode $m = 0$ in the halo
$pa_{\rm h1}$ (°)	Pitch angle of the horizontal magnetic field with mode $m = 1$ in the halo
β_2, $\beta_{\rm h1}$ (°)	Pitch angle of the horizontal magnetic field Azimuthal angle at which the corresponding mode $m \neq 0$ is a maximum
ψ_{0i} (°)	Intrinsic polarization angle of layer i = d,h (disk or halo)
α	Parameter to distinguish between isotropic ($\alpha = 1$) and anisotropic case ($\alpha = 2$ in the disk and $\alpha = 1.5$ in the halo)
σ_I	Total isotropic random magnetic field
σ_A	Total anisotropic random magnetic field
I_i	Synchrotron total intensity of layer i = d,h (disk or halo)
I	Sum of the synchrotron total intensity of each layer along the lone-of-sight ($I = \sum_i I_i$)
ϵ_i	Synchrotron emissivity of layer i = d,h (disk or halo)
c	Constant to calculate synchrotron emissivity
L_i (pc)	Path length through the entire layer i = d,h (disk or halo)
R_i (rad m^{-2})	Faraday depth of layer i = d,h (disk or halo)
$\sigma_{{\rm RM}i}$ (rad m^{-2})	Faraday dispersion of the intrinsic RM within the volume of the telescope beam of layer i = d,h (disk or halo)
d_i (pc)	Diameter of a turbulence cell in layer i = d,h (disk or halo)
$l = -20$ (°)	Inclination ($l = 0°$ means face-on orientation; Tully, 1974)
$\phi = 100$ (°)	Azimuthal angle of the considered sector
$\sigma_{{\rm RM},D} = 15$ (rad m^{-2})	Dispersion of observed RM at λ 6 cm with 15″ resolution (Fletcher et al., 2011)
$D = 600$ (pc)	Linear size of the 15″ telescope beam

magnetic field components can be written as:

$$\begin{aligned}
B_r &= B_0 \sin(pa_0) + B_2 \sin(pa_2) \cos(2\phi - \beta_2), \\
B_\phi &= B_0 \cos(pa_0) + B_2 \cos(pa_2) \cos(2\phi - \beta_2), \\
B_z &= 0, \\
B_{\mathrm{h}r} &= B_{\mathrm{h}0} \sin(pa_{\mathrm{h}0}) + B_{\mathrm{h}1} \sin(pa_{\mathrm{h}1}) \cos(\phi - \beta_{\mathrm{h}1}), \\
B_{\mathrm{h}\phi} &= B_{\mathrm{h}0} \cos(pa_{\mathrm{h}0}) + B_{\mathrm{h}1} \cos(pa_{\mathrm{h}1}) \cos(\phi - \beta_{\mathrm{h}1}), \\
B_{\mathrm{h}z} &= 0
\end{aligned} \tag{6.1.1}$$

The different modes are reflected in the indexing in the different terms in Equation 6.1.1. B_0 and B_2 are the amplitudes of the horizontal total magnetic field component in the disk and β_2 is the azimuthal angle at which the corresponding $m \neq 0$ mode is a maximum. pa_0 and pa_2 are the pitch angles of the corresponding magnetic field component. The pitch angle is defined as the angle between the tangent to the spiral arm and the tangent to a perfect circle, measured at the point where the arm and the circle intersect (e.g. Carroll and Ostlie, 1996). The same nomenclature as for the disk holds for the horizontal magnetic field component in the halo where the index 'h' refers to the halo. ϕ is the azimuthal angle in the galaxy plane measured anti-clockwise from the north end of the major axis, whereas the major axis is defined as the axis with a position angle of PA $= -10°$ away from the north direction (Tully, 1974). Figure 6.1.4 illustrates the geometrical situation in M51. In the following, we summarize the different ingredients included in the Shneider et al. (2014a) depolarization models.

Regular magnetic field

Following Berkhuijsen et al. (1997), the regular disk and halo magnetic field components are projected onto and perpendicular to the sky plane as

$$\begin{aligned}
\overline{B}_x &= B_r \cos(\phi) - B_\phi \sin(\phi), \\
\overline{B}_y &= [B_r \sin(\phi) + B_\phi \cos(\phi)] \cos(l) + B_z \sin(l), \\
\overline{B}_\parallel &= -[B_r \sin(\phi) + B_\phi \cos(\phi)] \sin(l) + B_z \cos(l),
\end{aligned} \tag{6.1.2}$$

where $l = -20°$ is the inclination of the galaxy (Tully, 1974). The over-bar denotes the mean (regular) field. The Cartesian reference frame in the sky plane has its origin in M51's center, with the x-axis pointing towards the northern end of the major axis (compare Figure 6.1.4), while the z-axis (the line-of-sight or 'parallel' component $\parallel$) is pointing towards the observer. From this, the total regular magnetic field strength can be calculated by:

$$\overline{B}_{\mathrm{tot}} = \sqrt{\overline{B}_\perp^2 + \overline{B}_\parallel^2} = \sqrt{\overline{B}_x^2 + \overline{B}_y^2 + \overline{B}_\parallel^2} \tag{6.1.3}$$

Fitted model parameters for the disk ($m = 0, 2$) and halo ($m = 0, 1$) magnetic fields are given as ratios B_0/B_2 and $B_{\mathrm{h}0}/B_{\mathrm{h}1}$ in Fletcher et al. (2011), where 'h' denotes the component in

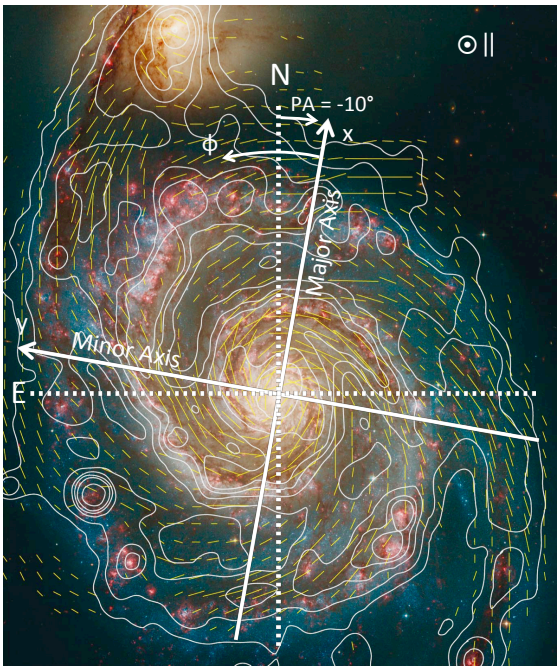

Figure 6.1.4: Geometrical situation in M51. The azimuthal angle ϕ is measured anti-clockwise from the north end of the major axis, which is the axis with the position angle of PA $= -10°$ relative to the north direction on the sky. The Cartesian coordinate system of the projection of the galaxy onto and perpendicular to the sky plane $(x, y, \|)$ is illustrated as well.

the halo. From this and Equations 6.1.1 and 6.1.3 it follows

$$
\begin{aligned}
B_0 &= \overline{B}_{\mathrm{tot,d}} \left[1 + \left(\frac{R_2}{R_0}\right)^2 \cos^2(2\phi - \beta_2) + 2\left(\frac{R_2}{R_0}\right) \cos(2\phi - \beta_2) \cos(p_0 - p_2)\right]^{-1/2}, \\
B_2 &= \overline{B}_{\mathrm{tot,d}} \left[1 + \left(\frac{R_0}{R_2}\right)^2 \cos^2(2\phi - \beta_2) + 2\left(\frac{R_0}{R_2}\right) \cos(2\phi - \beta_2) \cos(p_0 - p_2)\right]^{-1/2}, \\
B_{\mathrm{h0}} &= \overline{B}_{\mathrm{tot,h}} \left[1 + \left(\frac{R_{\mathrm{h1}}}{R_{\mathrm{h0}}}\right)^2 \cos^2(\phi - \beta_{\mathrm{h1}}) + 2\left(\frac{R_{\mathrm{h1}}}{R_{\mathrm{h0}}}\right) \cos(\phi - \beta_{\mathrm{h1}}) \cos(p_{\mathrm{h0}} - p_{\mathrm{h1}})\right]^{-1/2}, \\
B_{\mathrm{h1}} &= \overline{B}_{\mathrm{tot,h}} \left[1 + \left(\frac{R_{\mathrm{h0}}}{R_{\mathrm{h1}}}\right)^2 \cos^2(\phi - \beta_{\mathrm{h1}}) + 2\left(\frac{R_{\mathrm{h0}}}{R_{\mathrm{h1}}}\right) \cos(\phi - \beta_{\mathrm{h1}}) \cos(p_{\mathrm{h0}} - p_{\mathrm{h1}})\right]^{-1/2}, \quad (6.1.4)
\end{aligned}
$$

where R_0, R_2, R_{h1}, and R_{h2} are the fitted mode strengths modeled in Fletcher et al. (2011) (see their Table A1), also given in Table 6.2. This can now be used to calculate the regular disk and halo magnetic field components in and perpendicular to the sky plane $\left(\overline{B}_x, \overline{B}_y, \overline{B}_{\|}\right)$.

Turbulent magnetic field

Since **b** and its components $(b_r,\, b_\phi,\, b_z)$ are Gaussian random variables with zero mean, one

can express the turbulent components of the total random magnetic field by its standard deviations (σ_r, σ_ϕ, σ_z). To distinguish between cases with isotropic and anisotropic turbulent fields, the parameter $\alpha > 0$ was introduced. Since anisotropy is considered to be caused by compression in spiral arms and by shearing effects from differential rotation, hence *only* in the disk plane and not in vertical direction, we have

$$\sigma_\phi^2 = \alpha\,\sigma_r^2\,, \qquad \sigma_r = \sigma_z\,. \tag{6.1.5}$$

For isotropy, we have $\alpha = 1$, hence $\sigma_\phi = \sigma_r = \sigma_z$. In Cartesian coordinates, the turbulent disk and halo magnetic field components are

$$\begin{aligned}
\sigma_x^2 &= \sigma_r^2 \left[\cos^2(\phi) + \alpha \sin^2(\phi)\right], \\
\sigma_y^2 &= \sigma_r^2 \left\{\left[\sin^2(\phi) + \alpha \cos^2(\phi)\right] \cos^2(l) + \sin^2(l)\right\}, \\
\sigma_\parallel^2 &= \sigma_r^2 \left\{\left[\sin^2(\phi) + \alpha \cos^2(\phi)\right] \sin^2(l) + \cos^2(l)\right\}.
\end{aligned} \tag{6.1.6}$$

From this, the total random magnetic field can be calculated as

$$b_{\rm tot} = \sqrt{\sigma_x^2 + \sigma_y^2 + \sigma_\parallel^2}\,. \tag{6.1.7}$$

For isotropy $\sigma_x = \sigma_y = \sigma_\parallel = \sigma_I$ applies which results in a total isotropic turbulent field of

$$b_{\rm tot}^2 = \sigma_x^2 + \sigma_y^2 + \sigma_\parallel^2 = 3 \cdot \sigma_I^2 = (2 + \alpha) \cdot \sigma_I^2\,, \tag{6.1.8}$$

with $\alpha = 1$. In case of an anisotropic turbulent field, the total random field is

$$b_{\rm tot}^2 = (2 + \alpha) \cdot \sigma_A^2\,, \tag{6.1.9}$$

with $\alpha > 1$. Anisotropy in the halo is assumed to be smaller because no compression in spiral arms can occur, i.e. $\alpha = 2$ in the disk and $\alpha = 1.5$ in the halo.

To describe the degree of polarization as a function of wavelength, other physical parameters besides the strength of the regular and turbulent magnetic field are needed. In the next paragraph we discuss the observational parameters.

Observables

For a purely regular magnetic field, the intrinsic polarization angle (in the sky plane) is given by (e.g. Berkhuijsen et al., 1997)[2]

$$\psi_0 = \frac{1}{2}\pi - \arctan[\cos(l)\tan(\phi)] + \arctan\left(\overline{B}_y / \overline{B}_x\right)\,. \tag{6.1.10}$$

If turbulent magnetic fields are present as well, the last term for the intrinsic polarization angle changes to

$$\langle\psi_0\rangle = \frac{1}{2}\pi - \arctan[\cos(l)\tan(\phi)] + \frac{1}{2}\arctan\left(\frac{2\overline{B}_x\overline{B}_y}{\overline{B}_x^2 - \overline{B}_y^2 + \sigma_x^2 - \sigma_y^2}\right)\,, \tag{6.1.11}$$

[2]Note if using python package, the numpy function arctan2 should be used, to make sure using the right quadrant of the arctan function while calculating the polarization angle.

where $\langle ... \rangle$ denotes ensemble averaging. For a detailed derivation of this modification please see Sokoloff et al. (1998) and Appendix A of Shneider et al. (2014a). To connect the degree of polarization as a function of wavelength with the observed quantities I, Q, and U, one starts with the complex polarization $\mathbf{P} = |\mathbf{P}|(\cos(2\psi) + i\sin(2\psi)) = |\mathbf{P}|e^{2i\psi}$ (see Section 2.2). $\psi = \frac{1}{2}\tan^{-1}\left(\frac{U}{Q}\right)$ is the observed polarization angle. $|\mathbf{P}|$ is the length of the complex polarization vector and is defined as the observed polarized intensity $PI = \sqrt{Q^2 + U^2}$. The observed degree of polarization is $p = PI/I$, where I is the total non-thermal intensity. The total rotation measure R_i, where i denotes different layers, in this case either disk 'd' or halo 'h', and the dispersion of the RM σ_{RM_i} within the telescope beam of an individual layer, both given in rad m^{-2}, are needed as well. R_i, σ_{RM_i}, and the per-layer total synchrotron intensity I_i are dependent on the path length through the emission layer L_i (in pc):

$$I_i = \epsilon_i \, L_i \,, \tag{6.1.12}$$

$$R_i = 0.81 \, n_{\mathrm{e}i} \, \overline{B}_{\parallel i} \, L_i \,, \tag{6.1.13}$$

$$\sigma_{\mathrm{RM}_i} = 0.81 \, n_{\mathrm{e}i} \, b_{\parallel i} \, (L_i d_i)^{1/2} \tag{6.1.14}$$

The synchrotron emissivity is defined as $\epsilon = c\,\overline{B_\perp^2}$, with constant c and $\overline{B_\perp^2} = \overline{B}_\perp^2 + \sigma_x^2 + \sigma_y^2$. Physically, the constant c corresponds to the CRE density in the emitting volume whose value is not significant as it cancels out upon computing p (Shneider et al., 2014a). The total synchrotron intensity from all layers is given by the sum of the synchrotron emission of individual layers along the line-of-sight $I = \sum_i I_i$. $n_{\mathrm{e}i}$ is the average thermal electron density (in cm^{-3}), $\overline{B}_{\parallel i}$ and $b_{\parallel i}$ are the strengths of the regular and turbulent magnetic field components (in μG) along the line-of-sight, and d_i (in pc) is the turbulence cell size which is defined as (Fletcher et al., 2011)

$$d_i \simeq \left[\frac{D \, \sigma_{\mathrm{RM},D}}{0.81 \, n_{\mathrm{e}i} \, b_{\parallel i} \, (L_i)^{1/2}} \right]^{2/3} \,, \tag{6.1.15}$$

with $\sigma_{\mathrm{RM},D}$ is the RM dispersion (in rad m^{-2}), in Shneider et al. (2014a) erroneously referred to as the RM dispersion within the beam but actually it is the dispersion of RM *between* the beams (the RM dispersion from the histogram, see Figure 5.4.3). According to this, $\sigma_{\mathrm{RM,D}} = \sigma_{\mathrm{RM}}/\sqrt{N}$, where $N = (D/d)$ is the number of turbulent cells within the beam of a linear diameter D (in pc). Note that for purely regular magnetic fields $\sigma_x = 0$ and $\sigma_y = 0$. In this case the emissivity becomes $\epsilon = c \cdot \overline{B}_\perp^2$. In the following we name the synchrotron total intensity for purely regular fields I_i and for models including turbulent fields $\tilde{I}_i$, where $\tilde{\epsilon} = c\left(\overline{B}_\perp^2 + \sigma_x^2 + \sigma_y^2\right)$.

In general, the depolarization models given in Shneider et al. (2014a) simulate the galaxy M51 as a multi-layer magneto-ionic medium with regular and turbulent magnetic fields. The different models distinguish between scenarios of different magnetic field configurations in terms of (1) regular magnetic fields, (2) isotropic random magnetic fields, and (3) anisotropic random magnetic fields. The different models include either one of those or a mixture of the different magnetic field configurations. Those magnetic field configurations are independently considered to be present in different layers (disk and/or halo). The thermal electron density

Table 6.2: Fixed Model Parameter Values.

Parameter (Unit)	Disk	Halo	Parameter[a] (Unit) cont.	Disk	Halo
$B_{\rm tot}$ (μG)	5	5	R_0 (rad m^{-2})	-46 ± 3	
$b_{\rm tot}$ (μG)	14	4	R_2 (rad m^{-2})	-33 ± 2	
$n_{\rm e}$ (cm^{-3})	0.11	0.01	pa_0 ($^\circ$)	-20 ± 1	
$n_{\rm CRE}$ (arbitrary)	constant	constant	pa_2 ($^\circ$)	-12 ± 2	
L (pc)	800	5000	β_2 ($^\circ$)	-8 ± 5	
d (pc)	55	370	$R_{\rm h0}$ (rad m^{-2})		$+23 \pm 6$
α (anisotropy)	2.0	1.5	$R_{\rm h1}$ (rad m^{-2})		$+76 \pm 11$
			$pa_{\rm h0}$ ($^\circ$)		-43 ± 13
			$pa_{\rm h1}$ ($^\circ$)		-45 ± 5
			$\beta_{\rm h1}$ ($^\circ$)		$+44 \pm 5$

Notes. Fixed parameters in the disk and halo used to model the degree of polarization as a function of wavelength. The electron densities and path lengths are from Fletcher et al. (2011), while the turbulence cell size d was computed using Equation 6.1.15 with the given parameter values. For the number density of CREs, a constant number of 0.1 (in arbitrary units) was used for modeling, while its value is not significant since its cancelling out during the calculation of (p/p_0). [a] from Fletcher et al., 2011

is always constant in individual layers, assuming different values in the disk and halo. The magnetic field strengths are also constant in each layer, using different values for the regular, and (isotropic and anisotropic) turbulent fields. The fixed parameters and their values are given in Table 6.2. Other fixed parameters that are dependent on the geometry of the galaxy and the location of the considered region of emission (see Section 6.1.3) are the inclination $l = -20^\circ$, the position angle PA $= -10^\circ$, and the azimuthal angle $\phi = 100^\circ$.

Since magnetic fields and thermal and cosmic ray electrons are present in all layers, possible depolarization mechanisms are (1) differential Faraday rotation, (2) internal Faraday dispersion, (3) external Faraday dispersion, and (4) a mixture of all mechanisms. In the case where turbulent magnetic fields are 'switched on', wavelength-independent depolarization such as beam depolarization has to be considered as well. The case of depolarization caused by gradients of RM across the observational telescope beam is not taken into account (Sokoloff et al., 1998). Shneider et al. (2014a) also included external Faraday dispersion caused by turbulent magnetic fields in a foreground screen in their models. They only considered turbulent fields here because for regular magnetic fields, a foreground screen only affects the observed RM but not the degree of polarization. Note that *external* refers to the turbulent fields between the observer and the source (but not within the source) hence, in the near-side halo for the two-layer system, and the disk and near-side halo in case of a three-layer system.

Wavelength-independent depolarization

In Section 2.2.2 wavelength-independent depolarization such as beam depolarization was introduced, in the following denotes as W. Wavelength-independent depolarization only occurs if turbulent magnetic fields are present in the emission region (and if the turbulence is unresolved by the telescope beam). For purely regular magnetic fields $W = 1$. For anisotropic random fields, wavelength-independent depolarization is given by (Sokoloff et al., 1998)

$$(W_\mathrm{A})_i = \left\{ \frac{\left[\left(\overline{B}_x^2 - \overline{B}_y^2 + \sigma_x^2 - \sigma_y^2\right)^2 + 4\overline{B}_x\overline{B}_y\right]^{1/2}}{\overline{B}_\perp^2} \right\}_i , \tag{6.1.16}$$

where i denotes either disk or halo. In the isotropic case ($\sigma_x = \sigma_y = \sigma_\parallel = \sigma$) this reduces to

$$(W_\mathrm{I})_i = \left(\frac{\overline{B}_\perp^2}{\overline{B}_\perp^2 + 2\sigma^2} \right)_i . \tag{6.1.17}$$

If both anisotropic and isotropic random fields are present, the wavelength-independent depolarization term is given by

$$(W_\mathrm{AI})_i = \left(\frac{\overline{B}_\perp^2}{\overline{B}_\perp^2 + 2\sigma^2} \right)_i \underbrace{\left\{ \frac{\left[\left(\overline{B}_x^2 - \overline{B}_y^2 + \sigma_x^2 - \sigma_y^2\right)^2 + 4\overline{B}_x\overline{B}_y\right]^{1/2}}{\overline{B}_\perp^2} \right\}_i}_{\sigma_x \neq \sigma_y} . \tag{6.1.18}$$

The wavelength-independent depolarization defines the starting point of the degree of polarization (the value of the polarization fraction at $\lambda = 0$).

Wavelength-dependent depolarization can be caused by differential Faraday rotation due to purely regular magnetic fields, and internal and external Faraday dispersion caused by turbulent fields (see Section 2.2.2 for details). In the following the equations describing the different effects for a two-layer and three-layer system are given.

Differential Faraday rotation (DFR)

When we consider one thick layer with regular magnetic fields and both, CREs and thermal electrons, differential Faraday rotation occurs. The degree of polarization as a function of wavelength has the form of a Sinc function or Burn slab. Differential Faraday rotation means that each thin layer experiences different amount of Faraday rotation on the way to the observer: The plane of linear polarization from the most distant thin layer gets rotated most while the nearest thin layer has still its intrinsic polarization angle. The polarized emission of two thin layers may cancel out each other (if their polarization angles differ by 90°). This happens more often as wavelength increases because the angle rotates as a function of λ: $\psi \propto \mathrm{RM}\lambda^2$. In a thick layer, for wavelengths smaller than the first null of

the Sinc function-like trend of the degree of polarization, the remaining polarized emission is coming from layers in the middle of the original thick layer (whose thickness decreases with increasing λ) because only the polarization emitted from this region do not cancel out. The resulting observed RM (which causes Faraday rotation) is half of the RM from the entire thick layer: $\mathrm{RM}_i = \frac{1}{2}R_i$, where R_i is the total rotation measure from individual thick layers (the disk and/or the halo) given by Equation 6.1.13. In case of differential Faraday rotation with two thick layers (disk and halo) the degree of polarization as a function of wavelength has the form of a 'double' Sinc function, decreasing with increasing wavelength (Sokoloff et al., 1998)

$$\left(\frac{p}{p_0}\right)_{\mathrm{2layer}} = \left\{A_\mathrm{d}^2 + A_\mathrm{h}^2 + 2A_\mathrm{d}A_\mathrm{h}\cos\left[2\Delta\psi_\mathrm{dh} + (R_\mathrm{d} + R_\mathrm{h})\lambda^2\right]\right\}^{1/2}, \tag{6.1.19}$$

where

$$A_i = (I_i/I)\,\mathrm{sinc}\left(R_i\lambda^2\right), \tag{6.1.20}$$

with i denoting either disk or halo and $\Delta\psi_\mathrm{dh} = \langle\psi_\mathrm{0d}\rangle - \langle\psi_\mathrm{0h}\rangle$[3]. $I = \sum_i I_i$ is the sum of the synchrotron total intensity of all layers. For a three-layer model the corresponding equation is:

$$\begin{aligned}\left(\frac{p}{p_0}\right)_{\mathrm{3layer}} =& \Big(2A_\mathrm{h}^2\left\{1 + \cos\left[2(R_\mathrm{d} + R_\mathrm{h})\lambda^2\right]\right\} + A_\mathrm{d}^2 \\ &+ 2A_\mathrm{d}A_\mathrm{h}\Big\{\cos\left[-2\Delta\psi_\mathrm{dh} + (R_\mathrm{d} + R_\mathrm{h})\lambda^2\right] \\ &+ \cos\left[2\Delta\psi_\mathrm{dh} + (R_\mathrm{d} + R_\mathrm{h})\lambda^2\right]\Big\}\Big)^{1/2}\end{aligned} \tag{6.1.21}$$

Equations 6.1.19 and 6.1.21 are basically additions of Sinc functions, each resulting from differential Faraday rotation in individual layers. The intrinsic degree of polarization in each layer is dependent on the polarized emission originating in the layer and therefore of the rotation measure per layer R_i as given by Equation 6.1.13. The angle of the polarization plane of the emitted polarized wave experiences Faraday rotation on its way through the layers with $\mathrm{RM}_i = \frac{1}{2}R_i$ in one layer and $\mathrm{RM}_j = R_j$ in every other layer along the line-of-sight, acting as a Faraday screen (with i and j denoting e.g. disk or halo; Sokoloff et al., 1998). The Sinc functions are weighted with the fractional synchrotron intensity (I_i/I).

Internal Faraday dispersion (IFD)

For a purely turbulent magnetic field in the same volume as the emission region, internal Faraday dispersion occurs. In this case A_i in Equation 6.1.20 needs to be modified to

$$\tilde{A}_i = (I_i/I)\,\frac{\sinh\left(\sigma_{\mathrm{RM}_i}^2\lambda^4\right)}{\left(\sigma_{\mathrm{RM}_i}^2\lambda^4\right)}\exp\left(-\sigma_{\mathrm{RM}_i}^2\lambda^4\right). \tag{6.1.22}$$

[3]The Sinc function is defined as $\mathrm{sinc}(x) = \sin(x)/x$. Note if using python's numpy package to calculate the model predictions, an additional factor of $1/\pi$ needs to be given in the argument of the Sinc function.

With this, Equation 6.1.19 and 6.1.21 are modified to

$$\left(\frac{p}{p_0}\right)_{\text{2layer}} = (W_A)_\text{d}\,\tilde{A}_\text{d} + (W_A)_\text{h}\,\tilde{A}_\text{h}\,, \tag{6.1.23}$$

$$\left(\frac{p}{p_0}\right)_{\text{3layer}} = 2\,(W_A)_\text{h}\,\tilde{A}_\text{h} + (W_A)_\text{d}\,\tilde{A}_\text{d}\,. \tag{6.1.24}$$

Here, only an example with anisotropic turbulent fields is given. For the isotropic case, $(W_A)_i$ becomes $(W_I)_i$ and if both anisotropic and isotropic turbulent fields are present we use $(W_{AI})_i$. Internal Faraday dispersion decreases the degree of polarization proportional to λ^4 and the RM dispersion within the telescope beam σ_{RM_i}, while the RM dispersion is dependent on the turbulent magnetic field strength and other parameters (see Equation 6.1.14). Further, the degree of polarization is weighted by wavelength-independent depolarization. Including turbulent magnetic fields changes the trend of the degree of polarization compared to the trend when considering a uniform Burn slab: Instead of a Sinc function-like behavior with periodically occurring drops to zero the degree of polarization shows a monotonically decreasing function.

Differential Faraday rotation + Internal Faraday dispersion (DFR + IFD)
For a case where both regular and turbulent magnetic fields are present in the emission region, DFR together with IFD occurs. For a two-layer system the observed degree of polarization is then given by

$$\begin{aligned}\left(\frac{p}{p_0}\right)_{\text{2layer}} = \Bigg\{ & W_\text{d}^2 \left(\frac{I_\text{d}}{I}\right)^2 \left(\frac{1 - 2\text{e}^{-\Omega_\text{d}}\cos C_\text{d} + \text{e}^{-2\Omega_\text{d}}}{\Omega_\text{d}^2 + C_\text{d}^2}\right) \\ & + W_\text{h}^2 \left(\frac{I_\text{h}}{I}\right)^2 \left(\frac{1 - 2\text{e}^{-\Omega_\text{h}}\cos C_\text{h} + \text{e}^{-2\Omega_\text{h}}}{\Omega_\text{h}^2 + C_\text{h}^2}\right) \\ & + W_\text{d} W_\text{h} \frac{I_\text{d} I_\text{h}}{I^2} \frac{2}{F^2 + G^2} \Big[\{F,G\}(2\Delta\psi_\text{dh} + C_\text{h}) \\ & + \text{e}^{-(\Omega_\text{d}+\Omega_\text{h})}\{F,G\}(2\Delta\psi_\text{dh} + C_\text{d}) \\ & - \text{e}^{-\Omega_\text{d}}\{F,G\}(2\Delta\psi_\text{dh} + C_\text{d} + C_\text{h}) \\ & - \text{e}^{-\Omega_\text{h}}\{F,G\}(2\Delta\psi_\text{dh}) \Big] \Bigg\}^{1/2}\,,\end{aligned} \tag{6.1.25}$$

with the substitutions $\Omega_\text{d} = 2\sigma_{\text{RM}_\text{d}}\lambda^4$, $\Omega_\text{h} = 2\sigma_{\text{RM}_\text{h}}\lambda^4$, $C_\text{d} = 2R_\text{d}\lambda^2$, $C_\text{h} = 2R_\text{h}\lambda^2$, $F = \Omega_\text{d}\Omega_\text{h} + C_\text{d}C_\text{h}$, $G = \Omega_\text{h}C_\text{d} - \Omega_\text{d}C_\text{h}$, and $\{F,G\}(a) = F\cos(a) - G\sin(a)$. The first term in Equation 6.1.25 represents the depolarization by differential Faraday rotation and internal Faraday dispersion, hence by regular and turbulent magnetic fields in the disk. W_d describes the wavelength-independent depolarization by the random magnetic fields. The second term represents the same as the first one but in this case for the halo. The rest are mixed terms from taking the absolute value of the complex polarization ($p = |\mathbf{P}|$; see Section 2.2). For a

three-layer system we have:

$$\begin{aligned}\left(\frac{p}{p_0}\right)_{\text{3layer}} =& \left(2W_\text{h}^2\left(\frac{I_\text{h}}{I}\right)^2\left\{\frac{\left(1-2\text{e}^{-\Omega_\text{h}}\cos C_\text{h}+\text{e}^{-2\Omega_\text{h}}\right)\left[1+\cos(C_\text{d}+C_\text{h})\right]}{\Omega_\text{h}^2+C_\text{h}^2}\right\}\right.\\ &+W_\text{d}^2\left(\frac{I_\text{d}}{I}\right)^2\left(\frac{1-2\text{e}^{-\Omega_\text{d}}\cos C_\text{d}+\text{e}^{-2\Omega_\text{d}}}{\Omega_\text{d}^2+C_\text{d}^2}\right)\\ &+W_\text{d}W_\text{h}\frac{I_\text{d}I_\text{h}}{I^2}\frac{2}{F^2+G^2}\left\{\{F,-G\}(-2\Delta\psi_\text{dh}+C_\text{d})\right.\\ &+\{F,G\}(2\Delta\psi_\text{dh}+C_\text{h})\\ &+\text{e}^{-(\Omega_\text{d}+\Omega_\text{h})}\left[\{F,G\}(2\Delta\psi_\text{dh}+C_\text{d})+\{F,-G\}(-2\Delta\psi_\text{dh}+C_\text{h})\right]\\ &-\text{e}^{-\Omega_\text{d}}\left[\{F,G\}(2\Delta\psi_\text{dh}+C_\text{d}+C_\text{h})+\{F,-G\}(-2\Delta\psi_\text{dh})\right]\\ &\left.\left.-\text{e}^{-\Omega_\text{h}}\left[\{F,-G\}(-2\Delta\psi_\text{dh}+C_\text{d}+C_\text{h})+\{F,G\}(2\Delta\psi_\text{dh})\right]\right\}\right)^{1/2}\end{aligned} \tag{6.1.26}$$

Equation 6.1.26, is a typo-corrected form of the equation as it appears in Shneider et al. (2014a): Compared to the third row of Equation 25 in Shneider et al. (2014a) the term $\cos(D)$ was replaced by $\cos(C_\text{h})$ and in the fourth row the term $\cos(C)$ was corrected to $\cos(C_\text{d})$.

Specific Modeling Examples

The above equations are for general cases. If one wants to explicitly give equations including different magnetic field configurations the equations are mixed. In the following, equations for a sample of models (summarized in Table 6.3) are given. Capital letters 'D' and 'H' denotes regular magnetic fields in the disk and halo while 'I' and 'A' denoting isotropic and anisotropic turbulent fields. For example 'DAIHI' means a configuration of regular fields together with isotropic and anisotropic turbulent magnetic fields in the disk (DAI), and regular and only isotropic turbulent fields in the halo (HI). We only chose to show some of the simplest combinations of the models summarized above. We exclude models which have turbulent magnetic fields only in the halo but not in the disk, because those are unrealistic since the driving source of turbulence are supernova remnants and stellar winds which are known to be present mainly in the disk. We always give equations for the degree of polarization as a function of wavelength for both two-layer and three-layer systems.

To compute the depolarization within a galaxy with only regular fields in the disk and in the halo, we use Equation 6.1.19:

$$\left(\frac{p}{p_0}\right)^{\text{DH}}_{\text{2layer}} = \left\{A_\text{d}^2+A_\text{h}^2+2A_\text{d}A_\text{h}\cos\left[2\Delta\psi_\text{dh}+(R_\text{d}+R_\text{h})\lambda^2\right]\right\}^{1/2} \tag{6.1.27}$$

Table 6.3: Model settings of Equations 6.1.27 to 6.1.34 with regular and both isotropic and anisotropic turbulent magnetic field configurations in the disk and halo.

	Disk			Halo		
	Reg.	Iso.	Aniso.	Reg.	Iso.	Aniso.
DH	✓			✓		
DAH	✓		✓	✓		
DIHI	✓	✓		✓	✓	
DAIHI	✓	✓	✓	✓	✓	

Notes. The table shows model configurations which are used in this work to discuss the degree of polarization as a function of wavelength for different magnetic field configurations present in M51. Magnetic field configurations are individually given for the disk and the halo. Capital letters 'D' and 'H' stands for regular fields in the disk and halo. Capital letters 'I' and 'A' denotes isotropic and anisotropic turbulent fields. The checkmarks show which fields are switched "on" and "off".

$$\left(\frac{p}{p_0}\right)^{\mathrm{HDH}}_{\mathrm{3layer}} = \Big(2A_\mathrm{h}^2\left\{1+\cos\left[2(R_\mathrm{d}+R_\mathrm{h})\lambda^2\right]\right\} + A_\mathrm{d}^2 + 2A_\mathrm{d}A_\mathrm{h}\Big\{\cos\left[-2\Delta\psi_\mathrm{dh}+(R_\mathrm{d}+R_\mathrm{h})\lambda^2\right] + \cos\left[2\Delta\psi_\mathrm{dh}+(R_\mathrm{d}+R_\mathrm{h})\lambda^2\right]\Big\}\Big)^{1/2} \tag{6.1.28}$$

To model regular and turbulent fields together (DAH) we make use of Equation 6.1.25 using a wavelength-independent depolarization of $W_\mathrm{h} = 1$ in the halo (denoted as $(W=1)_\mathrm{h}$), since in this example, only regular magnetic fields are present in the halo. In this case, $I = \tilde{I}_\mathrm{d} + I_\mathrm{h}$, and $\tilde{I}_\mathrm{d} = \tilde{\epsilon}_\mathrm{d}\, L_\mathrm{d}$ is the synchrotron total intensity including turbulent magnetic fields (in this case $\tilde{\epsilon}_\mathrm{d} = c\cdot\left(\overline{B}_\perp^2 + \sigma_x^2 + \sigma_y^2\right)$ in the disk). Also the term G needs to be replaced by $G = -\Omega_\mathrm{d} C_\mathrm{h}$ since $\Omega_\mathrm{h} = 0$. The degree of polarization for the DAH model in a two-layer

system is given by:

$$\left(\frac{p}{p_0}\right)^{\mathrm{DAH}}_{\mathrm{2layer}} = \Bigg\{ (W_{\mathrm{A}})^2_{\mathrm{d}} \left(\frac{\tilde{I}_{\mathrm{d}}}{\tilde{I}_{\mathrm{d}} + I_{\mathrm{h}}}\right)^2 \left(\frac{1 - 2\mathrm{e}^{-\Omega_{\mathrm{d}}} \cos C_{\mathrm{d}} + \mathrm{e}^{-2\Omega_{\mathrm{d}}}}{\Omega^2_{\mathrm{d}} + C^2_{\mathrm{d}}}\right)$$
$$+ (W=1)^2_{\mathrm{h}} \left(\frac{I_{\mathrm{h}}}{\tilde{I}_{\mathrm{d}} + I_{\mathrm{h}}}\right)^2 \left(\frac{1 - 2\mathrm{e}^{-\Omega_{\mathrm{h}}} \cos C_{\mathrm{h}} + \mathrm{e}^{-2\Omega_{\mathrm{h}}}}{\Omega^2_{\mathrm{h}} + C^2_{\mathrm{h}}}\right)$$
$$+ (W_{\mathrm{A}})_{\mathrm{d}} (W=1)_{\mathrm{h}} \frac{\tilde{I}_{\mathrm{d}} I_{\mathrm{h}}}{(\tilde{I}_{\mathrm{d}} + I_{\mathrm{h}})^2} \frac{2}{F^2 + G^2} \Big[\{F,G\}(2\Delta\psi_{\mathrm{dh}} + C_{\mathrm{h}})$$
$$+ \mathrm{e}^{-(\Omega_{\mathrm{d}} + \Omega_{\mathrm{h}})} \{F,G\}(2\Delta\psi_{\mathrm{dh}} + C_{\mathrm{d}})$$
$$- \mathrm{e}^{-\Omega_{\mathrm{d}}} \{F,G\}(2\Delta\psi_{\mathrm{dh}} + C_{\mathrm{d}} + C_{\mathrm{h}})$$
$$- \mathrm{e}^{-\Omega_{\mathrm{h}}} \{F,G\}(2\Delta\psi_{\mathrm{dh}}) \Big] \Bigg\}^{1/2} \tag{6.1.29}$$

And for a three-layer system (HDAH) the degree of polarization as a function of wavelength can be modeled as:

$$\left(\frac{p}{p_0}\right)^{\mathrm{HDAH}}_{\mathrm{3layer}} = \Bigg(2\,(W=1)^2_{\mathrm{h}} \left(\frac{I_{\mathrm{h}}}{\tilde{I}_{\mathrm{d}} + 2I_{\mathrm{h}}}\right)^2 \left\{ \frac{\left(1 - 2\mathrm{e}^{-\Omega_{\mathrm{h}}} \cos C_{\mathrm{h}} + \mathrm{e}^{-2\Omega_{\mathrm{h}}}\right) [1 + \cos(C_{\mathrm{d}} + C_{\mathrm{h}})]}{\Omega^2_{\mathrm{h}} + C^2_{\mathrm{h}}} \right\}$$
$$+ (W_{\mathrm{A}})^2_{\mathrm{d}} \left(\frac{\tilde{I}_{\mathrm{d}}}{\tilde{I}_{\mathrm{d}} + 2I_{\mathrm{h}}}\right)^2 \left(\frac{1 - 2\mathrm{e}^{-\Omega_{\mathrm{d}}} \cos C_{\mathrm{d}} + \mathrm{e}^{-2\Omega_{\mathrm{d}}}}{\Omega^2_{\mathrm{d}} + C^2_{\mathrm{d}}}\right)$$
$$+ (W_{\mathrm{A}})_{\mathrm{d}} (W=1)_{\mathrm{h}} \frac{\tilde{I}_{\mathrm{d}} I_{\mathrm{h}}}{(\tilde{I}_{\mathrm{d}} + 2I_{\mathrm{h}})^2} \frac{2}{F^2 + G^2} \Bigg\{ \{F,-G\}(-2\Delta\psi_{\mathrm{dh}} + C_{\mathrm{d}})$$
$$+ \{F,G\}(2\Delta\psi_{\mathrm{dh}} + C_{\mathrm{h}})$$
$$+ \mathrm{e}^{-(\Omega_{\mathrm{d}} + \Omega_{\mathrm{h}})} [\{F,G\}(2\Delta\psi_{\mathrm{dh}} + C_{\mathrm{d}}) + \{F,-G\}(-2\Delta\psi_{\mathrm{dh}} + C_{\mathrm{h}})]$$
$$- \mathrm{e}^{-\Omega_{\mathrm{d}}} [\{F,G\}(2\Delta\psi_{\mathrm{dh}} + C_{\mathrm{d}} + C_{\mathrm{h}}) + \{F,-G\}(-2\Delta\psi_{\mathrm{dh}})]$$
$$- \mathrm{e}^{-\Omega_{\mathrm{h}}} [\{F,-G\}(-2\Delta\psi_{\mathrm{dh}} + C_{\mathrm{d}} + C_{\mathrm{h}}) + \{F,G\}(2\Delta\psi_{\mathrm{dh}})] \Bigg\} \Bigg)^{1/2} \tag{6.1.30}$$

The same equation holds also for the DIH model. Only those parameters which are specifically calculated for an anisotropic case needs to be replaced for the isotropic case (e.g. $W_A \rightarrow W_I$). The next equation shows the model for depolarization resulting from regular

and (isotropic) turbulent fields in the disk and halo (DIHI):

$$\begin{aligned}\left(\frac{p}{p_0}\right)^{\mathrm{DIHI}}_{\mathrm{2layer}} =& \Bigg\{ (W_I)^2_{\mathrm{d}} \left(\frac{\tilde{I}_{\mathrm{d}}}{\tilde{I}}\right)^2 \left(\frac{1 - 2\mathrm{e}^{-\Omega_{\mathrm{d}}}\cos C_{\mathrm{d}} + \mathrm{e}^{-2\Omega_{\mathrm{d}}}}{\Omega^2_{\mathrm{d}} + C^2_{\mathrm{d}}}\right) \\ &+ (W_I)^2_{\mathrm{h}} \left(\frac{\tilde{I}_{\mathrm{h}}}{\tilde{I}}\right)^2 \left(\frac{1 - 2\mathrm{e}^{-\Omega_{\mathrm{h}}}\cos C_{\mathrm{h}} + \mathrm{e}^{-2\Omega_{\mathrm{h}}}}{\Omega^2_{\mathrm{h}} + C^2_{\mathrm{h}}}\right) \\ &+ (W_I)_{\mathrm{d}} (W_I)_{\mathrm{h}} \frac{\tilde{I}_{\mathrm{d}}\tilde{I}_{\mathrm{h}}}{\tilde{I}^2} \frac{2}{F^2 + G^2} \Big[\{F,G\}(2\Delta\psi_{\mathrm{dh}} + C_{\mathrm{h}}) \\ &+ \mathrm{e}^{-(\Omega_{\mathrm{d}}+\Omega_{\mathrm{h}})} \{F,G\}(2\Delta\psi_{\mathrm{dh}} + C_{\mathrm{d}}) \\ &- \mathrm{e}^{-\Omega_{\mathrm{d}}} \{F,G\}(2\Delta\psi_{\mathrm{dh}} + C_{\mathrm{d}} + C_{\mathrm{h}}) \\ &- \mathrm{e}^{-\Omega_{\mathrm{h}}} \{F,G\}(2\Delta\psi_{\mathrm{dh}}) \Big] \Bigg\}^{1/2} \end{aligned} \tag{6.1.31}$$

$$\begin{aligned}\left(\frac{p}{p_0}\right)^{\mathrm{HIDIHI}}_{\mathrm{3layer}} =& \Bigg(2\,(W_I)^2_{\mathrm{h}} \left(\frac{\tilde{I}_{\mathrm{h}}}{\tilde{I}_{\mathrm{d}} + 2\tilde{I}_{\mathrm{h}}}\right)^2 \left\{ \frac{\left(1 - 2\mathrm{e}^{-\Omega_{\mathrm{h}}}\cos C_{\mathrm{h}} + \mathrm{e}^{-2\Omega_{\mathrm{h}}}\right)\left[1 + \cos(C_{\mathrm{d}} + C_{\mathrm{h}})\right]}{\Omega^2_{\mathrm{h}} + C^2_{\mathrm{h}}} \right\} \\ &+ (W_I)^2_{\mathrm{d}} \left(\frac{\tilde{I}_{\mathrm{d}}}{\tilde{I}_{\mathrm{d}} + 2\tilde{I}_{\mathrm{h}}}\right)^2 \left(\frac{1 - 2\mathrm{e}^{-\Omega_{\mathrm{d}}}\cos C_{\mathrm{d}} + \mathrm{e}^{-2\Omega_{\mathrm{d}}}}{\Omega^2_{\mathrm{d}} + C^2_{\mathrm{d}}}\right) \\ &+ (W_I)_{\mathrm{d}} (W_I)_{\mathrm{h}} \frac{\tilde{I}_{\mathrm{d}}\tilde{I}_{\mathrm{h}}}{(\tilde{I}_{\mathrm{d}} + 2\tilde{I}_{\mathrm{h}})^2} \frac{2}{F^2 + G^2} \Bigg\{ \{F, -G\}(-2\Delta\psi_{\mathrm{dh}} + C_{\mathrm{d}}) \\ &+ \{F,G\}(2\Delta\psi_{\mathrm{dh}} + C_{\mathrm{h}}) \\ &+ \mathrm{e}^{-(\Omega_{\mathrm{d}}+\Omega_{\mathrm{h}})} \left[\{F,G\}(2\Delta\psi_{\mathrm{dh}} + C_{\mathrm{d}}) + \{F, -G\}(-2\Delta\psi_{\mathrm{dh}} + C_{\mathrm{h}})\right] \\ &- \mathrm{e}^{-\Omega_{\mathrm{d}}} \left[\{F,G\}(2\Delta\psi_{\mathrm{dh}} + C_{\mathrm{d}} + C_{\mathrm{h}}) + \{F, -G\}(-2\Delta\psi_{\mathrm{dh}})\right] \\ &- \mathrm{e}^{-\Omega_{\mathrm{h}}} \left[\{F, -G\}(-2\Delta\psi_{\mathrm{dh}} + C_{\mathrm{d}} + C_{\mathrm{h}}) + \{F,G\}(2\Delta\psi_{\mathrm{dh}})\right] \Bigg\} \Bigg)^{1/2} \end{aligned} \tag{6.1.32}$$

At last we give an equation for both regular and turbulent magnetic fields present in the disk where both isotropic and anisotropic random fields are considered and regular plus turbulent

fields with only isotropic random fields in the halo (DAIHI):

$$\left(\frac{p}{p_0}\right)^{\mathrm{DAIHI}}_{\mathrm{2layer}} = \Bigg\{ (W_{AI})^2_{\mathrm{d}} \left(\frac{\tilde{I}_{\mathrm{d}}}{\tilde{I}}\right)^2 \left(\frac{1 - 2\mathrm{e}^{-\Omega_{\mathrm{d}}}\cos C_{\mathrm{d}} + \mathrm{e}^{-2\Omega_{\mathrm{d}}}}{\Omega^2_{\mathrm{d}} + C^2_{\mathrm{d}}}\right) + (W_I)^2_{\mathrm{h}} \left(\frac{\tilde{I}_{\mathrm{h}}}{\tilde{I}}\right)^2 \left(\frac{1 - 2\mathrm{e}^{-\Omega_{\mathrm{h}}}\cos C_{\mathrm{h}} + \mathrm{e}^{-2\Omega_{\mathrm{h}}}}{\Omega^2_{\mathrm{h}} + C^2_{\mathrm{h}}}\right) + (W_{AI})_{\mathrm{d}} (W_I)_{\mathrm{h}} \frac{\tilde{I}_{\mathrm{d}}\tilde{I}_{\mathrm{h}}}{\tilde{I}^2} \frac{2}{F^2 + G^2} \Big[\{F,G\}(2\Delta\psi_{\mathrm{dh}} + C_{\mathrm{h}}) + \mathrm{e}^{-(\Omega_{\mathrm{d}}+\Omega_{\mathrm{h}})}\{F,G\}(2\Delta\psi_{\mathrm{dh}} + C_{\mathrm{d}}) - \mathrm{e}^{-\Omega_{\mathrm{d}}}\{F,G\}(2\Delta\psi_{\mathrm{dh}} + C_{\mathrm{d}} + C_{\mathrm{h}}) - \mathrm{e}^{-\Omega_{\mathrm{h}}}\{F,G\}(2\Delta\psi_{\mathrm{dh}}) \Big] \Bigg\}^{1/2} \tag{6.1.33}$$

$$\left(\frac{p}{p_0}\right)^{\mathrm{HIDAIHI}}_{\mathrm{3layer}} = \Bigg(2\,(W_I)^2_{\mathrm{h}} \left(\frac{\tilde{I}_{\mathrm{h}}}{\tilde{I}_{\mathrm{d}} + 2\tilde{I}_{\mathrm{h}}}\right)^2 \left\{ \frac{\left(1 - 2\mathrm{e}^{-\Omega_{\mathrm{h}}}\cos C_{\mathrm{h}} + \mathrm{e}^{-2\Omega_{\mathrm{h}}}\right)\left[1 + \cos(C_{\mathrm{d}} + C_{\mathrm{h}})\right]}{\Omega^2_{\mathrm{h}} + C^2_{\mathrm{h}}} \right\} + (W_{AI})^2_{\mathrm{d}} \left(\frac{\tilde{I}_{\mathrm{d}}}{\tilde{I}_{\mathrm{d}} + 2\tilde{I}_{\mathrm{h}}}\right)^2 \left(\frac{1 - 2\mathrm{e}^{-\Omega_{\mathrm{d}}}\cos C_{\mathrm{d}} + \mathrm{e}^{-2\Omega_{\mathrm{d}}}}{\Omega^2_{\mathrm{d}} + C^2_{\mathrm{d}}}\right) + (W_{AI})_{\mathrm{d}} (W_I)_{\mathrm{h}} \frac{\tilde{I}_{\mathrm{d}}\tilde{I}_{\mathrm{h}}}{(\tilde{I}_{\mathrm{d}} + 2\tilde{I}_{\mathrm{h}})^2} \frac{2}{F^2 + G^2} \Big\{ \{F, -G\}(-2\Delta\psi_{\mathrm{dh}} + C_{\mathrm{d}}) + \{F,G\}(2\Delta\psi_{\mathrm{dh}} + C_{\mathrm{h}}) + \mathrm{e}^{-(\Omega_{\mathrm{d}}+\Omega_{\mathrm{h}})}\left[\{F,G\}(2\Delta\psi_{\mathrm{dh}} + C_{\mathrm{d}}) + \{F, -G\}(-2\Delta\psi_{\mathrm{dh}} + C_{\mathrm{h}})\right] - \mathrm{e}^{-\Omega_{\mathrm{d}}}\left[\{F,G\}(2\Delta\psi_{\mathrm{dh}} + C_{\mathrm{d}} + C_{\mathrm{h}}) + \{F, -G\}(-2\Delta\psi_{\mathrm{dh}})\right] - \mathrm{e}^{-\Omega_{\mathrm{h}}}\left[\{F, -G\}(-2\Delta\psi_{\mathrm{dh}} + C_{\mathrm{d}} + C_{\mathrm{h}}) + \{F,G\}(2\Delta\psi_{\mathrm{dh}})\right] \Big\} \Bigg)^{1/2} \tag{6.1.34}$$

Figures 6.1.5 and 6.1.6 show the influence of different magnetic fields strengths on the degree of polarization as a function of wavelength for a scenario with only regular magnetic fields (DH) and with regular plus turbulent magnetic fields (DAH) in a two-layer system, respectively. For clarity we only change one parameter at a time in each plot. We used a "cool" color scheme to show the change of regular magnetic field strength and "warm" colors for the change of turbulent field strength. In the title of each plot, the *italic*-written letter denotes the parameter which has changed (also shown in the legend). For example in the left panel of Figure 6.1.5, we changed the total regular magnetic fields strength in the disk (*D*H). The fixed parameter values are the same as given in Shneider et al. (2014a), reported in Table 6.2. In case of purely regular magnetic fields, the intrinsic degree of polarization (at $\lambda = 0$) starts at its theoretical maximum (chosen to be 70 %). The overall trend is Sinc function-like, as it is expected for a uniform Burn slab. Comparing the left and right panel

of Figure 6.1.5 one can see that in the case of changing the magnetic field strength in the disk, the positions of "null" remains always the same whereas increasing the magnetic field strength in the halo decreases the wavelengths at which the degree of polarization drops to zero (stronger depolarization at shorter wavelengths for higher magnetic field strengths). This shows that in case of the DH model, the halo dominates the trend of the degree of polarization as a function of wavelength. The reason is that the parameters used to model the degree of polarization are the same in the disk and in the halo, except for the path length L_i (and the thermal electron density n_{ei}). The path length was used to calculate the total synchrotron intensity emitted by individual layers. Because the path length through the halo is by a factor of 6 larger than the path length through the disk, the emission from the halo dominates the observed degree of polarization.

Figure 6.1.6 shows the degree of polarization as a function of wavelength for the DAH scenario. Since turbulent fields are involved, the intrinsic degree of polarization at $\lambda = 0$ decreases significantly compared to scenarios with purely regular magnetic fields due to wavelength-independent depolarization but the overall trend of the degree of polarization as a function of wavelength remains Sinc function-like. In the top left and top right panels of Figure 6.1.6 one notes that for the case of changing the regular magnetic field strength in the disk, the wavelength-independent depolarization has only a small impact on the intrinsic degree of polarization at $\lambda = 0$, whereas for an increasing regular magnetic field in the halo, the intrinsic degree of polarization also increases. This is again because the halo term in Equation 6.1.29 (the second term) dominates the degree of polarization (the wavelength-independent depolarization term is $W_\mathrm{h} = 1$, which strongly impact the degree of polarization at $\lambda = 0$).

Comparing the model DH and DAH, we find that the nulls appear at the same wavelengths, namely at $\sim\lambda\,23$ and 33 cm (when comparing the left panel in Figure 6.1.5 and the top left panel in Figure 6.1.6). The nulls appear at wavelengths depending on the total RM of the layer ($\mathrm{RM}\lambda^2 = n\pi$, where RM is the total rotation measure through the whole layer, while RM/2 is the observed rotation measure), depending on the regular magnetic field strength which is assumed to be equal in the disk and halo. The turbulent field in the DAH model only attenuates the amplitude of the degree of polarization, especially at short wavelengths. Since the regular magnetic field strength is equal in the disk and the halo and therefore the RM is the same for model DH and DAH, the nulls appear at the same wavelength.

Replacing the anisotropic random fields to isotropic random fields (compare red solid and red dashed line in Figure 6.1.7) only decreases the intrinsic degree of polarization at $\lambda = 0$ (by a few %). This is expected when comparing fields with equal field strengths because we consider anisotropy caused by compression along spiral arms and by shear from differential rotation, hence only in the disk plane and not in vertical direction. Therefore, within the beam the depolarizing component along the line-of-sight for anisotropic random magnetic field is smaller compared to isotropic random fields which includes magnetic field lines in all directions (also in vertical direction).

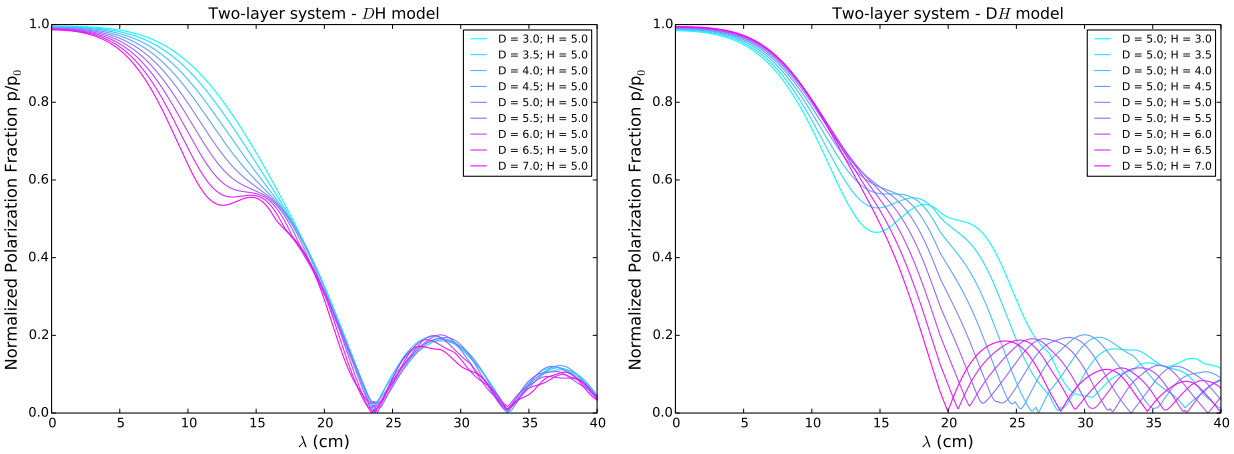

Figure 6.1.5: Normalized degree of polarization as a function of wavelength for the model DH in a two-layer system. Different colors show a varying total regular magnetic field strength in the disk (left panel) and in the halo (right panel) in μG.

6.1.3 Application to M51

In Figure 6.1.7, selected model predictions for a two-layer (left panel) and three-layer (right panel) system are shown. The simplest scenario contains only regular magnetic fields in the disk and halo (denoted as DH). Figure 6.1.8 shows a simplified illustration of the situation in M51 for the different models. The model parameter values are given in Table 6.2.

To compare the model predictions with observations, the observed degrees of polarization at X-band (8.35 GHz), C-band (4.85 GHz), S-band (2.56 - 3.56 GHz), and L-band (1.12 - 1.84 GHz) are also shown in Figure 6.1.7. We considered the total and polarized intensity integrated in a sector with an azimuthal angle centered at 100° and an opening angle of 20° and radial boundaries 2.4 – 3.6 kpc (see Fletcher et al., 2011). This sector was chosen because it represents an inter-arm region where the degree of polarization is high and with high signal-to-noise ratio in polarized intensity. To perform the analysis per pixel is not the right approach because one needs enough independent turbulent cells within the considered region to have deterministic expressions for the observed degree of polarization. If we consider a turbulence cell size of 50 pc, our beam of 15″ contains about 10 turbulent cells and the considered sector contains about 5 beams, hence about 50 turbulent cells. This is sufficient to be deterministic (Sokoloff et al., 1998). As discussed in Section 4.3.2, polarized emission is generated by non-thermal synchrotron radiation. To calculate the non-thermal fractional polarization, the thermal fraction of the observed total intensity must be subtracted from the Stokes I values. To obtain the non-thermal total flux density at the location of the considered sector, we assumed a thermal fraction $f^{\rm th}_{\nu_0}$ of 9 % at $\nu_0 = 3$ GHz (Tabatabaei et al., 2017) and extrapolated the non-thermal flux densities at frequency ν via $S_\nu = f^{\rm th}_{\nu_0} \left(\frac{\nu}{\nu_0}\right)^{-0.1} S_{\nu_0}$ (compare Equation 4.3.5 in Section 4.3.2). This was done for all spectral windows at S-band, at 4.85 and 8.35 GHz, and at all channels of the L-band data

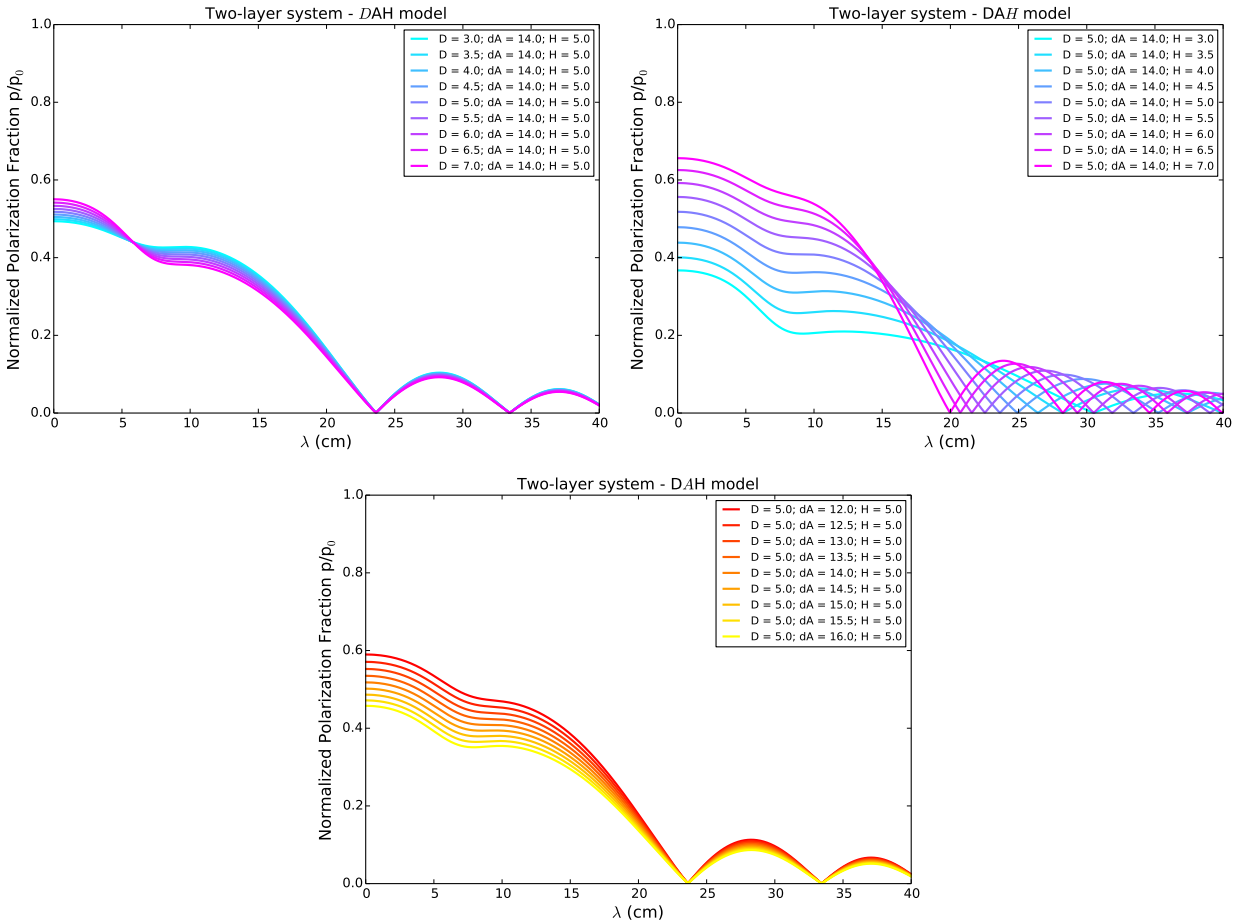

Figure 6.1.6: Normalized degree of polarization as a function of wavelength for the model DAH in a two-layer system. Different colors show a varying total regular magnetic field strength in the disk (top left panel) and in the halo (top right panel) and a varying anisotropic turbulent magnetic field strength in the disk (bottom panel) in μG.

set. Assuming that the thermal fraction in the sector is equal to the global average value is reasonable since the region where the integrated total and polarized flux density were measured is located at an inter-arm location away from star-forming regions and hence with low thermal emission. However, we explored the influence of a varying thermal fraction between 0 – 20 % on the degree of polarization (as it was found in inter-arm regions of NGC 628 at S-band, Mulcahy et al., 2017): A higher thermal fraction increases the degree of polarization (with respect to the degree of polarization computed using a global thermal fraction of 9 %) while the effect is strongest at short wavelengths and barely noticeable at L-band. For a thermal fraction of 20 %, the degree of polarization at λ 3.6 cm is underestimated by a factor of 1.5 when using 9 % thermal fraction while at the central wavelength of S-band (at about 10 cm) the degree of polarization is only underestimated by a factor of $\sim$ 1.2.

The values of the degree of (non-thermal) polarization using a thermal fraction of 9 % are shown in Table 6.4. The error bars reflect only the rms noise level in the images and

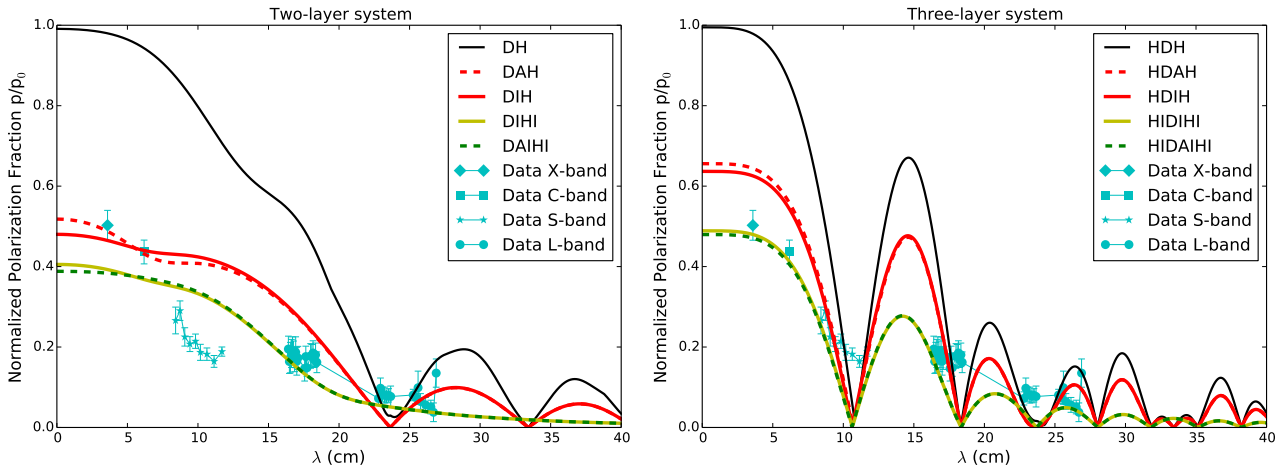

Figure 6.1.7: Normalized degree of polarization as a function of wavelength for a two-layer system (left) and a three-layer system (right) in M51. The observed degree of (non-thermal) polarization values are displayed with error bars. The plots show some selected reconstructed models from Shneider et al. (2014a), also seen in Figure 6.1.2 with same color. All model profiles featured have been constructed from among the a set of parameters given in Table 6.2. Please see Table 6.3 for nomenclature and description of the model types appearing in the legend.

are calculated via Gaussian error propagation using the rms noise in the Stokes I, Q, and U images: $\mathrm{rms} \cdot \sqrt{N_{\mathrm{beams}}}$, where N_{beams} is the number of beams (about 5) within the integration area. In a future analysis, a proper separation of the thermal and non-thermal emission of each pixel in the observed total intensity maps can be performed. This method takes spatial variations of the thermal fraction across the galaxy into account and would make sure to compare the the models to a more truthful degree of (non-thermal) polarization.

By comparing the observed degree of polarization to the models, one can rule out models with only regular magnetic fields in the disk and halo (DH) since the observed data deviate most (a factor of 4 lower at S-band) from those model predictions. This is in agreement with observations of turbulent magnetic fields in the ISM of spiral galaxies (e.g. Beck, 2016). Especially at short wavelengths the model DH has a degree of polarization close to the intrinsic value without any wavelength-independent depolarization but because our resolution does not resolve the turbulence, beam depolarization always occur. However, it appears that none of the model predictions with the parameter values given in Table 6.2 is in agreement with the observed data at S-band. For the two-layer system, the data points deviates by a factor of about 2 from the models whereas for the three-layer case, some data points are well reproduced by the model predictions but the model drops to zero at $\lambda \approx 11\,\mathrm{cm}$ which is clearly ruled out by the observed data. In any case, our new S-band data (the polarized emission from the disk-halo transition region) are crucial to evaluate whether the model predictions fit the observations.

The discussed models contain many free parameters. However, some of the parameters,

Table 6.4: Observed Degree of (non-thermal) Polarization.

X-band λ (cm)	(p/p_0)	C-band λ (cm)	(p/p_0)	S-band λ (cm)	(p/p_0)	L-band λ (cm)	(p/p_0)
3.59	0.50 ± 0.04	6.18	0.44 ± 0.03	8.41	0.27 ± 0.03	16.41	0.19 ± 0.03
				8.73	0.29 ± 0.02	16.48	0.16 ± 0.03
				9.07	0.23 ± 0.02	16.55	0.17 ± 0.04
				9.43	0.21 ± 0.02	16.63	0.18 ± 0.03
				9.83	0.21 ± 0.02	16.70	0.19 ± 0.03
				10.17	0.19 ± 0.02	16.78	0.19 ± 0.02
				10.64	0.18 ± 0.02	16.85	0.17 ± 0.03
				11.14	0.16 ± 0.01	16.93	0.19 ± 0.04
				11.70	0.19 ± 0.01	17.00	0.16 ± 0.03
						17.08	0.17 ± 0.03
						17.56	0.15 ± 0.03
						17.65	0.18 ± 0.03
						17.73	0.15 ± 0.02
						17.98	0.18 ± 0.03
						18.07	0.18 ± 0.03
						18.16	0.19 ± 0.03
						18.25	0.17 ± 0.02
						18.34	0.18 ± 0.03
						18.43	0.16 ± 0.03
						22.80	0.07 ± 0.02
						22.94	0.10 ± 0.03
						23.08	0.08 ± 0.02
						23.22	0.08 ± 0.02
						23.37	0.08 ± 0.02
						23.51	0.08 ± 0.02
						23.66	0.08 ± 0.03
						25.26	0.08 ± 0.01
						25.43	0.07 ± 0.02
						25.60	0.10 ± 0.04
						25.78	0.06 ± 0.02
						26.14	0.06 ± 0.02
						26.51	0.05 ± 0.02
						26.70	0.04 ± 0.02
						26.89	0.14 ± 0.04

Notes. The total and polarized intensity values to calculate the degree of polarization were integrated in a sector with an azimuthal angle centered at 100° and an opening angle of 20° and radial boundaries 2.4 – 3.6 kpc (see Fletcher et al., 2011).

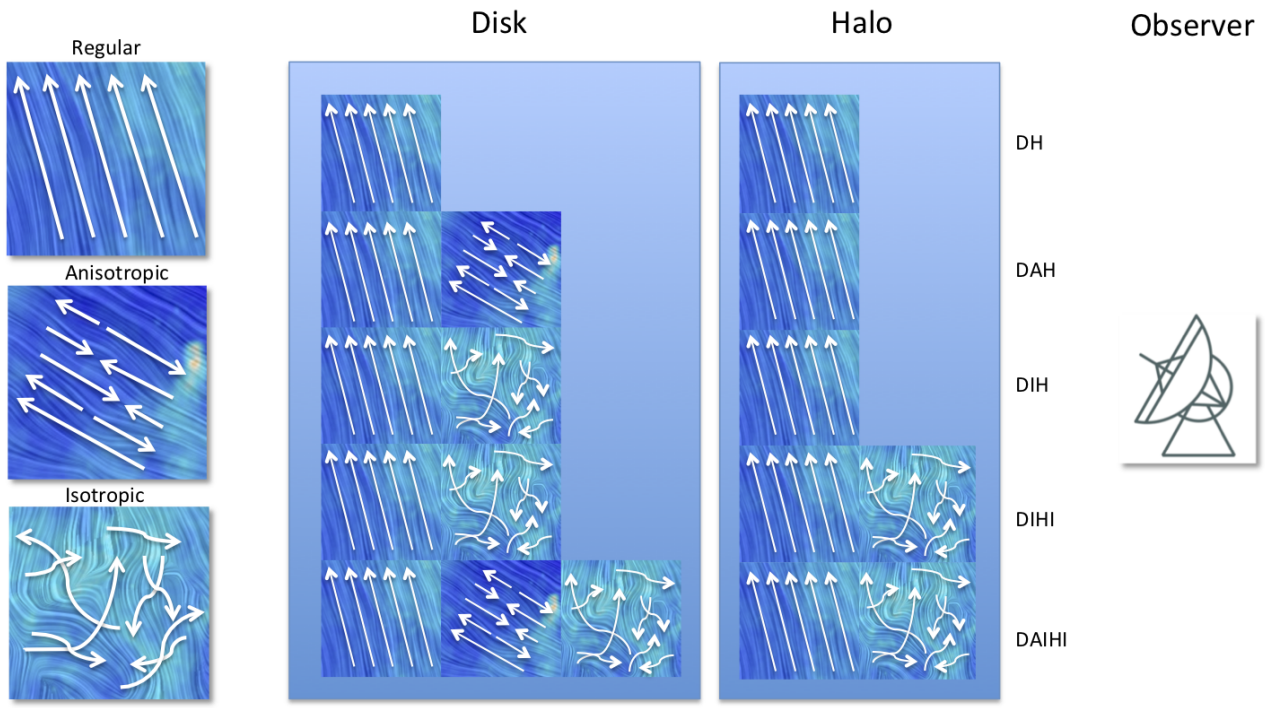

Figure 6.1.8: Simplistic illustration of magnetic field components present in a spiral galaxy causing wavelength-dependent depolarization of the observed polarized signal considered in our analysis. Illustrated are different layers referred as disk and halo including regular and anisotropic turbulent and/or isotropic turbulent magnetic fields. Note that in reality, magnetic field lines are always connected, which is not illustrated in this Figure.

specifically those in Table 6.2, like the path length L and the turbulence cell size as well as the fitted parameters of the different Fourier modes in the disk and halo (pitch angle, azimuth, and amplitudes of the Fourier modes), are constrained using prior studies (Berkhuijsen et al., 1997; Fletcher et al., 2011). The remaining free parameters are the regular field strengths and isotropic and anisotropic turbulent field strengths, both in the disk and halo. Also the thermal electron densities in the disk and halo could vary significantly in the considered sector from the global value.

Finding the "Best fit" Parameter Values

The most uncertain parameters in the Shneider et al. (2014a) model are the total regular and turbulent magnetic field strengths and the thermal electron densities in the disk and in the halo. For those values we only have global estimates which are strongly dependent on assumptions, e.g. the field strengths are estimated assuming equipartition between the energy densities of magnetic fields and cosmic rays (Fletcher et al., 2011; Beck and Krause, 2005; Berkhuijsen et al., 1997). The global values may also differ from those in individual

Table 6.5: Free Parameters and "Best fit" for the Interactive Tool.

Parameter	Starting Value	Range	DAH two-layer	HDAH three-layer
$B_{\mathrm{tot,d}}$	$5\,\mu$G	0 - $20\,\mu$G	$10\,\mu$G	$10\,\mu$G
$B_{\mathrm{tot,h}}$	$5\,\mu$G	0 - $20\,\mu$G	$3\,\mu$G	$3\,\mu$G
$b_{\mathrm{tot,d}}$	$14\,\mu$G	0 - $28\,\mu$G	$14\,\mu$G	$16\,\mu$G
$b_{\mathrm{tot,h}}$	$4\,\mu$G	0 - $8\,\mu$G	-	-
$n_{\mathrm{e,d}}$	$0.11\,\mathrm{cm}^{-3}$	0.00 - $0.22\,\mathrm{cm}^{-3}$	$0.07\,\mathrm{cm}^{-3}$	$0.07\,\mathrm{cm}^{-3}$
$n_{\mathrm{e,h}}$	$0.01\,\mathrm{cm}^{-3}$	0.000 - $0.020\,\mathrm{cm}^{-3}$	$0.01\,\mathrm{cm}^{-3}$	$0.01\,\mathrm{cm}^{-3}$

Notes. Free parameters used to model the degree of polarization as a function of wavelength (Figure 6.1.9). The range of parameters are chosen around a starting value reported in Shneider et al. (2014a). The last two columns give the "best fit" values of the DAH model for a two-layer and three-layer system.

sectors (especially for the thermal electron densities).

The question is now if changing some of the model parameter values in a reasonable range would better match the model predictions to the observed degrees of polarization. For this purpose, we developed an interactive tool in Python where some selected model parameter values (such as the total regular and turbulent magnetic field strength and thermal electron densities in the disk and halo) can be changed simultaneously to visually inspect if the model matches the data with physically reasonable parameter values (Figure 6.1.9). This is an important step towards an automatic least-square fit of the models to the data, since those values can then later be used as initial conditions to perform e.g. a fit with a χ^2 analysis. A χ^2 fit will provide a strong method to determine the values of the parameters accurately (if it converges to the right solutions). Furthermore, the interactive tool allows one to gain intuitively how the degree of polarization as a function of wavelength changes when various parameters are changed. The free parameters used in the interactive tool and their ranges are summarized in Table 6.5.

Figure 6.1.10 shows the "best fit" of the model DAH (red dashed line). We explored visually whether any reasonable combination of the free parameters can reproduce the observed degree of polarization. These "best fit" magnetic field strengths and electron densities are listed in Table 6.5 and are all physically plausible values. For the three-layer system it is not possible to lift up the nulls in the model by changing any parameter in the given range. Therefore, this three-layer model can be ruled out or, in other words, we do not detect polarized emission from the far side halo. It is highly likely that the polarized emission from the far-side halo gets completely depolarized by the disk, so the third layer (the far-side halo) is redundant in the model. For the total regular magnetic field strength we found $B_{\mathrm{tot,d}} \approx 10\,\mu$G in the disk and $B_{\mathrm{tot,h}} \approx 3\,\mu$G in the (near-side) halo. For the total turbulent magnetic field in the disk we found $b_{\mathrm{tot,d}} \approx 14\,\mu$G. The estimated uncertainties of the field strengths are of the order of about $0.5-1\,\mu$G (this is the range of field strengths where the model can be matched to all data points including the errorbars).

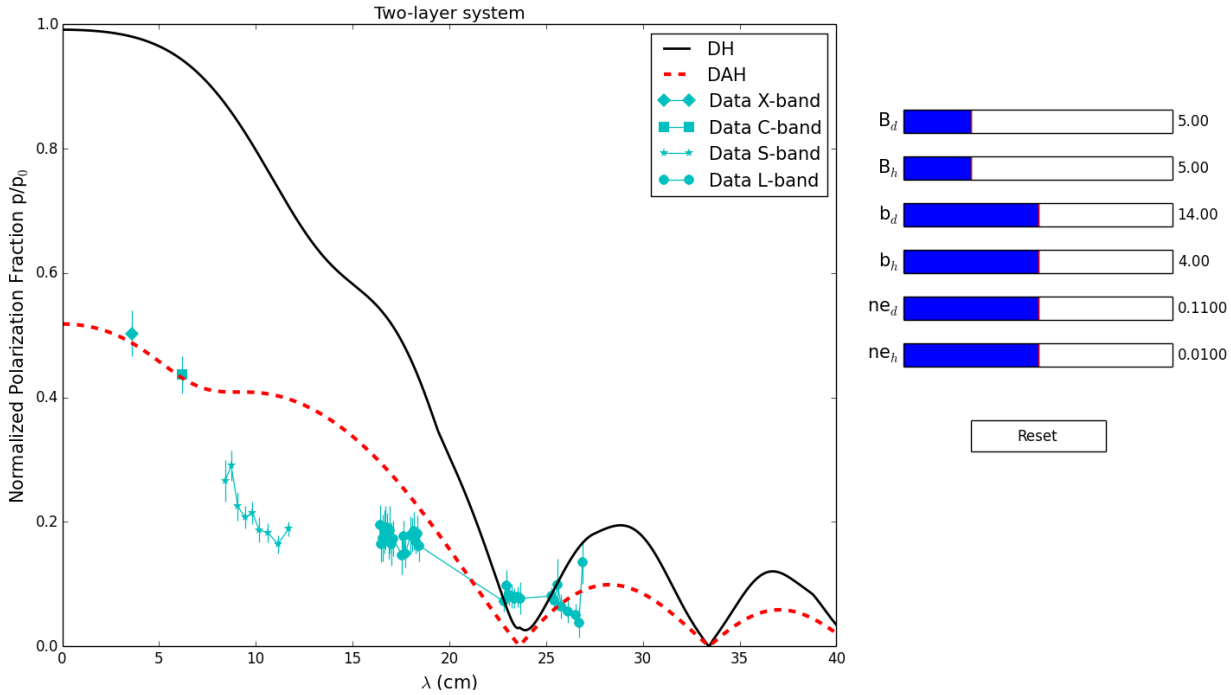

Figure 6.1.9: Interactive tool to adjust different model parameters. We only show two selected models (DH and DAH) which are the same as in Figure 6.1.7. This tool was developed within Python 2.7 Software Foundation (Python Language Reference, version 2.7, available at http://www.python.org) using the module Matplotlib (Hunter, 2007).

Using the interactive tool, we matched the model DAH also to the observed polarization fraction in two neighboring sectors. Both sectors are located at the same radius, one towards the north (at azimuthal angle of about 90°) of the original sector and one towards the south (at azimuthal angle of about 120°). For both sectors we found the same magnetic field strengths to be matched as for the original sector. Consistency between matches to different sectors is a strong indication that the model is physically meaningful. Using the interactive tool it turned out that from the compilation of models considered here (compare Table 6.3), only the model DAH is able to represent the observed data well using reasonable field strengths in the original sector as well as in the two neighboring sectors. To judge whether the field strength is reasonable we compared the turbulent and total field strengths in the disk with the observed values at $\lambda\,6\,\mathrm{cm}$ by Fletcher et al. (2011): They found strengths of the ordered field (anisotropic turbulent) of $b_{\mathrm{tot,d}} \approx 13\,\mu\mathrm{G}$ and a total magnetic field strength ($B_{\mathrm{d}} = \sqrt{B^2_{\mathrm{tot,d}} + b^2_{\mathrm{tot,d}}}$) of $15-20\,\mu\mathrm{G}$ in the inter-arm regions of M51.

Only for the DAH model it was possible to match the data points of all three sectors with field strengths within those boundaries. For example, trying to match the model DIHI (which includes turbulent fields in the halo) gives a regular field strength of about the same strength in the disk and halo as for the model DAH but due to the turbulent field in the halo the turbulent field in the disk has to be increased by about $5-6\,\mu\mathrm{G}$ to match the data.

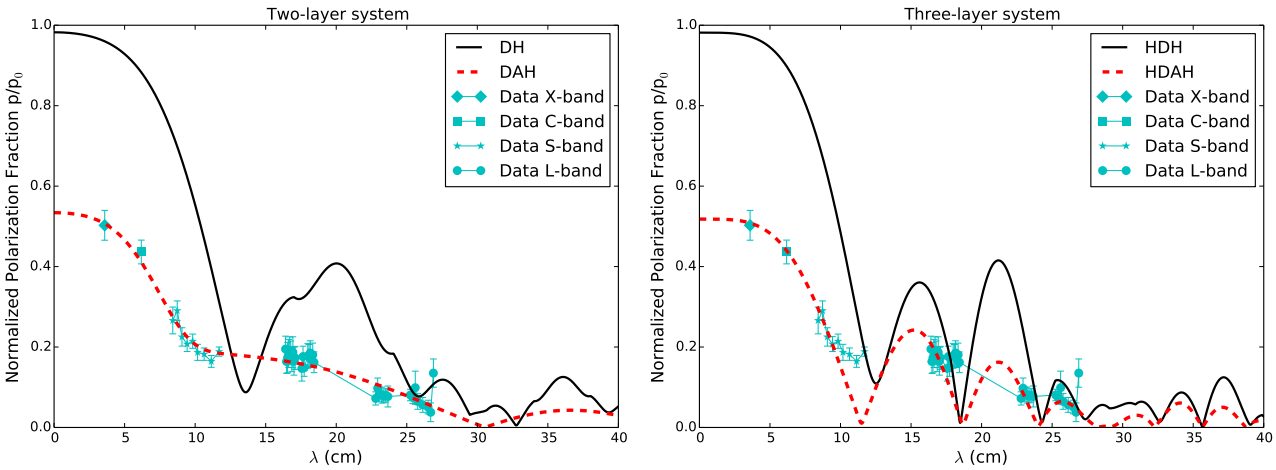

Figure 6.1.10: "Best fit" of the model DAH (red dashed line) for a two-layer system (left panel) and a three-layer system (right panel) in M51 to the observed degree of polarization at multiple wavelengths.

This gives a total magnetic field strength which is too large (by about $5\,\mu$G) compared to the boundaries given by the observations at $\lambda\,6$ cm by Fletcher et al. (2011). The same holds for the model DIH in the northern sector. However, since those boundaries are only global average values, we can not completely rule out the models DIH and DIHI. Nevertheless, the model DAIHI gives strengths of the total random magnetic field a factor of $2-3$ smaller compared to the regular magnetic field but this can only be the case (physically) if the degree of polarization is very high (if $(p/p_0) > 0.6$) which is not the case in our observations. Because we could only match the DAH model to the observations in the three sectors it looks like the anisotropic field in the disk is essential. This could be a piece of evidence for the presence of anisotropic random fields.

In their second paper, Shneider et al. (2014b) fitted the field strengths of the regular and isotropic and anisotropic random fields in the disk and halo in 4 rings across the galaxy M51. They used the models from the first paper (Shneider et al., 2014a) in different rings and fitted the models to get the best-fit magnetic field configuration at each ring (statistical comparison via χ^2 analysis of predicted to observed polarization maps). They found that a two-layer system provides better fits (consistent with our findings), although the best-fit magnetic field strengths for a three-layer system are comparable. They found field strengths of $B_{\rm tot,d} \approx 10\,\mu$G, $b_{\rm tot,d} \approx 11-14\,\mu$G and $B_{\rm tot,h} \approx 3\,\mu$G. This is in excellent agreement with the field strengths found using our interactive tool. In Shneider et al. (2014b) the models were compared to observational data at only three wavelengths. The observational capabilities of our new broadband S-band radio polarimetric data will allow us to better determine whether a two-layer or three-layer modeling approach is best suited for describing the data and also to have tighter estimates for the regular and (isotropic and anisotropic) turbulent field strengths in the disk and halo by fitting the degree of polarization as a function of the azimuthal angle in 4 separated rings. This will be done in a future project.

6.1.4 Discussion

The Shneider et al. (2014a) model has some advantages compared to 'traditional' depolarization model fitting (QU-fitting, see Sokoloff et al., 1998; O'Sullivan et al., 2012): This approach can directly give us the strengths of the (1) regular magnetic field, (2) anisotropic turbulent magnetic field, and (3) isotropic turbulent magnetic field in the disk and halo, respectively. QU-fitting gives us 'only' RM, $\sigma_{\rm RM}$, p_0 and the intrinsic polarization angle ψ_0 within the telescope beam and for only one layer (QU-fitting treats multiple components by putting them into the sky plane instead of stacking them along the line-of-sight). The Shneider et al. (2014a) model considers multiple layers along the line-of-sight which allows us to consider more complicated scenarios. So far, this model is the only one which distinguishes between isotropic and anisotropic turbulent fields and includes multiple layers along the line-of-sight.

However, the Shneider et al. (2014a) model has certain limitations given by the considered assumptions:

- The assumption that the thermal electron density is constant within the disk and also within the halo of the galaxy is not physical. The ISM of galaxies is a complicated system with varying thermal electron densities as a function of radius, azimuthal angle, vertical height. However, because we considered only one sector, assuming a constant electron density should be a sufficient approximation.

- For the CRE density, Shneider et al. (2014a) assumed the same value in the disk and halo. However, this is inconsistent with the exponential scale heights of the synchrotron emission in edge-on galaxies (Heesen et al., 2018). A typical scale height of $h_{\rm syn} \simeq 1.5\,{\rm kpc}$ gives a CRE scale height $h_{\rm CR} = h_{\rm syn} \cdot (3 + \alpha_{\rm syn})/2 \simeq 3$ kpc (assuming energy equipartition between CRs and magnetic fields), so that the CRE density should decrease by a factor of about 2 – 7 from the disk to the halo (heights of 2 – 6 kpc above the disk). Would a different value in the disk and halo affect the models? If the values in the disk and halo are different, they do not cancel out by calculating (p/p_0). A different CRE density would also change the synchrotron intensity. Figure 6.1.11 shows the influence of different CRE densities in the halo compared to the disk on the degree of polarization as a function of wavelength. A cosmic ray density of a factor of 10 smaller in the halo decreases (p/p_0) for the DAH model by a factor of 1.6 and for DIH by a factor of 2.7 at $\lambda = 0$, respectively. However, even a CRE density a factor of 10 smaller in the halo does not help to "lift up" the nulls in the three-layer model and thus, it is still not possible to fit the HDAH model to the data with reasonable parameters.

- Also the synchrotron spectral index and therefore the intrinsic degree of polarization (at $\lambda = 0$) can be different in the disk and halo (also within a layer and along the line-of-sight), because of energy losses as it is observed in edge-on galaxies (e.g. Schmidt et al. 2019, submitted).

- Assuming a constant size of turbulence cells within the disk and within the halo could be too simplistic. There could be spatial variations of the turbulent properties. At different locations, the size of the turbulence cell could vary: The turbulence cell at the gas spiral arms could be smaller compared to the size of turbulence at inter-arm locations (due to star forming processes, which mainly takes place in the dense spiral arms, driving the turbulence). For example, in the Milky Way Haverkorn et al. (2008) found a turbulence cell size less than 10 pc at the gaseous spiral arms, while in the inter-arm locations the turbulence cell size amounts to about 100 pc. According to Poezd et al. (1993), potential driving mechanisms of turbulence in the halo of spiral galaxies are galactic fountains (with a typical scale of 0.3 to 1 kpc), Parker instabilities (about 1 kpc scale), and supernova explosions with remnants of about 0.3 kpc size (McKee and Ostriker, 1977). The authors adopt a turbulence cell size a factor of 5 larger in the halo, compared to the one in the disk. The turbulence cell size in M51 calculated via Equation 6.1.15 is by a factor of 6.7 greater in the halo compared to the turbulence cell size in the disk (compare Table 6.2). This large turbulence cell size in the halo could arise from using the same RM dispersion ($\sigma_{\mathrm{RM},D} = 15\,\mathrm{rad\,m^{-2}}$) in the disk and in the halo, as assumed by Shneider et al. (2014a). Their assumptions of the same turbulence cell size and the same RM dispersion in disk and halo are incompatible with observations: According to our study of the RM distribution at different frequencies (in different layers; see Section 5.4.1), the RM dispersion is different in the disk and halo. At L-band (tracing only the polarized emission from the halo) we found $\sigma_{\mathrm{RM},D} \approx 9\,\mathrm{rad\,m^{-2}}$ (this is measured from the standard deviation of the historgram in the considered sector at L-band). This would give a turbulence cell size a factor of 1.4 smaller in the halo (260 pc; a factor of 4.7 greater compared to the disk). This is close to the difference in the size of turbulence scale in the disk and halo discussed in Poezd et al. (1993).

- The assumption of a perfectly symmetric halo field (quadrupole-type) with identical properties of the near and far-side halo in a three-layer system, is hardly realistic because such magnetic field configurations possess a vertical component which however has been neglected (see below). Furthermore, the densities of thermal and CR electrons could be distributed non-symmetric.

Limitations which can not be solved by the presented models are:

- For the three-layer model it is not possible to "lift up" the zero drops by changing any of the free parameters. Even when including turbulent fields, the Sinc function trend of the degree of polarization as a function of wavelength remains (which is not the case when including turbulent fields in the halo of the two-layer system). The reason is that in the model, the regular field in the halo always dominates the trend of the degree of polarization because of the large path length through the halo.

- Another problem of the model is that Shneider et al. (2014a) only considered the degree of polarization as a function of wavelength. One future step would be fitting

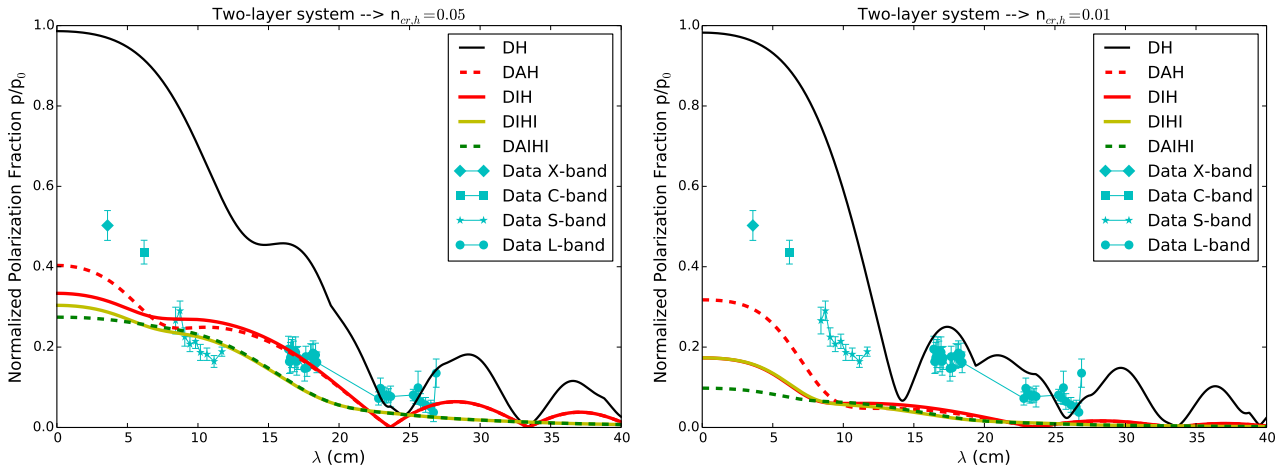

Figure 6.1.11: Influence of different CRE densities in the disk and halo. The left panel shows the considered depolarization models with a CRE density of $n_{\mathrm{CR,h}} = 0.05$ (arbitrary units) and the right panel with a CRE density of $n_{\mathrm{CR,h}} = 0.01$ (arbitrary units) in the halo.

the Shneider et al. (2014a) model to the observed Stokes $Q(\lambda)$ and $U(\lambda)$ values. This is considering not only the amplitude of the polarized signal but also the phase between Stokes Q and U. Furthermore, the rms noise in Stokes Q and U has Gaussian statistics which makes a proper error analysis easier (the rms noise in polarized intensity is not defined and hence we used the average rms noise in Stokes Q and U to estimate the error of PI and thus the error of p).

- In the Shneider et al. (2014a) model vertical regular magnetic fields are completely neglected. For the considered sector this is reasonable since the mean RM amounts to only about $2\,\mathrm{rad\,m^{-2}}$. However, for other sectors this assumption may be invalid. From polarization observations of edge-on galaxies we know that vertical magnetic fields exists in spiral galaxies and also some face-on galaxies show clear evidence of vertical regular field patterns in the RM distribution. Mao et al. (2015) found a signature of an overall vertical magnetic field component in their L-band data (in the halo) of M51 which produces a RM of $\sim -9\,\mathrm{rad\,m^{-2}}$. From dynamo theory we know that each configuration of magnetic fields in spiral galaxies have a non vanishing vertical component. For a quadrupolar magnetic field configuration as it was considered in the discussed depolarization models, vertical magnetic field lines (with respect to the disk plane) are required to fulfill the divergence-free condition (compare Figure 1.2.3 (c) in Section 1.2). In a quadrupolar magnetic field, the negative direction of the vertical field (away from us) must be accompanied by an outward-directed radial field in the disk, which is indeed observed (see Figure 14 in Fletcher et al., 2011). Therefore, neglecting a vertical field component in the models of depolarization is not physical.

6.2 Summary and Future Work

Our comparison of the observed degree of polarization between 1 – 8 GHz with depolarization models of a multi-layer magneto-ionic medium shows that a two-layer system is more likely for M51. This does not mean that the far-side halo does not exist, but instead we are simply not able to detect the polarized emission from the far-side halo probably due to strong depolarization by the turbulent magnetic disk. We demonstrate that the comparison of the observed degree of polarization to the wavelength-dependent depolarization models is a powerful tool to put constraints on the magnetic field strengths and thermal electron density in different regions of the galaxy. In the following, I summarize all results from studying the wavelength-dependent depolarization in M51:

- S-band data (the polarized emission from the disk-halo transition region) are critical to distinguish between a two-layer (disk – halo) and a three-layer (halo – disk – halo) model.
- The data can be fitted well by the two-layer model and thus, the two-layer model more likely describes the magneto-ionic medium of M51.
- For the simplified three-layer system it is not possible to lift up the nulls in the model by changing any parameter. Therefore, this three-layer model can be ruled out. In other words, we do not detect any polarized emission from the far side halo.
- The DAH model can be well fitted to the data with reasonable field strengths. The model can be fitted to neighboring sectors with the same field strengths which is a strong indication that the model is physically meaningful even with the unrealistic assumptions discussed above.
- Because we could only fit the DAH model to the observations in the three sectors with reasonable field strength it looks like the anisotropic field in the disk is essential. This could be a new piece of evidence for the presence of anisotropic random fields.
- We found $B_{\mathrm{tot,d}} \approx 10\,\mu\mathrm{G}$ in the disk and $B_{\mathrm{tot,h}} \approx 3\,\mu\mathrm{G}$ in the (near-side) halo and $b_{\mathrm{tot,d}} \approx 14\,\mu\mathrm{G}$ in the disk. Those magnetic field strengths are well in agreement with the field strengths found by Shneider et al. (2014b).

Performing a least-square fit of the different models to the data will answer the question of which depolarization model fits best to the data in a systematic way. For model fitting, starting values for the free parameters must be chosen carefully. Therefore, using the interactive tool described above to put constraints on the parameter values is an important step for a successful model fit. As a next step, we will apply the same method to other sectors with different azimuthal angles and radii in M51. Further, since the different models distinguish between isotropic and anisotropic turbulent magnetic fields, by comparing the observed degree of polarization in different regions of the galaxy with the model predictions, we can investigate turbulent magnetic field configurations at different locations in M51. The

Shneider et al. (2014a) depolarization model is so far the only one which distinguishes between isotropic and anisotropic turbulent fields. Applying the depolarization models to other nearby face-on spiral galaxies will help us to better understand the magnetic field properties in spiral galaxies in general. A proper separation of the thermal and non-thermal emission of each pixel in the observed total intensity maps can be performed in the future. This method takes spatial variations of the thermal fraction across the galaxy into account and would make sure to compare the models to a more truthful degree of (non-thermal) polarization. This would also help to compare the fractional synchrotron intensity I_i/I calculated by the model with observations of edge-on oriented spiral galaxies to prove whether the model generates meaningful fractions of the synchrotron intensity in the disk and halo.

As discussed in Section 6.1.4, the Shneider et al. (2014a) model includes several simplified assumptions. Assuming a constant (and *equal*) CRE density in the disk and in the halo is difficult to justify. Using different values in the disk and halo, based on e.g. observation of edge-on galaxies, would improve the depolarization models. Also, a careful analysis of the thermal emission in M51 would help to put stronger constraints on locally varying values of the thermal electron density. Another problem which comes with the models is that it completely neglects vertical magnetic fields which is not compatible with dynamo theory. In a future analysis, including vertical fields would help to study possible influences of the vertical magnetic field on the modeled degree of polarization. One can test for example if there is a signature of a quadrupole or a dipole halo field in the equations by e.g. flipping the sign of the vertical component. This would provide an important step towards understanding the symmetry properties of different magnetic field configurations. However, the model already gives a very good approximation for a multi-layer magneto-ionic medium and has strong advantages compared to classical depolarization models: it contains much more – galaxy specific – details and is able to decompose different layers along the line-of-sight, which is especially advantageous in case of the complicated magnetic field configuration in M51 (having different configuration in the disk and halo).

Another possibility to constrain the parameters to describe the multi-layer magnet-ionic medium of a face-on galaxy one can compare the observations with numerical simulations. But to my point of view, analytical approaches (such as the one developed by Shneider et al., 2014a) can highly complement these numerical simulations because using numerical simulations to study the magnetic field in galaxies would be difficult, since the parameters to describe the complicated ISM of a spiral galaxy are almost uncountable.

CHAPTER 7

The Nature of Extragalactic Sources with Unusually High Fractional Polarization

7.1 Introduction

Besides mapping the diffuse polarized synchrotron emission of extended nearby objects as it was done in Chapter 5 and 6 on the nearby spiral galaxy M51, observations of linearly polarized emission from extragalactic radio sources (EGSs) can provide information on the intrinsic magnetic field of active galactic nuclei (AGNs), which are most likely the origin of polarized emission of EGSs. For synchrotron emission with spectral indices between -0.1 and -1.0 ($I \propto \nu^{\alpha_{\mathrm{syn}}}$) the maximum observable fractional linear polarization can reach up to 67 – 75 % for a perfectly ordered magnetic field (compare Equation 2.2.9 in Chapter 2). However, the majority of extragalactic radio sources appear to have low fractional polarization: The distribution of polarized emission in the sky shows a mean value of only $\sim 2\,\%$ fractional polarization (Tucci et al., 2004), based on the National Radio Astronomy Observatory (NRAO) Very large Array (VLA) Sky Survey (NVSS)[1] catalog conducted by Condon et al. (1998) at 1.4 GHz and 45″ resolution. This indicates that most of the polarized radiation from EGSs experience strong depolarization intrinsic to the source (by e.g. tangled magnetic fields) and/or on the way to the observer as well as within the telescope configuration such as the telescope beam and the observing bandwidth.

At the high end of the distribution of the observed fractional polarization of EGSs, there have been studies investigating the origin of the extremely high fractional polarization. Shi et al. (2010) identified 129 unresolved sources in the NVSS catalog with polarization percentage $> 30\,\%$. These ultra highly polarized radio sources have fractional polarizations at 1.4 GHz that far exceeds what is expected from typical radio-loud AGN (7.5 % for FR Is and; 4 – 10 % for FR IIs[2], e.g. Burn, 1966; Gardner and Whiteoak, 1966; Gaensler et al., 2015). While a small region of a radio-loud AGN at high frequencies could reach such a high

[1] http://www.nrao.edu

[2] FR I and FR II stands for Fanaro-Riley Class 1 and 2 (Fanaroff and Riley, 1974).

integrated degree of polarization (e.g. 3C 9 in Kronberg et al., 1996), when integrated over the entire source (at the NVSS resolution of 45″) the polarization level often reduces. These highly polarized EGSs have comparable fractional polarizations at 1.4 GHz to objects with some of the highest fractional polarization ever measured: the "Sausage" radio relic in the galaxy cluster CIZA J2242 with 60 % fractional polarization at 8.35 GHz (Kierdorf et al., 2017); J06587-558, a radio source in the field of a galaxy cluster, is 54 % polarized at 8.8 GHz Liang et al. (2001). Note that the degree of polarization usually decreases with increasing wavelength (by differential Faraday rotation, and internal and external Faraday dispersion, see Section 2.2.2 in Chapter 2). Hence, the extremely high fractional polarizations at 1.4 GHz of these EGSs are exceptional and are worth to investigate and to probe the causes. According to Shi et al. (2010), except for their ultrahigh fractional polarization, the optical spectra, radio luminosity, linear size and spectral index of their sample of 129 sources appear to be typical for radio-loud AGNs. Thus, it has been suggested that their high fractional polarization is likely intrinsic. Therefore, sources with ultrahigh fractional polarization in the NVSS catalog could represent a class of EGSs with intrinsically extremely well ordered magnetic fields.

Not only do polarization properties of individual sources reveal to us their intrinsic magnetic field structures, polarized EGSs are also used background probes to study the magnetic properties in intervening systems such as in the intra-cluster medium of galaxy clusters (e.g. Bonafede et al., 2010; Pizzo et al., 2011), intervening galaxies along the line of sight (e.g. Gaensler et al., 2005; Mao et al., 2008; Feain et al., 2009) and our own Galaxy (e.g. Taylor et al., 2009; Mao et al., 2010; Harvey-Smith et al., 2011; Van Eck et al., 2011). Thus, understanding their polarization and magnetic properties is essential to distinguish the intrinsic and intervening signal.

Strongly polarized radio emission of EGSs is most likely produced by magnetic fields in relativistic jets of powerful AGNs (e.g. Kravchenko et al., 2017). Our knowledge on the detailed structure and strength of the magnetic fields in those distant and compact sources is limited by angular resolution. Studying wavelength-dependent depolarization using broadband polarization data (see Section 2.2.2 in Chapter 2) as well as applying rotation measure (RM)-Synthesis (see Section 3.2 in Chapter 3) can lead to better understand the magneto-ionic medium of those distant and compact objects. Both methods can distinguish multiple components caused by different magnetic field structures and strengths within the beam and/or along the line-of-sight. Thus, studying the linear polarization properties of unresolved EGSs at radio wavelengths provides a new opportunity to probe the magneto-ionic medium on spatial scales below the resolution limit (e.g. Burn, 1966; Gardner and Whiteoak, 1966; Gaensler et al., 2015) and to learn more about the environment and evolution of radio galaxies and AGNs (e.g. Goodlet and Kaiser, 2005; Bernet et al., 2008).

A physical reason for the high degrees of polarization in spatially unresolved EGSs observations at 1.4 GHz are possibly (1) well-ordered intrinsic magnetic fields in the plane of the sky on scales as large as the entire emitting region, thus on kpc scales (to minimize beam depolarization) and (2) environments with low thermal electron density and weak line-of-sight magnetic fields to minimize Faraday depolarization (see Section 2.2.2 in Chapter 2). High

resolution and multifrequency radio polarization observations of a large sample of highly polarized sources are necessary to investigate the reason for their exceptionally high fractional polarization.

We selected 77 sources from the Shi et al. (2010) sample, only choosing sources away from the Galactic plane with latitude $|b| > 10^{\circ}$, to avoid depolarization and Faraday rotation by the Galactic disk (e.g. Oppermann et al., 2012). The selected sources were observed with high angular resolution (up to about $9''$) and broadband receivers using the VLA at L-band (1 – 2 GHz). The sample of Shi et al. (2010) consists of highly polarized, unresolved radio sources (at $45''$ resolution) which lie in regions well isolated from neighboring sources and imaging artifacts. They visually excluded sources in the NVSS which are in fields with strong side-lobes as a result of a nearby strong source, sources which are part of diffuse emission, and sources with a neighboring source within $90''$. In order to confirm the high polarization observed by the NVSS, Shi et al. (2010) observed 11 sources with higher spatial resolution using the VLA and the Australia Telescope Compact Array (ATCA) at 1.4 GHz (using narrow band receivers). Characterizing the polarization properties of ultra highly polarized EGSs from *broadband* observations opens a new window towards understanding the process that generates highly ordered magnetic fields. Our new broadband observations of a sample of 77 highly polarized EGSs provide an excellent dataset to extract information on the in-band total intensity spectral index but importantly to perform RM-Synthesis on the polarization data (Brentjens and de Bruyn, 2005, see also Section 3.2 in Chapter 3) to verify the reported high degrees of polarization in the NVSS and to find out what causes those exceptionally high polarization fractions.

The structure of this chapter is as follows. In Section 7.2 we describe the observations and data reduction procedure. Section 7.3 presents the results of our study, followed by a conclusion with a future outlook in Section 7.4.

7.2 Observation and Data Reduction

The observations were taken with the VLA at L-band (1 – 2 GHz) in continuum mode in full polarization (see Table 7.1 and 7.2). The observations were split into five sessions, i.e. 5 measurement sets (MSs), each covering different sections on the sky to minimize slewing time. The MSs consist of 3 – 26 sources, each observed at L-band containing 16 spectral windows with 64 1-MHz channels. The observations were done using the VLA to reach high spatial and spectral resolution as well as a wide frequency coverage to archive the most suitable data set to study the polarization properties of EGSs by e.g analyzing their Faraday complexity using RM-Synthesis (see Section 3.2 in Chapter 3). Each source was observed in the snapshot mode with an on-source time of $\sim$ 90 seconds. The observations were carried out in C, CnB, and B-array configurations. 3C 48 and 3C 286 were observed as flux density calibrators, while 3C 286 and 3C 138 were used as polarization angle calibrators whose polarization angles are $+33^{\circ}$ and -11° across the effective frequency band of L-band (see Section 7.2.1), respectively (Perley and Butler, 2013b).

Table 7.1: Radio Continuum Observational Parameters of the Ultra-Highly Polarized EGSs.

Frequency (GHz)	1 – 2 (reduced to 1.32-1.93 after flagging)
Bandwidth (MHz)	1000 (reduced to 600 after flagging)
No. of spectral widows	16 (reduced to 8 after flagging)
Total no. of channels	1024
Central Frequency (GHz)	1.63
Array Configuration	C; CnB; B
Observing dates	18 Feb/30 April 2012;
	04/05/21 May 2012; 28 July 2012
Total Flux Density Calibrator	3C 286, 3C 48
Polarization Angle Calibrator	3C 286, 3C 138

Table 7.2: Detailed Observational Parameters of Different Array Configurations.

No. of sources	MS	Config.	t_{int} min	θ arcsec	σ_{th} μJy beam^{-1}
(1)	(2)	(3)	(4)	(5)	(6)
13	1,2	C	1.5/target	$> 24 \times 15$	~ 60
38	3,4	CnB	1.5/target	$> 14 \times 10$	~ 60
26	5	B	1.5/target	$> 5 \times 4$	~ 58

Notes. (1) Number of sources; (2) Name of measurement sets (MSs); (3) Array configuration; (4) Total on source integration time; (5) Resolution in the synthesized images; (6) Theoretical rms noise (Equation 3.1.3 in Chapter 3) for the full bandwidth.

7.2.1 Flagging and Calibration

Calibration and data reduction were done using the NRAO *Common Astronomy Software Applications* (CASA) package (McMullin et al., 2007). Calibration and flagging was performed for each MS separately. After automatic flagging of the beginning and end of each spectral window due to decreasing sensitivity towards the edges and the first 10 seconds of each scan, Hanning smoothing was applied to smooth the side lobes of the Sinc function, resulting from the Fourier transformation of a box function (the visibilities in frequency space are present at separate frequency channels with 1 MHz channel width, causing a box function-like distribution) to make it easier to detect Radio Frequency Interference (RFI). An initial quick bandpass calibration was applied on the flux density calibrators to improve the detection rate of RFIs using the automatic flagging algorithm RFlag. After applying RFlag, the visibilities of each source (calibrators and science targets) in the MSs were carefully inspected for further RFI excisions manually. Due to flagging of RFI, and flagging the beginning and end of each spectral window, the effective frequency band is reduced to 600 MHz (1.32 GHz – 1.93 GHz) in each MS, respectively.

Individual antennas are moved on rails and thus, it is physically impossible to move them on the exact right position (with sufficient accuracy). Because the visibilities u and v are a function of position, to use the right baseline positions is crucial for a good image quality with no artifacts. Therefore, as a first step of calibration, the CASA task `gencal` was used for an a priori antenna position correction. Then, the CASA task `setjy`, using the standard Perley and Butler (2013a) flux density scale, was used to determine the absolute flux density of the total flux density calibrators 3C 48 (MS1, MS5) and 3C 286 (MS2, MS3, MS4) by placing the correct visibilities of the flux density calibrator into the model column of the MS. Whenever it was possible, 3C 286 was used as flux density calibrator, since it is a strong quasar with well-known and stable total flux density scale of 15.0 Jy at 1.465 GHz (Perley and Butler, 2013a). To prevent small atmospheric and instrumental variations of the phase with time, an initial phase calibration was done using the task `gaincal`, averaging over 30 second intervals within the bandpass. For phase calibration, a bright unresolved source near the since target was used. The next step is to solve for antenna-based delays of the signal of each antenna relative to a reference antenna. The reference antenna can be chosen by the user, taking care to use one which is located near the center of the antenna array. For this observations antenna "ea09" was used as reference antenna. To solve for variations with frequency, a bandpass calibration of the total flux density calibrator is needed. The variations are caused by slightly different antenna bandpasses. Bandpass calibration was done for both amplitude and phase for each spectral window of 3C 48 (MS1, MS5) and 3C 286 (MS2, MS3, MS4). Then, `gaincal` was used to calibrate for the complex gain (amplitude and phase) for all calibrators and since targets. Because the flux density scale of the flux density calibrator is known, the task `fluxscale` can then be used to set the right flux density scale to all other sources, comparing the complex gains of each source with those of the flux density calibrator.

Because 3C 286 (MS2, MS3, MS4) and 3C 138 (MS1, MS5) have well-known fractional polarization and polarization angles (Perley and Butler, 2013b), they are suitable for polarization calibration. The initial run of `setjy` only sets the total intensity of the flux density calibrator source. Using the manual mode in `setjy`, the polarized flux density model can be generated using the known polarization angles and fractional polarizations (Perley and Butler, 2013b). Likewise it was necessary to solve for antenna-based delays in total intensity, one needs to solve for the cross-hand delays due to delay differences between right-handed and left-handed circular polarization. This was done using `gaincal` with gaintype KCROSS. In polarization, another important step of calibration is to solve for instrumental polarization. For this purpose an unpolarized calibrator needs to be observed. Leakage polarization calibration was done using the CASA task `polcal`. As a last step of calibration, one needs to set the right polarization position angle into the model column of the calibrators 3C 286 and 3C 138. To do so, the task `polcal` using the parameter poltype='Xf' for position angle (X) and frequency-dependent (f) calibration, was used.

All the tasks and steps described above generate calibration tables. The calibration solutions in those tables must be applied to the raw data column of each source. This was done by CASAs task `applycal`, which writes the calibration results into the corrected data column, which can then be used for further scientific analysis. When applying the calibration

solutions to the data, the solutions which are nearest (in time) to the data visibilities were interpolated. After calibration and flagging was done, the visibilities of the target sources were split from the observed MSs to individual MSs of each target.

7.2.2 Imaging

Images of the targets in Stokes I, Q, and U were created using the `clean` algorithm in CASA. Details on the synthesized imaging procedure are give in Section 3.1.1 in Chapter 3. Primary beam correction was not necessary since each target source is located at the pointing center, where the antenna response is unadulterated. Images in Stokes I, Q and U were created (1) using the entire frequency band to have images with the highest possible signal-to-noise ratio and (2) by averaging over 16 MHz to get enough data points to study the synchrotron spectrum within the observational frequency band and to be able apply RM-Synthesis. To maximize the signal-to-noise ratio of the particularly weak sources, natural weighting were used during imaging. To speed up the imaging process, clean regions were used around all radio sources found in the field of view (FOV) of each target. The images were cleaned down to a threshold of about three times the image noise. The rms image noise was measured in a box free of emission with size of about 20 beams and only a few beams away from the target of interest. We used a cell size of $2''$ for sources observed in C, and CnB-array configuration and $1''$ for sources observed in B-array configuration.

The average rms noise of images using the entire band belongs to about 500 μJy beam^{-1} (a factor of about 10 greater than the theoretical rms noise). Due to strong radio sources off the phase center which lie within the primary beam, about 50 % (39 out of 77) of the total intensity images are strongly affected by artifacts. One example is shown in the left panel of Figure 7.2.1. The science target in the image center is located on top of a stripe-like artifact, caused by the strong source in the north-east of the field. Stripe-like artifacts which proceed parallel to each other through the entire image, not particularly resulting from a strong radio source in the field can be seen in about 20 % of the images (15 out of the 77 observations). One example of such *interference*-artifacts (Ekers, 1999) is shown in the right panel of Figure 7.2.1. They result from interfering signals within the oberving band. Because of the short observation time and the resulting poor *uv*-coverage, it is not possible to eliminate those artifacts. Self-calibration, where the model image of the target is used as a new model for calibration, was tested but did not improve the results – most likely because the sources are not strong enough. Within the 77 observed targets, 11 sources were not detected in Stokes I within our detection limits due to large artifacts caused by strong point sources in the FOV. The rms noise in those images amounts to 1 – 2 mJy beam^{-1}, a factor of 20 – 30 greater than the theoretical rms noise and a factor 2 – 4 larger than the average rms noise in the Stokes I images of all other targest obtained by using the entire frequency band. This reduces our sample to 66 sources.

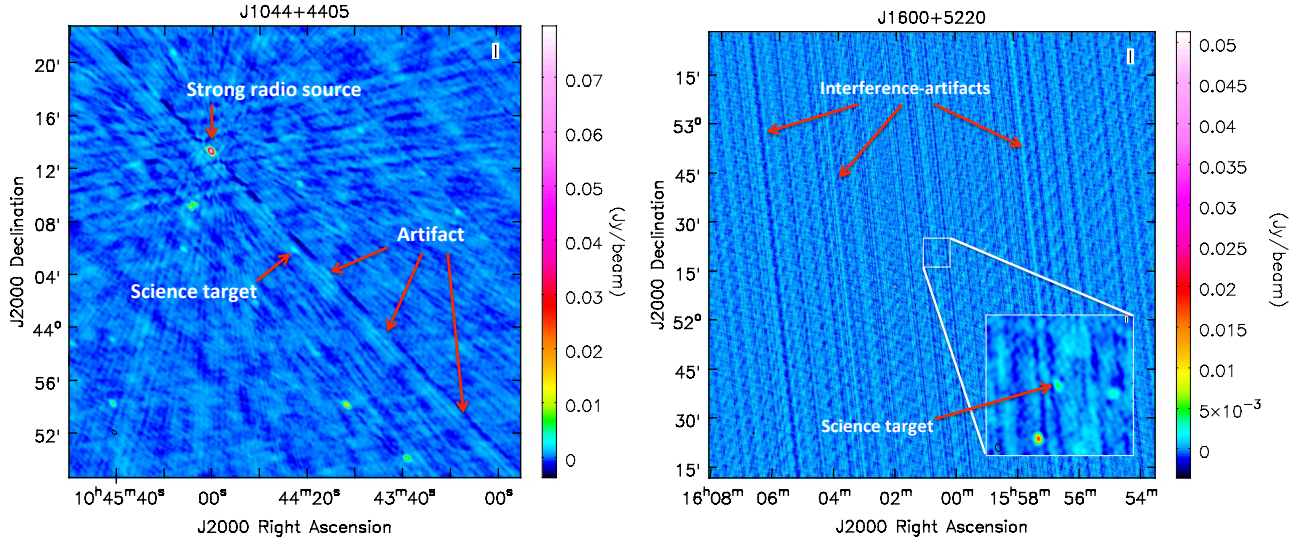

Figure 7.2.1: Total intensity images of two targets and their surrounding field. The left panel shows an example of artifacts caused by a strong point source in the field. The right panel shows an example of artifacts referred as *interference* with repeating diagonal stripes across the entire image, not resulting from a strong point sources.

7.2.3 Flux Density Measurements

One difficulty of this project was to find the optimal way of measuring the flux density of the particularly weak sources. For unresolved sources at the NVSS beam of $45'' \times 45''$, the NVSS flux densities were obtained by fitting elliptical Gaussians to the point sources, using the resulting peak value (Condon et al., 1998). A radio source is unresolved or "point-like" when the integrated flux density is equal to the peak flux density. For our sample, 55 out of 66 detections (about 80 %) have $0.6 < I/I_{\rm max} < 1.4$, while the average error is about 0.7 mJy. Hence, the majority of the sources within this project are unresolved in our observations. The rest of the sources are partly resolved with slightly larger angular scale than one beam but not as resolved that one can recognize different components. Because of the poor *uv*-coverage in our observations, most images are affected by artifacts which makes a Gaussian fit to obtain the flux densities inappropriate (see Figure 7.2.1). Also the low signal-to-noise ratio of the targets in Stokes I prevent us from fitting elliptical Gaussians to measure the flux densities. To obtain the integrated flux densities in Stokes I, the flux densities were integrated within the contour of 3 times the rms noise in Stokes I (σ_I). σ_I was measured by taking the average rms of 4 boxes free of emission near the target source in the total intensity images. The flux densities in Stokes Q and U were obtained within the same integration area as the total intensity. The disadvantage of this method is that the flux density in Stokes Q and U can include positive and negative pixels. Hence, integration gives a lower limit of the true polarized flux density.

7.3 Results

Out of the 66 detections, only 30 sources have signal-to-noise ratio (SNR) greater than 10 in Stokes I across L-band. Sources with lower SNR (< 10) were excluded for further analysis. Only 12 of the sources with high SNR in Stokes I have SNR greater than 6 in polarized intensity (only 4 with SNR greater than 10 in PI - see Section 7.3.2). According to the study of George et al. (2012), a SNR of 6 in polarized intensity is necessary for a sufficiently low false detection rate of peaks in the Faraday spectrum. Some of our sample of high SNR sources suffer from little artifacts (in all Stokes images) described in the previous section (Section 7.2.2) and some are simply strong enough to reach a signal to noise > 10 in Stokes I. The properties of the resulting final sample of 12 sources are summarized in Table 7.3. In Figure 7.3.9 images of the final sample sources are shown.

For the 12 sources we found 5 matches with the optical Sloan Digital Sky Survey (SDSS). The redshift of those sources ranging from 0.04 up to a redshift of 0.7. Using the angular diameter distance formula we computed spatial scales of our resolution elements of about 10 kpc up to about 100 kpc, assuming a cosmology of $H_0 = 69\,\mathrm{km^{-1}\,s^{-1}\,Mpc}$, $\Omega_\mathrm{M} = 0.3$ and $\Omega_\lambda = 0.7$.

7.3.1 Total Intensity and Spectral Index

We reached angular resolutions from around 50″ (for D-configuration observations) up to 9″ (for B-configuration observations) in the total intensity maps. About 80 % of the targets are spatially unresolved. As discussed in Section 7.2.3, we measured the integrated flux densities in total intensity (Stokes I) by integrating within the contour level of 3 times the rms noise in Stokes I (σ_I). The flux density error given by the image noise is calculated via $\Delta I = \sigma_I \cdot \sqrt{N_\mathrm{beams}}$, where N_beams is the number of beams within the integration area.

To measure the in-band spectral index α_tot ($I \propto \nu^{\alpha_\mathrm{tot}}$) we made images for each target, averaging over 16 MHz within the effective frequency band (after flagging). This results in about 30 flux density measurements across the effective frequency band for each target. A power law fit to the data points gives α_tot and the corresponding uncertainty while the fit is weighted by the error of each data point (given by the image rms noise). Figure 7.3.1 shows the in-band total intensity spectrum of the source J0302+1537 as an example. Our analysis shows that the error in spectral index from power-law fit decreases with an increasing number of data points across the band (even if each data point has a larger error). Therefore, using 16 MHz averaged images gives the most precise spectral indices with the smallest errors. In regular circumstances the best-fit error should not change when changing the number of data points within a given frequency interval. However, we assume that some subtle imaging procedures could be the reason for getting a smaller error when averaging in 16 MHz chunks. The distribution of the in-band spectral indices of our sample of 12 sources is shown in Figure 7.3.3. The mean spectral index of our sample is $\overline{\alpha}_\mathrm{tot} = -0.79$ with a standard deviation of 0.83. Since the SNR of the sources in the 16 MHz images is low, which causes large errors in

Table 7.3: Results of the Final Sample of 12 Sources with signal-to-noise ratio > 10 in Stokes I and ≥ 6 in PI.

Source	$I \pm \Delta I$ (mJy)	rms_I (mJy b^{-1})	$I_{\max}$ (mJy b^{-1})	PI (mJy)	rms_{QU} (mJy b^{-1})	$p \pm \Delta p$ (%)	$\phi \pm \Delta\phi$ (rad m^{-2})	$\alpha_{\mathrm{tot}} \pm \Delta\alpha_{\mathrm{tot}}$	SN_{PI}	SN_I	Beam ($''$)
(1)	(2)	(3)	(4)	(5)	(6)	(7)	(8)	(9)	(10)	(11)	(12)
J0108+2808	4.20 ± 0.62	0.40	4.18	2.11	0.35	50.3 ± 11.2	-44 ± 10	0.67 ± 0.73	6.0	10.5	10×9
J0302+1537	14.20 ± 0.82	0.44	11.70	5.31	0.35	37.4 ± 3.3	-14 ± 4	-0.88 ± 0.29	15.2	26.6	22×18
J0642+4522	13.64 ± 0.78	0.46	12.59	5.23	0.59	38.4 ± 4.8	$+18 \pm 7$	-1.05 ± 0.38	8.9	27.4	12×9
J0742+6057	10.42 ± 1.03	0.69	9.27	3.97	0.51	38.0 ± 6.2	-14 ± 8	-0.52 ± 0.46	7.8	13.4	12×9
J0851−1424	14.12 ± 1.42	0.80	10.50	3.57	0.37	25.3 ± 3.7	$+18 \pm 6$	-1.90 ± 0.29	9.6	13.1	44×23
J1107+2601	5.97 ± 0.53	0.37	6.06	1.63	0.20	27.3 ± 4.1	$+2 \pm 7$	-0.25 ± 0.44	8.2	16.4	21×18
J1111+2711	8.90 ± 0.48	0.26	7.82	4.28	0.31	48.1 ± 4.3	-4 ± 4	-0.21 ± 0.27	13.8	30.1	22×18
J1223+2104	5.80 ± 0.58	0.37	5.23	2.43	0.18	42.0 ± 5.2	-8 ± 5	-0.14 ± 0.33	13.5	14.1	25×18
J1340+4255	7.76 ± 0.83	0.51	7.24	2.31	0.16	29.7 ± 3.8	$+8 \pm 4$	-1.45 ± 0.28	14.4	14.2	28×16
J1419+3407	9.32 ± 0.70	0.41	8.75	3.38	0.23	36.3 ± 3.7	$+10 \pm 4$	-1.27 ± 0.44	14.7	21.3	37×17
J1723+7829	10.79 ± 1.00	0.62	10.55	2.19	0.29	20.3 ± 3.3	-52 ± 8	-2.39 ± 0.48	7.5	17.0	28×16
J2022−2915	10.28 ± 0.62	0.36	9.36	2.68	0.38	26.1 ± 4.0	-34 ± 8	-0.12 ± 0.61	7.0	26.0	52×15

Notes. (1) NVSS source name; (2) Integrated total flux density; (3) rms noise in total intensity; (4) Peak total intensity; (5) Total linear polarization obtained by RM-Synthesis; (6) rms noise in Stokes Q and U; (7) Percentage polarization; (8) Faraday depth; (9) In-band total intensity spectral index; (10) signal-to-noise ratio in polarized intensity; (11) signal-to-noise ratio in total intensity; (12) Beam size in arcsec.

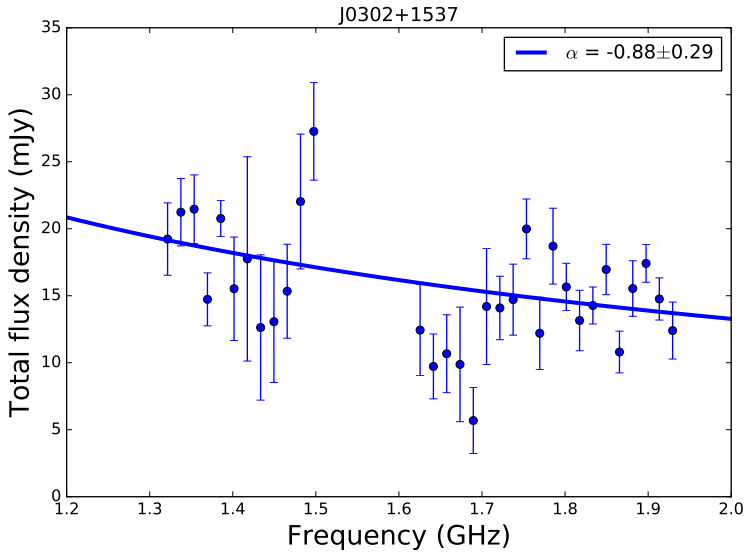

Figure 7.3.1: Total intensity spectrum of the source J0302+1537. The solid line represents the power-law fit to obtain the spectral index α_{tot}.

α_{tot}, the distribution of our in-band spectral indices should be taken with caution (compare Table 7.3). Our sample has a very broad distribution of synchrotron spectral indices with steep, flat and inverted spectra. The same holds if we include all sources from our sample, i.e. those with low SNR in Stokes I. Due to the broad distribution and the large errors of the spectral indices, we cannot draw *any* conclusion.

We note that some of our targets have matches in the Faint Images of the Radio Sky at Twenty-Centimeters (FIRST) catalog at 1.4 GHz and 5″ resolution, but FIRST data lack polarization information. 5 sources from our high SNR sample were measured in FIRST. Figure 7.3.2 shows the direct comparison of the peak and integrated Stokes I flux density of those sources from our new broadband observations and the values reported in the FIRST catalog. There is a systematic shift of data points below the 1:1 line. Thus, the flux densities of the FIRST measurements seems to be underestimated which could result from missing fluxes of the slightly resolved sources in FIRST: The FIRST data were obtained in VLA's B-array configuration. At 1.4 GHz, the largest detectable angular scale in B-configuration (for snapshot observations) amounts to about 60″. For emission structures larger than the detectable angular scale, the VLA cannot detect emission – the flux density is simply missed also referred to as "resolved out".

7.3.2 Polarized Flux Densities

The polarized flux densities (in Stokes Q and U) were obtained within the same integration area as the total intensity (see Section 7.2.3). To obtain the polarized intensity PI and the Faraday depth ϕ for each source, we performed RM-Synthesis on the polarization data ob-

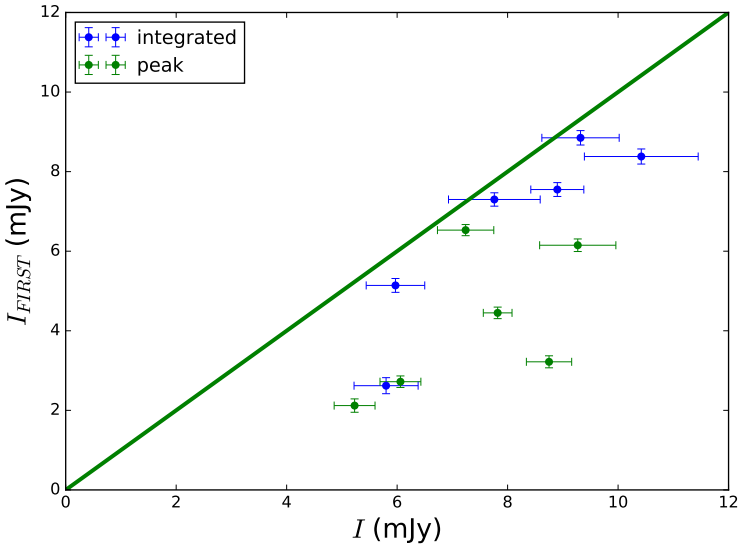

Figure 7.3.2: Comparison of the peak and integrated total intensity I from our new wide-band observations to the values reported in the FIRST catalog. The green solid line represents the 1:1 line.

tained from flux density integration. RM-Synthesis was performed using the python-based code developed by Michael Bell[3], based on RM-Synthesis techniques of Brentjens and de Bruyn (2005). RM-clean, a technique to deconvolve polarized flux density from clean models, similar to the CLEAN algorithm used in interferometric imaging (e.g. Heald et al., 2009) is included in this package and was applied to the data as well. We performed RM-Synthesis on all sources but in our analysis we only discuss those with a SNR greater than 6 in polarized intensity. The Faraday spectra of our selected sample of 12 sources are shown in the right panels of Figure 7.3.9. The polarized flux density PI is given by the amplitude and the Faraday depth ϕ by the position of the highest peak. The parameters used during the application of RM-Synthesis and the limitations given by our L-band observations are summarized in Table 7.4. The error in Faraday depth can be obtained by $\sigma_\phi = 0.5\,\delta\phi/(\mathrm{S/N}_{PI})$ where $\mathrm{S/N}_{PI}$ is the SNR in polarized intensity and $\delta\phi$ is the resolution in Faraday depth (e.g., Iacobelli et al., 2013). The error in PI is given by the rms of Stokes Q and U in Faraday depth spectra, obtained from all data 3× the full width half maximum (FWHM) away from the highest peak (shown as a green line in the Faraday spectra in Figure 7.3.9).

The fractional polarization p is the ratio of the linear polarization PI and the total intensity I. Since the polarized intensity is a positive-definite quantity, the noise in Stokes Q and U (assumed to be Gaussian) results in a positive value for PI even if no signal is present. Therefore, the distribution of the polarized intensity is given by a Rician distribution and thus needs to be corrected for polarization bias. For sources with very high SNR in PI (as it was the case for our M51 observations, see Chapter 5), no polarization bias correction is needed. For this project, the polarized intensities are corrected for polarization bias by

[3] http://www.github.com/mrbell/pyrmsynth

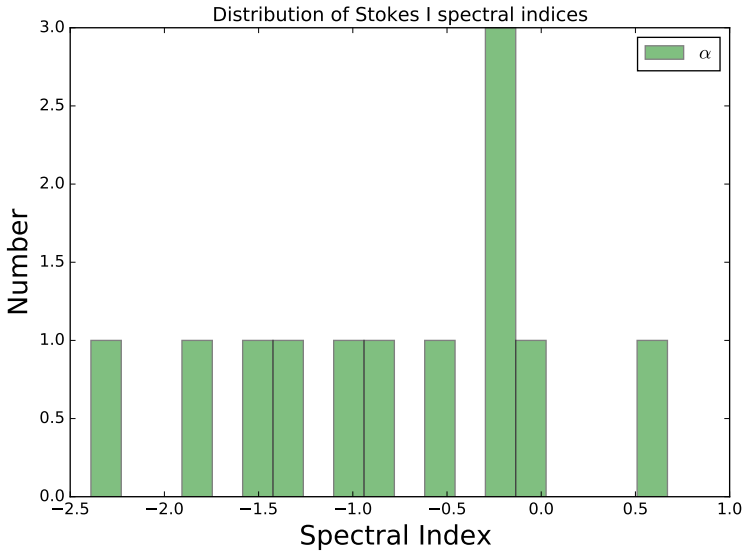

Figure 7.3.3: Distribution of the total intensity spectral index of the sample of 12 sources with SNR $>$ 10 in Stokes I and $\geq$ 6 in PI. The mean spectral index is $\overline{\alpha}_{\rm tot} = -0.79$ with a standard deviation of 0.83. Since the SNR of the sources in the 16 MHz images is low, which causes large errors in $\alpha_{\rm tot}$, the distribution of our in-band spectral indices should be taken with caution (compare Table 7.3).

$PI_{\rm corr} = \sqrt{PI^2 - 2.3\sigma_{QU}^2}$ where σ_{QU} is the rms noise of Stokes Q and U and PI the peak polarized intensity in the Faraday depth spectrum (George et al., 2012). The results of 12 sources from our sample are shown in Table 7.3. The distribution of the degree of polarization is shown in Figure 7.3.4 with fractional polarizations between 20 – 50 % with a mean of 34.9 % and a standard deviation of 9.0 %.

The distribution of Faraday depths obtained by performing RM-Synthesis on the sources is shown in Figure 7.3.5. For all sources except J0302+1537 and J0642+4522 these are the first measurements of Faraday depth since they are not included in the NVSS RM catalog (Taylor et al., 2009) due to low SNR ($<$ 8) in polarized intensity in NVSS. J0302+1537 and J0642+4522 are included in the NVSS RM catalog with Faraday depth of $-4.2 \pm 12.5\,\mathrm{rad\,m^{-2}}$ and $+36.1 \pm 11.7\,\mathrm{rad\,m^{-2}}$, respectively. Within the error bars only the Faraday depth of J0302+1537 from NVSS RM catalog agrees with the Faraday depth obtained from our broadband analysis[4]. In the histogram only sources with SNR $\geq$ 6 in polarized intensity from RM-Synthesis are displayed (compare right panels in Figure 7.3.9). The Faraday depth distribution is broad as evident in the histogram between about -50 and $+20\,\mathrm{rad\,m^{-2}}$ with a mean of $-9.5\,\mathrm{rad\,m^{-2}}$ and a standard deviation of $22.4\,\mathrm{rad\,m^{-2}}$.

Every Faraday spectrum from our sample of 12 sources only has one single component

[4]To check whether the values are in agreement within the error bars, the following criterion must be fulfilled: $\frac{|m_1 - m_2|}{\sqrt{\Delta m_1^2 + \Delta m_2^2}} < 1$, where m_1 and m_2 are the values of measurement 1 and 2 and Δm_1 and Δm_1 are the corresponding error bars.

Table 7.4: RM-Synthesis Parameters and Specifications at L-band.

Parameter	Value (Unit)	Explanation
ϕ_{min}	-2000 (rad m^{-2})	Minimum Faraday depth
N_ϕ	2000 (rad m^{-2})	Number of steps
$d\phi$	2 (rad m^{-2})	Step size
cutoff	$6\,\sigma_{\mathrm{QU}}$ (Jy)	RM-Clean cutoff
λ^2_{min}	0.0242 (m^2)	Minimum wavelength
$\delta\lambda^2$	0.0039 (m^2)	Channel width
$\Delta\lambda^2$	0.0275 (m^2)	Wavelength-coverage
$\delta\phi$	126 (rad m^{-2})	Resolution in ϕ-space
$\|\|\phi_{\mathrm{max}}\|\|$	1400 (rad m^{-2})	Maximum detectable ϕ
max-scale	130 (rad m^{-2})	Maximum detectable scale

(with a resolution in Faraday depth of 126 rad m^{-2}, see Table 7.4). The Faraday depth is therefore likely produced by a simple Faraday screen (with a regular magnetic field) in front of the synchrotron emitting medium (Burn, 1966). This means the sources experience little Faraday depolarization which is in agreement with the detected high fractional polarization. Furthermore, the mainly low Faraday depths, with a mean of only -9.5 rad m^{-2}, are probably caused by a low line-of-sight magnetic field component which is again in agreement with a strong perpendicular component and therefore with the high degree of polarization.

Besides investigating the distribution of p, α_{tot}, and ϕ, we examined possible correlations between these variables. We could not identify any correlation between fractional polarization and Faraday depth (left panel of Figure 7.3.6). However, between fractional polarization and spectral index (see right panel of Figure 7.3.6) there seems to be a (possibly linear) correlation with a correlation coefficient of 0.7 (the degree of polarization increases with increasing spectral index). One interpretation could be radio jets in AGNs being responsible for the polarized emission of EGSs: The jet should be collimated (the magnetic field more ordered) near the core where in turn particles get freshly accelerated (e.g Romero et al., 2017) which means they emit synchrotron emission with a flat spectral index. In other words, the radio emission of EGSs with flat spectral indices originates from the region near the central core of the AGN whereas the spectral index gets steeper along the jet (Hovatta et al., 2014) and in turn the magnetic field of the jet is more highly collimated (more ordered) near the core and thus the degree of polarization of EGSs with emission from the core region (with flat spectral indices) should be higher. Certainly, this result should be taken with caution because we only consider a sample of 12 sources where both the fractional polarization and spectral indices suffer from large errors. In Section 7.4 we discuss how new observations can examine this correlation.

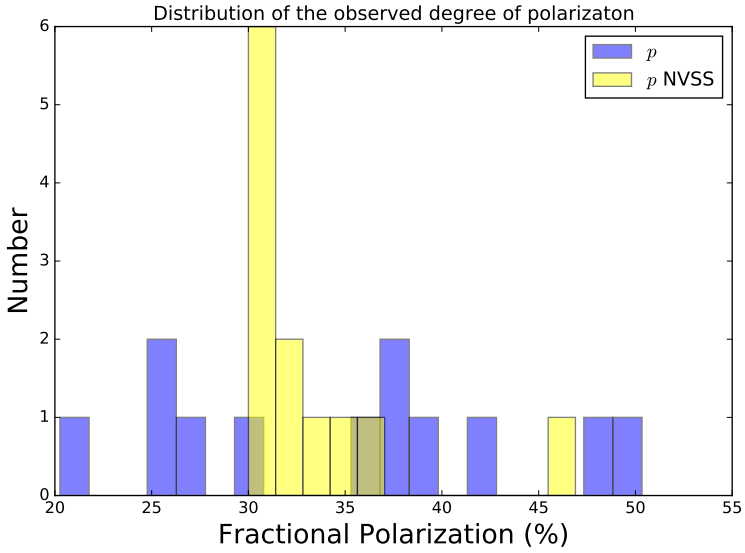

Figure 7.3.4: Distributions of the observed degree of polarization of the sample of 12 sources with SNR in our broadband observations > 10 in Stokes I and ≥ 6 in PI. The blue color shows the broadband results while the yellow color shows the histogram of the values reported in the NVSS catalog. The mean polarization fraction of our broadband high SNR sample is $\overline{p} = 34.9\,\%$ with a standard deviation of $9.0\,\%$ while the NVSS distribution shows a mean of $33.2\,\%$ and a standard deviation of $4.6\,\%$.

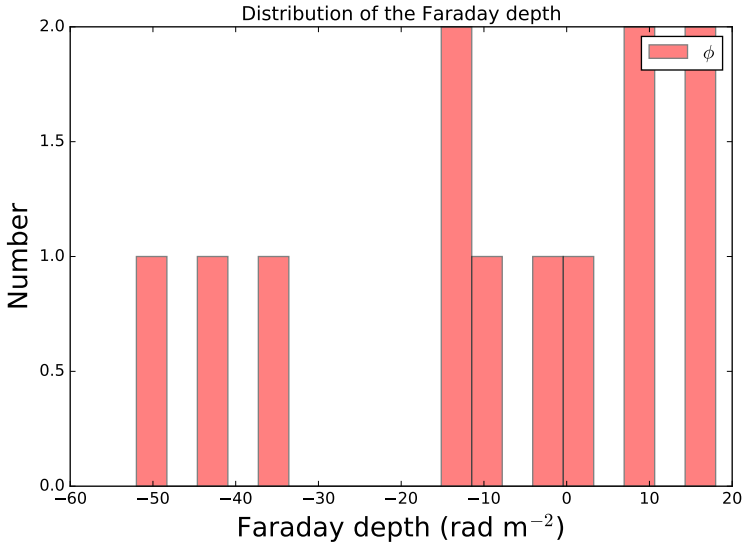

Figure 7.3.5: Distribution of the Faraday depth obtained by RM-Synthesis of the sample of 12 sources with SNR > 10 in Stokes I and ≥ 6 in PI. The mean Faraday depth is $\overline{\phi} = -9.5\,\mathrm{rad\,m^{-2}}$ with a standard deviation of $22.4\,\mathrm{rad\,m^{-2}}$.

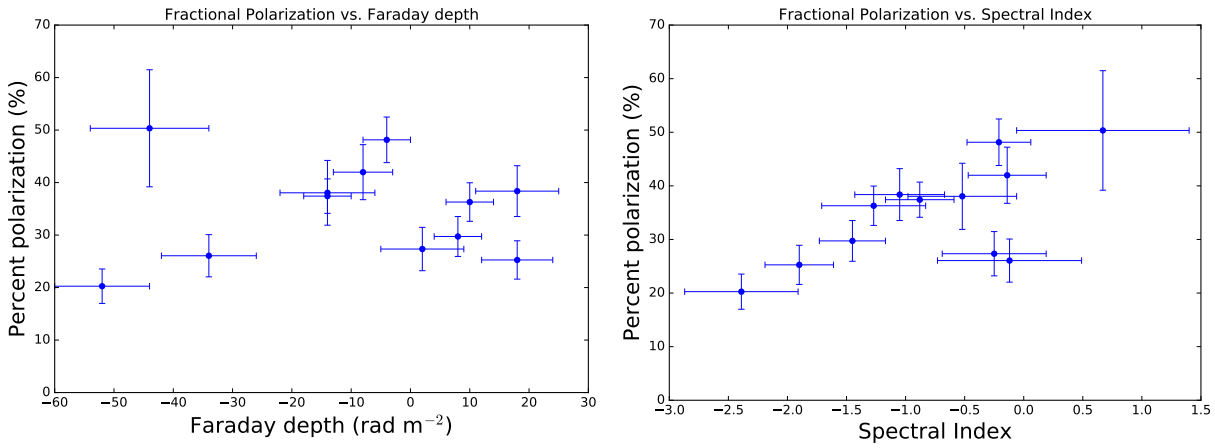

Figure 7.3.6: Observed degree of polarization versus the Faraday depth (left) and the in-band spectral index (right).

7.3.3 Comparison with the results from Shi et al. (2010)

In order to confirm the high polarization observed by the NVSS, Shi et al. (2010) observed 11 sources with higher spatial resolution using the VLA and the Australia Telescope Compact Array (ATCA) at 1.4 GHz (using narrow band receivers). Shi et al. (2010) confirm with their observations that the high linear polarizations measured by the NVSS are reliable but their observations show that the fractional polarizations do not agree exactly with those listed in the NVSS, ranging from 8 to 50 % (see their Figure 8). Three sources of our sample of high SNR sources coincide with their sample of high resolution observations (J0302+1537, J0642+4522, and J0742+6057). For those candidates, the fractional polarizations of the observations of Shi et al. (2010)[5] only agree for the source J0302+1537 within the error bars with our values (compare Table 7.3).

7.3.4 Comparison with the NVSS

About half of our sample sources show lower polarization fractions than those published in the NVSS catalog (Condon et al., 1998): 5 out of 12 sources in our sample show fractional polarizations $< 30\,\%$ which was our target selection criterion from NVSS. In Figure 7.3.7 we plot the values of the total and polarized intensity and the degree of polarization of our new measurements and the NVSS values for direct comparison. The NVSS values are reported in Table 7.5. From the direct comparison of the high SNR sources with the values reported in the NVSS catalog, 5 out of 12 sources agree within the error bars in Stokes I. For polarized intensity, 9 out of 12 sources have consistent values within their error bars, while in fractional polarization 7 sources have agreeing NVSS and new measurement values. We found the same number of sources with values of Stokes I, PI, and p above and below the

[5] J0302+1537: $p = 40 \pm 7\,\%$, J0642+4522: $p = 31 \pm 4\,\%$, and J0742+6057: $p = 49 \pm 8\,\%$.

Table 7.5: NVSS Values of Sources from our Final Sample with signal-to-noise ratio > 10 in Stokes I and ≥ 6 in PI in our New Measurements.

Source	$I_{\mathrm{NVSS}} \pm \Delta I_{\mathrm{NVSS}}$ (mJy)	$PI_{\mathrm{NVSS}} \pm \Delta PI_{\mathrm{NVSS}}$ (mJy)	$p_{\mathrm{NVSS}} \pm \Delta p_{\mathrm{NVSS}}$ (%)	θ (′)
(1)	(2)	(3)	(4)	(5)
J0108+2808	9.2 ± 0.5	2.8 ± 0.6	30.4 ± 6.7	13.23
J0302+1537	13.5 ± 0.6	4.2 ± 0.4	31.1 ± 3.3	12.25
J0642+4522	16.4 ± 0.6	5.1 ± 0.5	31.1 ± 3.3	12.08
J0742+6057	12.1 ± 0.6	3.7 ± 0.5	30.6 ± 4.4	10.81
J0851-1424	11.4 ± 0.6	4.0 ± 0.7	35.1 ± 6.4	1.02
J1107+2601	5.2 ± 0.4	1.9 ± 0.4	36.5 ± 8.2	10.04
J1111+2711	9.2 ± 0.5	2.8 ± 0.6	30.4 ± 6.7	11.73
J1223+2104	4.9 ± 0.5	2.3 ± 0.5	46.9 ± 11.3	12.49
J1340+4255	7.0 ± 0.4	2.1 ± 0.4	30.0 ± 6.0	8.50
J1419+3407	9.2 ± 0.5	2.9 ± 0.6	31.5 ± 6.7	5.18
J1723+7829	10.0 ± 0.6	3.2 ± 0.5	32.0 ± 5.4	7.73
J2022-2915	9.4 ± 0.6	3.1 ± 0.6	33.0 ± 6.7	9.85

Notes. (1) NVSS source name; (2) Total NVSS flux density; (3) Total NVSS linear polarization; (4) NVSS fractional polarization; (5) Distance from pointing center in arcmin.

1:1 line. Therefore, a systematic that shifts the data points in just one direction can be ruled out for the observed discrepancy. However, note that the measurements of our total and polarized flux densities are performed differently in the NVSS in the following ways: (1) The total intensity flux densities of our observations are measured within the $3\,\sigma_I$ contour (see Section 7.2.3) while the flux densities reported in the NVSS catalog are the peak values from elliptical Gaussian fits. (2) The bandwidth of our observation is significantly larger (about 600 MHz compared to only 42 MHz for the NVSS observations). For our broadband images we did not apply multi-frequency synthesis, where the spectral dependency of the sky's flux density across the band is fitted by a polynomial Taylor expansion. To test whether this method influences the total intensity significantly, we applied this method to one source of our sample (source J1107+2601). The result shows that the flux density does not change significantly, only the rms noise decreases by a factor of 1.5. However, as a future work we will apply the multi-frequency algorithm to all Stokes I and also to Stokes Q and U data. (3) NVSS images have slightly larger beam sizes (45″ compared to the beam sizes reported in Table 7.3 between about $10'' - 50''$). Therefore, confusion within the slightly larger NVSS beam could be responsible for the discrepancy in total intensity. However, this effect would systematically shift the NVSS flux densities to larger values but the comparison shows that the data differ in both directions.

In the comparison of the new broadband measurements with the values reported in the NVSS described above, different strategies of imaging and flux density measurements could cause the disagreement of both data sets. To compare "apples with apples", we downloaded the Stokes I, Q, and U postage stamps of the 12 high SNR sources in our sample. For the

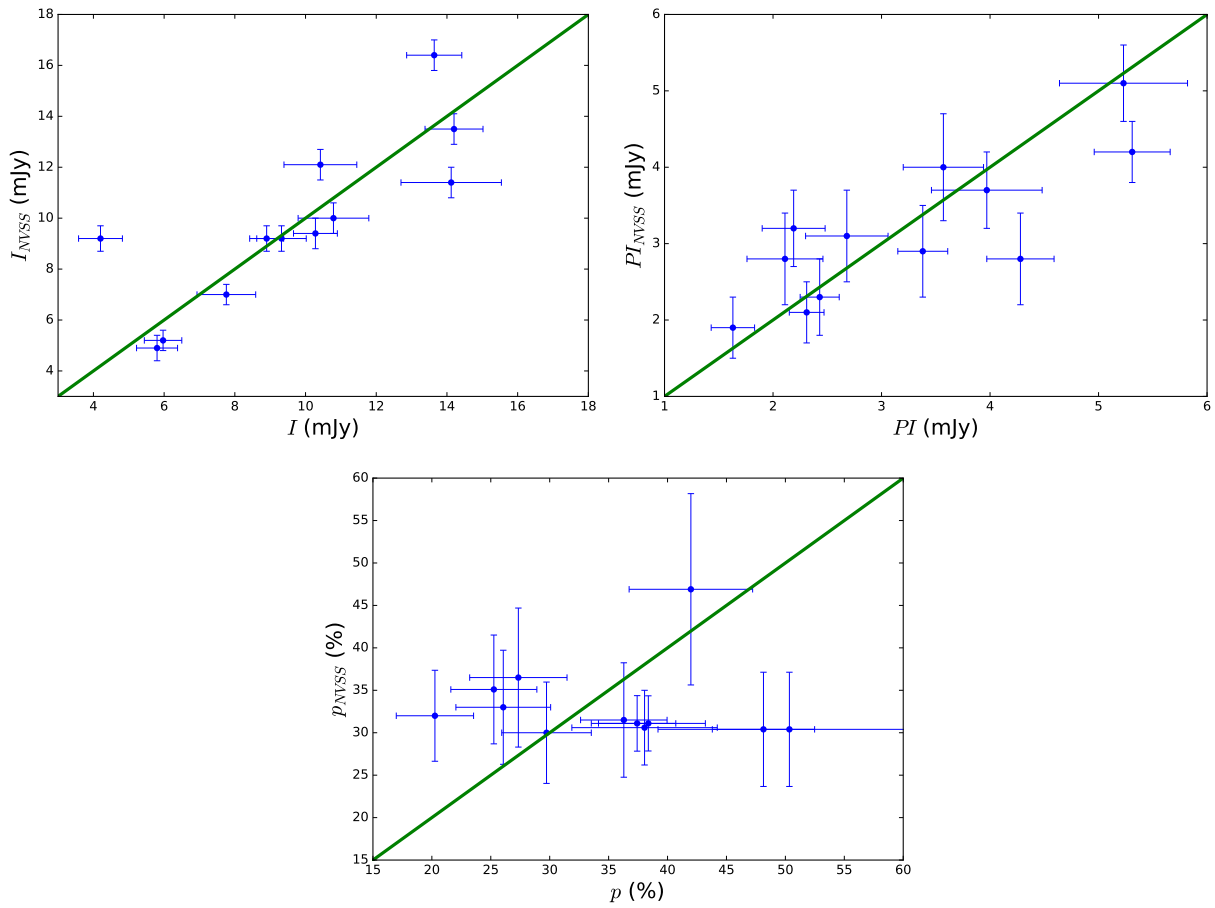

Figure 7.3.7: Comparison of the total intensity I (top left), linearly polarized intensity PI (top right), and degree of polarization p (bottom) from our new wideband observations to the values reported in the NVSS catalog. The green solid line represents the 1:1 line.

same sources we produced images using only the *uv*-data of our new observations within the narrow NVSS bands of 42 MHz. The flux density in both data sets were measured using the peak pixel value in Stokes I and the pixel value of Stokes Q and U at the same position. Note that we did *not* smooth our images to the 45″ beam of the NVSS postage stamps because the image quality (rms noise) of our data using the narrow NVSS band is extremely bad and smoothing would decrease the image quality (increases the rms noise) even further. This might affect the comparison in the sense that the NVSS data points show a systematic shift towards larger values.

A direct comparison of these samples show that 5 out of 12 of the polarized intensity values are larger and 6 out of 12 are equal within the error bars in the NVSS postage stamps compared to the new VLA data. Only one source has a higher polarized intensity in our new narrow band images. The smaller beam size of our new measurements should result in the opposite effect: due to beam depolarization the NVSS images should give smaller polarized flux densities. For the Stokes Q and U values 12 out of 24 data points agree within the error

bars while about equal number of sources appear above and below the 1:1 line. However, the polarization fractions from the NVSS postage stamps are systematically larger: 8 sources have larger polarization fraction, 5 sources agree (within the error bars) and one source has lower polarization fraction in the NVSS postage stamps compared to our new observations).

Assuming no other systematic effects in either set of the observations, there can be a physical reasons for a lower/higher fractional polarization in our new observations namely source variability for both higher and lower total intensity and polarization. Note that there is no systematic change of the flux densities in terms of changes in the same/opposite direction in both Stokes I and PI. The data of the NVSS were observed in the late 1990s, about 15 years before we observed them again. Because we only selected sources by their fractional polarization measured 15 years ago in the NVSS epoch, the sample could contain some sources in a phase of lower/higher polarization during our new observations. The amplitude of variability (the discrepancy in the flux densities) in Stokes I ranges from a factor of about 1.4 less flux density up to a factor of about 2.5 higher flux density in the new observations. In polarized intensity the discrepancy is always similar by an average factor of about 1.2 higher values in the old observations. Since the epochs of observation is separated by 15 years, this amount of variability is easy to achieve: Based on long-term observations of about 70 (radio-loud) AGNs over 30 years by e.g. Peterson (2001) and Hovatta et al. (2008), variability of both total intensity and polarization is a common characteristic of AGNs and occurs with multiple timescales and appear to be aperiodic and have variable amplitude.

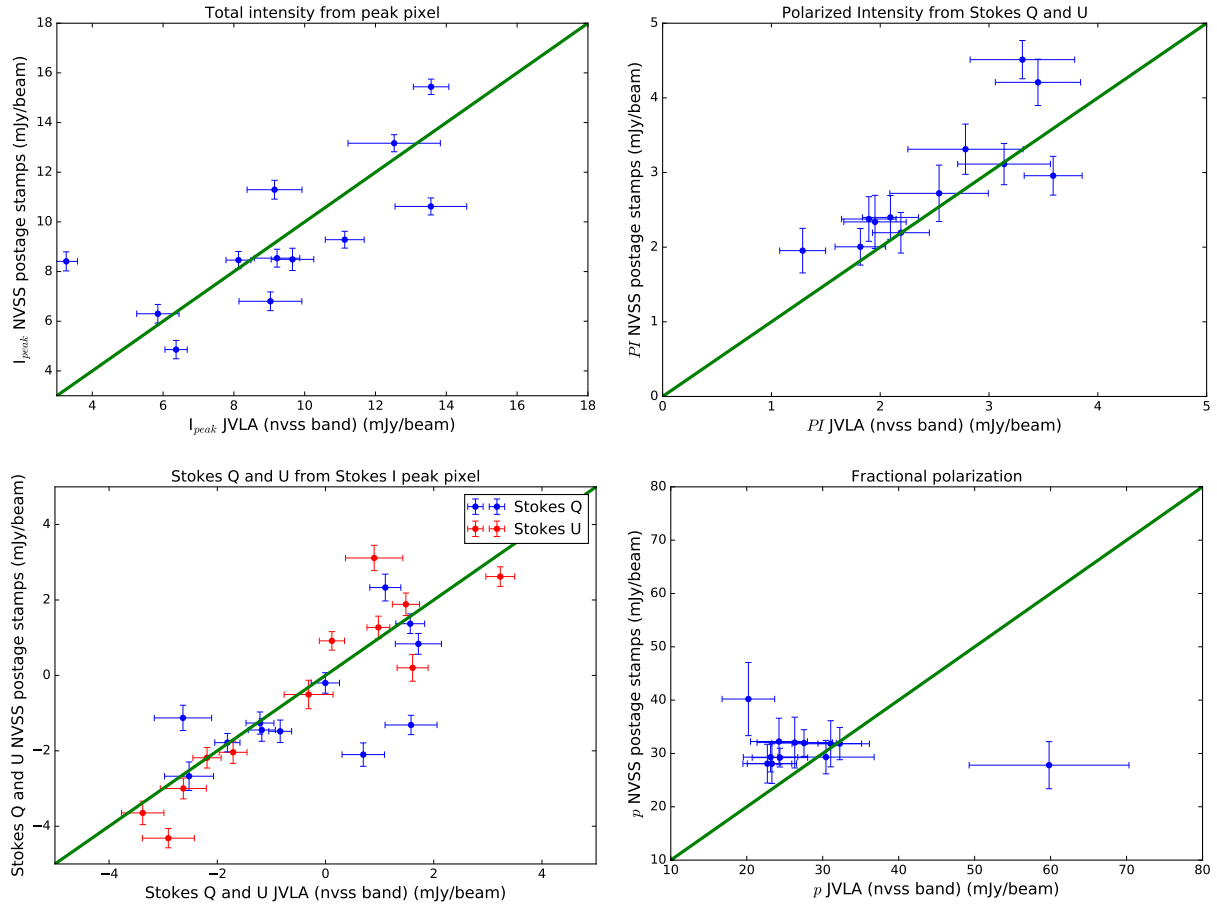

Figure 7.3.8: Comparison of the total intensity (top left), linearly polarized intensity (top right), Stokes Q and U (bottom left), and the degree of polarization (bottom right) measured from images created using uv-data from our new observations only in the NVSS frequency (narrow) band to the values from NVSS postage stamps images. All flux densities are measured using the same method described in the main text. The green line represents the 1:1 line. Shown are only 12 sources from our sample with high SNR in Stokes I and PI. Note that the images have different resolutions (the NVSS postage stamp images have $45''$ resolution while the images from our new observations have resolutions between about $10'' - 50''$, see Table 7.3).

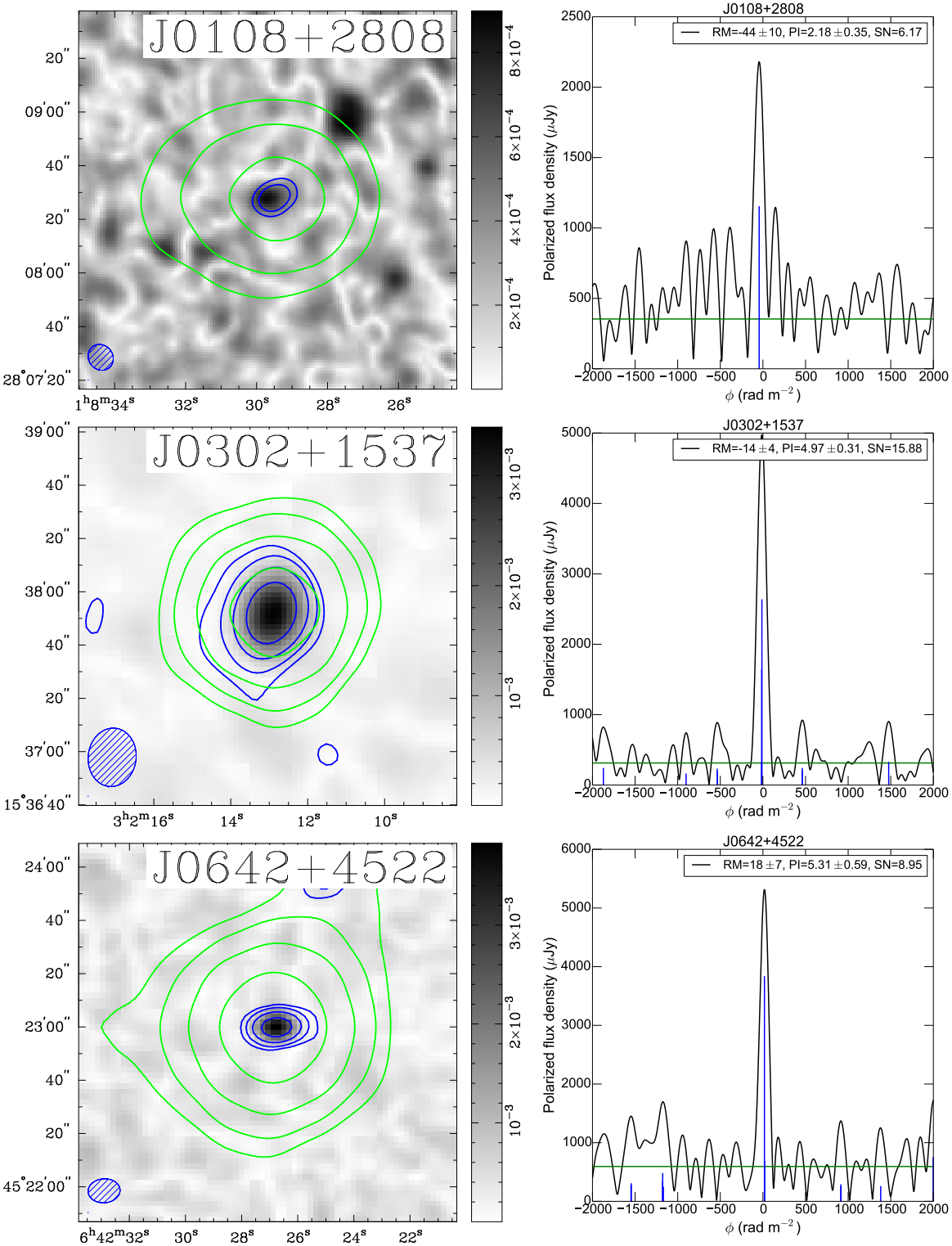

Figure 7.3.9: (**Left**) Linearly polarized flux density (gray scale in Jy beam^{-1}) overlaid with total intensity contours at levels of [3, 6, 12, 24] $\times\, \sigma_I$ (blue) where σ_I is reported in Table 7.3 with the corresponding beam shown in the bottom left corner. The green contours show the NVSS total intensities with 45″ resolution and the same contour levels. (**Right**) Faraday depth spectrum. The black line shows the polarized intensity distribution as a function of Faraday depth, the blue lines the RM-clean components and the green line shows the rms level.

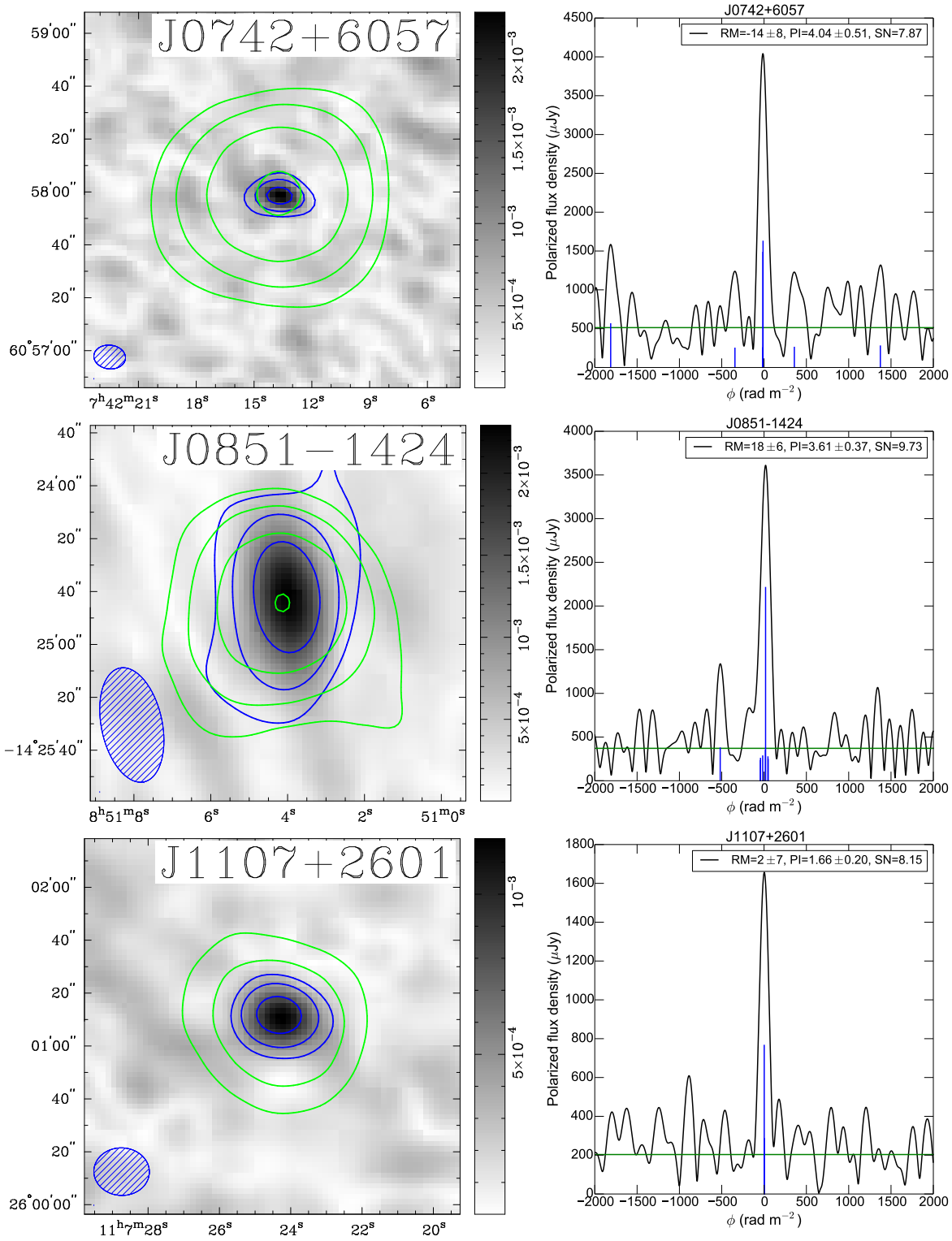

Figure 7.3.9: – Continued.

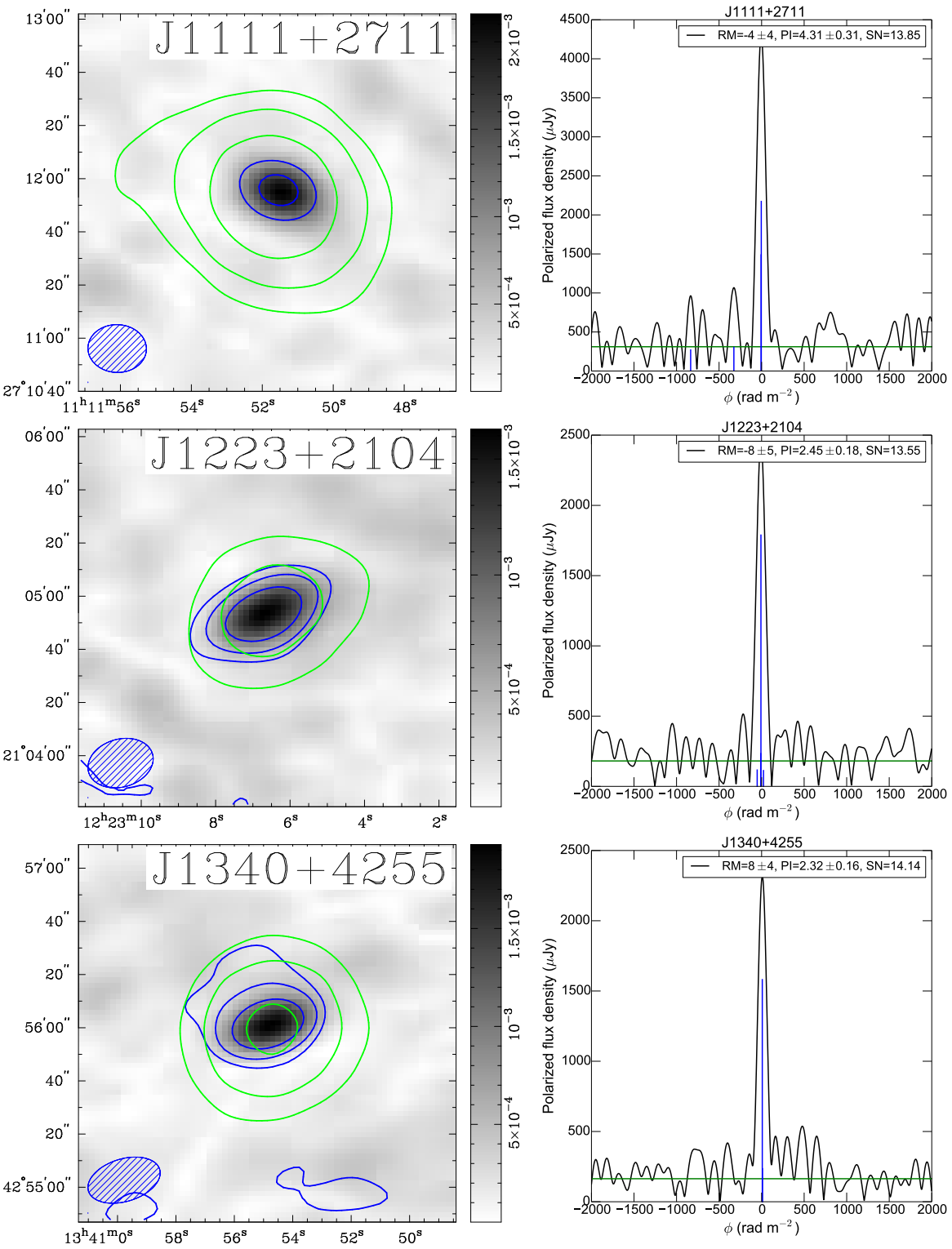

Figure 7.3.9: – Continued.

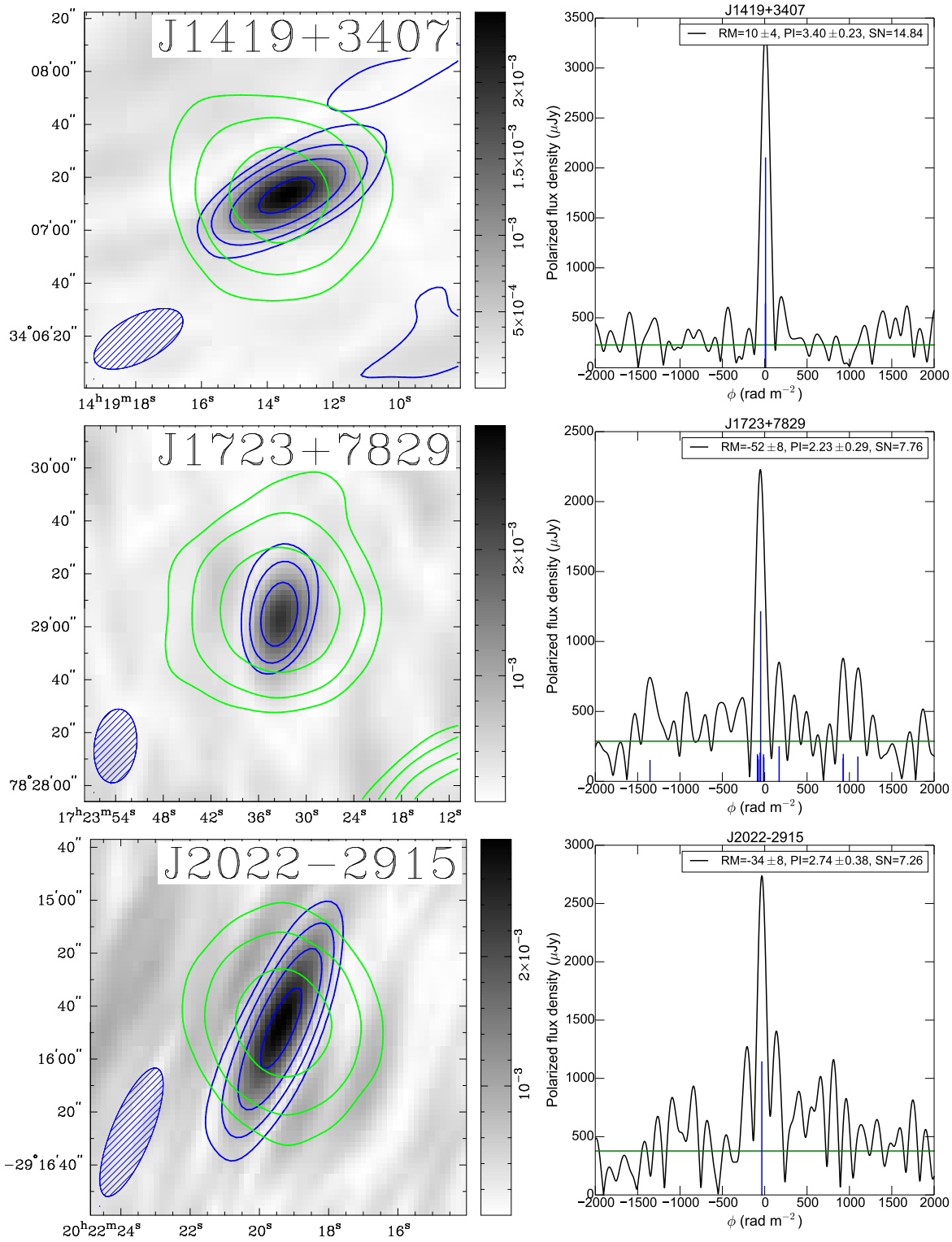

Figure 7.3.9: – Continued.

7.4 Summary and Future Work

The results of our observations of ultrahighly polarized EGSs at high angular resolution and wide frequency coverage show a broad distribution of Stokes I spectral indices. However, due to the large errors of the in-band spectral indices we cannot conclude whether the synchrotron emission is generated at a particular location within the AGN (e.g. Hovatta et al., 2014). To decrease the uncertainty level of α_{tot}, detections of a subset of sources from our sample at other frequencies and longer integration times are needed to improve the frequency coverage and SNR of Stokes I within the narrow 16 MHz frequency channels. But because the flux densities are low (a few mJy only), detecting these candidates at higher frequencies is a challenge and only practical for a few sources.

Our polarization studies show a broad distribution in fractional polarization between $20-50\,\%$. 5 out of 12 sources in our sample show fractional polarizations $< 30\,\%$ which was our selection threshold from NVSS. However, some sources exhibit higher degrees of polarization in our observations. Because those sources are particularly weak in Stokes I (the source with the highest integrated flux density has only 14 mJy in Stokes I), the sample could suffer from systematic effects, causing the discrepancy with the values reported in the NVSS catalog. Different possibilities are discussed in detail in Section 7.3.4.

We found a correlation between fractional polarization and spectral index (see right panel of Figure 7.3.6) with a correlation coefficient of 0.7 (the degree of polarization increases with increasing spectral index). Possible reasons are discussed in Section 7.3.2.

Given our resolution in Faraday depth of about $126\,\mathrm{rad\,m^{-2}}$, all sources with high fractional polarization show only one prominent peak. As discussed in Section 3.2.3 in Chapter 3, the effective bandwidth of L-band is sufficient to fulfill the requirement of detecting Faraday thick sources. Therefore we can conclude that we detect only Faraday simple sources. The Faraday depth is therefore probably produced by one or more simple Faraday screens (with a regular magnetic field) in front of the synchrotron emitting medium (Burn, 1966). This means the sources experience little Faraday depolarization which is in agreement with the detected high fractional polarization. Similar trends were observed in other work as well: For example the broadband radio-polarimetric study of 100 AGNs by O'Sullivan et al. (2017) shows that sources with high integrated degrees of polarization at 1.4 GHz have low Faraday depolarization and are typically dominated by a single RM component in the Faraday spectrum.

In our study we found a very broad distribution of total flux density spectral indices but these values suffer from large errors. Therefore, to improve the frequency coverage and additionally the resolution, we performed follow-up observations at higher frequencies for some sources of our previous sample. To avoid selection bias, we selected sources with both steep and flat spectral indices where the expected total flux density is high enough to be detectable at higher frequencies. With our analysis we were able so select a representative sample of sources for a follow-up project. In the following the observations and goals of the new project are summarized.

Higher angular resolution observations would help to better understand the nature and morphology of these highly polarized sources and their magnetic field structure. This would help in the interpretation what kind of sources we are considering here and that these sources may be a special class of polarized EGSs. We performed new follow-up observations of a sub-sample of 12 (5 of them are included in our high SNR sample) ultra highly polarized radio sources with the VLA in A-configuration at L-band and S-band, with the goal to better understand the origin of their unusually high degree of polarization, what remains unresolved in our current study. The new observations provide high angular resolution to spatially resolve the sources and hence, to obtain information on their morphologies to fully understand the nature of these sources and to get detailed information on the magnetic field structure. We note that some of our targets have matches in the FIRST catalog at $5''$ resolution, but FIRST data lack polarization information. At $5''$ angular resolution of the FIRST survey, we find indications that these sources are unlikely to remain unresolved at 10 times better angular resolution than the NVSS. With new observations in A-configuration at S-band we are able to reach sub-arcsecond resolution ($0.65''$ at 3 GHz). Furthermore, the new observations will improve the frequency coverage to study the in-band spectral index nature of the sources significantly. We expect to reduce the error of the spectral index by a factor of ~ 3.

With new L and S-band observations we expect to reach higher resolution in Faraday depth of about $40\,\mathrm{rad\,m^{-2}}$ to resolve possible multiple RM components along the line-of-sight. Additionally, applying RM-Synthesis on high angular resolution Stokes Q and U images, will allow us to obtain spatially resolved RM maps of the highly polarized sources and study their magnetic field structures in detail, assuming that the RM originates in the same emission region. For example, consistent RM sign along a highly polarized source (after subtracting the Galactic foreground) will allow us to distinguish whether the high fractional polarization is due to genuinely coherent magnetic field (with consistent direction), or due to compressed anisotropic magnetic fields with changing RM sign. On the other hand, transverse RM gradients are expected to be present in the inner parts of the jet and suggest helical magnetic field structures (e.g. Gabuzda et al., 2015).

Larger λ^2-coverage in Stokes Q and U will also allow us to perform QU-fitting. If the highly polarized sources show complex Faraday spectra (more than one Faraday rotating component within the telescope beam or along the line-of-sight), it is necessary to consider different Faraday depolarization models (see Section 2.2.2) to get detailed information on the Faraday rotating components, describing both the change of polarization angle with wavelength $\psi(\lambda^2)$ and the change in the degree of polarization with wavelength $p(\lambda^2)$. For the different scenarios O'Sullivan et al. (2012) summarized several models where the $Q(\lambda^2)$ and $U(\lambda^2)$ data are fitted simultaneously to various models. By doing this, it is possible to figure out the physical parameters of the magneto-ionic medium, such as the intrinsic fractional polarization p_0, the RM dispersion σ_{RM}, and the RM. To distinguish between different scenarios it is crucial to have a large range of λ^2.

To apply QU-fitting it is necessary to measure the flux density of Stokes Q and U images per channel (averaged over $4-16$ MHz depending on RM and SNR). Further, to robustly

measure the Stokes Q and U flux density, it is essential to have sufficient SNR while CLEANing to avoid imaging related artifacts. In our previous observations, due to only 90 seconds on-source time, we could only reach about 2σ sensitivity per channel after averaging over 16 MHz. This is insufficient to perform QU-fitting. With the new observations, we expect to reach 3σ sensitivity per 4-MHz channel, i.e. 6σ per 16-MHz channel. Further, the new higher sensitivity L-band observations along with S-band would provide us excellent λ^2-coverage ($0.006\mathrm{m}^2 - 0.09\mathrm{m}^2$) to robustly perform QU-fitting and distinguish between different Faraday depolarization models.

CHAPTER 8

Summary, Conclusions, and Outlook

In this thesis, I present the radio observational study of astronomical objects regarding their magnetic field properties, namely their strength, structure, and ordering. Cosmic magnetic fields on different astronomical scales were studied in two separated projects: I probed the diffuse polarized synchrotron emission of the nearby face-on oriented spiral galaxy M51 where the obtained observations provide us high spatial resolution on scales down to several hundreds of pc and polarized emission from a sample of extragalactic background sources where I investigated magnetic fields on kpc scales. The observations for both projects were performed using the Very Large Array (VLA) which is one of the leading radio interferometers, providing high spatial resolution and good sensitivity. Additionally, using broadband polarization data allows me to probe the frequency-dependent character of the polarized emission and thus to study depolarization mechanisms caused by different underlying magnetic field configurations.

8.1 Analyzing Wideband Polarimetry Data

In Chapter 4, I presented details on the observation, data reduction, and imaging procedures of the M51 wideband data. The observations of M51 were carried out at S-band between 2 – 4 GHz where no polarization data of this galaxy exists previously. Finding the best possible imaging parameters for extended structures using wideband interferometric data is not trivial and required a detailed discussion. I showed that the multi-frequency synthesis algorithm in CASA's task `clean` (which is the common astronomical data reduction software used for VLA data) provides in-band total intensity spectral indices which are too steep by about a factor two and thus unreliable. As a consequence, the integrated total intensity obtained using the entire broadband was underestimated by about 10 %.

8.2 The Magnetized Disk-halo Transition Region in M51

All scientific results of the study of the unknown polarization layer at S-band are presented in detail in Chapter 5. Studying M51 at S-band traces a so-far unknown polarized layer which is proposed to probe the *transition region between the disk and halo*. The goal was to make a major step towards understanding how large-scale magnetic fields are generated in the halo of spiral galaxies and how they are connected to the disk field. Here, I highlight some of the major findings and discuss prospects for future works.

The linearly polarized emission in M51 at S-band has a complicated appearance: The peaks in polarized intensity (referred as *magnetic arms* if they are located in inter-arm regions) are located at arbitrary positions relative to the gas spiral arms which is different from observations of other nearby face-on spiral galaxies. This is consistent with previous radio observations of M51 at higher (5 and 8 GHz) and lower (1.5 GHz) frequencies. The discrepancy could result from tidal interactions with the small irregular companion galaxy NGC 5195, located at the northern end of M51.

Furthermore, I found an increasing degree of polarization as a function of radius at S-band which implies a decrease of the wavelength-dependent depolarization. This was confirmed by calculating the depolarization between different frequency bands which implies a decreasing turbulent magnetic field strength and/or a decreasing thermal electron density towards larger radii in M51.

I found the observed RM in the disk-halo transition region to be dominated by fluctuations. This was also shown by the RM structure function at S-band. A fluctuating RM pattern indicates that the RM in the disk-halo transition region is dominated by vertical (with respect to the galaxy plane) magnetic fields.

8.3 The Mystery of M51's Multi-layer Magneto-Ionic Medium: Application of an Analytical Depolarization Model

M51 shows different patterns of the polarized intensity, magnetic field structure, and RM at high (5 and 8 GHz) and low (1.5 GHz) frequencies. The different patterns were proposed to originate from different magnetic field configurations in the disk and in the halo. To get information on the field strength and structure in those different layers, I studied wavelength-dependent depolarization between 1 – 8 GHz. The new S-band polarization data were combined with VLA observations at C- and X-band at 4.85 GHz and 8.35 GHz and with broadband L-band (1 – 2 GHz) VLA data. I compared the observed degree of polarization as a function of wavelength to a depolarization model which takes a multi-layer approach and hence is advantageous compared to 'classical' depolarization models which cannot handle different line-of-sight components of the magnetic field.

The results of the model comparison with the observational data are summarized in detail

in Chapter 6. The new S-band data are critical to distinguish between a two-layer (disk – halo) and a three-layer (halo – disk – halo) system. I found that a possible far-side halo is inconsistent with the radio polarization observations between 1 – 8 GHz and thus, a two-layer system is more likely for M51. The depolarization model contains physical parameters whit initial values that are required to be updated to match the observed degree of polarization at S-band. As an important first step towards finding the best-fit model parameter values, I developed an interactive tool in Python where the values of the regular and turbulent magnetic field strength, and of the thermal electron density can be changed simultaneously to visually inspect if the model fits the data with physically reasonable parameter values.

In the future, the best-fit parameter values from the interactive tool can be used as initial conditions to perform a least-square fit of the depolarization models to the observed degree of polarization as a function of wavelength. A least-square fit will provide a robust method to determine the values of the parameters accurately (if it converges to the right solutions). Applying the model fit to numerous sectors across the galaxy will enable me to study spatial variations of different magnetic field configurations. Further, the model can be adapted to be applicable to other nearby face-on oriented spiral galaxies (e.g. NGC 6946, IC 342, and NGC 628).

Despite being able to describe the observations, the analytical depolarization model that I am working with contains limitations and unrealistic assumptions: Assuming an equal cosmic ray electron density in the disk and in the halo is not physical. Also, the depolarization model neglects the presence of vertical magnetic fields whereas from dynamo theory it is known that each configuration of magnetic fields in spiral galaxies have a non vanishing vertical component. Furthermore, signatures of vertical magnetic fields were detected in the observed RM at S-band (see Section 5.4 in Chapter 5). In a future analysis, including vertical fields would help to study possible influences of the vertical magnetic field on the modeled degree of polarization.

8.4 The Nature of Extragalactic Sources with Unusually High Fractional Polarization

The second topic of my thesis, where I study magnetic field properties of extragalactic polarized background sources, is presented in Chapter 7. I observed a sample of 77 extragalactic radio sources (EGSs) with the VLA at L-band (1 – 2 GHz). The sample sources were selected to be highly polarized with polarization fractions $> 30\,\%$ in the NRAO VLA Sky Survey (NVSS) catalog at 1.4 GHz. This exceptionally high degree of polarization was postulated to originate from extremely well-ordered magnetic fields. Since polarized emission of EGSs is most likely produced by radio jets and/or radio lobes of AGNs, studying polarization properties of EGSs provides a new tool to investigate the formation and structure of magnetic fields in radio jets and lobes.

Due to imaging issues such as artifacts from poor uv-coverages and particularly weak

signals of the targets in total intensity, only 12 sources were usable for scientific analysis. The final sample consists of sources with the highest signal-to-noise ratio in total intensity (> 10) and polarized intensity (≥ 6). For those sources, I find a linear correlation (with a correlation coefficient of 0.7) between the observed degree of polarization and the total intensity synchrotron spectral index. I propose that this correlation can be produced by different emission regions traced by the observation of the EGSs: The radio emission of EGSs with flat spectral indices could originate from a region near the central core of the AGN where the jet is highly collimated and hence the magnetic field is well-ordered. This results in an observed flat spectral index and a high degree of polarization.

Due to the large wavelength coverage of the L-band observations I was able to apply RM-Synthesis on the polarization data with a resolution of $126\,\mathrm{rad\,m^{-2}}$ in Faraday depth (this is a factor of about five better compared to the resolution in Faraday depth at S-band). For the final sample of 12 high signal-to-noise ratio sources I found all Faraday spectra to be simple, containing only one prominent peak in Faraday depth (given the Faraday depth resolution and with a signal-to-noise ratio greater than 6). The Faraday depth is therefore likely by one or multiple simple Faraday screens (with a regular magnetic field) between the synchrotron emitting medium and the observer. This means that the sources experience little Faraday depolarization which is in agreement with the detected high fractional polarization.

The NVSS catalog was observed using the legacy system about 15 years before the expanded VLA project was completed. I compared my new observations with the values reported in the NVSS catalog and found the two data sets to note have matching total intensity, polarized intensity and hence, polarization fraction. The observed total intensity, polarized intensity, and fractional polarization disagree in the sense that either the new values are lower or higher. 5 out of 12 sources in my sample show fractional polarizations $< 30\,\%$ which is below my selection threshold from the NVSS. On the other hand, 6 sources exhibit higher degrees of polarization in my observations (one agrees exactly). Because the sources have both higher and lower degrees of polarization in the new measurements the discrepancy is unlikely caused by systematics such as confusion of background sources within the larger NVSS beam or bandwidth depolarization in the new broadband polarization observations.

Assuming no systematic effects in either set of the observations, a physical reason for a lower/higher fractional polarization in my new observation could be source variability in both total intensity and polarization. NVSS sources were observed in the late 1990s, about 15 years before I observed them again. Variability of both total intensity and polarization is a common characteristic of AGNs and occurs with multiple timescales and appear to be aperiodic and have variable amplitude (based on long-term observations of 70 AGNs over 30 years).

With my analysis I was able so select a representative sample of 12 sources for a follow-up project. I performed new observations of a sub-sample of 12 (5 of them are included in my high signal-to-noise ratio sample) ultra highly polarized radio sources with the VLA in A-configuration at L-band and S-band in March and April 2018, with the goal to better understand the origin of their unusually high degree of polarization, what remains unre-

solved in my current study. The new observations provide high angular resolution (down to sub-arcseconds) to spatially resolve the sources and hence, to obtain information on their morphologies to fully understand the nature of these sources and to get detailed information on the magnetic field structure.

8.5 The New Era of Wideband Radio Polarimetry

This thesis provides insights into a new era of polarimetric observations using *broadband* capabilities. Broadband multi-channel potentialities allow simultaneous observation at multiple frequencies which drastically decreases the amount of observing time. Furthermore, broadband observations solve the problem of unambiguous RM detections when using polarization measurements at only two separated wavelengths. Also, deviations from the linear λ^2 dependency of the polarization angles can be detected only with a well sampled wavelength-coverage. With broadband polarization data, depolarization mechanisms can be used as a powerful new tool to probe the 3D structure of magnetic fields in galaxies. Most of the depolarization mechanisms are caused by Faraday rotation, so that they are wavelength-dependent and related to the thermal electron density and the magnetic field component along the line-of-sight. Observations at cm and mm-wavelengths are well-suited to measure the variation of the degree of polarization as a function of wavelength for the typical ISM properties (μG magnetic field strengths and thermal electron density of the order of $0.01-0.1\,\mathrm{cm}^{-3}$). Additionally, modern techniques like RM-Synthesis combine broadband multi-channel observations into Faraday depth spectra which encode the polarized emission from different origins along the line-of-sight and with the observing resolution element. For both tools, the key instrumental aspect for a successful scientific polarization analysis is the total wavelength coverage, the spectral resolution, and the minimum observing wavelength (see Section 2.2.2 in Chapter 2, and Section 3.2.3 in Chapter 3). In my thesis I successfully applied those tools to new broadband observational data of both diffuse polarized emission of a nearby spiral galaxy and polarized emission from unresolved polarized background sources and devised new ways of analyzing and interpreting these broadband multi-channel data. Future prospects provided by the new Square Kilometre Array (SKA) with dramatically improved broadband coverage and excellent surface brightness sensitivity will highly complement the study of magnetic fields in the ISM of nearby galaxies. For those new radio astronomy era, my thesis was an important step towards analyzing and interpreting these broadband polarization data.

Bibliography

Adebahr, B., M. Krause, U. Klein, et al. (July 2013). "M82 – A radio continuum and polarisation study. I. Data reduction and cosmic ray propagation". In: *A&A* 555, A23, A23.

Aller, M. F., H. D. Aller, and P. A. Hughes (Mar. 2003). "Pearson-Readhead Survey Sources. II. The Long-Term Centimeter-Band Total Flux and Linear Polarization Properties of a Complete Radio Sample". In: *ApJ* 586, pp. 33–51.

Anderson, C. S., B. M. Gaensler, I. J. Feain, et al. (Apr. 2016). "Erratum: "Broadband Radio Polarimetry and Faraday Rotation of 563 Extragalactic Radio Sources" (ApJ, 815, 1, 49)". In: *ApJ* 820, 144, p. 144.

Arshakian, T. G. and R. Beck (Dec. 2011). "Optimum frequency band for radio polarization observations". In: *MNRAS* 418, pp. 2336–2342.

Bagetakos, I., E. Brinks, F. Walter, et al. (Jan. 2011). "The Fine-scale Structure of the Neutral Interstellar Medium in Nearby Galaxies". In: *AJ* 141, 23, p. 23.

Balsara, D. S., J. Kim, M.-M. Mac Low, et al. (Dec. 2004). "Amplification of Interstellar Magnetic Fields by Supernova-driven Turbulence". In: *ApJ* 617, pp. 339–349.

Basu, A., S. A. Mao, A. A. Kepley, et al. (Jan. 2017). "Detection of an ∼20 kpc coherent magnetic field in the outskirt of merging spirals: the Antennae galaxies". In: *Monthly Notices of the Royal Astronomical Society* 464, pp. 1003–1017.

Beck, R. (Aug. 2007). "Magnetism in the spiral galaxy NGC 6946: magnetic arms, depolarization rings, dynamo modes, and helical fields". In: *A&A* 470, pp. 539–556.

— (Oct. 2009). "Galactic and extragalactic magnetic fields - a concise review". In: *Astrophysics and Space Sciences Transactions* 5, pp. 43–47.

— (June 2015). "Magnetic fields in the nearby spiral galaxy IC 342: A multi-frequency radio polarization study". In: *A&A* 578, A93, A93.

— (Feb. 2016). "Erratum: Erratum to: Magnetic fields in spiral galaxies". In: *AApR* 24, 7, p. 7.

Beck, R. and P. Hoernes (Jan. 1996). "Magnetic spiral arms in the galaxy NGC6946". In: *Natur* 379, pp. 47–49.

Beck, R. and M. Krause (July 2005). "Revised equipartition and minimum energy formula for magnetic field strength estimates from radio synchrotron observations". In: *Astronomische Nachrichten* 326, pp. 414–427.

Beck, R. and R. Wielebinski (2013). "Magnetic Fields in Galaxies". In: *Planets, Stars and Stellar Systems. Volume 5: Galactic Structure and Stellar Populations*. Ed. by T. D. Oswalt and G. Gilmore, p. 641.

Beck, R., U. Klein, and R. Wielebinski (Nov. 1987). "The magnetic field in M51". In: *A&A* 186, pp. 95–98.

Beck, R., A. Brandenburg, D. Moss, et al. (1996). "Galactic Magnetism: Recent Developments and Perspectives". In: *ARA&A* 34, pp. 155–206.

Beck, R., A. Fletcher, A. Shukurov, et al. (Dec. 2005). "Magnetic fields in barred galaxies. IV. NGC 1097 and NGC 1365". In: *A&A* 444, pp. 739–765.

Beck, R., P. Frick, R. Stepanov, et al. (July 2012). "Recognizing magnetic structures by present and future radio telescopes with Faraday rotation measure synthesis". In: *A&A* 543, A113, A113.

Bell, A. R. (Feb. 1978). "The acceleration of cosmic rays in shock fronts. II". In: *MNRAS* 182, pp. 443–455.

Berkhuijsen, E. M., C. Horellou, M. Krause, et al. (Feb. 1997). "Magnetic fields in the disk and halo of M 51." In: *A&A* 318, pp. 700–720.

Berkhuijsen, E. M., R. Beck, and P. Hoernes (Feb. 2003). "The polarized disk in M 31 at lambda 6 cm". In: *A&A* 398, pp. 937–948.

Bernet, M. L., F. Miniati, S. J. Lilly, et al. (July 2008). "Strong magnetic fields in normal galaxies at high redshift". In: *Natur* 454, pp. 302–304.

Biermann, L. (1950). "Uber den Ursprung der Magnetfelder auf Sternen und im interstellaren Raum (mit einem Anhang von A. Schluter)". In: *Zeitschrift für Naturforschung*, p. 65.

Black, A. R. S., S. A. Baum, J. P. Leahy, et al. (May 1992). "A study of FRII radio galaxies with Z less than 0.15. I - High-resolution maps of eight sources at 3.6 CM". In: *MNRAS* 256, pp. 186–208.

Blasi, P. (Nov. 2013). "The origin of galactic cosmic rays". In: *AApR* 21, 70, p. 70.

Bonafede, A., L. Feretti, M. Murgia, et al. (Apr. 2010). "The Coma cluster magnetic field from Faraday rotation measures". In: *A&A* 513, A30, A30.

Braun, R., G. Heald, and R. Beck (May 2010). "The Westerbork SINGS survey. III. Global magnetic field topology". In: *A&A* 514, A42, A42.

Bregman, J. N. (Mar. 1980). "The galactic fountain of high-velocity clouds". In: *ApJ* 236, pp. 577–591.

Brentjens, M. A. and A. G. de Bruyn (Oct. 2005). "Faraday rotation measure synthesis". In: *A&A* 441, pp. 1217–1228.

Bridle, A. H., D. H. Hough, C. J. Lonsdale, et al. (Sept. 1994). "Deep VLA imaging of twelve extended 3CR quasars". In: *AJ* 108, pp. 766–820.

Briggs, D. S. (Dec. 1995). "High Fidelity Interferometric Imaging: Robust Weighting and NNLS Deconvolution". In: *American Astronomical Society Meeting Abstracts*. Vol. 27. Bulletin of the American Astronomical Society, p. 1444.

Burn, B. J. (1966). "On the depolarization of discrete radio sources by Faraday dispersion". In: *MNRAS* 133, p. 67.

Byrd, G. G. and S. Howard (1990). "M51's material arms and density waves." In: *Dynamics and Interactions of Galaxies*. Ed. by R. Wielen, pp. 128–130.

Carlstrom, J. E. and P. P. Kronberg (Jan. 1991). "H II regions in M82 - High-resolution millimeter continuum observations". In: *ApJ* 366, pp. 422–431.

Carroll, B. W. and D. A. Ostlie (1996). *An Introduction to Modern Astrophysics*.

Chyzy, K. T., R. Beck, S. Kohle, et al. (Apr. 2000). "Erratum: Regular Magnetic Fields in the Dwarf Irregular Galaxy NGC 4449". In: *A&A* 356.

Ciardullo, R., J. J. Feldmeier, G. H. Jacoby, et al. (Sept. 2002). "Planetary Nebulae as Standard Candles. XII. Connecting the Population I and Population II Distance Scales". In: *ApJ* 577, pp. 31–50.

Condon, J. (Feb. 2015). "An Analysis of the VLASS Proposal". In: *ArXiv e-prints*.

Condon, J. J. (1992). "Radio emission from normal galaxies". In: *ARA&A* 30, pp. 575–611.

Condon, J. J., W. D. Cotton, E. W. Greisen, et al. (May 1998). "The NRAO VLA Sky Survey". In: *AJ* 115, pp. 1693–1716.

Cornwell, T. J. (Nov. 2008). "Multiscale CLEAN Deconvolution of Radio Synthesis Images". In: *IEEE Journal of Selected Topics in Signal Processing* 2, pp. 793–801.

Cox, A. N. (2000). *Allen's astrophysical quantities*.

Dobbs, C. L., C. Theis, J. E. Pringle, et al. (Apr. 2010). "Simulations of the grand design galaxy M51: a case study for analysing tidally induced spiral structure". In: *MNRAS* 403, pp. 625–645.

Draine, B. T. (2011). *Physics of the Interstellar and Intergalactic Medium*.

Dumas, G., E. Schinnerer, F. S. Tabatabaei, et al. (Feb. 2011). "The Local Radio-IR Relation in M51". In: *AJ* 141, 41, p. 41.

Durrer, R. and A. Neronov (June 2013). "Cosmological magnetic fields: their generation, evolution and observation". In: *AApR* 21, 62, p. 62.

Ekers, R. D. (1999). "Error Recognition". In: *Synthesis Imaging in Radio Astronomy II*. Ed. by G. B. Taylor, C. L. Carilli, and R. A. Perley. Vol. 180. Astronomical Society of the Pacific Conference Series, p. 321.

Elmegreen, B. G. and J. Scalo (Sept. 2004). "Interstellar Turbulence I: Observations and Processes". In: *ARA&A* 42, pp. 211–273.

Fanaroff, B. L. and J. M. Riley (May 1974). "The morphology of extragalactic radio sources of high and low luminosity". In: *MNRAS* 167, 31P–36P.

Feain, I. J., R. D. Ekers, T. Murphy, et al. (Dec. 2009). "Faraday Rotation Structure on Kiloparsec Scales in the Radio Lobes of Centaurus A". In: *ApJ* 707, pp. 114–125.

Ferriere, K. (June 1996). "Alpha-tensor and diffusivity tensor due to supernovae and superbubbles in the Galactic disk near the Sun." In: *A&A* 310, pp. 438–455.

Fletcher, A., R. Beck, A. Shukurov, et al. (Apr. 2011). "Magnetic fields and spiral arms in the galaxy M51". In: *MNRAS* 412, pp. 2396–2416.

Ford, H. C., P. C. Crane, G. H. Jacoby, et al. (June 1985). "Bubbles and jets in the center of M51". In: *ApJ* 293, pp. 132–147.

Frick, P., R. Stepanov, R. Beck, et al. (Jan. 2016). "Magnetic and gaseous spiral arms in M83". In: *A&A* 585, A21, A21.

Gabuzda, D. C., S. Knuettel, and A. Bonafede (Nov. 2015). "Evidence for a toroidal magnetic-field component in 5C 4.114 on kiloparsec scales". In: *A&A* 583, A96, A96.

Gabuzda, D. C., N. Roche, A. Kirwan, et al. (Dec. 2017). "Parsec scale Faraday-rotation structure across the jets of nine active galactic nuclei". In: *MNRAS* 472, pp. 1792–1801.

Gaensler, B., I. Agudo, T. Akahori, et al. (Apr. 2015). "Broadband Polarimetry with the Square Kilometre Array: A Unique Astrophysical Probe". In: *Advancing Astrophysics with the Square Kilometre Array (AASKA14)*, 103, p. 103.

Gaensler, B. M., J. M. Dickey, N. M. McClure-Griffiths, et al. (Mar. 2001). "Radio Polarization from the Inner Galaxy at Arcminute Resolution". In: *ApJ* 549, pp. 959–978.

Gaensler, B. M., M. Haverkorn, L. Staveley-Smith, et al. (Mar. 2005). "The Magnetic Field of the Large Magellanic Cloud Revealed Through Faraday Rotation". In: *Science* 307, pp. 1610–1612.

Gardner, F. F. and J. B. Whiteoak (1966). "The Polarization of Cosmic Radio Waves". In: *ARA&A* 4, p. 245.

George, S. J., J. M. Stil, and B. W. Keller (Oct. 2012). "Detection Thresholds and Bias Correction in Polarized Intensity". In: *Publications of the Astronomical Society of Australia* 29, pp. 214–220.

Gioia, I. M. and L. Gregorini (Sept. 1980). "Radio observations of a complete sample of spiral galaxies at 408 MHz". In: *A&AS* 41, pp. 329–334.

Goodlet, J. A. and C. R. Kaiser (June 2005). "The depolarization properties of powerful extragalactic radio sources as a function of cosmic epoch". In: *MNRAS* 359, pp. 1456–1468.

Hanasz, M., H. Lesch, T. Naab, et al. (Nov. 2013). "Cosmic Rays Can Drive Strong Outflows from Gas-rich High-redshift Disk Galaxies". In: *ApJL* 777, L38, p. L38.

Harvey-Smith, L., G. J. Madsen, and B. M. Gaensler (Aug. 2011). "Magnetic Fields in Large-diameter H II Regions Revealed by the Faraday Rotation of Compact Extragalactic Radio Sources". In: *Astronomical Journal* 736, 83, p. 83.

Haverkorn, M. and V. Heesen (May 2012). "Magnetic Fields in Galactic Haloes". In: *Space Science Reviews* 166, pp. 133–144.

Haverkorn, M., B. M. Gaensler, N. M. McClure-Griffiths, et al. (July 2004). "Magnetic Fields and Ionized Gas in the Inner Galaxy: An Outer Scale for Turbulence and the Possible Role of H II Regions". In: *ApJ* 609, pp. 776–784.

Haverkorn, M., J. C. Brown, B. M. Gaensler, et al. (June 2008). "The Outer Scale of Turbulence in the Magnetoionized Galactic Interstellar Medium". In: *ApJ* 680, pp. 362–370.

Heald, G. (Apr. 2009). "The Faraday rotation measure synthesis technique". In: *Cosmic Magnetic Fields: From Planets, to Stars and Galaxies*. Ed. by K. G. Strassmeier, A. G. Kosovichev, and J. E. Beckman. Vol. 259. IAU Symposium, pp. 591–602.

Heald, G., R. Braun, and R. Edmonds (Aug. 2009). "The Westerbork SINGS survey. II Polarization, Faraday rotation, and magnetic fields". In: *å* 503, pp. 409–435.

Heald, G. H. (Aug. 2012). "Magnetic Field Transport from Disk to Halo via the Galactic Chimney Process in NGC 6946". In: *ApJL* 754, L35, p. L35.

Heesen, V., E. Brinks, A. K. Leroy, et al. (May 2014). "The Radio Continuum-Star Formation Rate Relation in WSRT SINGS Galaxies". In: *AJ* 147, 103, p. 103.

Heesen, V., M. Krause, R. Beck, et al. (May 2018). "Radio haloes in nearby galaxies modelled with 1D cosmic ray transport using SPINNAKER". In: *MNRAS* 476, pp. 158–183.

Heiles, C. (1996). "A Comprehensive View of the Galactic Magnetic Field, Especially near the Sun". In: *Polarimetry of the Interstellar Medium*. Ed. by W. G. Roberge and D. C. B. Whittet. Vol. 97. Astronomical Society of the Pacific Conference Series, p. 457.

Hill, J. K., W. H. Waller, R. H. Cornett, et al. (Mar. 1997). "Ultraviolet Colors and Extinctions of H II Regions in the Whirlpool Galaxy (M51)". In: *ApJ* 477, pp. 673–678.

Högbom, J. A. (June 1974). "Aperture Synthesis with a Non-Regular Distribution of Interferometer Baselines". In: *A&AS* 15, p. 417.

Horellou, C., R. Beck, E. M. Berkhuijsen, et al. (Nov. 1992). "Faraday effects in the spiral galaxy M 51". In: *A&A* 265, pp. 417–428.

Hovatta, T. (2017). "Observational View of Magnetic Fields in Active Galactic Nuclei Jets". In: *New Frontiers in Black Hole Astrophysics*. Ed. by A. Gomboc. Vol. 324. IAU Symposium, pp. 149–156.

Hovatta, T., M. Tornikoski, H. J. Lehto, et al. (Jan. 2008). "Long term radio variability of AGN". In: *Blazar Variability across the Electromagnetic Spectrum*, p. 41.

Hovatta, T., M. F. Aller, H. D. Aller, et al. (June 2014). "MOJAVE: Monitoring of Jets in Active Galactic Nuclei with VLBA Experiments. XI. Spectral Distributions". In: *AJ* 147, 143, p. 143.

Hunter, J. D. (2007). "Matplotlib: A 2D graphics environment". In: *Computing In Science & Engineering* 9.3, pp. 90–95.

Iacobelli, M., M. Haverkorn, and P. Katgert (Jan. 2013). "Rotation measure synthesis at the 2 m wavelength of the FAN region: unveiling screens and bubbles". In: *Astronomy & Astrophysics* 549, A56, A56.

Iapichino, L. and M. Brüggen (July 2012). "Magnetic field amplification by shocks in galaxy clusters: application to radio relics". In: *MNRAS* 423, pp. 2781–2788.

Irwin, J., R. Beck, R. A. Benjamin, et al. (Aug. 2012). "Continuum Halos in Nearby Galaxies: An EVLA Survey (CHANG-ES). II. First Results on NGC 4631". In: *AJ* 144, 44, p. 44.

Jaffe, T. R., J. P. Leahy, A. J. Banday, et al. (Jan. 2010). "Modelling the Galactic magnetic field on the plane in two dimensions". In: *MNRAS* 401, pp. 1013–1028.

Jansson, R. and G. R. Farrar (Sept. 2012). "A New Model of the Galactic Magnetic Field". In: *ApJ* 757, 14, p. 14.

Kaplan, S. A. and S. B. Pikelner (1974). "Large-scale dynamics of the interstellar medium". In: *ARA&A* 12, pp. 113–133.

Kennicutt Jr., R. C. (Sept. 1989). "The star formation law in galactic disks". In: *ApJ* 344, pp. 685–703.

Kennicutt Jr., R. C., L. Armus, G. Bendo, et al. (Aug. 2003). "SINGS: The SIRTF Nearby Galaxies Survey". In: *Publications of the ASP* 115, pp. 928–952.

Kierdorf, M., R. Beck, M. Hoeft, et al. (Apr. 2017). "Relics in galaxy clusters at high radio frequencies". In: *A&A* 600, A18, A18.

Kierdorf, M., S. A. Mao, A. Fletcher, et al. (Oct. 2018). "The Magnetized Disk-Halo Transition Region of M51". In: *ArXiv e-prints*.

Kim, C.-G., W.-T. Kim, and E. C. Ostriker (Sept. 2006). "Interstellar Turbulence Driving by Galactic Spiral Shocks". In: *ApJL* 649, pp. L13–L16.

Klein, U. and D. T. Emerson (Jan. 1981). "A Survey of the Distributions of 2.8-CM Radio Continuum in Nearby Galaxies - Part One - Observations of 16 Spiral". In: *A&A* 94, p. 29.

Klein, U. and A. Fletcher (2015). *Galactic and Intergalactic Magnetic Fields*.

Klein, U., R. Wielebinski, and R. Beck (June 1984). "High frequency radio continuum investigation of M51". In: *A&A* 135, pp. 213–224.

Klein, U., R. Wielebinski, and H. W. Morsi (Jan. 1988). "Radio continuum observations of M82". In: *A&A* 190, pp. 41–46.

Krause, M. (Jan. 2012). "Magnetic fields and star formation as seen in edge-on galaxies". In: *Magnetic Fields in the Universe III - From Laboratory and Stars to Primordial Structures, proceedings of the conference held 21-27 August, 2011 in Zakopane, Poland. Edited by M. Soida et al. Jagiellonian University, Astronomical Observatory, 2012, p.155.* Ed. by M. Soida, K. Otmianowska-Mazur, E. M. de Gouveia Dal Pino, et al., p. 155.

— (Jan. 2014). "Magnetic fields and halos in spiral galaxies". In: *ArXiv e-prints*.

Kravchenko, E. V., Y. Y. Kovalev, and K. V. Sokolovsky (May 2017). "Parsec-scale Faraday rotation and polarization of 20 active galactic nuclei jets". In: *MNRAS* 467, pp. 83–101.

Kronberg, P. P. and J. J. Perry (Oct. 1982). "The detection of magnetic fields out to large redshifts." In: *JRASC* 76, p. 321.

Kronberg, P. P., C. C. Dyer, and H.-J. Roeser (Nov. 1996). "Estimates of the Global Masses of Two Distant Galaxies Using a New Type of Astrophysical Mass "Laboratory"". In: *ApJ* 472, p. 115.

Kulsrud, R. M. (2005). "The Origin of Galactic Magnetic Fields". In: *Cosmic Magnetic Fields*. Ed. by R. Wielebinski and R. Beck. Vol. 664. Lecture Notes in Physics, Berlin Springer Verlag, p. 69.

— (Jan. 2010). "The origin of our galactic magnetic field". In: *Astronomische Nachrichten* 331, p. 22.

Kulsrud, R. M. and E. G. Zweibel (Apr. 2008). "On the origin of cosmic magnetic fields". In: *Reports on Progress in Physics* 71.4, 046901, p. 046901.

Laing, R. A., A. H. Bridle, P. Parma, et al. (Dec. 2008). "Structures of the magnetoionic media around the Fanaroff-Riley Class I radio galaxies 3C31 and Hydra A". In: *MNRAS* 391, pp. 521–549.

Lamee, M., L. Rudnick, J. S. Farnes, et al. (Sept. 2016). "Magnetic Field Disorder and Faraday Effects on the Polarization of Extragalactic Radio Sources". In: *ApJ* 829, 5, p. 5.

Le Roux, E. (Feb. 1961). "Étude théorique du rayonnement synchrotron des radiosources". In: *Annales d'Astrophysique* 24, p. 71.

Leahy, J. P., A. R. S. Black, J. Dennett-Thorpe, et al. (Oct. 1997). "A study of FRII radio galaxies with z<0.15 - II. High-resolution maps of 11 sources at 3.6 CM". In: *MNRAS* 291, pp. 20–53.

Liang, H., R. D. Ekers, R. W. Hunstead, et al. (Dec. 2001). "J06587-5558: a very unusual polarized radio source". In: *MNRAS* 328, pp. L21–L26.

Lin, C. C. and F. H. Shu (Aug. 1964). "On the Spiral Structure of Disk Galaxies." In: *ApJ* 140, p. 646.

Lister, M. L. and D. C. Homan (Oct. 2005). "MOJAVE: Monitoring of Jets in Active Galactic Nuclei with VLBA Experiments. I. First-Epoch 15 GHz Linear Polarization Images". In: *AJ* 130, pp. 1389–1417.

Longair, M. S. (Feb. 2011). *High Energy Astrophysics*.

Mao, S. A., B. M. Gaensler, S. Stanimirović, et al. (Dec. 2008). "A Radio and Optical Polarization Study of the Magnetic Field in the Small Magellanic Cloud". In: *ApJ* 688, pp. 1029–1049.

Mao, S. A., B. M. Gaensler, M. Haverkorn, et al. (May 2010). "A Survey of Extragalactic Faraday Rotation at High Galactic Latitude: The Vertical Magnetic Field of the Milky Way Toward the Galactic Poles". In: *ApJ* 714, pp. 1170–1186.

Mao, S. A., B. M. Gaensler, S. Stanimirović, et al. (Feb. 2012a). "Erratum: "A Radio and Optical Polarization Study of the Magnetic Field in the Small Magellanic Cloud" <A href="/abs/2008ApJ...688.1029M">(2008, ApJ, 688, 1029)</A>". In: *ApJ* 745, 199, p. 199.

Mao, S. A., N. M. McClure-Griffiths, B. M. Gaensler, et al. (Aug. 2012c). "New Constraints on the Galactic Halo Magnetic Field Using Rotation Measures of Extragalactic Sources toward the Outer Galaxy". In: *ApJ* 755, 21, p. 21.

Mao, S. A., N. M. McClure-Griffiths, B. M. Gaensler, et al. (Nov. 2012b). "Magnetic Field Structure of the Large Magellanic Cloud from Faraday Rotation Measures of Diffuse Polarized Emission". In: *ApJ* 759, 25, p. 25.

Mao, S. A., E. Zweibel, A. Fletcher, et al. (Feb. 2015). "Properties of the Magneto-ionic Medium in the Halo of M51 Revealed by Wide-band Polarimetry". In: *ApJ* 800, 92, p. 92.

Marscher, A. P. (Sept. 2006). "Relativistic Jets in Active Galactic Nuclei". In: *Relativistic Jets: The Common Physics of AGN, Microquasars, and Gamma-Ray Bursts*. Ed. by P. A. Hughes and J. N. Bregman. Vol. 856. American Institute of Physics Conference Series, pp. 1–22.

McKee, C. F. and J. P. Ostriker (Nov. 1977). "A theory of the interstellar medium - Three components regulated by supernova explosions in an inhomogeneous substrate". In: *ApJ* 218, pp. 148–169.

McMullin, J. P., B. Waters, D. Schiebel, et al. (Oct. 2007). "CASA Architecture and Applications". In: *Astronomical Data Analysis Software and Systems XVI*. Ed. by R. A. Shaw, F. Hill, and D. J. Bell. Vol. 376. Astronomical Society of the Pacific Conference Series, p. 127.

Moss, D., D. Sokoloff, R. Beck, et al. (Mar. 2010). "Galactic winds and the symmetry properties of galactic magnetic fields". In: *A&A* 512, A61, A61.

Moss, D., R. Stepanov, T. G. Arshakian, et al. (Jan. 2012). "Multiscale magnetic fields in spiral galaxies: evolution and reversals". In: *A&A* 537, A68, A68.

Mulcahy, D. D., A. Horneffer, R. Beck, et al. (Aug. 2014). "The nature of the low-frequency emission of M 51. First observations of a nearby galaxy with LOFAR". In: *A&A* 568, A74, A74.

Mulcahy, D. D., A. Fletcher, R. Beck, et al. (Aug. 2016). "Modelling the cosmic ray electron propagation in M 51". In: *A&A* 592, A123, A123.

Mulcahy, D. D., R. Beck, and G. H. Heald (Apr. 2017). "Resolved magnetic structures in the disk-halo interface of NGC 628". In: *A&A* 600, A6, A6.

Mulcahy, David (2011). "8 Channel Polarimetry on M31". MA thesis. Germany: University of Bonn.

Murphy, E. J., J. J. Condon, A. Alberdi, et al. (Oct. 2018). "Science with an ngVLA: Radio Continuum Emission from Galaxies: An Accounting of Energetic Processes". In: *ArXiv e-prints*.

Oppermann, N., H. Junklewitz, G. Robbers, et al. (June 2012). "An improved map of the Galactic Faraday sky". In: *A&A* 542, A93, A93.

O'Sullivan, S. P. and D. C. Gabuzda (Nov. 2009). "Magnetic field strength and spectral distribution of six parsec-scale active galactic nuclei jets". In: *MNRAS* 400, pp. 26–42.

O'Sullivan, S. P., S. Brown, T. Robishaw, et al. (Apr. 2012). "Complex Faraday depth structure of active galactic nuclei as revealed by broad-band radio polarimetry". In: *MNRAS* 421, pp. 3300–3315.

O'Sullivan, S. P., C. R. Purcell, C. S. Anderson, et al. (Aug. 2017). "Broad-band, radio spectro-polarimetric study of 100 radiative-mode and jet-mode AGN". In: *MNRAS* 469, pp. 4034–4062.

Parker, E. N. (Sept. 1966). "The Dynamical State of the Interstellar Gas and Field". In: *ApJ* 145, p. 811.

— (1979). *Cosmical magnetic fields: Their origin and their activity*.

Pasetto, A., C. Carrasco-González, S. O'Sullivan, et al. (June 2018). "Broadband radio spectro-polarimetric observations of high-Faraday-rotation-measure AGN". In: *A&A* 613, A74, A74.

Patrikeev, I., A. Fletcher, R. Stepanov, et al. (Nov. 2006). "Analysis of spiral arms using anisotropic wavelets: gas, dust and magnetic fields in M 51". In: *A&A* 458, pp. 441–452.

Perley, R. A. and B. J. Butler (Feb. 2013a). "An Accurate Flux Density Scale from 1 to 50 GHz". In: *ApJS* 204, 19, p. 19.

— (June 2013b). "Integrated Polarization Properties of 3C48, 3C138, 3C147, and 3C286". In: *ApJS* 206, 16, p. 16.

Perley, R. A., J. W. Dreher, and J. J. Cowan (Oct. 1984). "The jet and filaments in Cygnus A". In: *ApJL* 285, pp. L35–L38.

Peterson, Bradley M. (1997). *An Introduction to Active Galactic Nuclei*.

Peterson, Bradley M. (Jan. 2001). "Variability of Active Galactic Nuclei". In: *Advanced Lectures on the Starburst-AGN*. Ed. by Itziar Aretxaga, Daniel Kunth, and Raúl Mújica, p. 3.

Pizzo, R. F., A. G. de Bruyn, G. Bernardi, et al. (Jan. 2011). "Deep multi-frequency rotation measure tomography of the galaxy cluster A2255". In: *A&A* 525, A104, A104.

Planck Collaboration, R. Adam, P. A. R. Ade, et al. (Sept. 2016). "Planck 2015 results. I. Overview of products and scientific results". In: *A&A* 594, A1, A1.

Poezd, A., A. Shukurov, and D. Sokoloff (Sept. 1993). "Global Magnetic Patterns in the Milky-Way and the Andromeda Nebula". In: *MNRAS* 264, p. 285.

Pudritz, R. E., M. J. Hardcastle, and D. C. Gabuzda (Sept. 2012). "Magnetic Fields in Astrophysical Jets: From Launch to Termination". In: *Space Science Reviews* 169, pp. 27–72.

Rau, U. and T. J. Cornwell (Aug. 2011). "A multi-scale multi-frequency deconvolution algorithm for synthesis imaging in radio interferometry". In: *A&A* 532, A71, A71.

Rodrigues, L. F. S., A. Shukurov, A. Fletcher, et al. (July 2015). "Galactic magnetic fields and hierarchical galaxy formation". In: *MNRAS* 450, pp. 3472–3489.

Rodrigues, L. F. S., G. R. Sarson, A. Shukurov, et al. (Jan. 2016). "The Parker Instability in Disk Galaxies". In: *ApJ* 816, 2, p. 2.

Romero, G. E., M. Boettcher, S. Markoff, et al. (July 2017). "Relativistic Jets in Active Galactic Nuclei and Microquasars". In: *Space Science Reviews* 207, pp. 5–61.

Ruzmaikin, A. A., D. D. Sokolov, and A. M. Shukurov, eds. (1988). *Magnetic fields of galaxies*. Vol. 133. Astrophysics and Space Science Library.

Rybicki, G. B. and A. P. Lightman (June 1986). *Radiative Processes in Astrophysics*, p. 400.

Schnitzeler, D. H. F. M. (Nov. 2010). "The latitude dependence of the rotation measures of NVSS sources". In: *MNRAS* 409, pp. L99–L103.

Schoenmakers, A. P., K.-H. Mack, A. G. de Bruyn, et al. (Oct. 2000). "A new sample of giant radio galaxies from the WENSS survey. II. A multi-frequency radio study of a complete sample: Properties of the radio lobes and their environment". In: *A&AS* 146, pp. 293–322.

Segalovitz, A. (Feb. 1977). "High resolution observations of M 51 at 21 and 49 CM". In: *A&A* 54, pp. 703–711.

Shapiro, P. R. and G. B. Field (May 1976). "Consequences of a New Hot Component of the Interstellar Medium". In: *ApJ* 205, pp. 762–765.

Shi, H., H. Liang, J. L. Han, et al. (Dec. 2010). "Radio sources with ultrahigh polarization". In: *MNRAS* 409, pp. 821–838.

Shneider, C., M. Haverkorn, A. Fletcher, et al. (July 2014a). "Depolarization of synchrotron radiation in a multilayer magneto-ionic medium". In: *A&A* 567, A82, A82.

— (Aug. 2014b). "Constraining regular and turbulent magnetic field strengths in M 51 via Faraday depolarization". In: *A&A* 568, A83, A83.

Simonetti, J. H., J. M. Cordes, and S. R. Spangler (Sept. 1984). "Small-scale variations in the galactic magnetic field - The rotation measure structure function and birefringence in interstellar scintillations". In: *ApJ* 284, pp. 126–134.

Sokoloff, D. and A. Shukurov (Sept. 1990). "Regular magnetic fields in coronae of spiral galaxies". In: *Natur* 347, pp. 51–53.

Sokoloff, D. D., A. A. Bykov, A. Shukurov, et al. (Aug. 1998). "Depolarization and Faraday effects in galaxies". In: *MNRAS* 299, pp. 189–206.

Stil, J. M., M. Krause, R. Beck, et al. (Mar. 2009). "The Integrated Polarization of Spiral Galaxy Disks". In: *ApJ* 693, pp. 1392–1403.

Tabatabaei, F. S., R. Beck, E. Krügel, et al. (Nov. 2007). "High-resolution radio continuum survey of M 33. II. Thermal and nonthermal emission". In: *A&A* 475, pp. 133–143.

Tabatabaei, F. S., E. Schinnerer, M. Krause, et al. (Feb. 2017). "The Radio Spectral Energy Distribution and Star-formation Rate Calibration in Galaxies". In: *ApJ* 836, 185, p. 185.

Tabatabaei, F. S., P. Minguez, M. A. Prieto, et al. (Jan. 2018). "Discovery of massive star formation quenching by non-thermal effects in the centre of NGC 1097". In: *Nature Astronomy* 2, pp. 83–89.

Taylor, A. R., J. M. Stil, and C. Sunstrum (Sept. 2009). "A Rotation Measure Image of the Sky". In: *ApJ* 702, pp. 1230–1236.

Tucci, M., E. Martínez-González, L. Toffolatti, et al. (Apr. 2004). "Predictions on the high-frequency polarization properties of extragalactic radio sources and implications for polarization measurements of the cosmic microwave background". In: *MNRAS* 349, pp. 1267–1277.

Tully, R. B. (May 1974). "The Kinematics and Dynamics of M51. 11. Axisymmetric Properties". In: *ApJS* 27, p. 437.

Van Eck, C. L., J. C. Brown, J. M. Stil, et al. (Feb. 2011). "Modeling the Magnetic Field in the Galactic Disk Using New Rotation Measure Observations from the Very Large Array". In: *ApJ* 728, 97, p. 97.

Vernstrom, T., B. M. Gaensler, V. Vacca, et al. (Apr. 2018). "Radio polarization properties of quasars and active galaxies at high redshifts". In: *MNRAS* 475, pp. 1736–1755.

Walsh, W., R. Beck, G. Thuma, et al. (June 2002). "Molecular gas in NGC 6946". In: *A&A* 388, pp. 7–28.

Walter, F., E. Brinks, W. J. G. de Blok, et al. (Dec. 2008). "THINGS: The H I Nearby Galaxy Survey". In: *AJ* 136, 2563-2647, pp. 2563–2647.

Wielebinski, R. and R. Beck, eds. (2005). *Cosmic Magnetic Fields*. Vol. 664. Lecture Notes in Physics, Berlin Springer Verlag.

Worrall, D. M., M. Birkinshaw, R. A. Laing, et al. (Sept. 2007). "The inner jet of radio galaxy NGC 315 as observed with Chandra and the Very Large Array". In: *MNRAS* 380, pp. 2–14.

Zweibel, E. G. (Aug. 2011). "Magnetic Fields in Galaxies". In: *Astrophysical Dynamics: From Stars to Galaxies*. Ed. by N. H. Brummell, A. S. Brun, M. S. Miesch, et al. Vol. 271. IAU Symposium, pp. 135–144.

List of Figures

List of Tables